UNIVERSITÀ
DEGLI STUDI
DI PADOVA

Sede Amministrativa: Università degli Studi di Padova

Dipartimento di Ingegneria Industriale

CORSO DI DOTTORATO DI RICERCA IN: Ingegneria Industriale
CURRICOLO: Ingegneria Dell'Energia
CICLO XXIX

ENERGY EFFICIENT BUILDING'S ENVELOPES

Numerical and experimental analysis of innovative solutions

(Research is funded by ERAMUS MUNDUS Lot 1 Fatima Al Fihri scholarship program)

Coordinatore: Ch.mo Prof. Paolo Colombo
Supervisore: Ch.mo Prof. Ernesto Benini
Co-Supervisori: Ch.mo Prof. Roberto Zecchin
Ch.mo Prof. Angelo Zarrella

Dottoranda: Hagar Elarga

الحمد لله الذي بنعمته تتم الصالحات

ACKNOWLEDGMENTS

This research would not be accomplished without the support of many persons, first my supervisor Prof Ernesto Benini, when I count my blessings in the three years of my PhD I count you twice, thank you for all the guidance, support encouragement and motivation. My co-supervisor Prof Roberto Zecchin, thank you for your help and technical advices. My friend and teacher Prof. Angelo Zarrella, thank you for your sincere support and all the teaching hours. Prof. Francesco Goia, my research's flourish phase has started by our collaboration, thank you for enforcing me to challenge myself.

I would like to thank Prof Valentina Serra for her support in carrying out the experimental analysis.

My friends Gabriele Bedon, Manuela Campanale and Valentina Tono, thank you for the support thorough my hardest times, laughter and good memories. Rima Alsaghier my friend, sister, soulmate, Abdelrahman my little brother and close friend, my niece Dilara, I am thankful to have you all in my life.

My parents, I am grateful for all the support, encouragement, containing and pushing to always be a better person. You rose me on kindness, hard working and to transform disappointments into successful achievements, Thank you.

To all infants with type 1 diabetes,

Abstract

The aim of this study is to set up a simplified and validated numerical platform to describe several technologies concerning the energy performance improvements of glazed and opaque building envelopes. The study included the validation of DIGITHON, a detailed simulation software and the development of a simplified transient numerical model in respect of glazed buildings. DIGITHON, was validated against experimental data, and then a parametric study was carried out through it to evaluate the air pre-heat efficiency of implementing the façade as an energy recovery unit. The simplified model was dedicated to the thermal engineering designers dealing with projects preliminary phases .The simplified model was validated against experimental data. Later an extensive comparison between the detailed software DIGITHON and the simplified model was carried out for different climatic conditions to evaluate the influence of considering indoor zones thermal inertia. Although the simplified model estimates thermal loads higher than DIGITHON, nevertheless this can be considered a beneficial design safety aspect as long as it is implemented in the preliminary design phases. Later an innovative locating of photovoltaic modules at building glazed facades was investigated through the commercial software TRNSYS. The methodology of modelling double skin-glazed façades combined with different strategies of ventilation applying TRNflow software was thoroughly clarified. The results show a reduction in thermal heating loads compared to conventional location of PV on external building surfaces. On the other hand the cooling loads are increased, hence to improve the performance of the system in summer hot season, the technology of phase changing material (PCM) was tackled in the research as a latent thermal storage system. A numerical investigation of the effect of PCM in building sector, solely and combined with PV modules to improve its thermal performance, has been carried out. Two numerical models (equivalent capacitance and enthalpy linearization methods) describing the PCM thermal and optical performance have been developed and validated. Results show that thermal loads reductions of a system implementing PV/PCM modules reach 30% in summer season. Afterwards, the research through experimental campaign and numerical heat transfer modelling optimised the selection and location of two technologies within a residential roof attic: the technologies considered were PCM modules and reflective surfaces; five transient numerical models have been developed and validated. The results clarify the influence of the proper selection for melting-solidification PCM range suiting each application in order to reach optimum specific heat capacity values which could improve the overall thermal balance of the inner zone. Finally, computational fluid dynamics CFD models have been applied to different case studies to describe the thermal performance of vertical glazed envelopes.

Involucro edilizio ad alta efficienza energetica.

Analisi sperimentale e numerica di soluzioni innovative.

Sommario

Lo scopo di questo studio è sviluppare e validare una piattaforma numerica semplificata per descrivere diverse tecnologie riguardanti i miglioramenti di prestazione energetica dell'involucro edilizio costituito da parti vetrate e opache. Lo studio comprende lo sviluppo e la validazione di due modelli numerici transitori in materia di edifici vetrati. Successivamente un software commerciale, TRNSYS, è stato applicato per indagare una modalità innovativa di integrazione di moduli fotovoltaici nell'involucro edilizio. Un altro tema promettente, affrontato in questa ricerca, è l'indagine numerica sui materiali con cambiamento di fase (PCM) nel settore delle costruzioni, da soli ed in combinazione con moduli fotovoltaici per migliorarne le prestazioni. Due modelli numerici (metodo della capacità equivalente e metodo della linearizzazione dell'entalpia) che descrivono le prestazioni termiche e ottiche dei PCM sono stati sviluppati e validati. Un'analisi sperimentale e numerica ha permesso di ottimizzare la selezione e la posizione di due tecnologie, moduli PCM e superfici riflettenti, nel sottotetto di un edificio residenziale. Cinque modelli numerici transitori sono stati sviluppati e validati a tal fine. Infine, modelli di fluidodinamica computazionale (CFD) sono stati applicati per descrivere le prestazioni termiche delle chiusure vetrate e analizzarle attraverso diversi casi di studio.

Keywords

Glazed and opaque buildings, transient numerical heat transfer, PCM, PV integrated in buildings, TRNSYS, MATLAB, CFD fluent.

Table of contents

Thesis outlines

In Europe, building sector consumes alone about 40% of the total energy consumption. Accordingly, the more researchers simplify the modelling and analysing of new technologies the more communities are close to the nearly zero energy building prevalence in order to meet Europe energetic goals of 2020. The research illustrates a numerical foundation of several technologies to improve the building energy performance including ventilated glazed facades, PV integrated in buildings, phase changing materials and their integration in envelopes and finally the application of CFD models taking into account the radiation heat transfer mode to simulate the glazed façade buildings.

The research is divided into six chapters. Chapter one is discussing the general heat transfer modes thorough glazed building envelopes. The finite difference and the resistance-capacitance (RC) methods have been highlighted briefly. The classification of glazed façade buildings in respect of ventilation mode, type and geometrical composition is added. Chapter two discusses the methodology of developing transient numerical codes taking into account the heat transfer through glazed elements. Two models (a detailed one represented by DIGITHON and a new simplified mathematical model) have been explained and validated. Later a thermal energy analysis has been carried out to evaluate the difference between simplified and detailed models. Chapter Three discusses the methodology of modelling through TRNSYS a glazed façade and PV integration in vertical envelopes. Results include a comparison of thermal loads and PV electrical production in different climatic conditions. Chapter Four reports and validates numerical methods of modelling PCM integration in buildings including shortwave radiation analysis in respect of the PCM phase change characteristic. Results include energy performance evaluation in different climatic conditions in respect of PV and PCM modules integration in buildings. Chapter five includes an experimental and numerical analysis of PCM and reflective surfaces integration in residential roof attic through fives samples. PCM type selection and location of reflective surfaces optimization are illustrated. The validation of five numerical models is added to expand the experimental analysis. Chapter Six reports CFD models to simulate glazed surfaces implementing solar tracing and radiation heat transfer models. Some case studies clarify the air circulation influence on the electrical production of integrated PV module inside the faced cavities.

Chapter -1
Glazed envelopes heat transfer analysis

1.1 Introduction

Energy crisis and environmental pollution are the main problems which threating the continuity of the mankind. Among diverse consuming energy sectors; from industrial, transportation to building sector, the latter alone is considered the highest. The primary energy consumed by buildings accounting for 23% in Spain, 25% in Japan, 28% in China, 39% in the United Kingdom, 40% in Europe, 42% for Brazil, 47% for Switzerland, and 50% for Botswana [1]. The United Nation Environment Programme [1] also reported that 30–40% of the world's total primary energy expenditure is consumed in buildings. However, building envelope's either (transparent or opaque) is closely connected to the building energy performance since that most of thermal heat losses and gains are happening through it. Many advanced and sustainable building materials have been developed for building envelope applications, such as fiber-reinforced plastic, unfired clay bricks, hollow bricks, concrete hollow blocks, aerated concrete blocks, sandwich panels, straw-clay mixtures, heat preservation and insulation glasses, hollow glasses, glass mosaic [2]. Chan KT et al. [3] reported that an energy-effective building envelope design saves 35% of the total cooling load and 47% of the peak cooling demand respectively. Using thermal-insulation materials in building envelopes not only reduces the energy consumption of HVAC system [4,5], but also obtains a more comfortable indoor thermal environment [6]. Friess et al. [7] investigated the influence of insulation materials on wall performance in Dubai. Results found that an energy saving of 30% can be achieved with proper insulation design. There are several strategies to improve building enveloped design. One novel strategy is to add self-shading components, including overhangs, light shelves, louvers, etc. to glaze-based envelopes to regulate solar radiation [8]. Large glazed area in modern buildings makes the indoor environment exposed to and dependent on solar radiation, which results in large cooling demand in hot-weather conditions and can help to reduce heating demand in cold-weather conditions. Self-shading envelopes block solar radiation in summer and permits it in winter, thus, contributes greatly to reduce the cooling load in summer and heating load in winter. Laura et al. [9] reported a critical analysis on the effects of different self-shading envelopes on thermal and lighting performances. Results showed that the self-shading envelope has a potential in improving indoor thermal and lighting environment. Steinar et al. [10] concluded that solar shading systems are vital for office building for the purpose of reducing the cooling demand. For south-facing façades, with a

proper design of shading devices, the energy demand can be reduced by 9%. Corgnati et al. [11] have mentioned that ventilated facade is subjected to dynamic behavior and adapting its working strategy to maintain an appropriate balance between optimum interior conditions and environmental performance. To conclude, the challenge is to optimize the building sector energy consumption both the newly and old constructed by:

- Comprehend building structure, heat transfer analysis and sources of energy losses.
- Analyze dynamic energetic performance of building components.
- Investigate the implementation of new technologies and materials.

This chapter is dedicated mainly to analyze heat transfer modes thorough glazed envelopes, different correlations to obtain convection heat transfer coefficients and finite difference method in the numerical heat transfer analysis.

1.2 Glazed Façade's theoretical heat transfer modes

Thermal performance of DSF is depending on different factors such as glazing system composition, glass technical characteristics, weather conditions and cavity ventilation type. In terms of thermo-physical parameters, transparent elements on one hand may lead to many savings due to natural lighting; on the other hand they are still one of the weakest components of the building envelope [12]. Accordingly, the clarified heat transfer through transparent elements is considered as the generic heat transfer case for building envelopes since it includes all heat transfer modes of opaque layers added to the short wave radiation term.

1.2.1 Heat transfer Modes through glazed Facades

All kind of heat transfer mechanisms come into action simultaneously and overlap each other through glazed facades (Fig.1.1a). Those mechanisms include conduction, convection and radiation. The theoretical energy balance through façade could be identified by a thermal resistance nodal network (Fig.1.1b). Heat travels from the external layer to the inside room passing through different resistances. R_k represents the conduction heat flow through glass layers, R_c represents the convection heat flow either from the external or internal air flow or the ventilation inside the facade cavity, and finally R_r represent the infrared radiation heat exchange between different surfaces of the façade module, added to solar radiation transmitted within the facade layer.

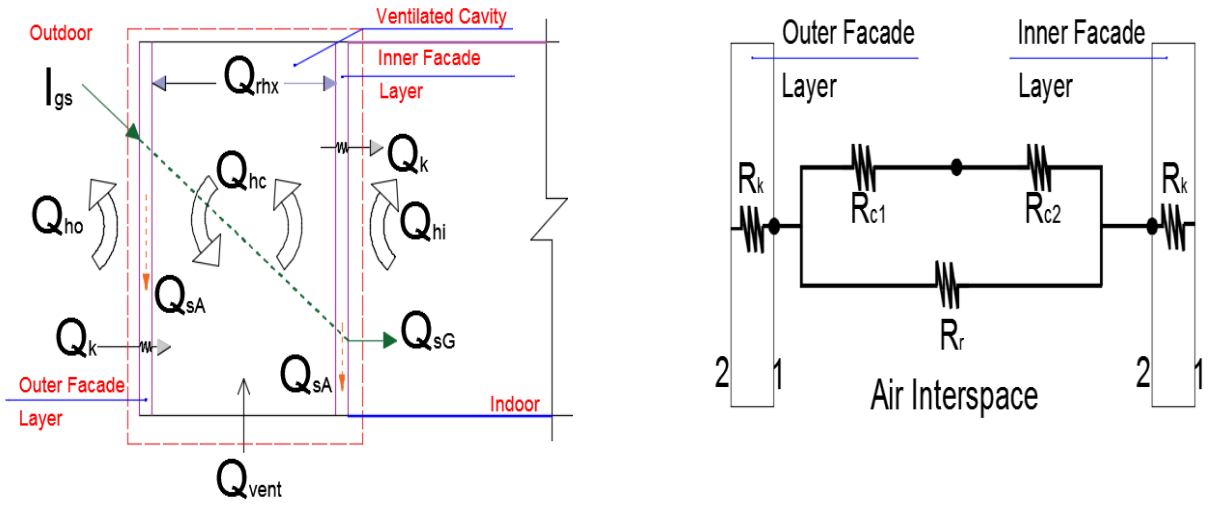

(a) **(b)**

Fig.1.1 Glazed façade: (a) Façade Energy Balance scheme, (b) Facade RC nodal scheme

a- Conduction heat transfer occurs inside substances; Thermal conduction resistance is identified by Equation (1.2) taking into consideration the thermal conductivity coefficient is constant, and thermal capacitances within glazed layer is assumed to be negligible.

$$Q_k = \frac{T_{(i)1} - T_{(i)2}}{R_k} \quad \textbf{(1.1)}$$

$R_k = \left(\frac{x}{k}\right)$ conduction thermal resistance of the layer ($m^2\ W^{-1}\ K$) **(1.2)**

b- Convection heat transfer occurs in different thermal modes (Fig.1.1b): between the external glazed layer and ambient air Q_{ho} , Equation (1.3), followed by convection transfer between ventilation air temperature and the air inside the cavity Q_c , Equation (1.4) , finally the convection heat transfer between the inside room air and internal glazed layer Q_{hi} , Equation (1.5). The ventilation thermal load $Q_{vent}$is obtained from Equation (1.6)

$$Q_{ho} = \frac{T_{ao} - T_{so}}{R_{co}} \quad \textbf{(1.3)}$$

$$Q_c = \frac{T_{s1} - T_{ac}}{R_c} \quad \textbf{(1.4)}$$

$$Q_{hi} = \frac{T_{ai} - T_{si}}{R_{ci}} \quad \textbf{(1.5)}$$

$$Q_{vent} = m^{\circ}\, c_p(T_{av} - T_{ac}) \quad \textbf{(1.6)}$$

Thermal convective resistance is identified by:

$$R_C = \frac{1}{h_c} \quad \text{Convection thermal resistance per unit of area } (m^2\ W^{-1}\ K) \quad \textbf{(1.7)}$$

Convection heat transfer coefficients

The convection heat transfer coefficient is an important parameter which is affecting thermal performance of the façade, hence the unit less numbers and correlations in Equations (1.8 to 1.12) were classified based on the considered glazed layer

- **Between outside ambient and external layer** [13]**:**

$$h_{co} = 5.62 + 3.9\,\nu \quad \textbf{(1.8)}$$

where ν is the wind velocity (ms^{-1})

- **Between inside ambient and internal layer** [13]**:**

$$h_{ci} = \left(\left[1.5 \cdot \left(\frac{\Delta T}{H}\right)^{1/4}\right]^6 + \left[1.23 \cdot (\Delta T)^{1/3}\right]^6\right)^{1/6} \quad \textbf{(1.9)}$$

Where:

H is the facade height (m)

ΔT is the difference between surface and ambient air temperature

- **Flow inside the cavity**

Characteristics of this case is a little more complicated, since the flow description inside the cavity has several possibilities:

- **The laminar plate flow with low solar irradiance values** [14]:

$$\mathrm{h_c} = \frac{k_{air}}{H}.0.664\,.Re_H^{0.5}\,\mathrm{Pr}^{1/3} \quad \textbf{(1.10)}$$

• **The laminar plate flow with high solar irradiance values** [15]:

$$h_c = \frac{k_{air}}{H}.0.906\,.Re_H^{0.5}\,\mathrm{Pr}^{1/3} \quad \textbf{(1.11)}$$

• **The natural convection** [16]:

$$h_c = \frac{k_{air}}{H}\,\frac{4}{3}\left(\frac{Gr_H}{4}\right)^{0.25} g(Pr) \quad \textbf{(1.12)}$$

where:

$$g(Pr) = \frac{0.75Pr^{0.5}}{(0.609 + 1.221\,Pr^{0.5} + 1.238Pr)^{0.25}} \quad \textbf{(1.13)}$$

• **The flow in narrow open cavity** [15]:

$$h_c = \frac{k_{air}}{L}\,0.68\,\left(Ra_L\frac{L}{H}\right)^{0.25} \quad \textbf{(1.14)}$$

Dimensionless numbers Re (i.e. the Reynolds number), Pr (i.e. the Prandtl number) and then the Nusselt number (Nu), Equations (1.15), (1.16) and (1.17) respectively:

$$R_e = \frac{\rho \times V \times L}{\mu} \quad \textbf{(1.15)}$$

$$P_r = \frac{\mu c}{\lambda} \quad \textbf{(1.16)}$$

The Prandtl number of air in building engineering applications is assumed constant with value Pr=0.72, [17].

The correlation in Equation(1.17) is used to calculate the average heat transfer coefficient over the entire plate, including laminar and turbulent conditions [18].

$$N_u = \left(0.037 \times {R_e}^{0.8} - 871\right){P_r}^{\frac{1}{3}}\ 5 \times 10^5 \le R_e \le 10^7 \text{ and } 0.6 \le P_r \le 60 \quad \textbf{(1.17)}$$

c- Radiation heat transfer

It does not rely upon any contact between the heat sources, no mass is exchanged and no medium is required in the process. The radiation heat transfer based on the Grey surface model is the most popular implemented method. It is defined by considering only spectral-average thermo-optical properties (one value in each band) corresponding to non-overlapping regions of the spectrum, with spectral uniformity in each of the two considered bands: solar i.e. short wave radiation, and infrared i.e. long wave radiation.

Long wave radiation. It is defined also as thermal radiation and included in the heat exchange between each i^{th} surface, (i) is the generic glazing element. This long wave radiation is governed by the temperature and emissivity of the surface.

Kirchhoff's Law

Real bodies radiate less effectively than black bodies. The measurement of this is the emittance ε, defined by Equation (1.18)

$$\varepsilon = \frac{E_{Real}}{E_{Black}} \tag{1.18}$$

Where E is the emitted radiation.

Kirchhoff's Law which implies that good radiators are good absorbers. Hence the level of the emittance can be related to the absorbance by Equation (1.19). It was derived for the case when $T_{body} = T_{surroundings}$ and it is not strictly true for all circumstances when the temperature of the body and surrounding are different but it is true when the absorbance and emittance are not function of wave lengths, this situation describes grey body.

$$\varepsilon = \frac{E_{Real}}{E_{Black}} = \alpha \tag{1.19}$$

On the other hand the rate of heat transfer between two surfaces depends on their characteristics and geometry (Fig.1.2) [16]. The net radiated heat is evaluated in Equation (1.20) and accordingly the radiation thermal resistance is determined by Equation (1.21).

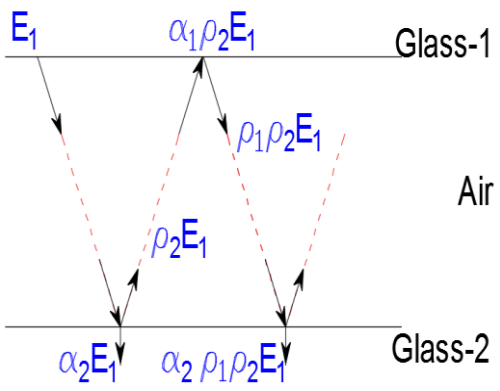

Fig.1.2 Path of a photon between two gray surfaces

$$q_{1-2} = \frac{\sigma({T_1}^4 - {T_2}^4)}{(\frac{1}{\varepsilon_1} + \frac{1}{\varepsilon_2} - 1)} \quad \textbf{(1.20)}$$

Thermal radiation resistance is obtained from Equation (1.21)

$$R_{rad} =. \frac{\left[\frac{1}{\varepsilon_{(i)_2}} + \frac{1}{\varepsilon_{(i+1)_1}} - 1\right]}{\left[4.\sigma.{T_{avg}}^3\right]} \quad \textbf{(1.21)}$$

Where:

σ is the Stefan-Boltzmann constant (W m^{-2} K^{-4})

T_{avg} is the mean temperature between the two opposed surfaces.

ε is the surface emissivity for long wave radiation.

Shortwave radiation

Solar radiation (shortwave radiation) plays an important role in the heat exchange phenomena through glazed façade. It depends on the global solar radiation, incident angle, optical and technical properties of the glazed system. Each glass layer is identified by absorption (α), reflection (ρ) and transmission (τ) factors where:

$$\alpha + \rho + \tau = 1 \quad \textbf{(1.22)}$$

Generally the analysis of the solar shortwave radiation is carried out by separating the beam solar radiation I_B, diffuse solar radiation I_D components and the beam solar incident angle θ_B. These components could be obtained directly from commercial soft wares such as TRNSYS or by available online data such as world solar radiation database WRDB (http://wrdc.mgo.rssi.ru/). However, diffuse solar radiation incident angle θ_D as a good approximation is assumed to be equal to 60°[19]. Afterwards the angular/ optical properties concluded in the absorption coefficient α_a for each glass element are identified based on a spectrum angles from 0° to 90° and it could be obtained from many commercial software's such as WINDOW 6[20], (Fig.1.3).

Hence a generalized equation for each glass layer could be derived to relate the hourly coincident Θ_B with absorption coefficient α_{aB}. On the other hand, in diffuse solar radiation only one value of α_{aD} is considered which is opposed to Θ_D equal to 60°, the value of the absorbed energy by each glass shall be considered in the thermal exchange by dividing its value equally between the two thermal nodes representing inner and outer layer of each glass layer (i).

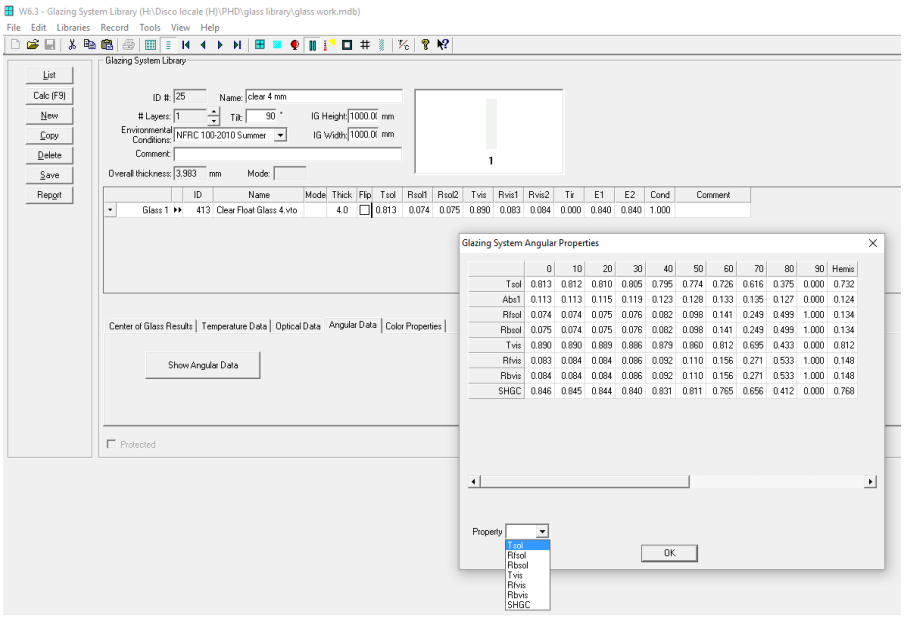

Fig.1.3 Glass angular data via Window6

$$\mathrm{I_{gs}} = \text{Global vertical solar Irradiance } (\mathrm{W/m^2}) \tag{1.23}$$

$$I_{ref} = I_{gs} \times \rho_{SB} \tag{1.24}$$

$$Q_{sA} = I_{gs} \times \alpha_{aB} \tag{1.25}$$

$$Q_{sG} = I_{gs} - \sum_{i=1}^{i^{th}} (Q_{sA}) - I_{ref} \tag{1.26}$$

1.3 Numerical dynamic heat transfer –Finite difference method

There are several computational approaches to describe numerical heat transfer. One of the most common is finite difference method. It is used to approximate differential equations. The result is a set of algebraic equations for the nodal unknowns with information from continuum replaced by information at discreet nodal points. The algebraic equations have to be solved simultaneously at discreet time steps for transient conditions. The simplicity of the replacement process and general ease of the algebraic equations solution account for the popularity of such a method. Considering a homogeneous medium within which there is no motion (advection) the temperature distribution *T*(*x*, *y*) is expressed in cartesian coordinates. an infinitesimally small (differential) control area, *dx, dy* is defined. In the absence of motion there are no changes in mechanical energy and no work being done

on the system. Only thermal forms of energy need be considered. The general equation describing two dimensional conduction heat transfer, Equation (1.27) applies:

$$\left(\frac{\partial^2 T}{\partial x^2} + \frac{\partial^2 T}{\partial y^2}\right) = \frac{1}{\alpha}\frac{\partial T}{\partial t} \qquad \textbf{(1.27)}$$

Where T is temperature, α the thermal diffusivity of the material and t is the time
The finite difference approximation can be created using direct approach. For the grid point (i, j) in (Fig.1.4) the two point central difference approximations for Equation (1.28) becomes:

$$\frac{T_{i+1,j} - 2\,T_{i,j} + T_{i-1,j}}{(\Delta x)^2} + \frac{T_{i,j+1} - 2\,T_{i,j} + T_{i,j-1}}{(\Delta y)^2} = \frac{1}{\alpha}\frac{\Delta T_{i,j}}{\Delta t} \qquad \textbf{(1.28)}$$

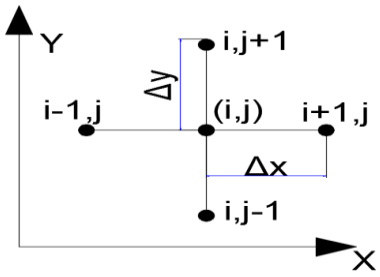

Fig.1.4 Five nodes grid

Where Δx and Δy represents horizontal and vertical distances between grid nodes. For each grid point this algebraic equation is formed, later a system of simultaneous equations may be written in a general matrix form as:

$$[A]\,(T) = (B) \qquad \textbf{(1.29)}$$

Where A is a square matrix, T is a column vector containing the unknowns nodal values of T and B is a column vector containing the source term and prescribed boundary conditions. The inverse matrix approach is used as:

$$(T) = [A]^{-1}\,(B) \qquad \textbf{(1.30)}$$

Where $[A]^{-1}$ is the inverse of the matrix A. The determinant of (A) must be non-zero for the inverse to exist.

1.4 Classification of Multiple skin façade

MSF is classified based on different categories such as:

1.4.1 Type of ventilation

There are several different typologies of ventilated DSF; they are usually grouped under box window facade, shaft-box facade, corridor facade, and multi-story facade [21, 22]. The type of ventilation refers to the air driving forces of façade cavity ventilation system. It could be characterized by:

1-Natural

2-Mechanical

3-Hybrid ventilation (mix between natural and mechanical ventilation)

1.4.2 Ventilation mode of the cavity

The ventilation mode refers to the origin and the destination of the air circulating in the ventilated cavity. The ventilation mode is independent of the type of ventilation applied. As clarified in (Fig.1.5) there are four ventilation modes as:

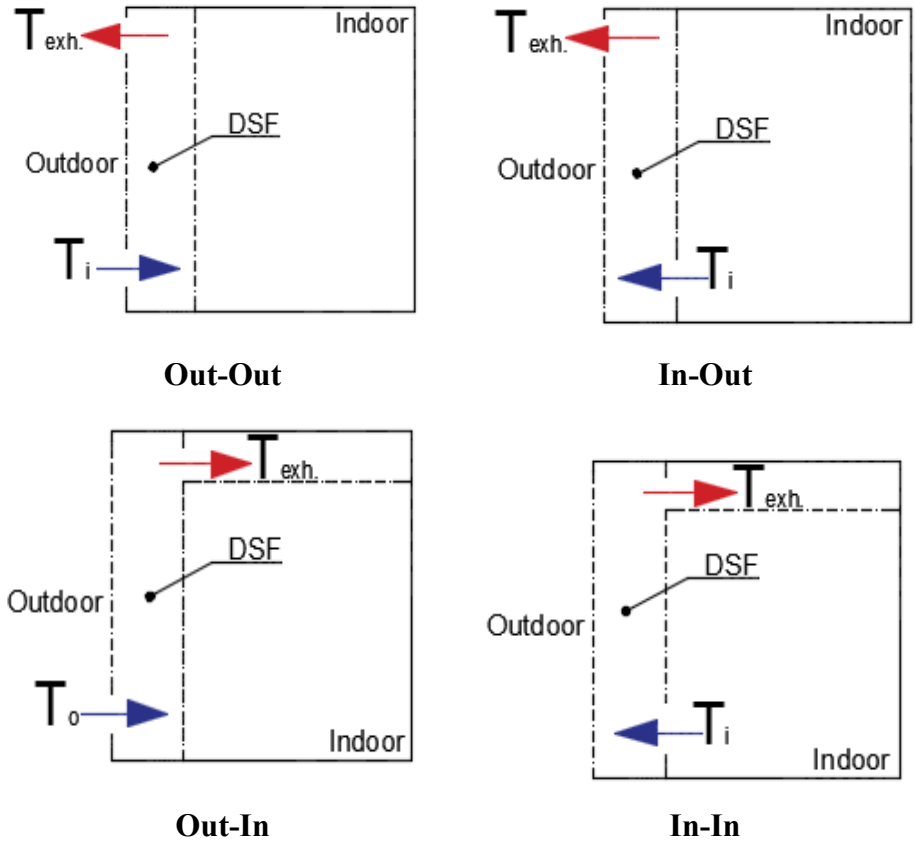

Fig.1.5 DSF ventilating techniques

Out-Out

In this ventilation mode, the air introduced into the cavity comes from the outside and is immediately rejected towards the outside. The ventilation of the cavity therefore forms an air curtain enveloping the outside façade.

Out -In

The ventilation of the façade is created with outdoor air. This air is then brought to the inside of the room or into the ventilation system. The ventilation of the façade thus makes it possible to supply the building with air.

In-Out

The air comes from the inside of the room and is evacuated towards the outside. The ventilation of the façade thus makes it possible to evacuate the air from the building.

In-In

The air comes from the inside of the room and is returned to the inside of the room or via the ventilation system. The ventilation of the cavity therefore forms an air curtain enveloping the indoor façade.

1.4.3 Geometrical composition

The partitioning of the cavity gives the information on how the cavity situated between the glazed layers is physically divided. There are several types such as (Box-window, corridor facades, multistory facades).

1. Nomenclature-Chapter 1

AFW	Air Flow Window
A_f	Area of facade
H	Plate height, (m)
h	Convection heat transfer coefficient (W/(m2.K))
I_{gs}	Global vertical radiation (W/m2)
I_{ref}	Reflective solar radiation (W/m2)
$I_{abs(i)}$	Absorbed solar radiation (W/m2)
I_{st}	Total solar radiation (W/m2)
I_{st-i}	Transmitted solar radiation through glass layer (i), (W/m2)
k	Thermal conductivity (W/m.K)
L	Plate length, (m)
R_C	Convection thermal resistance per unit area (m2 K)/W)
R_K	Conduction thermal resistance per unit area (m2 K/W)
R_{rad}	Radiation thermal resistance per unit area (m2 K/W)
Q_c	Heat flux caused by convection (W)
Q_k	Heat flux caused by conduction (W)
Q_R	Heat flux caused by radiation (W)
Q_{vent}	Heat flux caused by ventilation of the cavity (W)
QsA	Absorbed solar radiation (W)
Qsg	Solar gains (W)
QsG	Solar gain (W)
Nu	Nusselt number (-)
Pr	Prandtl number (-)
Re	Reynolds number (-)
T	temperature (˚C)
Tavg	Average temperature (˚C)
Tav	Air vent temperature (˚C)
$\Delta\tau$	Time step (S)
V	Flow velocity (m/s)
x	Glass thickness, (m)

α	Absorptivity
ρ_a	Air density (kg/m3)
η_P	Preheat efficiency
σ	Stefan-Boltzmann constant, 5.67 x 10-8 (W/(m2 K4))
τ_i	Transmission coefficient (-)
ε	Emissivity (-)
μ	Dynamic viscosity (kg/(m s))
θ_B	Beam Solar radiation incident angle (°)
θ_D	Diffuse Solar radiation incident angle (°)

1. References –Chapter 1

1 Tiantian Zhang, Yufei Tan, Hongxing Yang, Xuedan Zhang, The application of air layers in building envelopes: A review. Applied Energy 165 (2016) 707–734.

2 Goodhew S, Griffiths R. Sustainable earth walls to meet the building regulations. Energy Build 2005; 37(5):451–9.

3 Chan KT, Chow WK. Energy impact of commercial-building envelopes in the sub-tropical climate. Appl Energy 1998;60(1):21–39.

4 Chowdhury AA, Rasul MG, Khan MMK. Thermal-comfort analysis and simulation for various low-energy cooling-technologies applied to an office building in a subtropical climate. Appl Energy 2008; 85(6):449–62.

5 Kazim AM. Assessments of primary energy consumption and its environmental consequences in the United Arab Emirates. Renew Sustain Energy Rev 2007; 11(3):426–46.

6 Wang JC, Yan PY. Influence of external thermal insulation compound system on the indoor temperature and humidity. Low Temper Arch Technol, 2004; 2:80–1.

7 Friess WA, Rakhshan K, Hendawi TA, et al. Wall insulation measures for residential villas in Dubai: a case study in energy efficiency. Energy Build 2012; 44(1):26–32.

8 Capeluto IG. Energy performance of the self-shading building envelope. Energy Build 2003; 35(3):327–36.

9 Bellia L, Marino C, Minichiello F, et al. An overview on solar shading systems for buildings. Energy Procedia 2014; 62:309–17.

10 Grynning S, Time B, Matusiak B. Solar shading control strategies in cold climates – heating, cooling demand and daylight availability in office spaces. Sol Energy 2014; 107(9):182–94.

11 S.P. Corgnati, M. Perino, V. Serra, Experimental assessment of the performance of an active transparent façade during actual operating conditions, Solar Energy 81 (2007) 993–1013.

12 H. Manz, P. Menti, Energy performance of glazings in European climates, Renewable Energy 37 (2012) 226-232.

13 Fabio Zanghirella, Marco Perino, Valentina Serra, A numerical model to evaluate the thermal behaviour of active transparent facades. Energy and Buildings 43 (2011) 1123–1138

14 R. Charron, K.Andreas Athienitis, Optimization of the performance of double-facades with integrated photovoltaic panels and motorized blinds, Solar Energy 80 (2006) 482–491.

15 D.Saelens. 2002. Energy Performance Assessment of Single Storey Multiple-Skin Facades. PhD thesis publication, Katholieke Universiteit Leuven, Belgium.

16 F.P.Incropera, D.P.De Witt, 1990. Fundamentals of Heat and Mass Transfer, third ed. John Wiley and Sons, New York, pp. 468–585.

17 A. Bejan, Heat transfer, New York: Wiley, 1993.

18 Y. Çengel, Heat and mass transfer: a practical approach, 2nd edition, McGraw-Hill, 2007.

19 J.A. Duffie, W.A. Beckman, Solar Engineering of Thermal Processes, 2nd edition, John Wiley & Sons, New York, 1991.

20 Department of Energy-DOE, Window v6.3.9.0, Energy efficiency and renewable energy office of building technology, USA. 2010.

21 P.C. Wang, Natural ventilation in double-skin facade design for office buildings in hot and humid climate, Doctoral Thesis, University of New South Wales, Australia, 2008.

22 A. De Gracia, A. Castell, L. Navarro, E. Oro, L.F. Cabeza, Numerical modeling of ventilated facades: A review, Renewable and Sustainable Energy Reviews 22 (2013) 539‑549.

Chapter-02
Numerical heat transfer through glazed facades

Introduction

Apart of commercial transient software, the clarification of simplified numerical heat transfer codes, which could be used by non-specialist researchers i.e. user friendly is the focal purpose of this chapter. Concerning glazed enveloped buildings, the code has to be able to describe the energy performance accurately and simply without time consuming or high computing capabilities. The chapter includes the clarification and validation versus experimental measurements of two developed transient heat transfer models DIGITHON and simplified 1D model dedicated for the glazed façade buildings. Added to expanded case studies of diverse climatic conditions to evaluate double skin façade building energetic performance.

2.1 Numerical heat transfer of glazed envelopes background

Reliability and easy to apply of the building energy simulation software's are considered the cornerstones of more rigid steps towards smarter communities in the sense of estimating thermal energy requirements. It is important to highlight that there is a lack in simulation software concerning facades buildings in general or integrated with other technologies such as PV modules, phase changing materials PCM and how to investigate the influence of using facades different ventilation methodologies. Few (or even no) regulations, standards or well-established procedures are available to assess their performance [1]. It is well known that flow characteristics of DSF channel play a key role in the performance of the system. Grabe [2] developed and validated a simple simulation algorithm based on energy transport and Bernoulli equations to study the thermal behavior and flow characteristics of DSF. The model proves the sensitivity and the difficulty of modeling flow resistances in the air channel. Ciampi et al. [3] have presented a numerical method based on the electrical analogy to calculate the electrical energy savings in buildings due to the use of ventilated facades in Southern Europe climates during summer. The model was used to analyze two particular cases. In the first case, inner masonry wall was given and the authors optimized the air duct and the outer facing. On the other hand, in the second case, the outer facing was fixed, air duct and inner masonry were parameterized. It was concluded that in all cases the energy demand decreased with the air duct width and solar radiation. It was stated that the use of well-designed ventilated facades in buildings can reduce the electricity consumption for summer cooling by more than 40%. Shameri et al. [4] reviewed the literature related to DSF concluding that ventilation has

been widely studied, while lack of research has been carried out regarding to the day lighting capacity of the envelope. The high fire hazard risk of this type of envelopes and the need of more research for better understanding of the DSF effects was also mentioned. Sealens [5] has presented thermal performance and energy savings comparison between different facades typologies, such as IGU_i (Internal shading devices), IGU_e (external shading device), DSF, AFW (air flow window) and SUP (supply window). The AFW has the lowest transmission losses and the second lowest heating demand. The order in cooling efficiency differs from the order in heating efficiency. Nevertheless, the IGU_e has been found to have the lowest cooling load; these results contradict the findings of Haddad and Elmahdy [6]. The differences are a consequence of the different climate, but can also be attributed to the effect of the inlet temperature and single zone modeling. The results further indicate that because of the high temperatures in the cavity, natural ventilation of offices through DSFs is not a good option in summer. Park et al. [7,8] optimized the energy performance, visual comfort, as well as thermal comfort of a DSF by using motorized louvers slat in the cavity and ventilation openings. Authors have developed two-dimensional lumped simulation model under different operational modes. This numerical model, instead of using empirical correlations available in the literature, was calibrated based on a parameter estimation technique using in situ measured experimental data. It was demonstrated that in lumped models based on descriptions of physical processes and augmented by calibration parameters to deal with the assumptions (surface temperatures, constant convective heat transfer coefficients, etc.), the calibration process plays an important role in the performance of the model and improves the accuracy of the models in comparison to experimental data. Balocco [9] used non-dimensional analysis to determine the thermal performance of a naturally ventilated façade. Balocco and Colombari [10] have presented a dimensionless model of a mechanically ventilated facade. This methodology applies the Buckingham theorem to create correlations depending on dimensionless numbers; hence, the same parameters might describe the process at different scales. For the naturally ventilated DSF, 14 dimensionless numbers with physical meaning were used to create a correlation based on experimental data, and to determine the heat flux transferred to the inner environment throughout the wall. On the other hand, 12 dimensionless parameters were used to describe the thermal performance of the mechanically ventilated facade. Both correlations proved to be valid for a wider range of conditions and were validated using experimental data and CFD simulation results. Although CFD would provide greater accuracy and flexibility in evaluate thermal performance of DSF but it would increase the runtime substantially and increase the potential for incorrect input with users who are not familiar with it [11]. The non-dimensional models assume constant thermo-physical properties, except for air density, and they are presented as basic tools to evaluate some specific parameters which might be useful to design ventilated facades without using

high complex simulation programs. Hensen et al. [12] stated that the air flow network method treats every building component and relevant HVAC fluid flows systems as a network of nodes representing rooms, parts of rooms, and system components, with inter nodal connections representing the distributed flow paths associated with cracks, doors, pipes, pumps, ducts, fans, and the like. Conservation of mass for the inlet and outlet flows of each node leads to a set of simultaneous and non-linear Equations, which are integrated over time to characterize the flows. This airflow network modeling can provide fast useful information about bulk flows without consuming high computational resources. This method uses pressure differences and discharge coefficients for simple cross ventilation and network flow analysis where multiple inlets and outlets and internal flow branching occurs [13]. Fallahi et al. [14] described numerically an innovative design of DSF integrating passive thermal mass in the air channel. The airflow inside the channel was assumed one-dimensional and vertical, so no airflow modeling was needed and the given air flow rate was directly applied to reckon the convective heat transfer coefficients. On the other hand, when the façade is naturally ventilated, the nodal unidirectional airflow network method is applied. The authors used the numerical model to compare the annual heating and cooling loads of the new system against traditional DSF with and without thermal mass walls. The results showed that the use of the new system could reduce the cooling load in a 27% in comparison to a traditional DSF. It was also highlighted that the use of any of the ventilated facades skin (inner or outer wall) as a mass component reduces the cooling load, but increases the energy consumption during the winter period. This is because the thermal mass increases the stack effect inside the cavity. De Herde and Gratia [15] analyzed the parameters that influence the green house effect in a DSF cavity (solar radiation level, orientation and shading devices, opaque walls proportion, wind speed, color of shading devices, depth of the cavity, glazing type, and openings). The authors concluded that the greenhouse effect must be minimized when no natural cooling strategies are used. On the other hand if those strategies are applied, the greenhouse effect is favorable when the DSF is south oriented. Joe et al. [16] presented a study based on measurements on actual behavior of a multi-story DSF in South Korea. The simulation model was tuned against measured data, and a case study was conducted based on the model. Seasonal load characteristics of the DSF building were examined in comparison with the single skin facade (SSF) building. The DSF building resulted in 15.8% and 7.2% reductions in heating and cooling energy consumptions respectively, compared to the SSF building. During the heating seasons, heated air in the cavity was introduced to an outdoor air-mixing box of a HVAC system. These seasonal proposed models resulted in 28.2% and 2.3% reductions in heating and cooling energy consumption respectively. Crawley et al. [17,18] have presented a comparison

between twenty dynamic simulation tools, showing TRNSYS is one of the best options for HVAC systems integration.

Todorovic and Maric [19] developed a model for evaluating the thermal performance of a DSF system. Different methods for estimating the inter-space air temperature and the associated cooling/heating loads were presented. Calculations are made for the climatic conditions of Europe mid-latitude (45° N). Results showed that in winter double façade reduces heat losses by more than 50%, due to both the higher inter-space temperature and the decreased infiltration. In summer period air circulation is essential. The airflow velocity strongly influences the inter-space temperature, and hence the heat gains by transmission. Arons [20] developed a simplified numerical model of a typical DSF. The purpose of steady state model is to predict the energy performance of multiple types of DSF. The basic configuration for the window under study has a layer of insulating glass on the exterior, an air cavity and a single interior layer of glass. An inlet is assumed at the bottom and an outlet at the top of the DSF. The model runs into difficulty with evaluating very low mass flow rates because the difference of temperature in the channel is defined relative to the inverse of the mass flow rate. Stec and Paassen [21] developed a complete procedure to calculate the airflow and temperature distribution in the double skin façade using a static thermal heat balance network and considering wind and stack effect on the airflow, as well as the wind turbulence flow in the openings. The performance was analysed based on heat recovery efficiency and the g-value. Heat recovery efficiency for the average winter day may reach even 50%. Nevertheless, the yearly average efficiency calculated by a dynamic simulation can be much lower due to the fact that the preheated ventilation is not always needed. Saelens et al. [22] presented a numerical model that evaluates the thermal behaviour of active envelopes and compared with in site measurements. Agreement between the measurements and the simulations is considered good for the mechanical flow active envelope, but less so for the natural flow variant. The results were compared to those of a traditional cladding system, active envelopes proved to have lower transmission losses but higher transmission gains. The energy demand analysis shows that the energy performance strongly depends on the way the return cavity air is used. Manz et al. [23] presented an experimental and numerical study of a mechanically ventilated DSF with integrated shading device. Optical properties are calculated and a transient 2D computational fluid dynamic model. Simulated results are compared with data derived from an experimental investigation of a mechanically ventilated glass double façade built in an outdoor test facility it was concluded that a total solar energy transmittance of 7% means that solar energy absorbed in the façade is removed efficiently by mechanical ventilation. The use of numerical models to simulate the thermal and fluid dynamic behavior of active transparent façade can therefore be considered extremely useful to assist designers' during the concept phase and to develop suitable

control and integration strategies of the facade with the building installations [24]. Fuliotto et al. [25] discussed decoupling method to separate the radiative heat transfer effects on the thermal and flow features inside a ventilated DSF in order to overcome the limitation of CFD computationally demanding modelling of radiation heat transfer models; the authors assumed that optical analysis may be conducted separately from the thermal analysis, the effect of solar radiation on a DSF was considered through a separate program [26].

Gosselin et al. [27] proposed a four step computational method that uses both computational fluid dynamics and coded radiation calculations to determine airflow and heat transfer through an airflow window. Experimental tests on a full-scale dual airflow window system were used to obtain various indoor and outdoor air and window surface temperatures for validating the computer method. The difference obtained between the computed air and surface temperatures and the measured data was less than 1 K. Jiru et al. [28] presented the application of the zonal approach for modelling airflow and temperature in a ventilated double skin facade (DSF). The zonal airflow Equation, power-law, was employed to calculate the airflow through the shading device and cavities. The zonal energy equation was used to evaluate the temperature distribution in the DSF system. The inlet-outlet temperature difference increased as height of the DSF increased and when venetian blinds were installed but it was found to decrease as the airflow rate increased. Guardo et al. [29] evaluated, by means of computational fluid dynamics [30], the influence of several construction and operation parameters of the Active Transparent Facades (ATF), such as optical properties of the materials, geometrical relations of the facade or flow stream conditions, in terms of energy savings, measured as a reduction of the solar load entering the building. It was seen that an increase of the length-to-depth ratio causes a decrease on the ATF efficiency in terms of solar load gains. For the tested cases, an increase on the turbulence intensity does not lead to improvements in the reduction of solar load gains. It is recommended that the design of both HVAC system and facade should be optimized to reduce the costs and the energy consumption [31]. It is shown that it is possible to improve the building's energy efficiency in some way by using multiple-skin facades. Unfortunately, most typologies are incapable of lowering both the annual heating and cooling demand. Only by combining typologies or changing the system settings according to the particular situation, a substantial overall improvement. In order to correctly evaluate the energy efficiency, an annual energy simulation focusing on both heating and cooling load is necessary [32]. Facades integrated with venetian blinds have been investigated with Gratia and De Herde [33]. They examined the influence of the position and the color of the blinds on the cooling consumption. It was concluded from the study that cooling consumption could be decreased by 23.2%. Lee. et al. [34] mentioned that using single sided blinds decreased the loads 26.5%.

2.2 Dynamic heat transfer models for glazed envelopes

Glazed facades have to be analyzed based on transient heat transfer mode, since all parameters that govern its thermal performance are dynamic. Solar radiation intensity, solar incidence angle, external temperature and inside design temperature. Accordingly using a mathematical model capable of predicting thermal performance in buildings in which the energy evaluation can be carried out by means of a suitable thermo- hygrometric balance solved in unsteady state has been applied in two numerical tools as follows:

2.2.1 DIGITHON

DIGITHON is building energy simulation software developed in Padova University [35:38]. Based on heat transfer functions method it can predict the energy demands and thermal loads of multiple skin facades rooms based on defined time step by the user. (Fig.2.1) The dynamic heat conduction transfer, i.e. 'the response factor' technique is implemented [39, 40]. Response factors are calculated by using commercial software, namely HEAT2 [41], based on the Finite Difference Method (FDM) technique.

Objectives:

1-Identification of the numerical methodology to account for the facades as integrated module in the overall building energy balance.

2-Numrical modelling clarification of different façade ventilation methodologies.

3-Evaluation of implementing the glazed façade as an energy recovery unit.

Model theory

a. Overall description

The internal structural of the dynamic code ensure the friendly user concept. It is prepared to consider the insertion of new components without the need of interact with the main numerical initial code. Hence the management of new façade modules design with two or multiple glazed layers could be implemented simply. The code is able to manage multiple skin façade with only one ventilated cavity and the rest are considered closed. The venetian blinds also could be considered in the code located specifically in the middle of the ventilated cavity. The possibility of controlling inclination angle in respect of horizontal position is according to user needs is available. The data concerning glazing layers specifications, cavity, air flowing in the ventilated cavity and the venetian blinds are provided as inputs via text type files.

The code allows end user to choose between different types of MSF operation:

1-The cavity air ventilation direction from the bottom to the top or vice versa.

2- Facade ventilation type either out-out i.e. air from outdoor or in-out i.e. air from the indoor zone (see section 1.4.1).

3- The air flow rate ventilating the cavity could be independent on the fresh air flow rate supplied to the indoor zone in case of in-out ventilation methodology as long as it does not exceed the summation of the fresh and infiltration air flow rates.

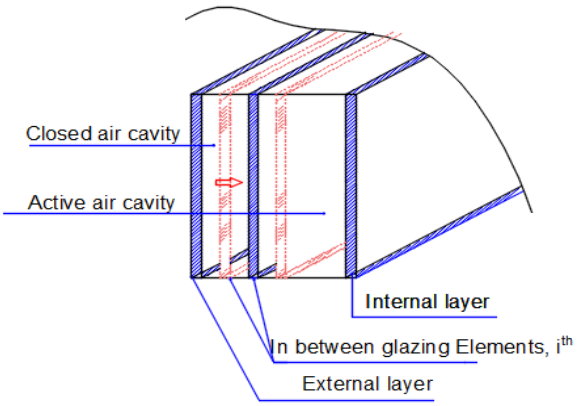

Fig.2.1 DIGITHON-Glazed Façade composition

The discretization of room components (external &internal walls, floor, roof and windows) in define numbers of tiles is considered the prelim step to implement DIGITHON. Each tile is characterized by its own surface temperature. Assuming a suitable discretisation of the time domain with an interval $\Delta\tau$, the general balance for the h^{th} sub-system that is assumed at uniform temperature may be approximated as follows in Equation (2.1)

$$\left(\sum_{g} q_g\right)_h = \left(\frac{M\ C_M\ [T_M - (T_M)_{\Delta\tau}]}{\Delta\tau}\right)_h + \left(\sum \dot{m}_s\ c_{ps} T_s\right)_h \quad \textbf{(2.1)}$$

The heat fluxes q_g may be either conductive, convective or radiative. The response factor technique is used for solving dynamic conduction problems, inside walls, while glazing elements are solved via simple resistances as it usually happens in dynamic energy balance software.

Mutual radiation between internal surfaces is calculated using the view factors calculated for each couple of tiles. An illustration of the discretization of a room equipped with a double skin facade schematic is shown in (Fig.2.2a) as for the DSF discretization (Fig.2.2b). The facade is divided into

vertical volumes from the bottom to the top. For each element of the considered volume, the temperature is considered uniform, while the surface temperature of the internal glass is defined by the overall balance of the room.

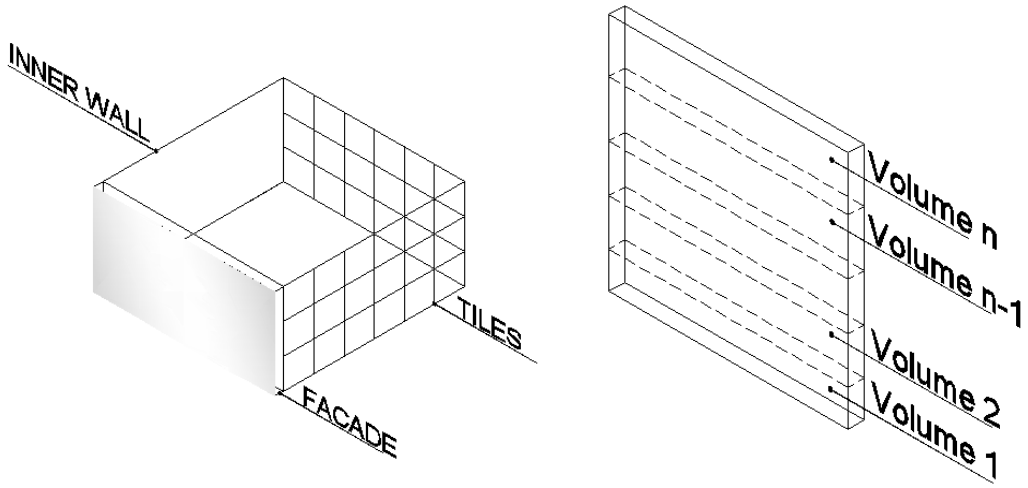

(a) **(b)**

Fig.2.2 Room discretization Scheme (a) and façade discretization (b)

b. Infrared solar radiation

The amount of solar radiation that enters the zone depends on the composition of the façade, the glazing system technical specifications such as absorption and transmission coefficients, and existence of intermediate layers such as venetian blinds. This simplified estimation is carried out according to an iterative process that minimizes the error and provides the solution. The method used is based on the radiation that leaves the glass on its outer face $I_1(i)$ and the one that leaves the same glass from inner surface $I_2(i)$ as a function of the boundary conditions and the technical characteristics of the glass, as shown in Fig.2.3).

Once identified the transmission coefficient $\tau(i)$ as well as, the reflection coefficients of inner $r_1(i)$ and outer $r_2(i)$ surfaces for the generic element (i) the following Equations (2.2) to (2.4) could be derived:

$$I_1(i) = I_1(i+1).\tau(i) + I_2(i-1).r_1(i) \quad \textbf{(2.2)}$$

$$I_2(i) = I_2(i-1).\tau(i) + I_1(i+1).r_2(i) \quad \textbf{(2.3)}$$

$$A(i) = I_1(i+1) + I_2(i-1) - I_1(i) - I_2(i) \quad \textbf{(2.4)}$$

Where A(i) is the absorbed solar radiation of the discretized i_{th} façade glazing element; this value depends on the incident angle of the solar radiation as well as on the composition of the whole

glazing package. Solar radiation, which becomes a direct load to the zone, shall be defined by applying the above equations to the whole package of glass. In addition, the value of the absorbed energy by each glass or screen shall be considered in the thermal exchange. The same rule of the glazed elements applied on the intermediate screens. Nevertheless, the values $\tau(i), \mathrm{r}(i)$of transmission and reflection coefficients should be changed accordingly.

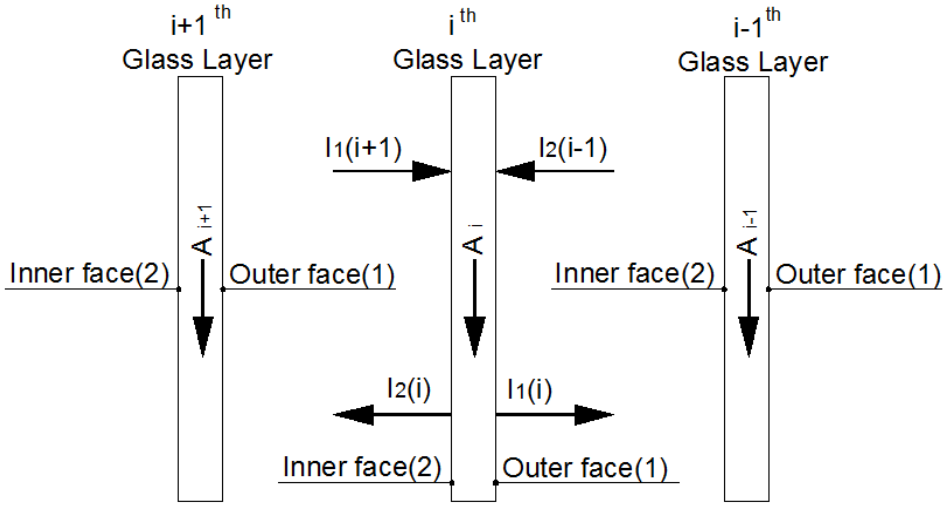

Fig.2.3 Infrared Solar radiation analysis in the glass element

c. Façade Cavity thermal balance

In each volume the façade is subdivided (Figure 1.a), the glazing elements are linked through a resistance network (Fig.2.4). The surfaces of each volume simultaneously exchange heat by conduction through the glass, by convection with the air layer in the cavity and by infrared radiation with other surfaces. Inside each cavity, the infrared heat exchange between surfaces is supposed to take place within the j_{th} volume only.

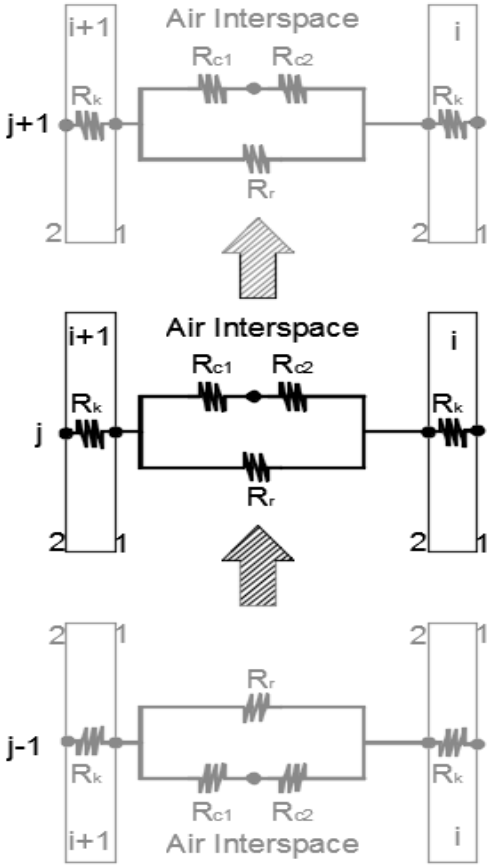

Fig.2.4 Façade Thermal model without venetian blinds

Air node balance has to consider the convective heat transfer on the face 2 of the glass element (i) $(q_{c2})_\tau$, convective heat transfer of glass element (i+1) on face 1 $(q_{c1})_\tau$, the heat transfer caused by the ventilation $(q_v)_\tau$ and the change of internal energy $\left(\frac{\Delta U_a}{\Delta \tau}\right)$ associated to the air volume $V_{a(j)}$. The following Equations (2.5) to (2.9) can be written at the time step τ(j):

$$(q_{c1})_{\tau(j)} + (q_{c2})_{\tau(j)} + (q_v)_{\tau(j)} = \frac{\Delta U_a}{\Delta \tau}_{(j)} \quad \textbf{(2.5)}$$

where

$$(q_{C1})_{\tau(j)} = h_a . S_{(j)} . (t_{1(i+1)} - t_a)_{(j)} \quad \textbf{(2.6)}$$

$$(q_{C2})_{\tau(j)} = h_a . S_{(j)} . (t_{2(i)} - t_a)_{(j)} \quad \textbf{(2.7)}$$

$$(q_v)_{\tau(j)} = \dot{m}_a . c_{pa} . (t_{a(j-1)} - t_{a(j)}) \quad \textbf{(2.8)}$$

$$\frac{\Delta U_{a(j)}}{\Delta \tau} = V_{a(j)} . \rho_a . c_{va} . \frac{\left((t_{a(j)})_\tau - (t_{a(j)})_{\tau-1}\right)}{\Delta \tau} \quad \textbf{(2.9)}$$

d. Glazing elements thermal balance

For each glass, the surface node thermal balance has to be written considering the conduction through the element $(q_k)_{\tau(j)}$, the convection $(q_c)_{\tau(j)}$ and the infrared radiation $(q_R)_{\tau(j)}$ with adjacent element, Equation (2.10).

$$(q_k)_{\tau(j)} + (q_c)_{\tau(j)} + (q_R)_{\tau(j)} = (q_A)_{\tau(j)} \quad \textbf{(2.10)}$$

Considering the surface 1 of the i_{th} element (the other surface balances can be similarly written) the following Equations (2.11) to (2.14) are applied:

$$(q_k)_{\tau(j)} = \frac{k}{s_i}.S_{(j)}.(T_{1(i)} - T_{2(i)})_{(j)} \quad \textbf{(2.11)}$$

$$(q_C)_{\tau(j)} = h_C.S_{(j)}.(T_a - T_{2(i)})_{(j)} \quad \textbf{(2.12)}$$

$$(q_R)_{\tau(j)} = S_{(j)}.\frac{4.\sigma.{T_{m1}}^3}{\left[\frac{1}{\epsilon_{(i+1)}}+\frac{1}{\epsilon_{2(i)}}-1\right]}.(T_{1(i+1)} - T_{2(i)})_{(j)} \quad \textbf{(2.13)}$$

$$S_{(j)}.\frac{4.\sigma.{T_{m1}}^3}{\left[\frac{1}{\epsilon_{(i+1)}}+\frac{1}{\epsilon_{2(i)}}-1\right]}.(T_{1(i+1)} - T_{2(i)})_{(j)} + \frac{k}{s_i}.S_{(j)}.(T_{1(i)} - T_{2(i)})_{(j)} + h_C.S_{(j)}.(T_a - T_{2(i)})_{(j)} = S_{(j)}.\frac{A_{(i,j)}}{2} \quad \textbf{(2.14)}$$

In the case of a screen presence, the air inter space shall face two possibilities. The first model (Fig.2.5), assumes that the temperature of the air has before and after blinds the same value, this means that air exchanges simultaneously with the surfaces of the glass facing façade cavity and the blinds (fully mixed condition inside the cavity). The second model (Fig.2.6), divides the cavity into two parts in front of (interspace B) and behind (interspace A) the screen. In this case, there is no mix of air inside the cavity.

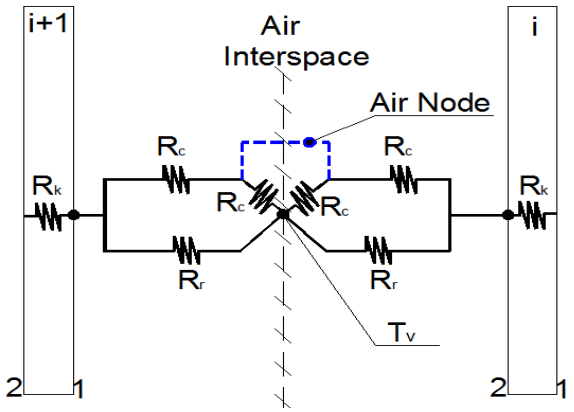

Fig.2.5 Façade thermal model with venetian blinds downward for volume j, with uniform temperature inside the air layer

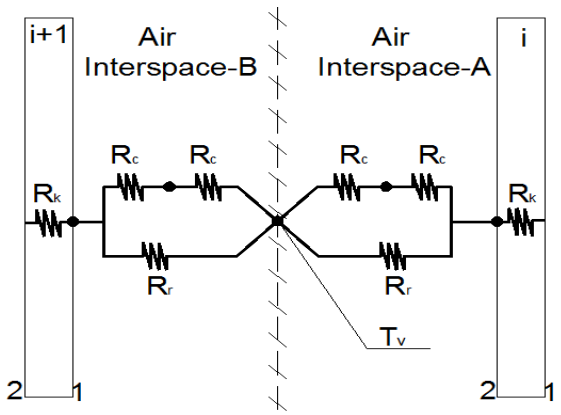

Fig.2.6 Façade Thermal model with two different temperatures inside air layer

In the first model (fully mixed condition) the heat balance of the surface node is again expressed by Equation (2.10). Surface node thermal balance is represented by Equations (2.15) and (2.16). The air node balance is defined by the Equation (2.17) through the convective heat transfer between the element (i) the element (i+1), and the venetian blinds (v); the air temperature is considered the same $t_{a(j)}$ in the whole volume (j).

$$(q_C)_{\tau(j)} = h_C.S_{(j)}.(T_a - T_{2(i)})_{(j)} \quad \textbf{(2.15)}$$

$$(q_R)_{\tau(j)} = S_{(j)}.\frac{4.\sigma.{T_{m2}}^3}{\left[\frac{1}{\epsilon_v}+\frac{1}{\epsilon_{2(i)}}-1\right]}.\left(T_v - T_{2(i)}\right)_{(j)} \quad \textbf{(2.16)}$$

$$h_{vs}.S_{(j)}.\left(T_{2(i)} - T_a\right)_{(j)} + h_{vs}.S_{(j)}.\left(T_{1(i+1)} - T_a\right)_{(j)} + 2h_{vs}.S_{(j)}.(T_v - T_a)_{(j)} + {m^o}_a.c_{pa}.\left(T_{a_{(j)}} - T_{a(j-1)}\right) = V_{(j)}.\rho_a.c_{va}\left(\frac{T_{a(\tau)} - T_{a(\tau-1)}}{\Delta\tau}\right)_{(j)} \quad \textbf{(2.17)}$$

In the second model (i.e. no mixing within the air cavity), there are two air nodes: the first node (A) is subjected to convective heat transfer between the element (i), the venetian blinds and half of ventilation mass flow rate air passes through the cavity with an inlet temperature $t^A_{a(j-1)}$ in Equation (2.18); the second node (B) depends on the convection heat exchanges with the element i+1, on the venetian blinds and half of the ventilation mass flow rate entering at temperature $t^B_{a(j-1)}$ as expressed in Equation (2.19).

$$h_{vs}.S_{(j)}.\left(T_{2(i)} - {T^A}_{a(j)}\right)_{(j)} + h_{vs}.S_{(j)}.\left(T_v - {T^A}_{a(j)}\right)_{(j)} + \frac{\dot{m}_a}{2}.c_{pa}.\left({T^A}_{a(j)} - {T^A}_{a(j-1)}\right) = V_{a_{(j)}}.\rho_a.c_{va}\frac{\left({T^A}_{a(\tau)} - {T^A}_{a(\tau-1)}\right)_{(j)}}{\Delta\tau} \quad \textbf{(2.18)}$$

$$h_{vs}.S_{(j)}.\left(T_{1(i+1)} - {T^B}_a\right)_{(j)} + h_{vs}.S_{(j)}.(T_v - {T^B}_a)_{(j)} + \frac{{m^o}_a}{2}.c_{pa}.\left({T^B}_{a(j)} - {T^B}_{a(j-1)}\right) = V_{a_{(j)}}.\rho_a.c_{va}\frac{\left({T^B}_{a(\tau)} - {T^B}_{a(\tau-1)}\right)_{(j)}}{\Delta\tau} \quad \textbf{(2.19)}$$

Surface node is represented again by Equations (2.20) and (2.21)

$$(q_C)_{\tau(j)} = h_C.S_{(j)}.({T^A}_a - T_{2(i)})_{(j)} \quad \textbf{(2.20)}$$

$$(q_R)_{\tau(j)} = S_{(j)}.\frac{4.\sigma.{T_{m2}}^3}{\left[\frac{1}{\epsilon_v}+\frac{1}{\epsilon_{2(i)}}-1\right]}.(T_v - T_{2(i)})_{(j)} \quad \textbf{(2.21)}$$

e. Validation of DIGITHON

In order to validate the DIGITHON model as a dynamic simulation software for integrated facades in buildings, experimental set of data including indoor and outdoor temperatures and vertical solar radiation of double skin façade building for a late measurement campaign were implemented [Appendix-A]. The measurements have been carried out in a room in an existing building in Padova (North East-Italy) during the official heating season (i.e. from 15 October to 15 April). For checking DIGITHON the measured weather conditions and the air temperature of the room have been used as

input data for the model. Working hours of the HVAC system been taken into consideration to make sure that ventilation was on. The test room is located in the third floor of an office building with an external façade East oriented; dimensions are illustrated in (Fig.2.7a), All inner walls, ceiling and floor were considered adiabatic. The DSF is made of three glass layers (Fig.2.7b) and its thermal properties were determined by WINDOW6 [42] and shown in Table2.1).

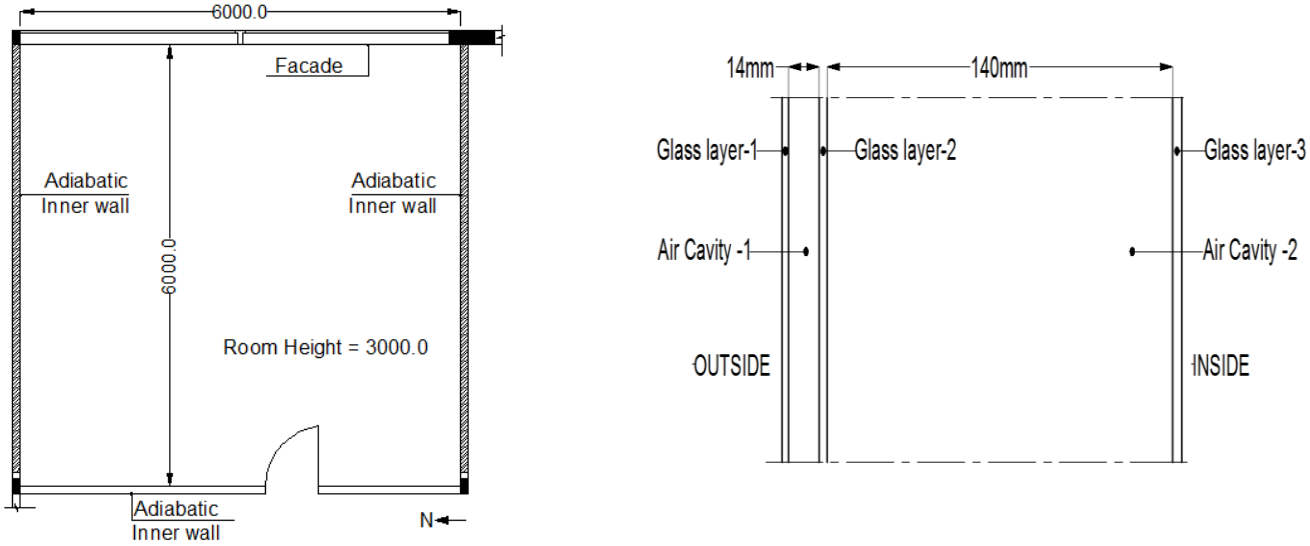

Fig.2.7 (a) Room plan (dimensions in mm) (b) Façade Composition

Table2.1 Glazing system Technical specifications

layer	Type	D mm	τ_{sol}	r_{sol1}	r_{sol2}	ε_1	ε_2	κ_{eff}
1	Clear glass	8	0.724	0.069	0.071	0.084	0.840	1
2	Closed Air cavity	14	-	-	-	-	-	0.302
3	Low-e glass	6	0.548	0.313	0.240	0.036	0.883	1
4	Mechanically ventilated air cavity	140	-	-	-	-	-	7.44
5	Clear glass	8	0.724	0.069	0.071	0.084	0.840	1

The facade air cavity is mechanically ventilated by using the interior air. The main input data have been summarized in **Errore. L'origine riferimento non è stata trovata.**). The comparison between DIGITHON calculated value of the exhaust air temperature (T_{exh}) and the corresponding measured

value has shown a good agreement. As shown in (Fig.2.8) most of DIGITHON results are in harmony with measured values. (Fig.2.9) shows in details 5 days (from 16 till 20 December). The evaluated root mean square error (RMSE) for temperature of exhaust air from the cavity is estimated as 2.4℃.

Table2.2 Internal loads

No of Persons	6
Ventilation air flow rate (m^3/hr)	240
Sensible heat gain (W)	1680
Latent heat gains (g/hr)	480

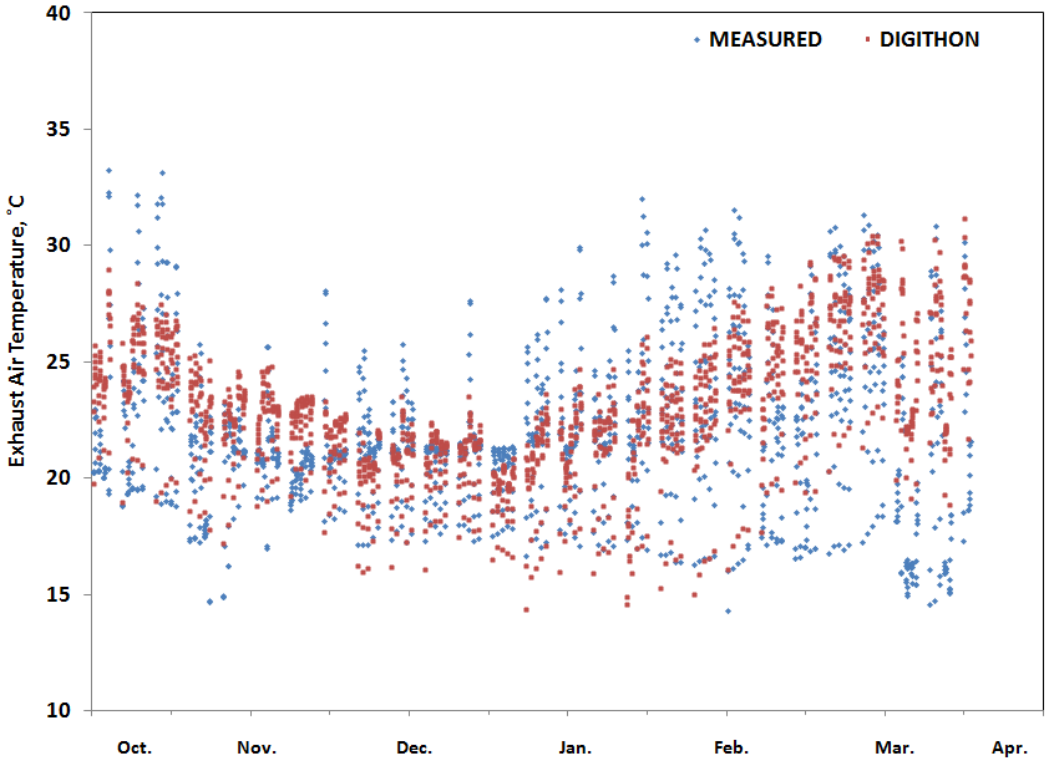

Fig.2.8 Measured and simulated exhaust air temperature during the working hours of the whole heating season

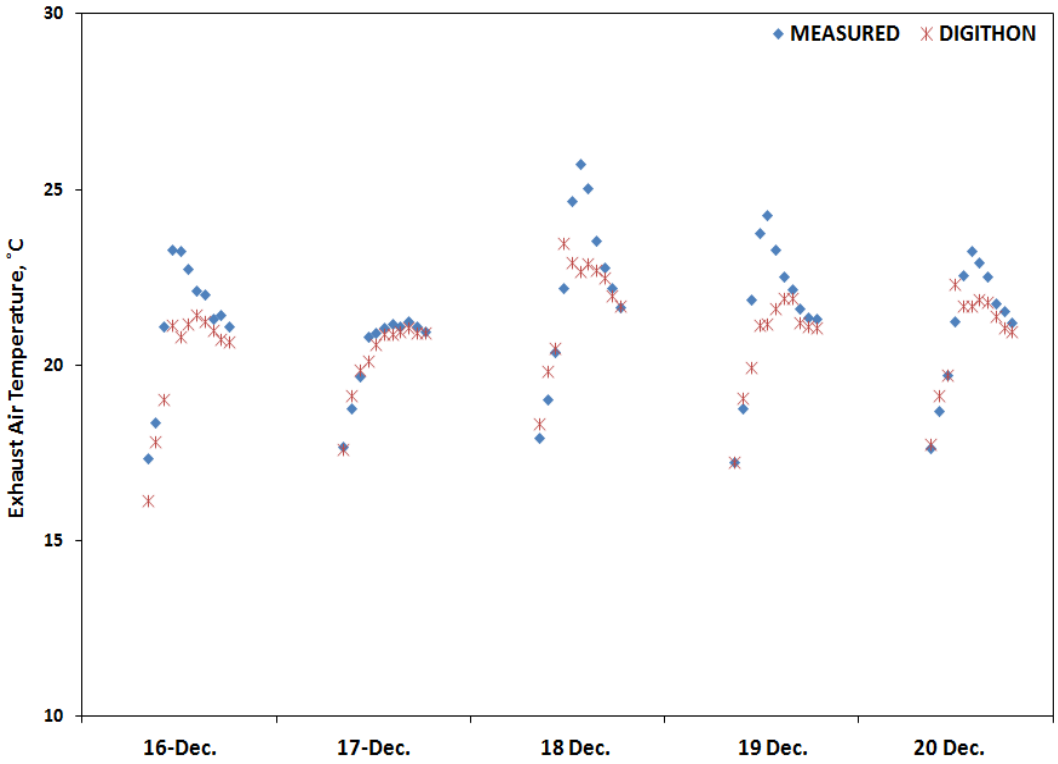

Fig.2.9 Measured-DIGITHON Exhaust Air Temperature Comparison on 5 days

f. Energy recovery evaluation through glazed façade -Case studies

Thermal performance in four different cities in Europe has been investigated utilizing DIGITHON. The main scope of this analysis was to evaluate the heating energy recovery beneficiary level within the façade. A further analysis has been focused on the possible benefit of using DSF, as an efficient pre-heat recovery unit. A heat recovery system shall have at least 50% recovery effectiveness [43]. The using of the heat recovery unit is very important to reduce ventilation energy consumption. The aim of the present work is to define pre-heating efficiency of the DSF; hence the efficiency of the DSF has been considered alone, without other types of heat recovery units, which may help in the decrement of energy demands for ventilation. For this purpose two systems have been considered, according to [19] In the first system (Fig.2.10a) the power required for heating the air form outdoor conditions (T_o) to supply temperature (T_s) is considered, Equation (2.22).

$$q_{eh} = \dot{m_a^{\circ}}.c_P.(T_s - T_o) \quad \textbf{(2.22)}$$

In the second system (Fig.2.10b) the power exchanged inside the DSF has been considered as the temperature difference between indoor air (T_i) and exhaust air from the cavity (T_{exh}), Equation (2.23).

$$q_f = \dot{m_a^{\circ}}.c_P.(T_{exh} - T_i) \quad \textbf{(2.23)}$$

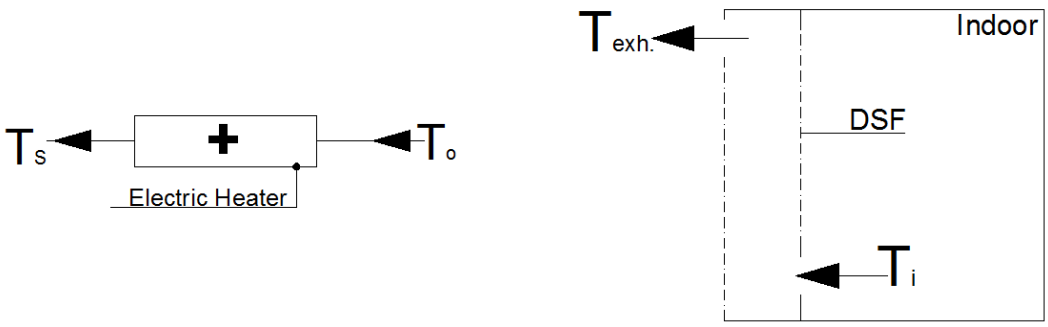

(a) **(b)**

Fig.2.10 Schematic representation of air flow and temperatures through Façade (a) Electric heater (b)

Pre-heating efficiency η_P is defined as the capacity of the façade to pre-heat the ventilation air flow rate during the cold season (heating period) [44] and it is considered as the ratio between sensible energy of air that flows inside the façade cavity q_f Equation (2.23) and the sensible energy required to heat the ventilation air q_{eh} Equation (2.22).

$$\eta_P = \frac{q_f}{q_{eh}} = \frac{T_{exh} - T_i}{T_s - T_o} \quad \textbf{(2.24)}$$

In Equation (2.24) the façade is used to exhaust the entire amount of ventilation air without considering the zone pressurization ratio and considering tight conditions of the DSF [44], hence:

- $\eta_P < 0$ means that temperature of the air that exits from the ventilated façade, T_{exh}, is lower than the temperature of the indoor air, T_i, and, as a consequence, there is no energy recovery;
- $0 < \eta_P < 1$ means that the air that exits from the façade is preheated at a temperature which is lower than the indoor one and the ventilation air still requires an extra heating before being introduced into the room;
- $\eta_P \geq 1$, the façade is able to completely preheat the ventilation airflow rate and theoretically the ventilation losses are equal to zero.

At the same time the evaluation of η_P has been calculated based on some assumptions:
Other than the mentioned assumptions above, it was considered that η_P=0 which indicates no benefit of using façade as a heat recovery.

For the efficiency evaluation, the heating season has been considered to last from November till March; based on measured data of Padova, the monthly average preheated efficiency values are ranging between -1.8% in November till the maximum value of 14% in March (Fig.2.11).

Using façade in thermal energy recovery process has been estimated to be only effective for short time of the heating season with a parley-accepted efficiency. This is mainly due to foggy and cloudy weather in Padova. In order to reach a subjective conclusion, η_P values have been presented in (Table2.3) based on the ratio of the hourly η_P values to the total number of hours per each month. The maximum value (η_P=1) happens in March by 9.4% with an opposite coincidence negative values of 79%.

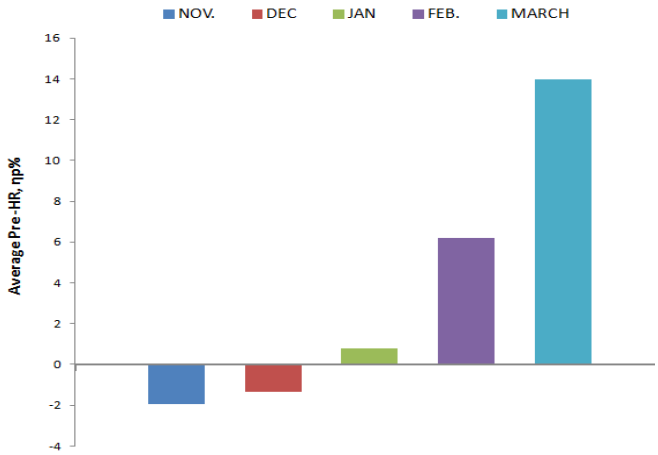

Fig.2.11 Average preheated efficiency per month-Padova city

Table2.3 Percentage ratio of η_P to the total hours per each month

	Nov.	Dec.	Jan.	Feb.	Mar.
$\eta_P\% = 1$	1.1	0.1	0.0	0.1	9.4
$0 < \eta_P\% < 1$	8.3	6.2	12.0	22.9	11.6
$\eta_P\% \leq 0$	90.6	93.7	88.0	76.9	79.0

In any case the above results cannot be generalized so far, since only one climate and one orientation have been considered. For this purpose, a parametric analysis based on DIGITHON has been carried out considering different climates and orientations. A typical test reference year (TRY) has been used in four European cities (Barcelona, Venice, Frankfurt and Helsinki) and for all the four orientations (West, East, North and South). Considering five months for the heating season from November till March. Average values of pre-heating efficiency η_P per each month and orientation are shown in (Fig.2.12) with open venetian blinds and in (Fig.2.13) with close venetian blinds. This parametric

analysis confirmed the previous measured results in Padova-Italy. The only place where DSF can work as pre-heating system is in Barcelona in south orientation (average value of 8%) and on west orientation (average value of 6%).

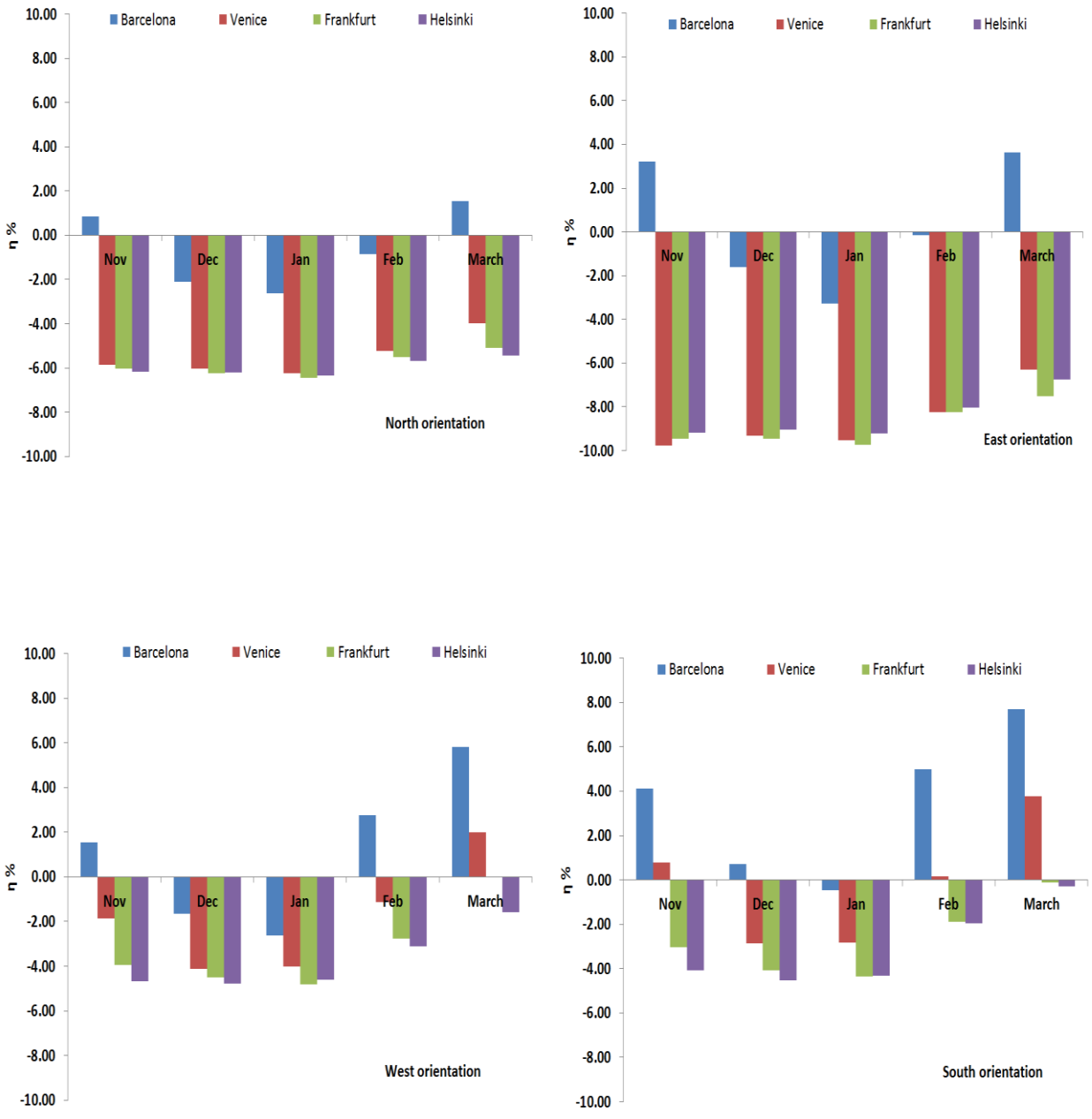

Fig.2.12 Average preheated efficiency for four considered cities, Open venetian blinds

In all the other cases results show poor preheating efficiency of DSF. Because of increment of heat storage caused by closed blinds, preheated efficiency values have been increased at the four cities and orientations. The maximum average value of pre-heat efficiency happened at south orientation of Venice in March with a value of 10%. A part of this case in all these locations results has been poor.

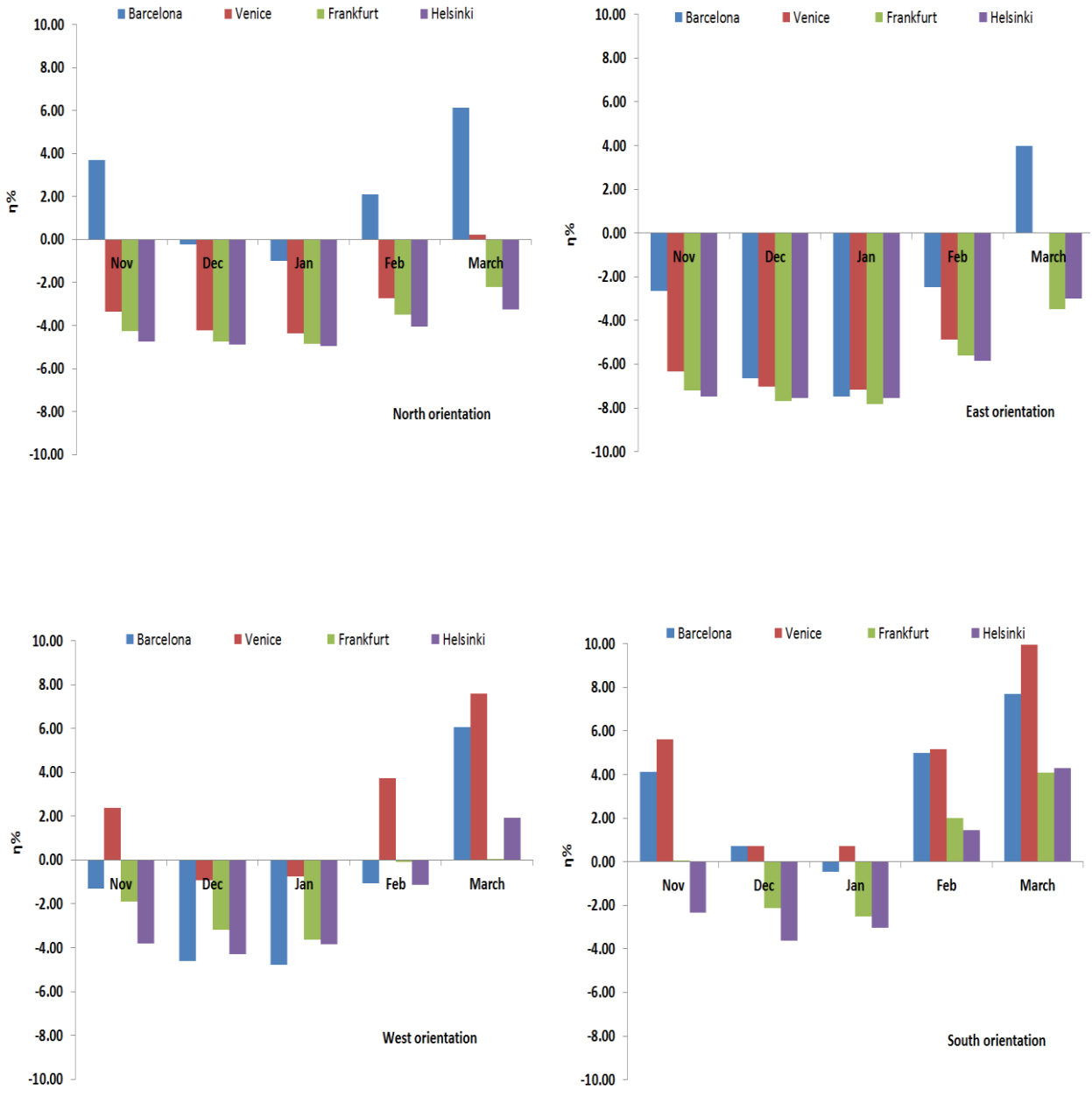

Fig.2.13 Average preheated efficiency for four considered cities, Closed Venetian blind

2.2.2 Finite difference method/ Resistance Capacitance model (RC)

In all construction projects the concept and preliminary phases are considered the most important steps because usually in those phases it is expected from all designers to put the project main idea, expected work frame and budget analysis. HVAC design engineers are obliged to present a reasonable study of air conditioning system that shall be used including expected service areas and system energy consumption hence based on this study all other trends (Architecture, Civil, Electrical) starts to provide the required mechanical service areas and electrical needs. In terms of the importance of these phases that affects both project initial and running costs, a simplified mathematical model capable of simulate the thermal behavior of mechanically ventilated DSF was illustrated. The model takes into accounts separately the beam and diffuses solar radiation components with hourly basis incident angles. The model is implemented in a Visual/Basic Microsoft Excel sheet; it does not need neither a deep scientific background to use it nor high computing time or capabilities. Moreover, the mathematical model was developed to estimate roughly the thermal energy needs due to convection losses from outer façade layer, solar gains and internal loads to help designers to take correct decisions in project preliminary phase. Validation was carried out by comparing numerical results with the experimental data [Appendix-A] also different comparisons accomplished between the simplified and the detailed simulation model DIGITHON for different cities.

Objectives:

1- Clarification of mathematical description for one-dimensional dynamic model.
2- Short wave radiation analysis through glazed elements.
3- Evaluation of the building thermal energy loads.

Model Theory

a. Resistance Capacitance models RC description

The thermal resistance is defined as the ratio of the temperature difference between two thermal nodes, (T_i-T_{i+1}), to the heat transfer Q that flows between the two thermal nodes. This is analogous to Ohm's law, in which the electrical resistance is defined as the ratio of the voltage drop across a resistor to the current flow across the resistor. Thermal resistances R_k, R_C and R_{rad} are representing respectively conduction, convection, and radiation heat transfer between façade layers, where:

$R_k = \left(\frac{x}{k}\right)$ is the conduction thermal resistance of the layer per unit of area, **(2.25)**

x is the layer thickness and k is its thermal conductivity, and

$R_C = \frac{1}{h_c}$ is the convection thermal resistance per unit of area. **(2.26)**

The convection heat transfer coefficient h_c correlations have been mentioned before in Chapter 1. Finally, radiation thermal resistance is:

$$R_{rad} =. \frac{1}{[h_r]} \quad \textbf{(2.27)}$$

Each element within façade composition is represented by a thermal node including air cavity in between the double glazed cavity. The assumed DSF configuration is consists of 3 glass layers and two cavities described in (Fig.2.14).

Nevertheless it is a simplified mathematical model the analysis of solar radiation gains were carried out in a detailed procedure. The vertical beam solar radiation I_B and diffuse solar radiation I_D of west orientation and its incident angle θ_B on hourly basis based on a typical test reference year (TRY) were determined by using Type15-6 of TRNSYS [45], while diffuse solar radiation incident angle θ_D were assumed constant and equal to 60°, which is a good approximation because diffuse solar radiation can be treated in the same manner as isotropic sky and ground-reflected diffuse radiation [46]. On the other hand absorption solar radiation Equation (2.28) was divided equally between the two thermal nodes representing inner and outer layer of each glass layer (i). The façade was composed in WINDOW 6 [42], a software used in modelling windows and shading devices, and all optical and angular data of façade layers including absorption coefficients a_1, a_2 and a_3 values were obtained for spectrum angles from 0° to 90°. Afterwards a generalized Equation for each glass layer derived to related different coincident Θ_B with absorption coefficient. On the other hand, in diffuse solar radiation only one value of a_D is considered which is opposed to Θ_D equal to 60°

$$I_{abs_{(i)}} = \left((I_B\,\Theta_B)\frac{a_{B(i)}}{2} + (I_D\,\Theta_D)\frac{a_{D(i)}}{2}\right) \quad \textbf{(2.28)}$$

The input data to the simplified mathematical models includes: inside room temperature T_i, which could be equal to the design room temperatures according to the required thermal comfort, external temperature T_e, beam diffuse solar radiation based on (TRY). On the other hand the expected output data are all glass layers temperatures and exhaust air temperature T_{exh} from the façade which is represented by the air node inside the cavity. In order to simplify the model the blinds have been considered with no mass and null thickness, the total difference in estimated thermal loads in case of considering the blinds effect in a detailed way and in a simplified way will not exceed 30% and it is considered as an accepted safety percentage for the preliminarily designing phase of projects.

b. Mathematical description (with venetian blinds)

Based on finite difference method FDM and the DSF configuration clarified in (Fig.2.14), the thermal resistance model is represented through 10 nodes and Equations from (29) till (36).

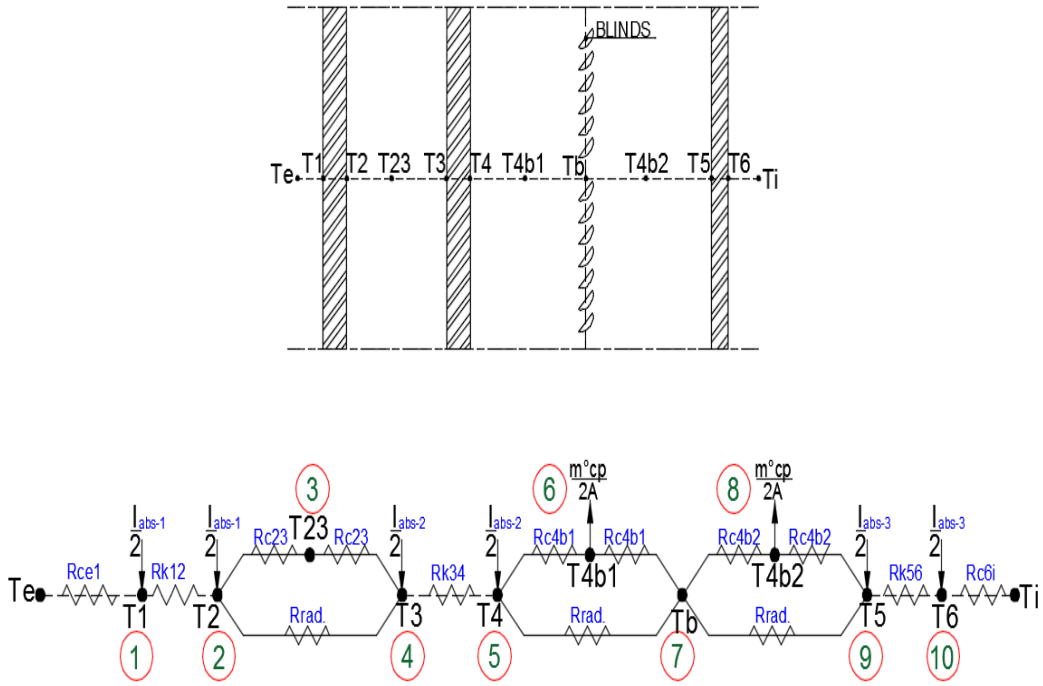

Fig.2.14 DSF thermal resistance model (with venetian blinds)

In node-1 and node-10 the thermal balance refers to convection heat transfer towards outside/ inside Rce1 Rc6i representing the convective resistances respectively and conduction through external/ internal glass panes with Rk1 Rk3 as conductive resistances.

Node: 1

$$\left[\left({}^{-1}/_{R_{ce1}}\right)+\left({}^{-1}/_{R_{K12}}\right)\right]T_1+\left({}^{1}/_{R_{k12}}\right)T_2=-I_{abs_{(1)}}-\left({}^{T_e}/_{R_{ce1}}\right) \qquad \textbf{(2.29)}$$

Node: 2

$$\left({}^{1}/_{R_{k12}}\right)T_1+\left[\left({}^{-1}/_{R_{rad}}\right)+\left({}^{-1}/_{R_{K12}}\right)+\left({}^{-1}/_{R_{c23}}\right)\right]T_2+\left({}^{1}/_{R_{c23}}\right)T_{23}+\left({}^{1}/_{R_{rad}}\right)T_3=-I_{abs_{(1)}} \qquad \textbf{(2.30)}$$

Convective heat transfer is only represented in node-3 due to its location inside the air cavity and between nodes 2 and 3

Node: 3

$$\left[\left({}^{1}/_{R_{c23}}\right)T_2+\left({}^{-1}/_{R_{c23}}\right)+\left({}^{-1}/_{R_{c23}}\right)\right]T_{23}+\left({}^{1}/_{R_{c23}}\right)T_3=0 \quad \textbf{(2.31)}$$

Again all forms of heat transfer have been presented in node 4 and node 5, convection, radiation heat exchange and conduction heat transfer between the 2 nodes.

Node: 4

$$\left({}^{1}/_{R_{rad}}\right)T_2+\left({}^{1}/_{R_{c23}}\right)T_{23}+\begin{bmatrix}\left({}^{-1}/_{R_{rad}}\right)+\left({}^{-1}/_{R_{K34}}\right)+\\ \left({}^{-1}/_{R_{c23}}\right)\end{bmatrix}T_3+ \quad \textbf{(2.32)}$$

$$\left({}^{1}/_{k_{34}}\right)T_4=-I_{abs_{(2)}}$$

Node: 5

$$\left[\left({}^{-1}/_{R_{rad}}\right)+\left({}^{-1}/_{R_{K34}}\right)+\left({}^{-1}/_{R_{c45}}\right)\right]T_4+\left({}^{1}/_{R_{c23}}\right)T_{45}+\left({}^{1}/_{k_{34}}\right)T_3+\left({}^{1}/_{R_{rad}}\right)T_5=-I_{abs_{(2)}} \quad \textbf{(2.33)}$$

Node-6 illustrating thermal mass balance inside the façade cavity, ventilating mass flow rate enters the cavity with temperature of inside room and leaves it by air node temperature of the cavity.

Node: 6

$$\left[\left(-\frac{Cp.\dot{m}}{A_f}\right)+\left({}^{-1}/_{R_{c45}}\right)+\left({}^{-1}/_{R_{c45}}\right)\right]T_{45}+\left({}^{1}/_{R_{c45}}\right)T_4=-\left(\frac{Cp.\dot{m}}{A_f}\right)T_i \quad \textbf{(2.34)}$$

Node: 7

$$\left[\left({}^{-1}/_{R_{rad}}\right)+\left({}^{-1}/_{R_{K34}}\right)+\left({}^{-1}/_{R_{c45}}\right)\right]T_5+\left({}^{1}/_{R_{c23}}\right)T_{45}+\left({}^{1}/_{k_{56}}\right)T_6+\left({}^{1}/_{R_{rad}}\right)T_4=-I_{abs_{(3)}}. \quad \textbf{(2.35)}$$

Conduction heat transfer within the third glass pane and then convection heat transfer between inner layer and inside room is represented in last thermal node.

Node: 8

$$\left[\left({}^{-1}/_{R_{k56}}\right)+\left({}^{-1}/_{R_{c6i}}\right)\right]T_6+\left({}^{1}/_{R_{k56}}\right)T_5=-I_{abs_{(3)}}-\left({}^{T_i}/_{R_{ci6}}\right) \quad \textbf{(2.36)}$$

c. Mathematical description (without venetian blinds)

Thermal resistance model of this case is shown in (Fig.2.15); the thermal balance is described from Equation (2.37) till Equation (2.40). The nodes from 1 till 4 are exactly the same as the previous mode. Equations starts to change from node-5 as illustrated below.

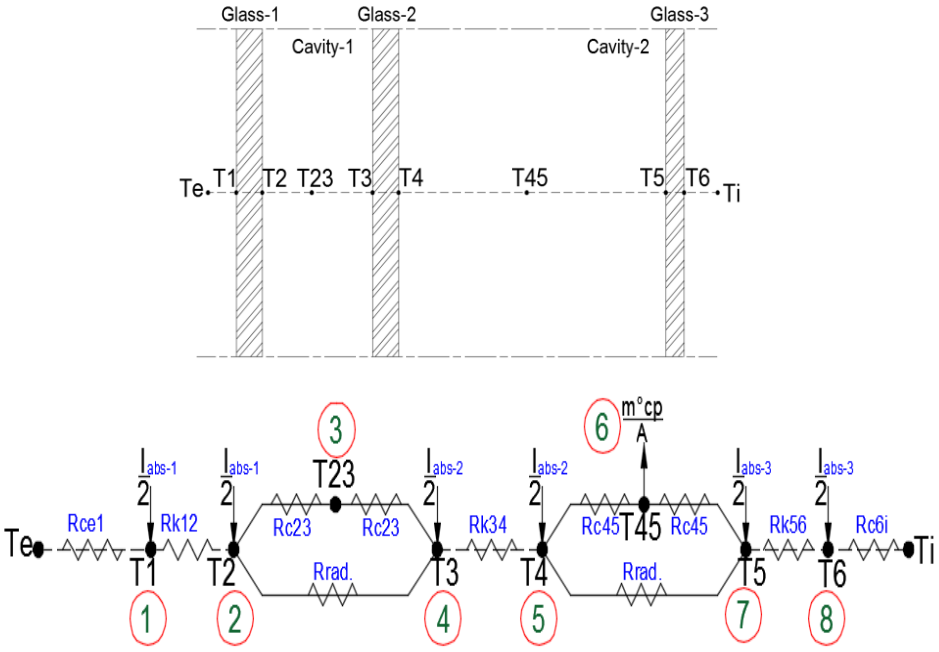

Fig.2.15 DSF thermal resistance model (without blinds)

Node-5 and node-7 are representing convection heat transfer inside the cavity, radiation heat exchange between the second and the third glass panes, and conduction heat transfer in each glass pane.

Node: 5

$$\left[\left({}^{-1}/_{R_{rad}}\right)+\left({}^{-1}/_{R_{K34}}\right)+\left({}^{-1}/_{R_{c45}}\right)\right]T_4+\left({}^{1}/_{R_{c23}}\right)T_{45}+\left({}^{1}/_{k_{34}}\right)T_3+\left({}^{1}/_{R_{rad}}\right)T_5 = -I_{abs_{(2)}} \quad \textbf{(2.37)}$$

Node-6 illustrating thermal mass balance inside the façade cavity, ventilating mass flow rate enters the cavity with temperature of inside room and leaves it by air node temperature of the cavity.

Node: 6

$$\left[\left(-\frac{Cp.m^{\circ}}{A_f}\right)+\left({}^{-1}/_{R_{c45}}\right)+\left({}^{-1}/_{R_{c45}}\right)\right]T_{45}+\left({}^{1}/_{R_{c45}}\right)T_4=-\left(\frac{Cp.m^{\circ}}{A_f}\right)T_i \quad \textbf{(2.38)}$$

Node: 7

$$\left[\left({}^{-1}/_{R_{rad}}\right)+\left({}^{-1}/_{R_{K34}}\right)+\left({}^{-1}/_{R_{c45}}\right)\right]T_5+\left({}^{1}/_{R_{c23}}\right)T_{45}+\left({}^{1}/_{k_{56}}\right)T_6 \quad \textbf{(2.39)}$$

$$+\left({}^{1}/_{R_{rad}}\right)T_4=-I_{abs_{(3)}}.$$

Conduction heat transfer within the third glass pane and then convection heat transfer between inner layer and inside room is represented in last thermal node.

Node: 8

$$\left[\left({}^{-1}/_{R_{k56}}\right)+\left({}^{-1}/_{R_{c6i}}\right)\right]T_6+\left({}^{1}/_{R_{k56}}\right)T_5=-I_{abs_{(3)}}-\left({}^{T_i}/_{R_{ci6}}\right) \quad \textbf{(2.40)}$$

d. Validation of the simplified mathematical model

The validation process was carried out in two steps. The first one was to investigate differences between simplified simulation results and measured set of data of exhaust temperature and heat flux through the façade cavity (Appendix-A). As illustrated in (Fig.2.16), the QQ plot of the measured data set and calculated by simplified model results shows a fairly good agreement between calculated and measured data, while in (Fig.2.17) a more closer clarification over five working days is reported. The evaluated root mean square error (RMSE) for temperature of exhaust air from the cavity is estimated as 3℃.

Moreover heat flux in the same period is illustrated in (Fig.2.18) and it was calculated according to Equation (2.41). As shown usually at the start working hours results obtained from the simplified model are higher than measured data, since the simplified method does not consider the thermal capacitance of the walls. However, a good consistency is generally attained.

$$Q_v=\ m^{\circ}\times\ c_p\times(T_{exh}-T_i) \quad \textbf{(2.41)}$$

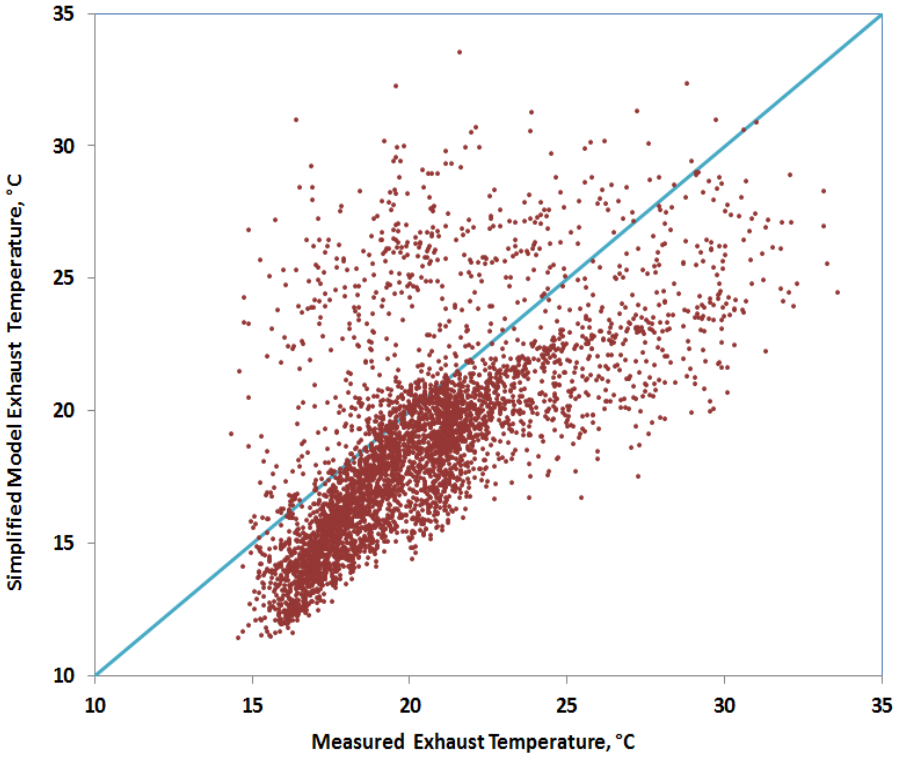

Fig.2.16 Measured-Calculated exhaust air temperature QQ plot

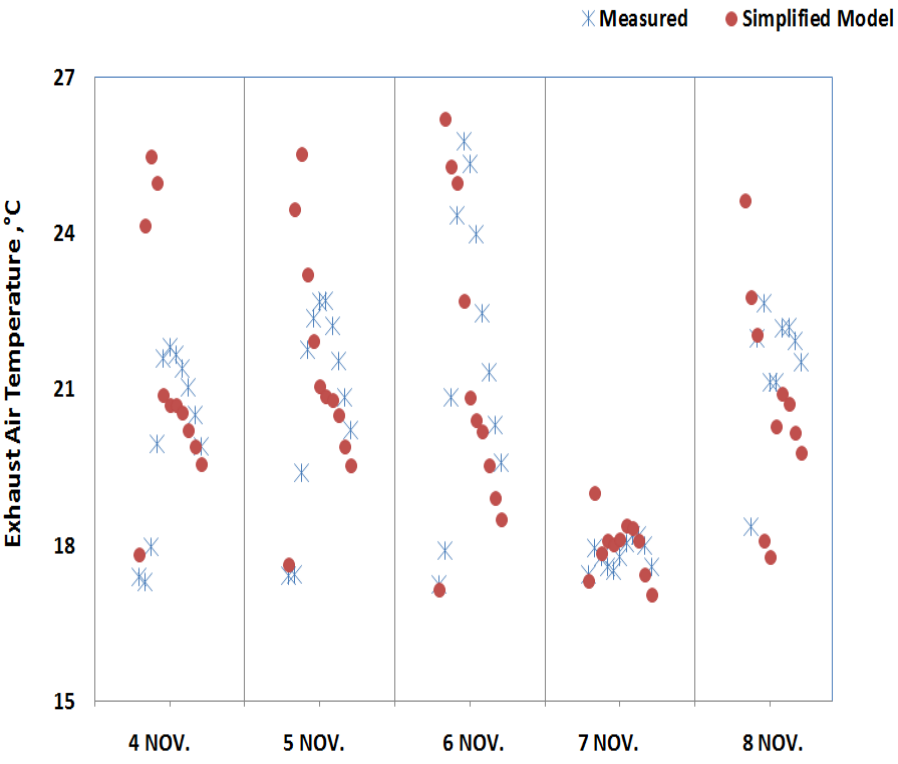

Fig.2.17 Measured-Calculated exhaust air temperature on five days

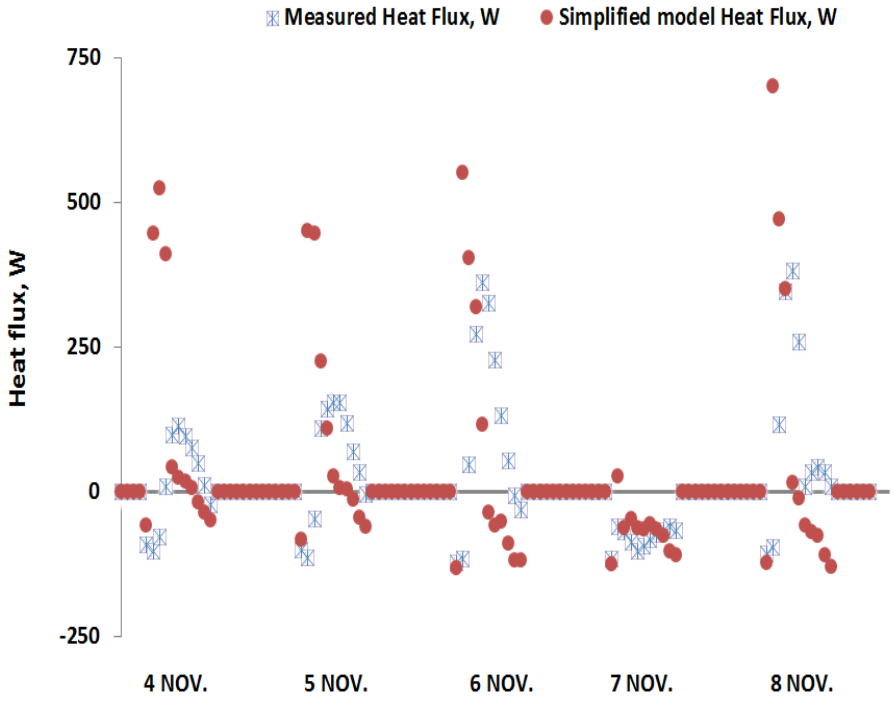

Fig.2.18 Measured-Calculated heat flux through façade cavity on five days

The second step included a numerical comparison between calculated results of a detailed dynamic DIGITHON code and the simplified model in order to assure the validation obtained for the latter. For the same indoor zone (Fig.2.7) exhaust air temperature were compared to investigate the influence of considering thermal inertia of indoor zone components (walls, ceiling and floor slab) accordingly the radiation heat exchange with indoor glazed layer surface temperature versus the mathematical model which only considers the heat and mass transfer inside the façade. As mentioned before, solar radiation was analyzed in a detailed way. Equations (2.42) to (2.44) were derived from façade angular data mentioned in (Table2.4) and implemented into the model to determine absorption coefficients opposed to hourly incident angles of hourly beam solar radiation I_B impinge the west vertical façade.

Table2.4 Absorption coefficients-Angular spectrum data

		Incident angle									
		0°	**10°**	**20°**	**30°**	**40°**	**50°**	**60°**	**70°**	**80°**	**90°**
Abs.Coeff	$\mathbf{a_1}$	0.265	0.266	0.269	0.267	0.248	0.294	0.302	0.302	0.268	0
	$\mathbf{a_2}$	0.103	0.104	.110	0.114	0.115	0.117	0.126	.131	0.093	0
	$\mathbf{a_3}$	0.063	0.064	0.064	0.064	0.064	0.062	0.056	0.042	0.022	0

$$a_1 = 0.265 + (3.14E^{-07} \times \theta^3) - (1.14E^{-16} \times \theta^8) \quad \textbf{(2.42)}$$

$$a_2 = 0.098 + (4.0E^{-05} \times \theta^2) - (6.04\,E^{-7} \times \theta^3) \quad \textbf{(2.43)}$$

$$a_3 = 6.3E^{-02} + (2.45E^{-04} \times \theta) + (4.73\,E^{-7}) \times \theta^3 + (8.84E^{-13} \times \theta^6) - (1.3E^{-10} \times \theta^5) - (1.85E^{-5} \times \theta^2) \quad \textbf{(2.44)}$$

Room inside temperature T_i values were assumed 20°C in winter season starting from October till April and 26°C in summer season starting from May till September. Hourly test reference year of Venice-Italy was used to determine external temperatures and solar radiation. The façade direction was considered West oriented and specific internal loads (IL) were assumed to be 46 W/m^2.

(Fig.2.19a) outlines the comparison between the mathematical model and DIGITHON in terms of exhaust air temperature over the entire year; (Fig.2.19 b) shows an enlargement over five days in summer season. Calculated values by means of the two models showed a good agreement. The separated intervals shown in (Fig.2.19b) illustrates working hours starting from 8 am to 7 pm. The consistent results have increased the confidence to use the mathematical model in a more detailed comparative study between four different European cities.

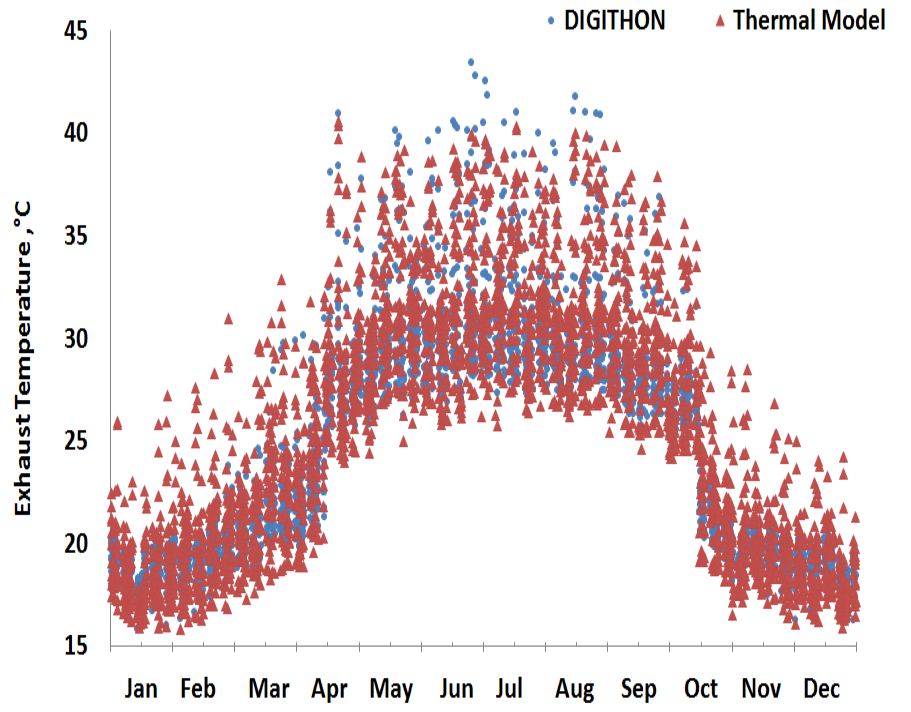

(a)

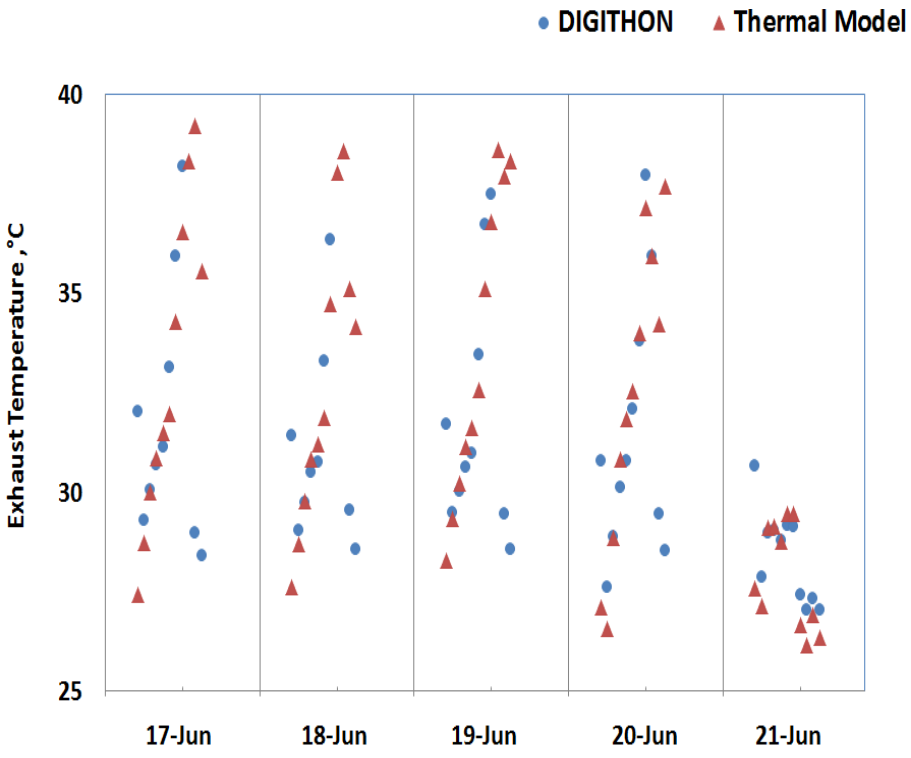

(b)

Fig.2.19 Comparison between T_{exh} calculated by DIGITHON and simplified model (a) all year (b) 5 days

2.3 Simplified model Vs DIGITHON analysis

In order to generalize the validation result a more detailed comparison between the mathematical models and DIGITHON through different climatic conditions in Europe is presented, this comparison included two main items:

- Exhaust air temperature from the facade cavity, $T_{exh.}$
- Building thermal energy demand.

The mentioned comparison items are fundamental for designers in the beginning of each project to evaluate if the energy recovery system is beneficiary to use within the façade based on T_{exh} from the cavity and to assess the HVAC system energy consumptions. A typical test reference year has been used in four cities (Barcelona, Venice, Frankfurt and Helsinki) and for all the four orientations (West, East, North and South). The calculations were based on the same facade composition illustrated in (Fig.2.7) T_i inside temperature was assumed to be equal to the design temperatures, i.e. 20 $^{\circ}$C and 26 $^{\circ}$C in winter and summer respectively.

2.3.1 Exhaust air temperature from the facade cavity

The following illustrated cases based on extreme results attained by the numerical simulation to present a generalized overview Exhaust air temperature form the façade cavity during all summer months is illustrated in the Q-Q plots between the detailed-simplified models in (Fig.2.20a) and (Fig.2.20b). Values are quite close to being normally distributed in the east façade of Barcelona. Also in Helsinki east façade, the distribution could be considered normal with a small percentage considered as outliers. These outliers are due to extreme case of Helsinki, in some summer days external temperature values ranges by 10 °C degrees within the same 24 hours, along with the low sun level which causes a late hour sunset with high total vertical solar radiation reached in some days of July 1000 W/m^2, and because simplified method does not considers thermal storage with in walls, this may affect the accuracy of results comparing to the detailed model. (Fig.2.21a) and (Fig.2.21b) are showing compared values of exit temperatures through only five days from 2 to 6 July in both south façade at Venice and Frankfurt, which emphasis the agreement between the two models. All mathematical model results in different orientations have attained an accepted level of accuracy compared to the dynamic simulation done by DIGITHON.

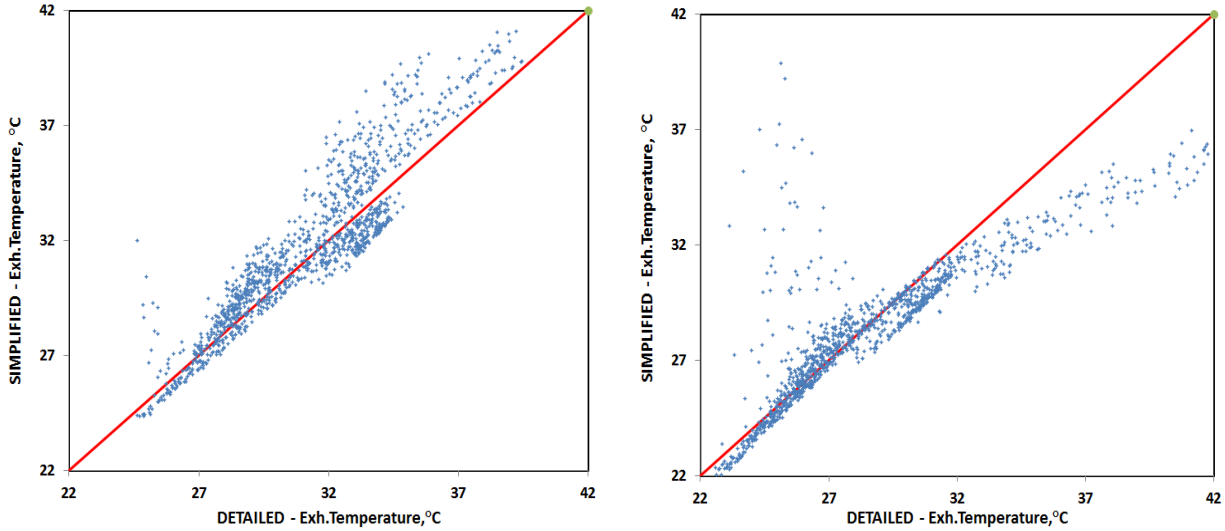

a)Barcelona -East Façade **b)Helsinki East Façade**

Fig.2.20 DIGITHON Vs. Simplified model Q-Q plot

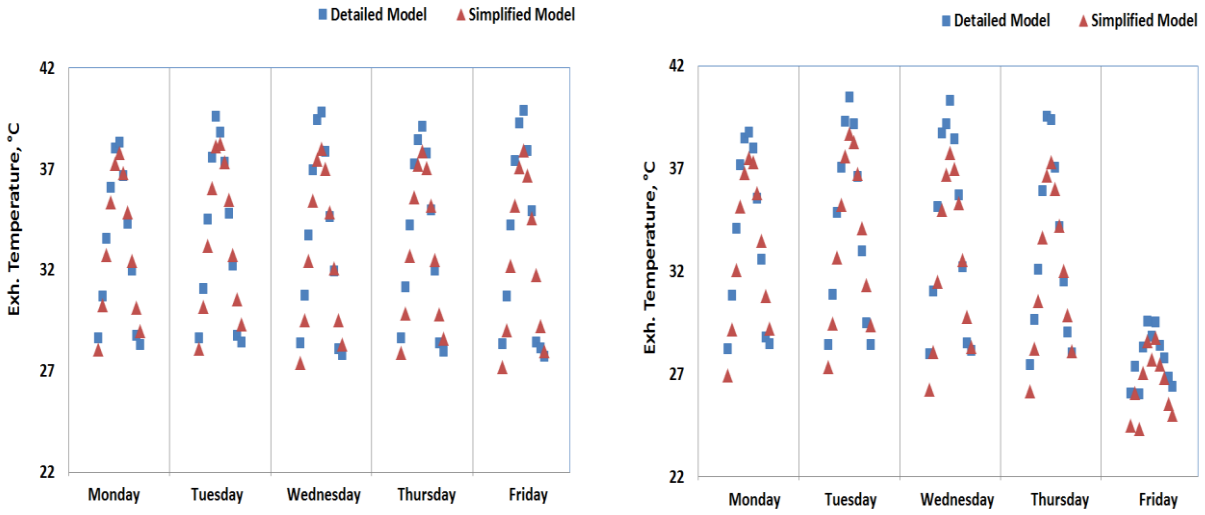

a)Venice -South Façade **b)Frankfurt -South Façade**

Fig.2.21 Exhaust air temperature by DIGITHON and simplified model during the cooling period (2July-6 July)

In winter season, also exhaust temperature were investigated (Fig.2.22a, b) outlines both the detailed and simplified models during working hours in west façade of Venice and Frankfurt respectively. Similarly, to the summer season, a good agreement between the two models was found.

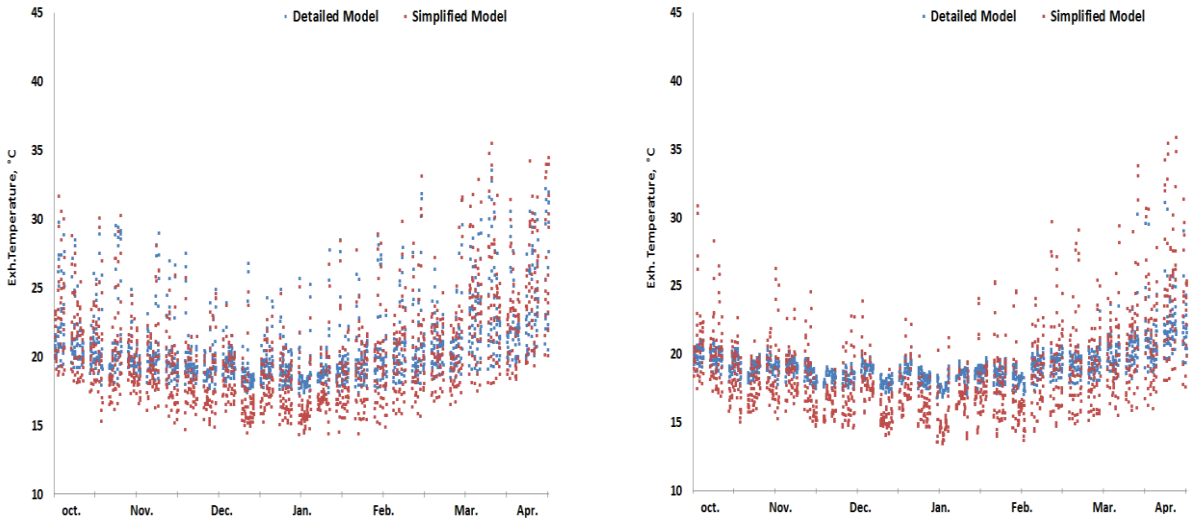

a) Venice – West Façade **b) Frankfurt - West Façade**

Fig.2.22 Exhaust air temperature by DIGITHON and simplified model during the heating period

2.3.2 Building thermal energy demand

The mathematical model has been developed to estimate thermal energy demands as a block load for the façade building. The room thermal energy was calculated based on the transmitted solar gains through facade layers according to the values of τ_i of different layers as illustrated in Equations (2.45, 2.46 and 2.47) plus convection heat transfer between façade inner glass surface temperature and inside temperatures added to internal loads and according to Equation (2.48). The heat fluxes have been determined as:

$$I_{st-1} = I_{st}.\tau_1 \quad \textbf{(2.45)}$$

$$I_{st-2} = I_{st-1}.\tau_2 \quad \textbf{(2.46)}$$

$$I_{st-3} = I_{st-2}.\tau_3 \quad \textbf{(2.47)}$$

$$Q_{room} = h_{ci}.A_f.\left(T_g - T_i\right) + I_{st-3}.\tau.A_f + IL \quad \textbf{(2.48)}$$

Where IL is the overall internal load including people, lighting, equipment. Hence a comparison between energy calculated from the two models in both summer and winter seasons for the four cities and to all orientations is presented. To attain a more refined argument for the simplified model

performance, two cases of internal loads have been taken into consideration. Case-1 with 46 W/m^2 and Case-2 with 22 W/ m^2 of internal loads as illustrated in (Table2.5).

Table2.5 Internal loads

	No of persons	W/person	Equipment W	Light (W/m^2)	Total IL (W)
Case-1	**6**	**80**	**840**	**10**	**1680**
Case-2	**2**	**80**	**280**	**10**	**800**

a. Monthly thermal energy demand during cooling season

Both mathematical model and DIGITHON are presenting hourly thermal loads, in order to obtain monthly thermal energy requirement all hours within each month have been summed. The comparison between the two models with respect to thermal energy requirements showed that simplified model results are higher than detailed model either in case-1 or case-2 the maximum increment of 27% at Barcelona in August while in Venice the maximum 23% in August too (Fig.2.23a&b). On the other hand, in case-2 the maximum difference percentage reached 15% at Frankfurt in August while in Helsinki the maximum percentage reached 38% in August (Fig.2.23c&d). This increment is considered as a positive point to the simplified model as long as it is used in the preliminary phase of the construction project because it would be better to overestimate the required loads with considerable percentage rather than underestimate it. This difference between the two models is due to thermal mass storage in room walls, which is considered in DIGITHON model while the simplified mathematical model only considers losses due to convection added to the internal loads and solar gains.

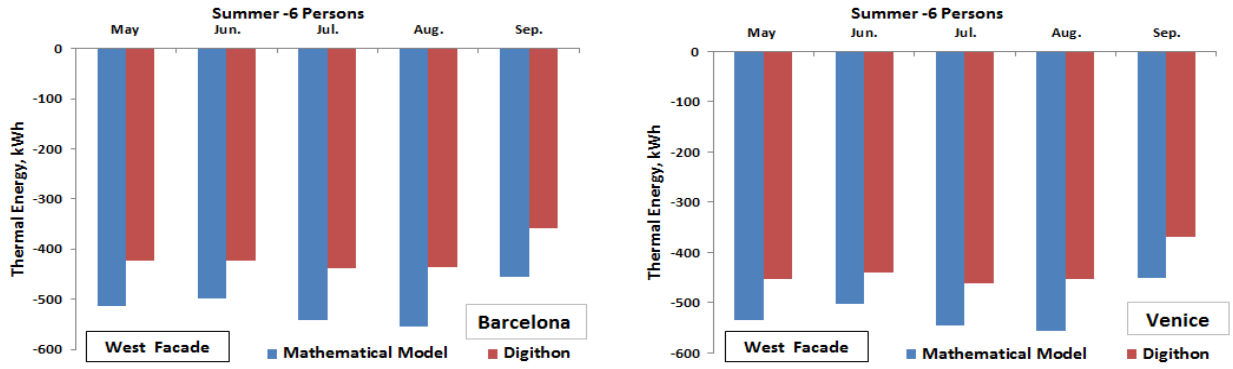

(a)

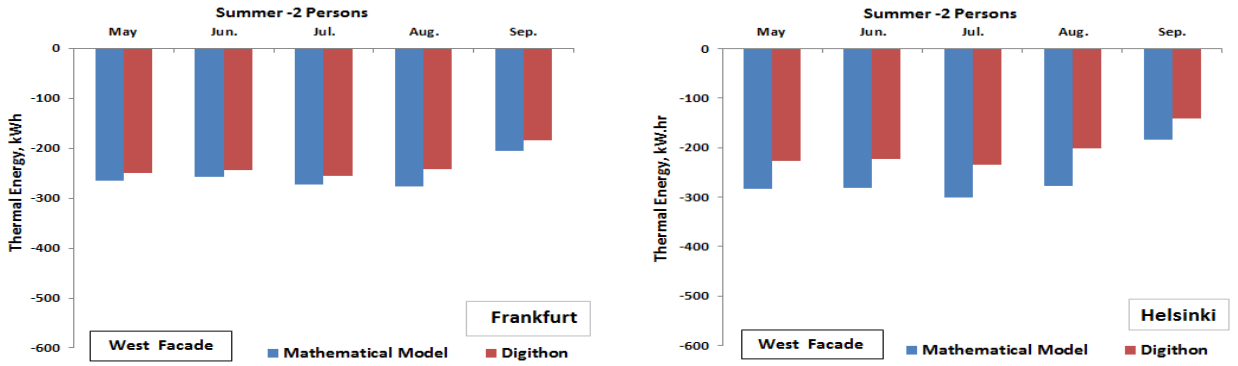

(b)

Fig.2.23 Monthly energy demands in cooling season(a) Case-1- High internal loads,(b) Case-2-Low internal load

b. Monthly thermal energy demand during heating season

The simplified model without venetian blinds has been used in heating season, nevertheless in winter the venetian blinds could be used to solve glare problems, but this assumption has been taken into account in order to have a fixed conditions for the calculation for each climate.

In the winter season case, there is no need for heating systems due to high internal loads and high insulation level, instead the cooling system is working but with lower capacities compared to the cooling season. The two models have estimated cooling loads to keep the design temperature of 20°C. The difference between the two models did not exceed 28% about at Helsinki and Frankfurt in February (Fig.2.24 a & b). In case-2 maximum difference occurs at Barcelona in February with 37%, while in Venice the maximum difference reached 33% in February (Fig.2.24 c & d).

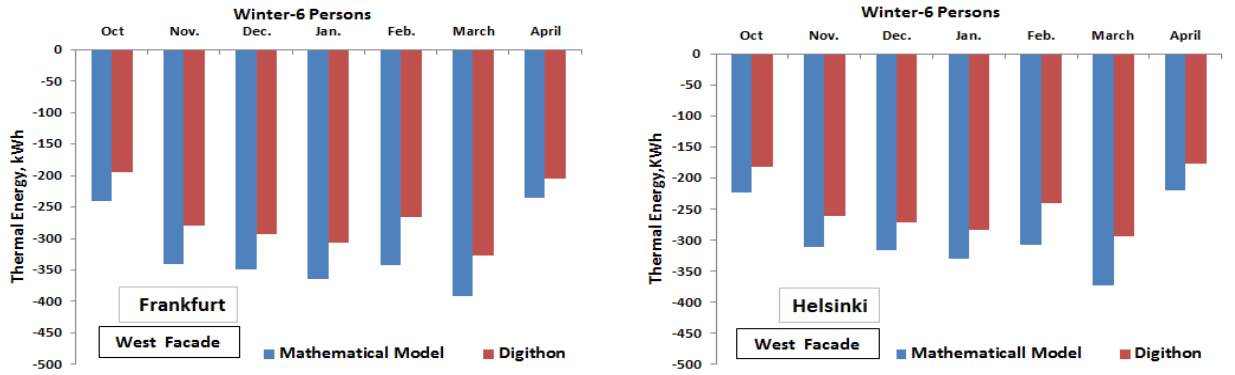

(a)

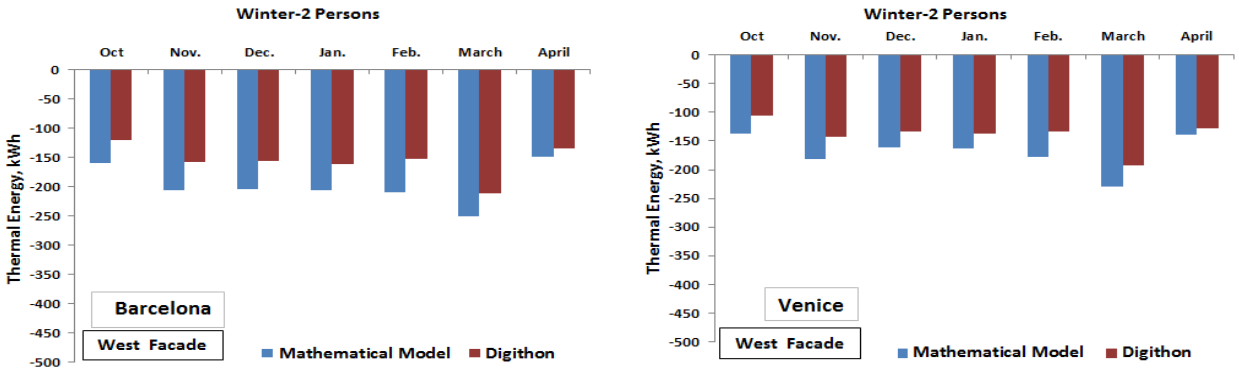

(b)

Fig.2.24 Monthly energy demands in heating season, (a) Case-1- High internal loads,(b) Case-2-Low internal loads

c. Simplified model implementation in TABS models

Standard ISO-11885-4 [47] is discussing four methods which predicting heat transfer in thermo-active building systems TABS. One of these methods is a simplified model based on Finite Difference Method (FDM) with expected error percentage of 6-10%. The model is based on the calculation of the heat balance for each thermal node defined within the slab and the room. The slab and the room are divided into thermal nodes used to calculate the main heat flows taking place during the day. The temperature of each thermal node during the hour under consideration depends on the temperatures of the other thermal nodes during the same hour. This particular method needs that transmission losses due to convection Q_t and solar gains loads Q_{sg} values have to be calculated separately by other software with a constant room temperature equal to the average room operative temperature during occupancy hours, which is typically what the simplified mathematical model calculates in complex facade. A comparison between DIGITHON and the simplified model is presented in (Fig.2.25) based on only transmission and solar gains in summer to examine the accuracy level. As shown consistent agreement between the two models have been achieved. Hence

the presented simplified mathematical model could also be used in TABS model of standard ISO-11885-4.

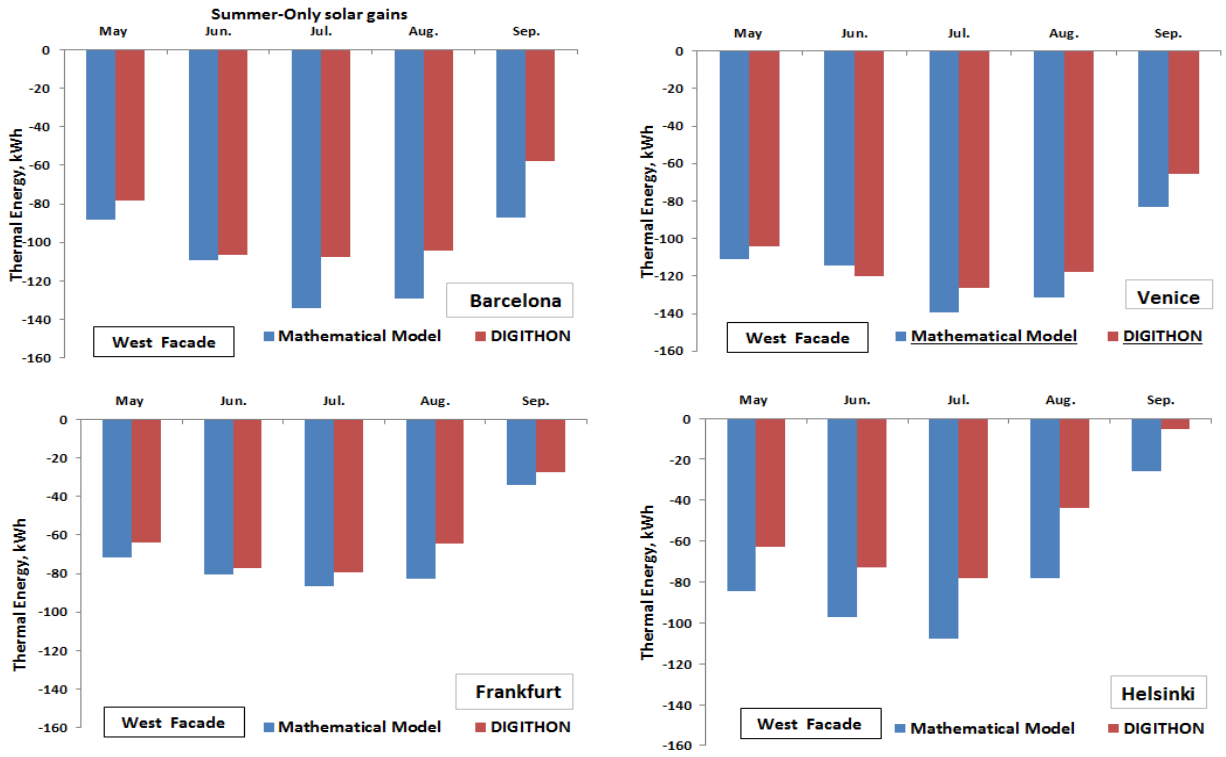

Fig.2.25 Energy loads-for only solar gains (cooling season)

2.4 Conclusions

In this chapter, the illustration and validation of two numerical dynamic simulation software's for multiple skin façades have been carried out. The first is DIGITHON as the detailed model implemented to evaluate the use of the multiple skin façade as a heat recovery unit. During the heating season measured air exhaust temperature data from the facade cavity at Padova-Italy has shown that pre-heating efficiency was -10.7% in November till it reached its maximum value in March with 14%. The seasonal average pre-heating efficiency of the total heating season did not exceed the value of 3.2%. The total ratio of pre-heating efficiency negative values happened on hourly basis over all heating months to the total number of hours of 87.7%. It is clear that pre-heating efficiency is quite low for most of the operation time of the HVAC system during the winter in which the building needs to be heated. A comparison between four European cities (Barcelona, Venice, Frankfurt and Helsinki) and for each orientation has been carried out. The façade has the highest average pre heating efficiency (about 6%) in Barcelona at March for the west orientation. Later a simplified one-dimensional model was developed. The validation of the simplified model was carried out by comparing its results both with experimental set of data and DIGITHON results. The comparison showed a good agreement to use the simplified model through preliminary design

phases. The study included many comparisons with two cases of internal loads in four European cities Barcelona, Venice, Frankfurt and Helsinki. Percentage difference between the simplified to DIGITHON model energy values in all orientations in winter with high internal loads ranges between 33% at Barcelona, west facade in February, to -15% at Frankfurt, west façade in March. In low internal loads difference ranges between 43% at Venice, west façade in February, to 10% at Barcelona west façade in April. While in summer with the high internal loads the difference ranges from 18% at Venice, west facade in May, to 27% at Barcelona west façade in August, in low internal loads it ranges between 6% at Frankfurt, west façade in May, to -30% at Helsinki, west façade in September. The average increment percentage between detailed and simplified models is considered equal to 35% and as preliminary phase anticipation it can be considered acceptable. Nevertheless the mathematical model could be implemented in other dynamic simulation codes such as the simplified method presented in ISO-11855-4 and this method needs a simplified dynamic model to identify solar radiation and convection losses based on operative inside temperature, so by comparing results of both the simplified and detailed models in summer season without any internal loads and only solar gains, the results showed a good consistency to depend on simplified model in such a TABS model.

2. Nomenclature-Chapter 2

$A_{(i)}$	Specific absorption heat flow (W/m2)
AFW	Air Flow Window
$a_{(i)}$	Solar absorption coefficient
A_f	Area of facade
c_M	Specific heat capacity at a constant pressure of the sub-system (J/(kg K))
c_p	Specific heat capacity at a constant pressure (J/(kg K))
c_{ps}	Specific heat capacity at constant pressure of the generic entering mass flow rate (J/(kg K)
c_v	Specific Heat capacity at a constant volume (J/(kg K))
h	Convection heat transfer coefficient (W/(m2. K))
IGU_i	Internal Glass Layer
IGU_e	External Glass Layer
$I_{1(i)}$	Radiation that leaves the glass (i) on its outer face 1 (W/m2)
$I_{2(i)}$	Radiation that leaves the glass (i) on its inner face 2 (W/m2)
IL	Internal Loads
I_B	Beam solar radiation (W/m2)
I_D	Diffuse solar radiation (W/m2)
$I_{abs(i)}$	Absorbed solar radiation (W/m2)
I_{st}	Total solar radiation (W/m2)
I_{st-i}	Transmitted solar radiation through glass layer (i), (W/m2)
k	Thermal conductivity (W/m.K)
L	Plate length, (m)

M	Generic mass of the sub-system (kg)
$\dot{m}_a$	Supply air mass flow rate to façade cavity (kg/s)
$\dot{m}_s$	Generic entering mass flow rate (kg/s)
R_C	Convection thermal resistance per unit area (m2 K)/W)
R_K	Conduction thermal resistance per unit area (m2 K/W)
R_{rad}	Radiation thermal resistance per unit area (m2 K/W)
q_c	Heat flux caused by convection (W)
q_g	Generic heat flux (W)
q_k	Heat flux caused by conduction (W)
q_R	Heat flux caused by radiation (W)
q_v	Heat flux caused by ventilation of the cavity (W)
Q_{eh}	Power required for heating ventilation air flow rate (W)
Q_f	Heat exchange in Façade for recovery (W)
Q_t	Transmission heat loss (W)
Q_{sg}	Solar gains (W)
Q_{room}	Thermal load of the room, (W)
$r_1(i)$	Reflection coefficient of outer face 1 of glass i (-)
$r_2(i)$	Reflection coefficient of inner face 2 of glass i (-)
S	Element surface area (m2)
SUP	Supply double skin façade
T_{exh}	Exhaust air temperature from the façade cavity (˚C)
T_i	Inside air room temperature (˚C)

T_o	Outside air room temperature (˚C)
T_S	Supply air coil temperature (˚C)
t_v	Venetian blinds surface temperature (˚C)
t_a	Air temperature inside the cavity (˚C)
$t_{1(i+1)}$	Surface temperature of element (i+1), face 1 (˚C)
$t_{2(i)}$	Surface temperature of element (i), face 2 (˚C)
T_{m1}	Mean temperature between $t_{1(i+1)}$, $t_{2(i)}$ (˚C)
T_{m2}	Mean temperature between t_v, $t_{2(i)}$ (˚C)
t_M	Temperature of the generic sub-system at current time step (°C)
$t_{M-\Delta\tau}$	Temperature of the generic sub-system at previous time step (°C)
t_s	Temperature of the generic entering flow rate (°C)
$t^A{}_{a(j)}$	Air temperature behind the screen (˚C)
$t^B{}_{a(j)}$	Air temperature front of the screen (˚C)
T_{exh}	Exhaust air temperature from the façade cavity (˚C)
T_i	Inside air room temperature (˚C)
T_e	External air temperature (˚C)
T_1	First glass pane left surface temperature (˚C)
T_2	First glass pane right surface temperature (˚C)
T_3	Second glass pane left surface temperature (˚C)
T_4	Second glass pane right surface temperature (˚C)
T_5	Third glass pane left surface temperature (˚C)
T_6	Third glass pane right surface temperature (˚C)

T_{23}	Cavity-1 air temperature (˚C)
T_{45}	Cavity-2 air temperature, in case of no blinds (˚C)
T_b	Venetian blinds temperature (˚C)
T_{b1}	Air temperature in front of blinds (˚C)
T_{b2}	Air temperature behind blinds (˚C)
T_g	Inner glass temperature (˚C)
T_m	Mean temperature (˚C)
$\Delta\tau$	Time step (S)
$\frac{\Delta U_a}{\Delta\tau}$	Change in internal energy of V_{aj} (W)
Vaj	Air volume (m3)
V	Flow velocity (m/s)
x	Glass thickness, (m)
ρ_a	Air density (kg/m3)
η_P	Preheat efficiency
σ	Stefan-Boltzmann constant, 5.67 x 10-8 (W/(m2 K4))
τ_i	Transmission coefficient (-)
ε	Emissivity (-)
μ	Dynamic viscosity (kg/(m s))
θ_B	Beam Solar radiation incident angle (°)
θ_D	Diffuse Solar radiation incident angle (°)

2. References –Chapter 2

1- V.Paassen, M.Voorden, Development of simplified tools for evaluation energy performances of double facades, In: Proceedings of International Building Physics Conference, Eindhoven, The Netherlands (2000) 347-355.

2- J. Von Grabe, A prediction tool for the temperature field of double facades, Energy and Buildings 34 (2002) 891–899.

3- M. Ciampi, F. Leccese, G. Tuoni, Ventilated facades energy performance in summer cooling of buildings, Solar Energy 75 (2003) 491–502.

4- M.A. Shameri, M.A. Alghoul, K. Sopian, M. Fauzi, M. Zain, O. Elayeb, Perspectives of double skin facade systems in buildings and energy saving, Renewable and Sustainable Energy Reviews 15 (2011) 1468–75.

5- D. Saelens, Energy performance assessment of multiple-skin facades, Doctoral Thesis, Laboratory for Building Physics, K.U. Leuven University, Leuven, Belgium, 2002.

6- M. Haddad and M. Elmahdy, Comparison of the Monthly Thermal Performance of a Conventional Window and a Supply-Air Window, ASHRAE Transactions 104 (1998) 1-10.

7- C.Park, G. Augenbroe, T.Messadi, M.Thitisawat, , N.Sadegh, , Calibration of a lumped simulation model for double-skin facade systems , Energy and Buildings. 36 (2004) 1117–30.

8- C.Park, G. Augenbroe, T.Messadi, M.Thitisawat, , N.Sadegh,Real-time optimization of a double-skin facade based on lumped modeling and occupant preference, Energy and Buildings 39 (2004) 939–48.

9- C. Balocco, A non-dimensional analysis of a ventilated double facade energy performance, Energy and Buildings 36 (2004) 35–40.

10- C. Balocco, M. Colombari, Thermal behavior of interactive mechanically ventilated double glazed facade: non-dimensional analysis, Energy and Buildings 38 (2006) 1–7.

11- I. Doebber, M.M. Arup, Analysis process for designing double skin facades and associated case study, SimBuild conference, Cambridge, MA, USA, 2006.

12- J. Hensen, M. Bartak, F. Drkal, Modeling and simulation of a double-skin facade system, ASHRAE Transactions 108 (2002) 1251–9.

13- R. Aynsley, A resistance approach to analysis of natural ventilation airflow networks, Journal of Wind Engineering and Industrial Aerodynamics 67 (1997) 711–719.

14- A. Fallahi, F. Haghighat, H. Elsadi, Energy performance assessment of double- skin facade with thermal mass, Energy and Buildings;42 (2010) 1499–509.

15- E. Gratia, A. De Herde, Green house effect in double skin façade, Energy and Buildings 39 (2007) 199–211.

16- J. Joe1, W. Choi1, and J. Huh, Load characteristics and operation strategies of building integrated with multi-story double skin façade, Energy and Buildings 60 (2013) 185–198.
17- D.Crawley, W.Hand, M.Kummert, B.Griffith, Contrasting the capabilities of building energy performance simulation programs, Building and Environment 43 (2008) 661–673.
18- H. Poirazis, Double skin facades for office buildings Report EBD-R-04/3, Lund University 2004.
19- B. Todorovic, B. Maric, Thermal Influences of Double-Façades, Proceedings of 20th International Congress of Refrigeration, Sydney, Australia, 1999.
20- D. Arons, Properties and Applications of Double-Skin Building Facades, MSc thesis, Massachusetts Institute of Technology, MA, USA, 2000.
21- W. Stec, D. van Paassen, Defining the performance of the double skin façade with the use of the simulation model, IBPSA 8th Conference, Eindhoven, Netherlands, 2003.
22- D. Saelens, J. Carmeliet, H. Hens, Modeling of Air and Heat Transport in Active Envelopes, Proceedings of ICBEST 2001, International Conference on Building Envelope Systems and Technologies, Ottawa, Canada, 2001.
23- H. Manz, A. Schaelin, H. Simmler, Ariflow patterns and thermal behavior of mechanically ventilated glass double facades, Building and Environment 39 (2004) 1023–1033.
24- F. Zanghirella, M. Perino, V. Serra, A numerical model to evaluate the thermal behavior of active transparent facades, Energy and Buildings 43 (2011) 1123–1138.
25- R. Fuliotto, F. Cambuli, N. Mandas, N. Bacchin, G. Manara , Q. Chen, Experimental and numerical analysis of heat transfer and airflow on an interactive building façade, Energy and Buildings 42 (2010) 23–28.
26- WIS. WIS User Guide. Advanced Windows Information System Project.http://www.windat.org/wis/html/index.html, 2006.
27- J.R. Gosselin, Q. Chen, A computational method for calculating heat transfer and air flow through a dual-airflow window, Energy and Buildings 40 (2008) 452-458.
28- T.E. Jiru, F. Haghighat, Modeling ventilated double skin facade--A zonal approach. Energy and Buildings 2008; 40:1567-1576.
29- A. Guardo, M. Coussirat ,E. Egusquiza ,P. Alavedra,R. Castilla, A CFD approach to evaluate the influence of construction and operation parameters on the performance of Active Transparent Facades in Mediterranean climates. Energy and Buildings 2009; 41:534-542
30- Fluent6.3.26 2006 Fluent Inc.- User guide.
31- W. Stec, A.H.C. van Paassen, Symbiosis of the double skin facade with the HVACsystem, Energy and Buildings 37 (5) (2005) 461–469.

32- D. Saelens, J. Carmeliet, H. Hens, Energy performance assessment of multiple skin facades, HVAC&R Research 9 (2) (2003) 167–185.
33- Gratia E, De Herde A, The most efficient position of shading devices in a double-skin façade, Energy and Buildings 39(2007) 364-373.
34- K.Lee, T.Kim, G.Lee, J.Lee, Cooling load reduction effect and its mechanism in between-glass cavity and venetian blind operation during the summer season, BUILD SIMUL 6(2013) 351–364.
35- M. De Carli, H. Elarga, A. Zarrella, M. Tonon, Evaluation of energy recovery of multiple skin facades: The approach of DIGITHON, Energy and Buildings 85 (2014) 337–345.
36- M. De Carli, M. Tonon, Effect of modelling solar radiation on the cooling performance of radiant floors, Solar Energy 85 (2011) 689–712.
37- M. De Carli, M. Scarpa, R. Tomasi, A. Zarrella, DIGITHON: A numerical model for the thermal balance of rooms equipped with radiant systems, Building and Environment 57 (2012) 126-144.
38- M. Tonon, Tecniche di simulazione dinamica per la determinazione del comportamento termico ed energetico degli edifici, Doctoral Thesis, Applied Physics Department, University of Padova, 2004. (in Italian)
39- G.P. Mitalas, D.G. Stephenson, Cooling load calculations by thermal response factors, ASHRAE Transactions 73(1) (1967) III.1.1–III.1.7.
40- T. Kusuda, Thermal response factors for multi-layer structures of various heat conduction systems, ASHRAE Transactions 75(1) (1969) 241-271.
41- T. Blomberg, Heat2 - A PC-program for heat transfer in two dimensions, Manual with brief theory and examples, Group for Computational Building Physics, University of Lund, Sweden 1999.
42- Department of Energy-DOE, Window v6.3.9.0, Energy efficiency and renewable energy office of building technology, USA., 2010.
43- ANSI/ASHRAE/IESNA Standard 90.1-2004.
44- S.P. Corgnati, M. Perino, V. Serra, Experimental assessment of the performance of an active transparent façade during actual operating conditions, Solar Energy 81 (2007) 993–1013.
45- S. Klein, W. Beckman, J. Mitchell, J. Duffie, N. Duffie, T. Freeman et al., TRNSYS 16 - A transient system simulation program, User manual, University of Wisconsin, Madison, US, 2004.
46- J.A. Duffie, W.A. Beckman, Solar Engineering of Thermal Processes, 2nd edition, JohnWiley & Sons, New York, 1991.
47- ISO 11855-4, Dimensioning and calculation of the dynamic heating and cooling capacity of Thermo Active Building Systems (TABS).

Chapter-3

PV integrated in buildings by TRNSYS

Introduction

The efficient integration of solar energy concluded in PV modules in building sector can support the energy performance improvements. On the other hand MSF buildings could be a nucleus for such an implementation. However there are obstacles such as lack in clarification of detailed dynamic models carried out by commercial software TRNSYS to overlook the yearly energy consumption. Nevertheless, the input parameters that control the efficient operation of PV integrated in façade buildings such as, façade composition, glass technical specifications and facade cavity ventilation methodologies. The main purpose of this chapter is to illustrate how to model multiple skin façade buildings integrated with PV modules on its vertical side in TRNSYS without the need of calling an external code .The used technique is clarified and validated by measured data. Later a detailed comparative study was clarified to distinguish between the energy efficiency of the PVIB system for an office building in different boundary conditions and installation methodologies. Three main comparative items were considered, the first is divers climatic conditions at (Abu Dhabi, Venice and Wurzburg) to track performance changes in the installed PV solar modules system, the second is two composition of the inner façade glazing layer and finally two typologies of the façade cavity ventilating system (i.e. natural and hybrid ventilation systems). The application of TRNflow was clarified thoroughly to investigate different ventilation methodologies within the façade.

Objectives:

1- Explain how to implement multiple skin facades within TRNSYS.

2- Discuss an innovative integration of PV modules in façade buildings and describe the numerical model.

3-Energy efficiency evaluation through an extensive parametric study.

3.1 Photo voltaic integrated in buildings PVIB background

Photovoltaic technology makes use of the abundant energy of the sun and converts it into electrical energy with little impact on the environment. The integration of efficient renewables systems in buildings is a major purpose. Generally building integration of photovoltaic (PV) cells is carried out on sloped roofs, flat roofs, facades and solar shading systems. PV cells may be mounted above or onto the existing or traditional roofing or wall systems. However, BIPV systems replace the outer building envelope skin, thus serving simultaneously as both a climate screen and a power source

generating electricity [1], .However so far the urban deployment of solar energy within building sector has not yet been tackled sufficiently. Infield et al [2] mentioned that ventilated photovoltaic (PV) facades are a promising way to integrate photovoltaics into a building structure in that they provide significant additional benefits over and above the electricity yield. Fung and Yang [3] presented a one-dimensional transient heat transfer model, the Semi-transparent Photovoltaic module Heat Gain (SPVHG) model, for evaluating the heat gain of semi-transparent photovoltaic modules for building-integrated applications. The annual total heat gain was evaluated by using the SPVHG model. It was found that the area of solar cells in the PV module has significant effects on the total heat gain, since nearly 70% of total heat gain can be reduced if the solar cell area ratio is 0.8. Song et al. [4] characterized the power output of PV module depending on incidence angle and the azimuth using a transparent thin-film solar cell in a mock-up model at various slopes south-oriented, as a building integrated photovoltaic system. It was found that the PV module with a slope of 30°, facing south, provided the best power performance in terms of annual power output (844.4 kWh/kWp annual power output). It produced about 2.5 times higher power output than the module with the vertical slope. Park et al. [5] investigated the electrical and thermal performance of a semi-transparent PV module that was designed as a glazing component. The experiment was performed under both Standard Test Condition (STC) and outdoor conditions. The results showed that the power decreased about 0.48% (in STC) and 0.52% (in outdoor conditions, under 500 W/m2) per 1°C increase of the PV module temperature. It was also found that the property of the glass used for the module affected the PV module temperature followed by its electrical performance, confirming that during a winter day, the module with the bronze glass had a higher temperature compared to the module with clear glass. Li Mei et al [6] presented a thermal building model that includes sub models of the ventilated PV facade and the additional solar air collectors have been described. Commercial PV elements only allow transforming about 14-20% of the incident solar radiation into electrical energy. The remaining incident solar radiation is converted into sensible heat, which results in warming-up the PV element [7]. Conversion efficiency of the PV cell is depending mainly on its surface temperature and solar illumination [8]. Commercial PV elements only allow transforming about 14-20% of the incident solar radiation into electrical energy. A preliminary CFD work has been carried out in order to investigate the possible improvements by cooling the cavity with an amount of exhaust air used for ventilating and maintaining proper indoor air quality in each office [9].

3.2 TRNSYS transient thermal model

3.2.1 Overall approach

The building simulation program TRNSYS [10] was developed at the University of Wisconsin –

Madison Solar Energy Lab and the University of Colorado Solar Energy Applications Lab. It became commercially available in 1975. TRNSYS simulates dynamically thermal behavior of buildings; it relies on modular approach to solve Equations described by FORTRAN subroutines. A TRNSYS project is typically setup by connecting components graphically in the Simulation Studio. Each Type of component is described by a mathematical model in the TRNSYS simulation engine and has a set of matching **Proforma's** in the Simulation Studio. The **proforma** has a black-box description of component: inputs, outputs, parameters, etc. The multi-zone building models in TRNSYS (TYPE 56) is a non-geometrical balance model with one air node per zone, representing the thermal capacity of the zone air volume and capacities which are closely connected with the air node (furniture, for example). Thus the node capacity is a separate input in addition to the zone volume. The transient heat exchange through the surfaces composing a zone is calculated with the z-transfer function method. The z-transfer function method as used in the TYPE 56 building model has been validated by Voit et al. [10]. The method of the transfer function or response factors can be described as the method to tell the "thermal history" of the wall. The wall is considered as a black box. The number of time-steps (k) related to the time-base (defined by the user) shows whether the wall is a heavy wall with a high thermal mass ($k < 20$) or if only a few time-steps have to be considered to describe the thermal behavior of this wall. If the time-base of the considered wall is higher than the time constant, the calculation of the Transfer-function matrix coefficients is stopped. Therefore such a "thin" wall can be replaced by a resistance definition neglecting the thermal mass. (Fig.3.1) shows a schematic representation of the most important heat fluxes in TYPE 56. At an exterior surface, the longwave radiation (qrhx,e) and the convective heat exchange (qconv,e) are separated and the absorbed solar radiation (qs,e) is accounted for. The long-wave radiation exchange between the surfaces (qrhx,i) within a specific zone is approximated by the star network method implemented by Seem [24]. The interior surface temperatures are linked to a so-called star temperature (T star,i) by equivalent resistances (Requ,j). The star temperature in turn, is linked to the zone air temperature (Ta,i) by means of a star resistance (R star,i). A detailed description of the resistance calculation method is available from Seem [24].

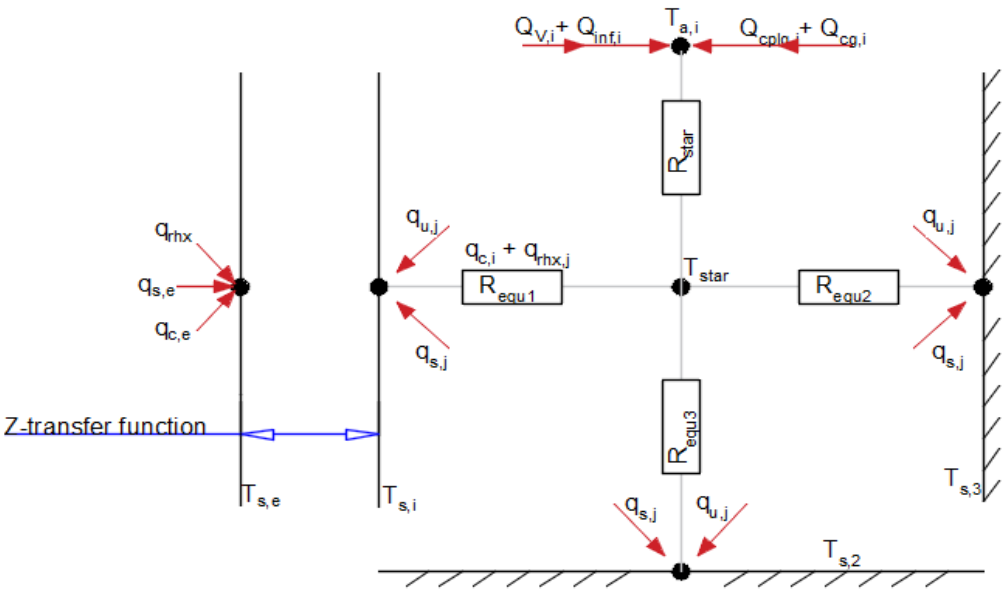

Fig.3.1 Building heat fluxes-TRNSYS

Where:

Ta,i = zone air temperature for zone i(K)

Rstar,i = star resistance (m²·K/W)

Tstar,i = star temperature for zone i(K)

Requ,j = equivalent resistance for surface j (m²·K/W)

Ts,j = surface temperature of surface j (K)

qc,j = convective heat flux from surface j (W/m²)

qs,j = solar radiation to surface j (W/m²)

qrhx,j = radiative heat exchange from surface j (W/m²)

Qinf,i = infiltration gain (W)

Qv,i = ventilation gain (W)

Qcg,i = convective heat gain (W)

Qcplg,i = ventilation due to coupling with other (W)

qu,j = user defined flux to surface j (W/m²)

3.2.2 Simulation of glazed façade surfaces

An external glazed surface is thermally considered as an external wall with no thermal mass, partially transparent to solar, but opaque to long-wave internal gains. Long-wave absorption is considered to occur only at the surfaces. In the energy balance calculation of the TYPE 56, the glazed external surface is described as a 2-node model shown in (Fig.3.2)

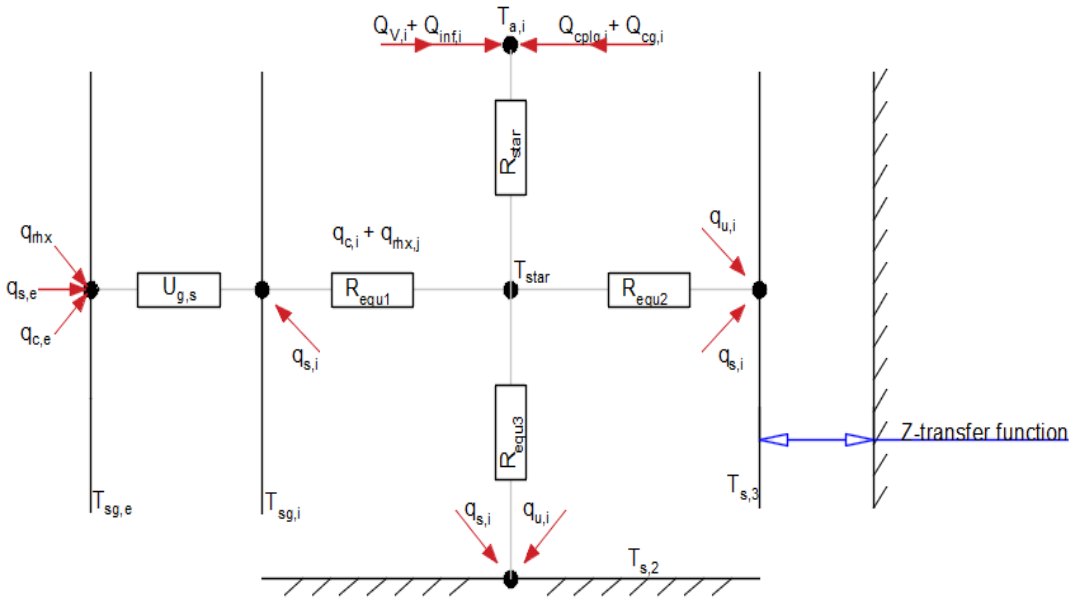

Fig.3.2 TRNSYS Glass element heat fluxes

For each glazing element of the facade, the resulting temperature is calculated considering transmission, absorption and reflection of incoming direct and diffuse solar radiation, diffuse short-wave radiation being reflected from the walls of the zone or an internal shading device, convective, conductive and long-wave radiative heat transfer between the individual panes and with the inner and outer environment (Fig.3.3).

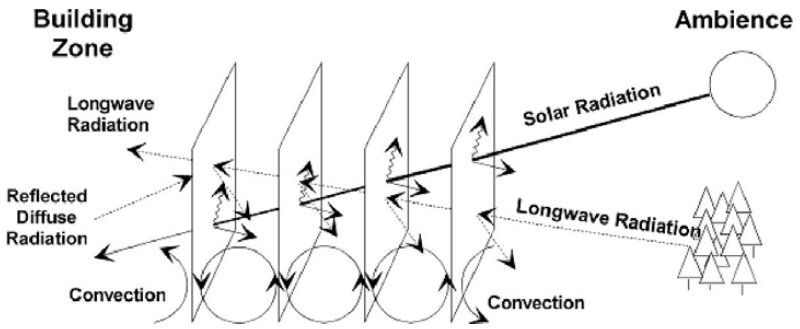

Fig.3.3 Radiation heat flux

3.2.3 MSF integration via TRNSYS

TRNSYS does not contain a specific (Type) to integrate MSF to buildings [11]. Accordingly the facade cavity is subdivided into thermal zones and they have been included in the building model (Type 56a) based on the number of glass layers .As illustrated in the scheme (Fig.3.4a) in case of having double skin façade, one thermal zone shall be implemented for each floor adjacent to the indoor zone or it could subdivided into more zones with a fictitious transparent surfaces (Fig.3.4b) in

between with high conductivity, negligible thermal mass and high emissivity, and the air nodes are coupled in the airflow network.

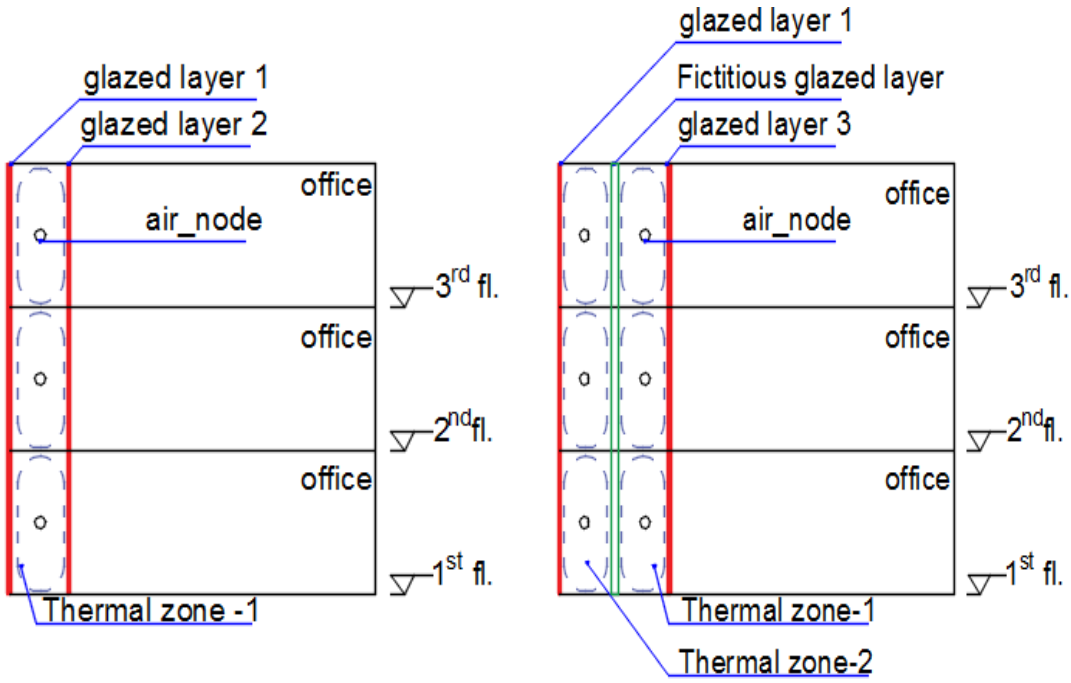

(a) **(b)**

Fig.3.4 Facade cavity thermal zones subdivision, (a) Double skin façade, (b) Multiple skin façade

The walls of cavity thermal zone are constructed from glass layers. Glazed layers technical specifications are computed within WINDOW [12] software developed by Lawrence and Berkeley lab-USA (Fig.3.5a). The detailed calculation of reflection between individual panes is performed hemi spherically for diffuse radiation and insteps of 10° incidence angle for direct solar radiation. The optical properties of the glass are written to ASCII file by the WINDOW program (Fig.3.5b). The output file has a standard format which makes the results available for TRNSYS thermal analysis. The output form is saved within TRNbuild window library by the user defined name. Accordingly, the façade cavity is identified based on the saved glass elements in library and end-user input geometrical data.

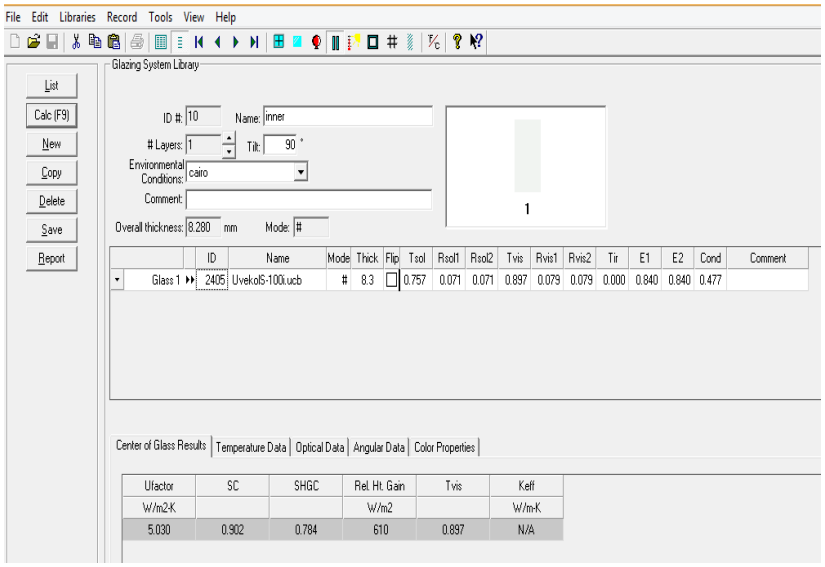

(a)

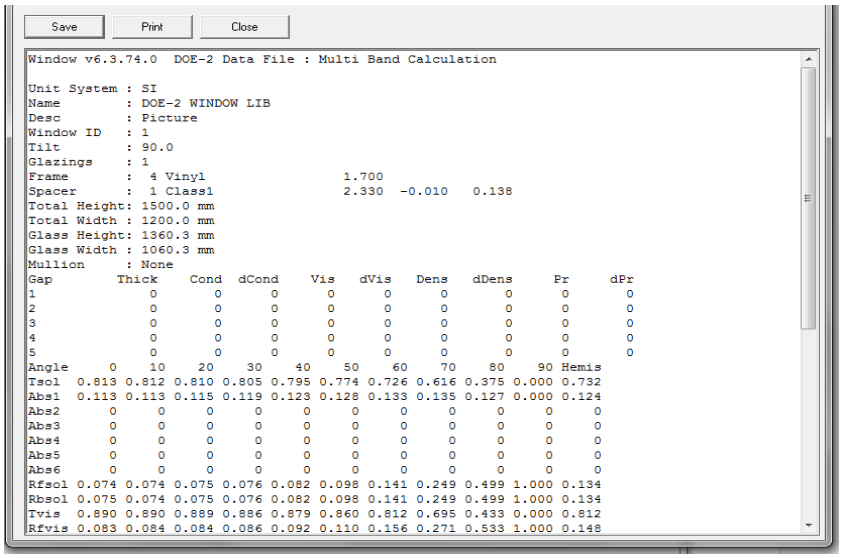

(b)

Fig.3.5 Window software[12], (a) pattern of a command screen, (b) ASCII file

3.2.4 Innovative PV modules integration in TRNSYS

An innovative installation within the vertical facades of glazed building includes locating the semi-transparent PV module inside the faced cavity (Fig.3.6) and by controlling properly the façade cavity ventilation, the outcome PV system energy is optimized. It is important to highlight that a preliminary CFD work has been carried out [9] in order to investigate the possible improvements by cooling the cavity with an amount of fresh air used for ventilating and maintaining proper indoor air quality in each office and it has been clarified in chapter (6).

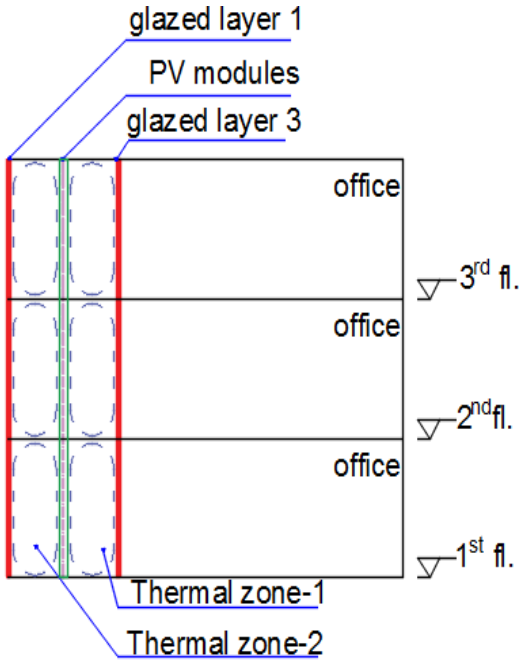

Fig.3.6 TRNSYS/PV integrated in glazed building

The PV semi-transparent selected type is a commercial amorphous silicon module with 10% clearness. (Table 3.1) clarified all technical and optical specifications.

Table 3.1 Semi-transparent PV module technical specifications

Cell type	a-si Thin film
Front glass	3mm tempered glass
PV glass	3.2 float glass
Temp coefficent ψ	-0.19 %/°C
η_r	15%
Sol. Transmission	9.4%
light Transmission	10.8%
Sol. Reflection	13.9%
Light reflection	52.9%

TRNSYS contains many Types defining photovoltaic panels, includes crystalline, PV thermal collectors, flat plate and thin film. Whilst one of the main scopes of this research is to integrated vertical PV modules to the building façade surface, unfortunately this option is not available in TRNSYS. Accordingly to solve this obstruction two steps were carried out, the first is to create a

fictitious glazed layer with all the technical and angular optical properties of the PV module estimated by Window [12] as clarified previously. ASCII file was created and named in the wall library at Type 56 as PV layer to be used as one of the cavity territory walls. This step particularly is to estimate the hourly external / internal layer surface and air cavities temperatures surrounding the fictitious PV layer. Consequently to obtain the hourly electrical energy production the second step included the linking of obtained temperature values as input data for the PV module Type 562. The selection of this PV Type was based on evaluating the dynamic variation of conversion efficiency in respect of operating surface temperature in which the electrical efficiency and hence the output power depend though linearly but rather strongly on it [8]. Type 562b is available on TRNSYS either glazed or unglazed photovoltaic module. Efficiency is variable, provided for reference conditions along with coefficients that describe the effect of cell temperature and incident radiation changes. The hourly produced power is estimated for the PV module Equations (3.1), (3.2) based on identifying the PV efficiency as a function of surface temperature and irradiance [10].

$$P = I\,\eta_m\,A_{PV} \quad \textbf{(3.1)}$$

$$\eta_m = \eta_r\,[1 - \psi\,(T_m - T_r] \quad \textbf{(3.2)}$$

Where:

η_m	PV module efficiency
η_r	PV module reference efficiency
ψ	Temperature coefficient of PV module (°C / %)
A_{PV}	Area of PV module

PV module energy balance

The input parameters includes different temperature values moderating the heat transfer modes through the PV panel, ambient, zone and Sky temperature, top and bottom heal loss convection coefficients, vertical solar radiation, total horizontal solar radiation and Panel slope. Type562 calculates incidence angle modifiers in order to come up with the solar radiation absorbed by the PV cells themselves. The overall incidence angle modifier is a weighted average of the component incidence angle modifiers and is given by Equation (3.3). The energy balance scheme is clarified in (Fig.3.7).

$$IAM = \frac{IAM_{beam}(I_{beam}) + IAM_{diffuse}(I_{diffuse}) + IAM_{ground}(I_{ground})}{I_{beam} + I_{diffuse} + I_{ground}} \quad (3.3)$$

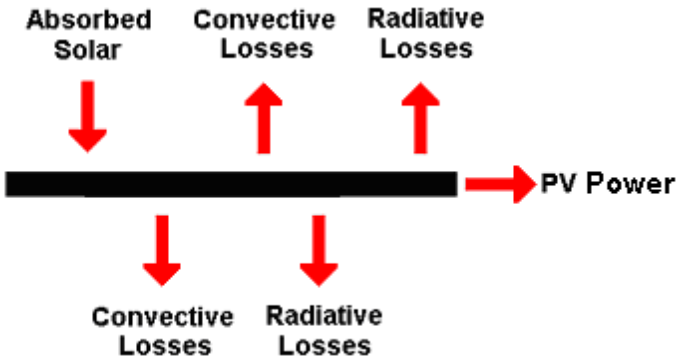

Fig.3.7 PV panel energy balance scheme

$$\dot{Q_{abs}} = IAM \ \dot{I}_T \ A \quad (3.4)$$

$$\dot{Q}_{top,conv} = h_{conv,top} \, A \, (T_{PV} - T_{amb.top}) \quad (3.5)$$

$$\dot{Q}_{top,rad} = h_{rad,top} \, A \, (T_{PV} - T_{sky}) \quad (3.6)$$

$$\dot{Q}_{back,conv} = h_{conv,back} \, A \, (T_{PV} - T_{amb.back}) \quad (3.7)$$

$$\dot{Q}_{back,rad} = h_{rad,back} \, A \, (T_{PV} - T_{rad.back}) \quad (3.8)$$

The only unknown in the above Equations is the cell temperature at which the PV is operating. Type562 performs an iterative search, repeatedly guessing and modifying the PV cell temperature until the various terms of the energy balance sum to 0.

3.2.5 Ventilation of the cavity

a Air coupling within TYPE56

The ventilation system is essential in MSF buildings to avoid air temperature increment due to greenhouse phenomena occurring inside the cavity accordingly the undesirable overheating loads within summer season. On the other hand in winter season it is an advantage to capture the solar radiation and decrease the transmission losses. Unfortunately, most MSF-typologies are incapable of lowering the heating and cooling demand simultaneously. However by combining typologies or by changing system settings according to the particular situation, the thermal loads reduction could be achieved [13]. On the other hand the applied ventilating system whether it is forced, natural or hybrid

is depending on many aspects such as ambient temperature, wind velocity and electrical fan consumption. Moreover in order to reduce the surface temperature of the integrated PV module inside the cavity, different ventilation typologies were investigated such as (Out – Out),(In-Out) , shown in (Fig.3.8).

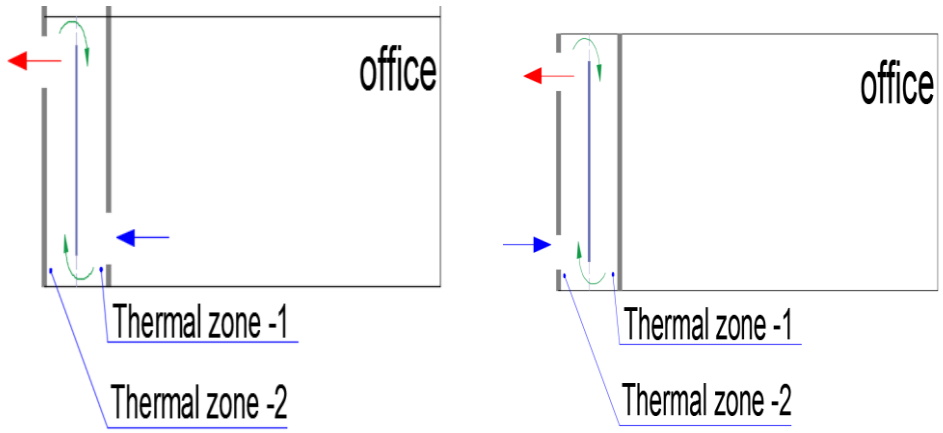

(a) **(b)**

Fig.3.8 Ventilation methodologies (a) In-Out, (b) Out-Out

Since façade's cavities are modeled as thermal zones, it was easy to apply the coupling of airflow option available in TRNbuild in between. The energy balance Equation (3.9) for connective from one zone to another:

$$Q_{clg} = V.\rho\,.c_p\,(T_{air,clg} - T_{air,zone}) \qquad \textbf{(3.9)}$$

The coupling allows the mass flowrate to transfer from a zone to another (Fig.3.9). The magnitude of this coupling will directly affect the zone temperature and zone humidity, but will have no effect on the adjacent zone from which the air flowrate originates. It is up to the user to insure proper mass balances for each zone. The mass flow rate due to coupling could be also scheduled as required. In a sense that coupled air flow rate is not exceeding the amount of treated fresh air supplied to the office zone to keep the indoor air quality and not penalty the cooling system any extra loads, added to diverse control strategies between summer and winter seasons to assure an effective thermal performance.

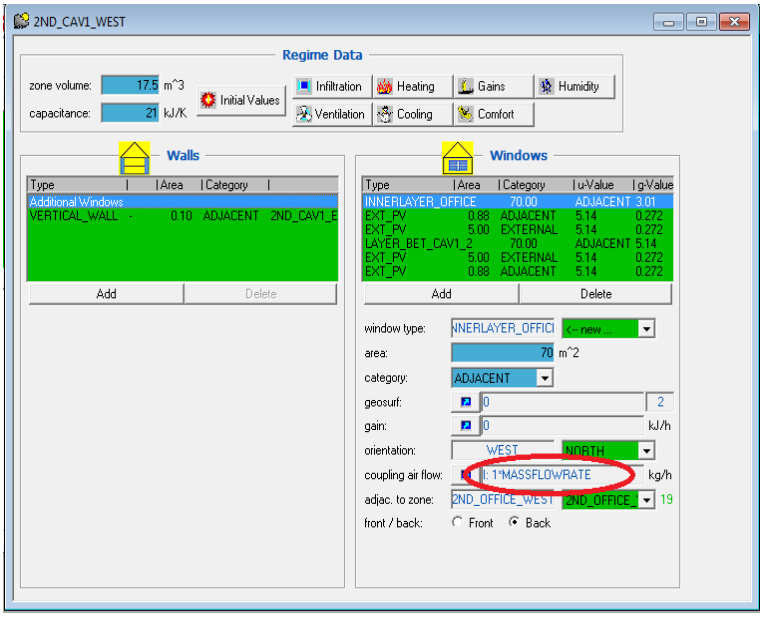

Fig.3.9 Coupling air flow

b TRNFLOW Implementation

TRNFLOW was applied to analyze natural, forced and hybrid ventilation strategies through cavity façade. TRNFLOW is ventilation network calculation software and add on program in TRNSYS that can iteratively solve the movement of air and heat simultaneously. The thermal and the air flow model are linked as black boxes. For simplification, the information flow between the two models is represented by one room air temperature node and one air flow variable. In fact there are at least as many air temperature nodes, as there are rooms in the building and each node has at least one air flow. In the solution process, the airflow model starts with the input node temperatures T_{int} and calculates the corresponding air flows m_i in of each node. These flows are used in the thermal model, which calculates the output room temperatures $T_{out,i}$, with an iterative solver algorithm the input temperatures set is found which matches the output temperatures set (Fig.3.10).

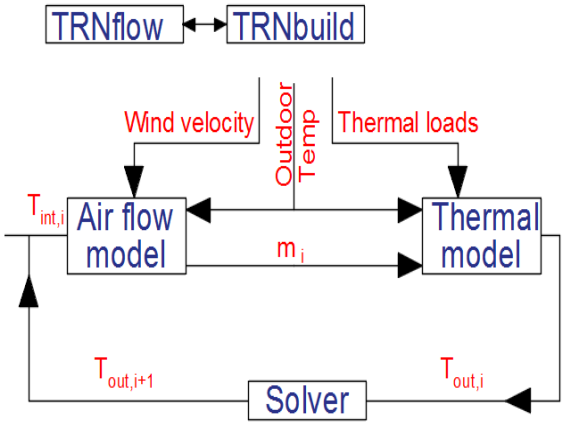

Fig.3.10 Combined thermal air flow models

The airflow model is based on a network model of the building. The air nodes are linked by non-linear conductance, modelling the air paths (air flow components: cracks, openings, ducts, fans an windows). Four classes of nodes are used to define the airflow network: constant pressure nodes, thermal zones, auxiliary nodes, and external nodes. Using air mass conservation in each node, a system of non-linear Equations is built and solved to determine the node pressures and the mass flows. The direction from "from node" to "to node" is defined as the positive flow direction. [10] To simulate ventilation across the two thermal zones describing the air cavity integrated with PV module, the air links in between were assumed to be large opening or window because it is capable of processing a two way air flow within one time step. As the pressure difference between two zones with different air densities is a function of the height z, the flow in a large opening has a vertical velocity profile. A numerical integration of this profile results into an air mass flow for both flow directions Equation (3.10):

$$m^{\circ} = c_d \int_0^H \sqrt{2 \cdot \rho(z) \cdot f(z) \cdot w(z)}\, dz \qquad \textbf{(3.10)}$$

As the air flow pattern can reverse in natural ventilation within one time step [14], Coefficient of discharge values were evaluated for all openings by using Equations (3.11), (3.12) and (3.13).

$$c_d = \varepsilon^{-0.5} \qquad \textbf{(3.11)}$$

$$\varepsilon = \lambda \frac{L}{D_h} \qquad \textbf{(3.12)}$$

$$D_h = \frac{4\,A}{P} \quad \textbf{(3.13)}$$

Friction factor is described by the implicit Colebrooke-White Equation (3.14) [14]:

$$\lambda^{-0.5} = 2\log\left[\left({}^{k}/_{D}\right) \times 3.72\right] + \left({}^{2.51}/_{R_e} \times \lambda^{-0.5}\right)\Big] \quad \textbf{(3.14)}$$

Natural ventilation driving forces

- **Wind Pressure**

The wind pressure on a façade is defined as the difference between the local pressure on the surface and the static pressure in the undisturbed wind on the same height. The relation factor of this pressure difference to the dynamic pressure of the reference wind velocity is known as wind pressure coefficient or Cp value, the resulting pressure from the wind effect is expressed by Equation (3.15) with wind velocity Equation (3.16) and wind pressure coefficients for external nodes α_o[15] which depends on the type of terrain, Table (3.2).

$$\Delta p = c_p \times 0.5 \times \rho \times {U_O}^2 \quad \textbf{(3.15)}$$

$$U_O = U_m \times (h_b/h_m)^{\alpha_m} \times (h_o/h_b)^{\alpha_o} \quad \textbf{(3.16)}$$

Where:

h_m Pylon height at meteo station (m)

h_b Height of boundary layer, 60m for α_o<0.34

U_o Wind Velocity at the building site (m/s)

U_m Wind velocity at the meteo station at pylon height (m/s)

α_o Wind velocity profile exponent at the building site (-)

Table 3.2 Wind velocity exponent

Class	Terrain description	α_o
1	Sea, flat terrain without obstacles	0.1-0.15
2	Open terrain with isolated obstacles	0.15-0.25
3	Wood, small city, suburb	0.25-0.35
4	City center	0.35-0.45

- **Buoyancy**

Buoyancy or stack effect is the movement of air caused by the difference in temperatures and accordingly in density. In (Fig.3.11) a link between an external node and a thermal zone is shown. The pressure difference between the two sides of the link is defined in Equations (3.17) to (3.19)

$$\Delta p = p_{L1} - p_{L2} \quad \textbf{(3.17)}$$

$$p_{L1} = p_{ref} - g\,\rho_1\,h_1 \quad \textbf{(3.18)}$$

$$p_{L2} = p_2 - g\,\rho_2\,h_{L2} \quad \textbf{(3.19)}$$

Where:

$p_{ref} = reference\ pressure, 0\ Pa$

Taking into consideration that ρ have been assumed to be uniform in the inner zone and in outer zone. Therefore the vertical position of the nodes and links must be given in TRNflow model.

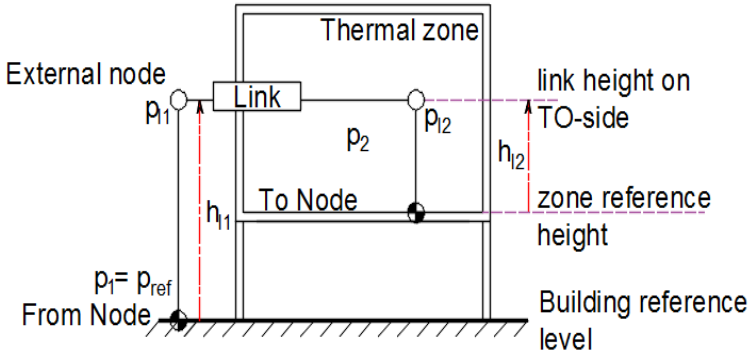

Fig.3.11 TRNFlow definition of links heights and pressures

3.2.6 Outdoor climate

Various weather data files are included in TRNSYS and could be uploaded in Type 16 to provide the following parameters for each time step to run the energy simulation (Fig.3.12):

-Outdoor temperature

- Relative ambient humidity level

-Fictive sky temperature

-Total solar radiation, incident beam radiation and angle of incidence for each orientation

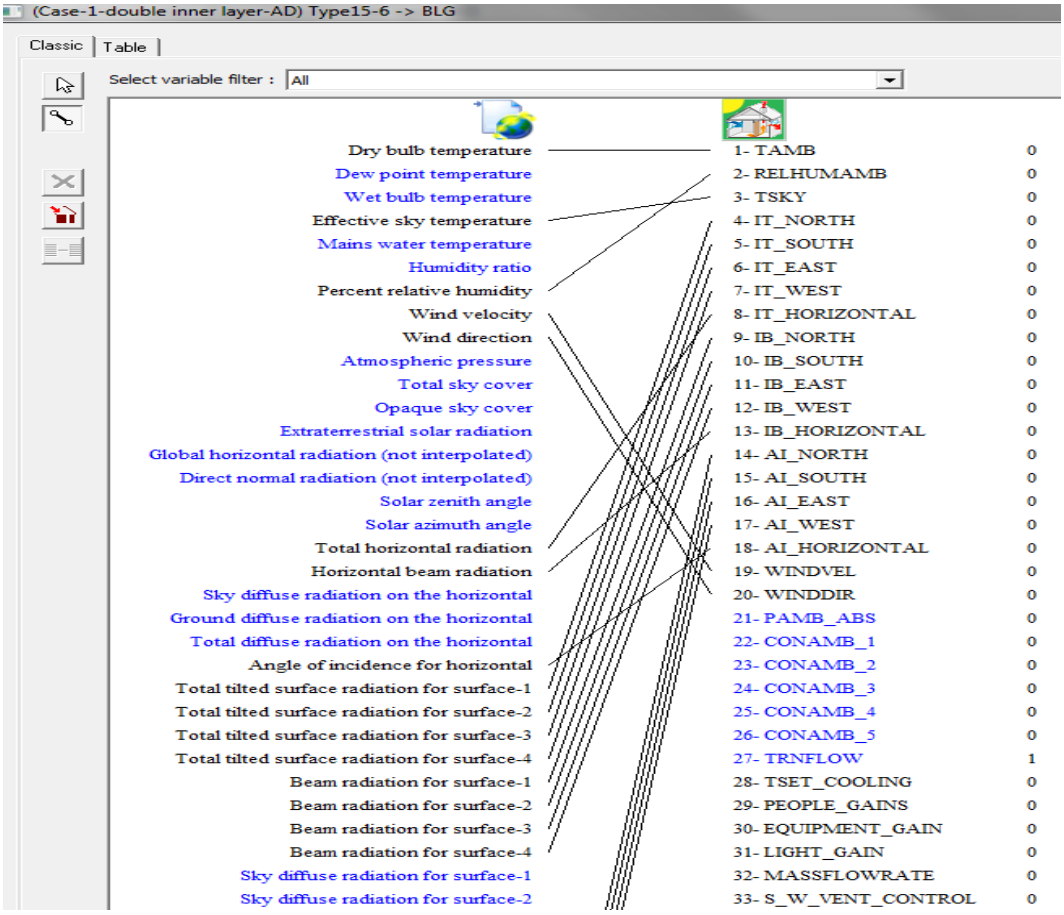

Fig.3.12 Connections between the outputs of Type 16 and links to Type 56

3.3 How the model works:

As clarified in (Fig.3.13) Type56 represents the building (2) is linked to Type 15(1) the weather station (1) to provides the time steps values of ambient and sky temperature, solar radiation based on the test reference year (TRY). The PV panels type 562(3) and as illustrated before, the façade cavity has been subdivided into two adjacent thermal zones, the common wall between the first and the second thermal zones is actually the considered PV module with its optical specifications. The input data includes the zone and ambient temperatures which were linked respectively to the air node temperatures of both cavities surrounding the PV panel, i.e. the two air nodes of thermal zones adjacent to the PV layer (Fig.3.14), the vertical solar radiation of the specific orientations where PV modules are installed west and east were linked from weather station Type 15. As for the front temperature which is related to radiation heat exchange between the front surface of the module and opposite surface, it was linked to the surface temperature of the front face of the outer glass layer and the back temperature was linked to the back surface temperature of the inner glass layer. The control schedule (4) provides the inside design temperature, internal loads, ventilation working hours. The fresh air handling unit (5) was constructed from cooling /heating coil, supply/exhaust fans and

energy recovery (ER) unit. Results of the dynamic simulation were printed including thermal demands; PV produced electrical energy and ventilation air thermal characteristics.

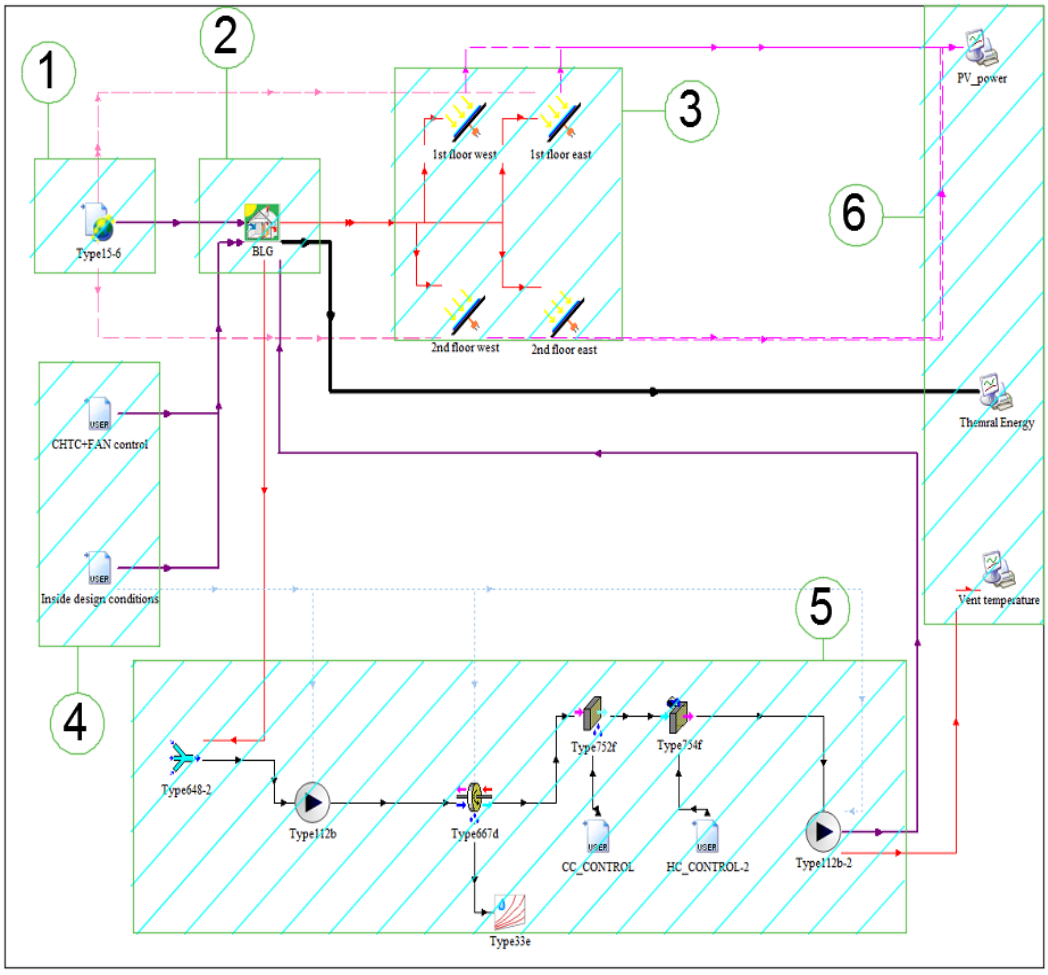

Fig.3.13 PV integrated in façade building simulation studio

Key Plan	
1	Weather station
2	Building
3	PV panels / each floor
4	(Ventilation + Thermal design control) dynamic schedule
5	Fresh Air Handling Unit equipped with Energy recovery ER unit
6	Results print

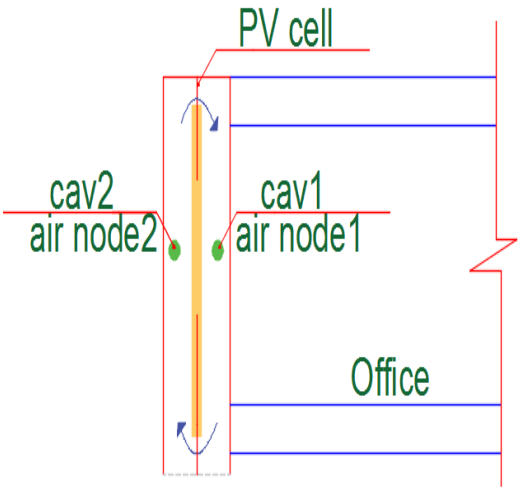

Fig.3.14 PV inside façade cavity Air nodes scheme

3.4 TRNSYS model validation

A validation of the integrated numerical model was carried out. Measured data refer to a mechanical ventilated double skin façade of an office room (Appendix –A) and the internal loads are specified in (Table 3.3).

Table 3.3 Internal loads

N. of Persons	Ventilation air flow rate (m3/h)	Sensible heat gains (W)
6	240	1680

The measured values of external temperature and solar radiation on the east vertical facade surface were used as input data to the TRNSYS model (Fig.3.15a) by using Type16c combined with Type9a. Type 33e and 69b were used to identify effective sky temperature based on the measured data. The measured exhaust air temperature values from the cavity were compared with TRNSYS results. As previously clarified air coupling technique which is implemented in Type 56 (multi zone building) (Fig.3.15b) were used to investigate the influence of connecting both air nodes of the office and adjacent faced cavity. A good agreement between the measured data and numerical results were attained, illustrated in (Fig.3.16).

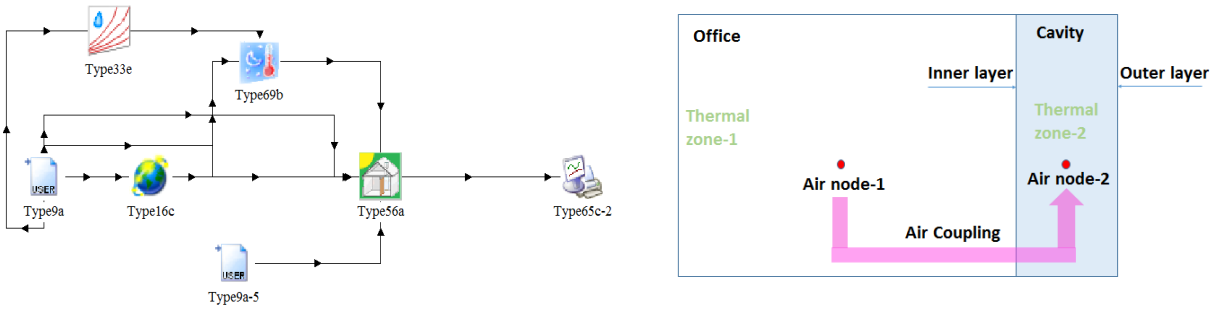

(a) (b)

Fig.3.15 (a) TRNSYS Simulation studio (b) Schematic of office integrated with façade

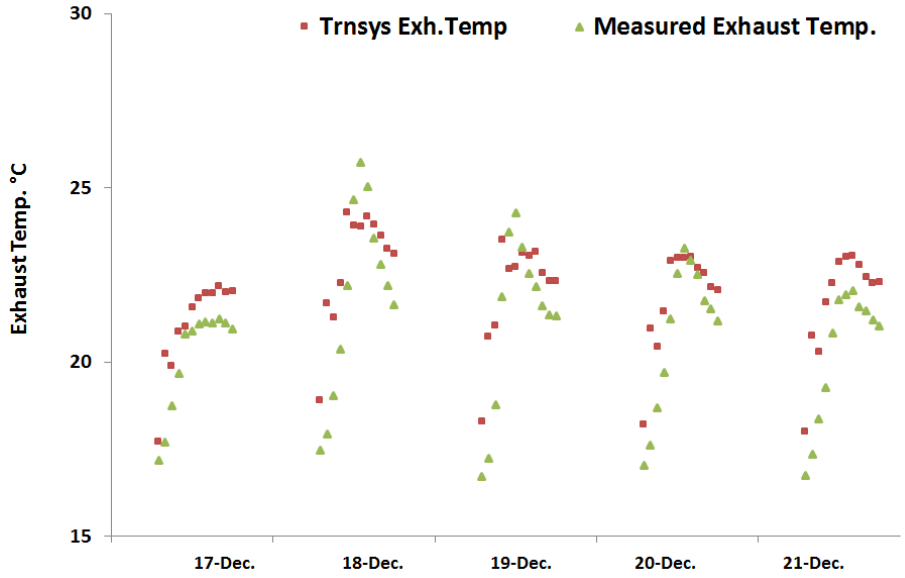

Fig.3.16 Façade Exhaust Temperature comparison within five working days from 17 till 21 December.

3.5 Parametric study through TRNSYS

TRNSYS model has been implemented in a parametric study to evaluate the energy efficiency of the system under different circumstances concluded in

- Facade cavity ventilation methodology
- Façade composition
- Three different weather conditions Abu Dhabi-UAE, Venice-Italy and Würzburg-Germany.

The considered office building consists of 5 floors, 4 typical and ground floors. The typical floors consist of two offices with area of each equal to 80 m^2 (Fig.3.17). Double skin façade starts from the 1^{st} typical floor till the 4^{th} floor. With an overall vertical area of $60m^2$ per floor for PV modules which are installed in the west and east sides of the building. In (Fig.3.18) the air balance scheme for

the fresh air supplying system is illustrated through all floors to evaluate the ventilation energy savings due to implementation of façade as an energy recovery unit. The summary of building specifications is shown in (Table 3.4).

Table 3.4 Office Building summary

Overall floor area (m^2)	330
Overall floor volume (m^3)	1115
Ventilation rate/floor (m^3/h)	2610
Occupants/floor	20

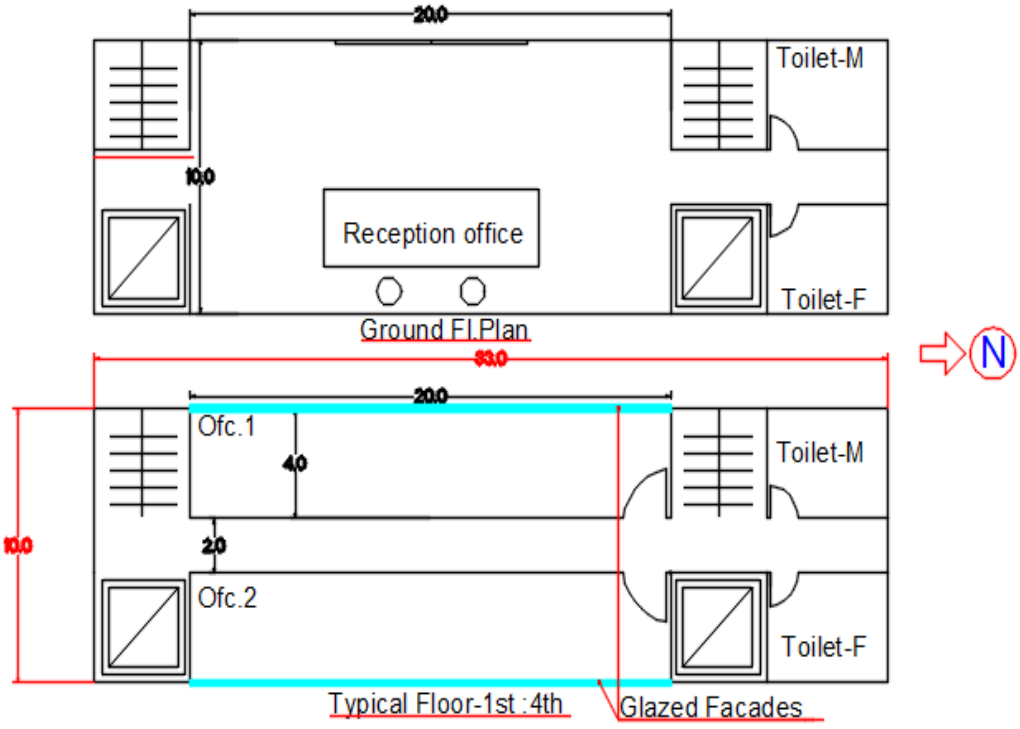

Fig.3.17 Office building plan

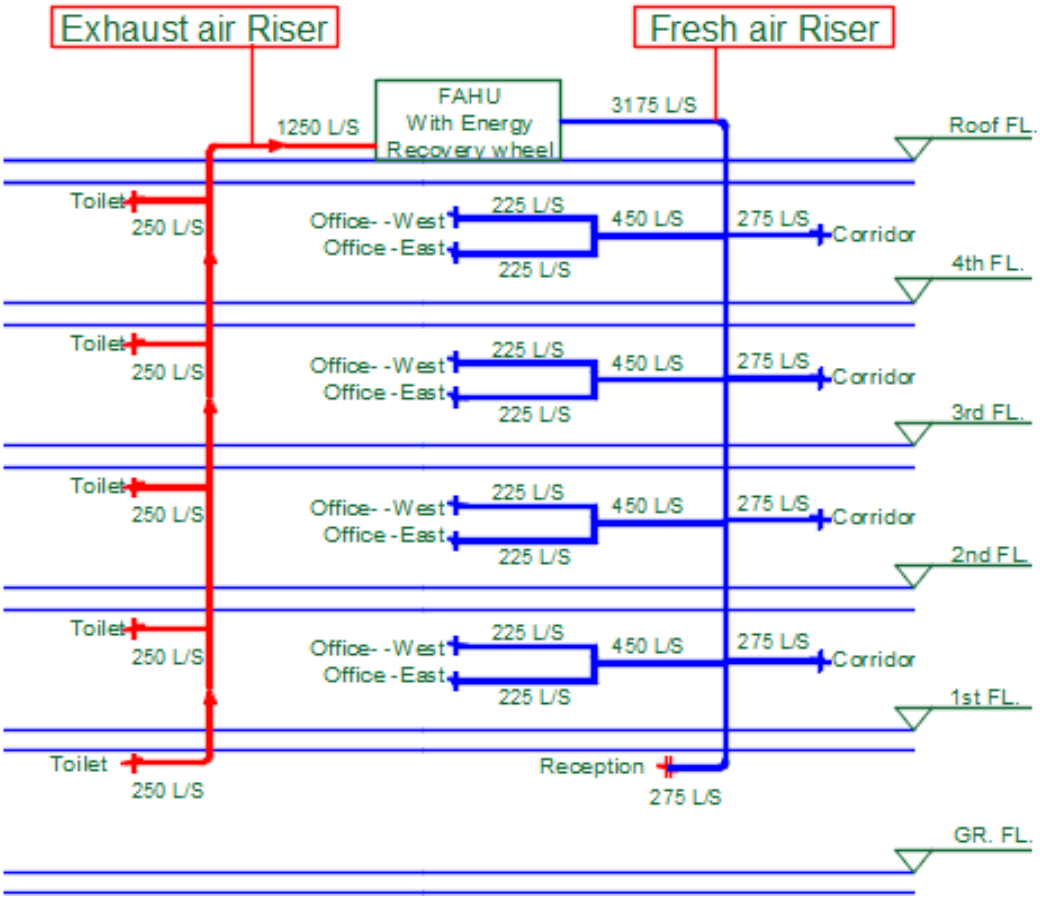

Fig.3.18 Air balance Scheme

3.5.1 Facade cavity ventilation methodologies

- **Case-1→ (Natural ventilation in winter, Forced ventilation in summer)**

In (Fig.3.19a) the yearly strategy of the ventilation is illustrated. In summer season the cavity is forced ventilated while in winter it is natural ventilated. During the forced ventilation in summer months (Fig.3.19b), the (Indoor-Outdoor) technique was applied. It means that a percentage of the cold air is extracted from adjacent office room to the façade cavity; this amount of air is limited by the fresh airflow rate supplied to the zone to attain the indoor air quality IAQ requirements [9].

(a)

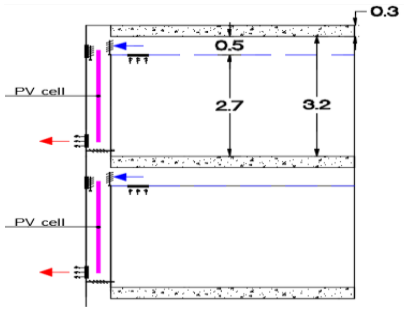

(b)

Fig.3.19 Case 1 ventilation strategy scheme

- **Case-2→ (Natural ventilation all year)**

In (Fig.3.20a & b) the scheme of natural ventilation applied strategy is shown. Air movement within the cavity is due to wind and buoyancy forces and it has been carried out via TRNFLOW as previously mentioned (Fig.3.21).

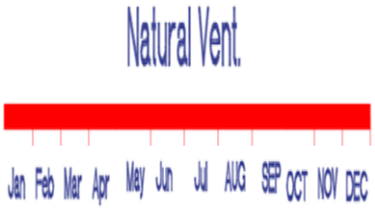

(a)

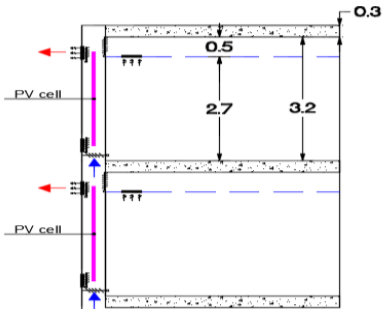

(b)

Fig.3.20 Case 2 ventilation strategy scheme

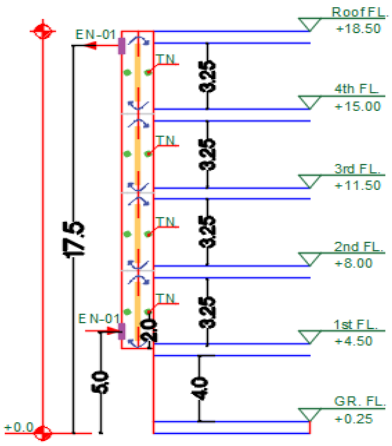

Fig.3.21 Thermal /external nodes schematic

3.5.2 Façade composition

The initial design of the facade is a significant factor that influences not only the energy consumption of a building but also the method and capacity of the HVAC system, going beyond any esthetic choice made by the architect [16] In the studies related to DSF that have been conducted thus far the window composition of the DSF included single glazing for the outer layer and double glazing (clear, low-e, solar control, etc.) for the inner layer. This is in accordance with the suggestion made by the BBRI [17]. Transparent double skin facades are predicted to increase cooling loads in office buildings in hot arid areas when compared to a single skin using reflective glazing.[18]. The addition of a double-skin always causes an increase in the cooling loads if the strategies of natural cooling are not applied [19]. Due to controverted energy performance patterns achieved by the different façade composition in the same weather conditions, two different compositions of facades have been compared to investigate the consequences on the thermal performance. Single inner layer SL (Fig.3.22a) and Double inner layer DL (Fig.3.22b). Glazing Optical data and technical specifications were obtained from Win [16] and illustrated in (Table 3.5).

Table 3.5 Optical specification of inner glass layer

	Composition	U W/m^2K	Transmissivity τ	Absorptivity α
SL	3mm clear glass	5.9	0.9	0.01
DL	3 mm clear glass 10mm Air 3 mm clear glass	2.8	0.7	0.1

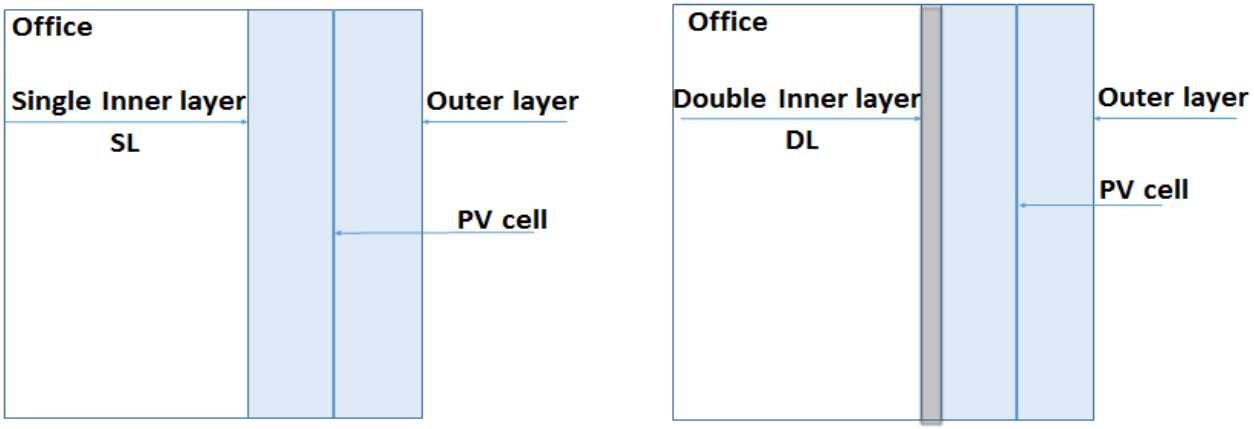

(a) **(b)**

Fig.3.22 Schematic of inner glass layers, (a)Single inner layer SL, (b) Double inner layer DL

3.5.3 Weather conditions

Weather conditions affect harshly the buildings thermal demands and govern the thermal design comfort standards. To obtain a more generalized perspective from the present study, three cities Abu-Dhabi city-UAE, Venice-Italy and Wurzburg –Germany were considered. Abu-Dhabi city is classified as hot arid desert precipitation [20]. On the other hand weather conditions and HVAC system designing standards are different than in the other two cities. Venice classified as fully humid hot summer and Wurzburg as warm summer [20]. (**Errore. L'origine riferimento non è stata trovata.**) summarizes thermal requirements for each city.

Table 3.6 Indoor /outdoor design conditions

City	Abu Dhabi	Venice / Wurzburg
Outdoor design conditions [15]	45.6°C	33°C / 31°C
Cooling inside air temp.(occupied)	23°C [21]	26°C [22]
Cooling inside air temp.(non occupied)	26°C [21]	32°C
Fresh air temp	18°C [21]	20°C [22]
Ventilation system	Working 24/7 [21]	Limited to working hours

3.6 Results

The results of the building simulation are shown within two main categories and have been clarified at the three cities of Abu Dhabi, Venice and Wurzburg respectively.

- Sensible cooling loads of the building.

- The electrical performance of PV modules system.

3.6.1 Sensible cooling loads of the building:

Thermal loads are identified as the summation of the building loads i.e.(internal loads + heat transfer losses) and treated ventilation air loads supplied to keep the required IAQ. Since it is more realistic and accurate to correlate the reflections induced by integration of PV cell, ventilating the cavity and the composition of the façade at the building envelope with the building energy performance the energy evaluation in this part has only included building loads without considering the ventilation energetic savings. In which will be explained in Section (3.7.1).

a-Abu Dhabi city case study

Daily cooling load performance is illustrated in (Fig.3.23a) for different considered cases. As shown combining double inner glass layer with ventilation technique of case-1 attaining the lowest daily cooling energy consumption 669kWh/day, on the other hand using case-1 with single inner layer increasing the energy consumption to 826kWh/day. However changing the ventilation technique is affecting the daily energy consumption, in DL-case-2 i.e. natural ventilation of the cavity, daily cooling energy reached 675kWh/day while in SL case-2, the value of day cooling load reached 833 kWh/day. As clarified cooling energy has slightly improved in DL case-1 compared to DL case-2 which emphasis that increasing thermal resistance of air conditioned glazed room has a larger effect on the cooling loads more than the used ventilation typology. Nevertheless to investigate thermal comfort the operative and inner glass temperature have been inspected. During a complete week starting form Monday till Saturday. Fig.3.23b is illustrating the difference between inner glass temperature DL case-1 and SL case-1, a range from 0.5 °C at the start working hours then reaches the maximum of 4.5 °C at the day peak hour of 16hr. The difference in the operative temperature between DL and SL is starting from 0.5 °C to 1.25°C at the peak hour. Within the weekend days Saturday and Sunday it is clear that operative temperature and accordingly the inner glass temperature are increased due to increment of design set temperature value.

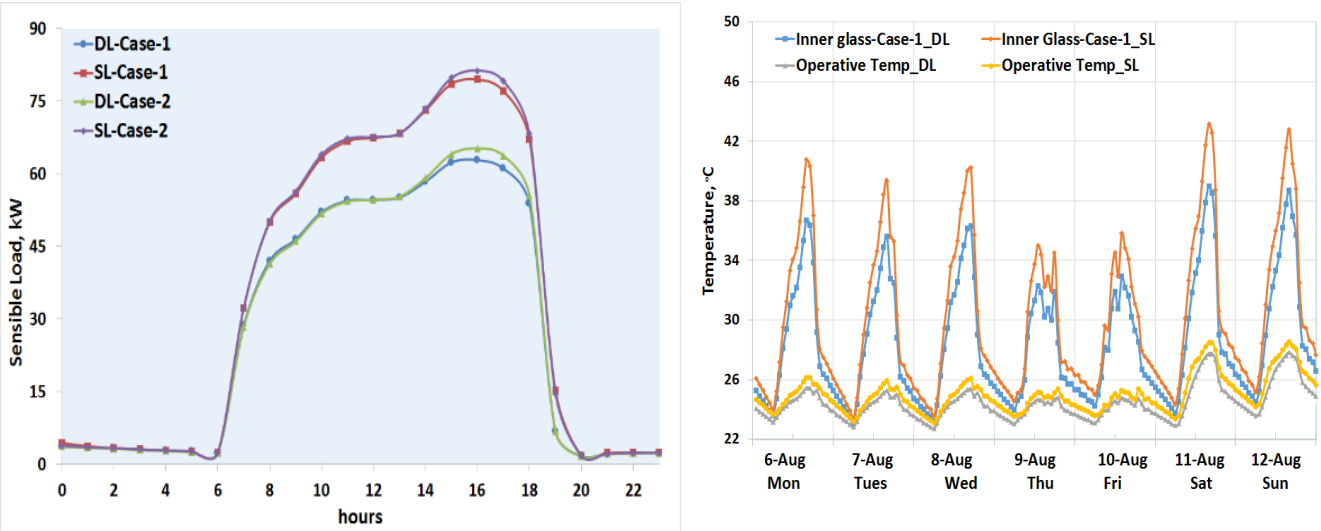

(a) **(b)**

Fig.3.23 Abu Dhabi city results (a) Building thermal energy, (b) Operative and inner glass temperature

b- Venice city case study

According to lower average external temperature during summer months in Venice city compared to the latter one, the improvements in energy performance has been realized not only by changing the composition of the facades but also by the implementation of the two ventilation typologies. In (Fig.3.24a) the daily cooling energy consumption reached 452kWh/day in DL case-1 increased to 538 kWh/day in SL case-1. On the other hand, energy performance in DL case-2 reached 503kWh/day while increased to 580kWh/day. Hence, it could be concluded that influence of facades ventilation system typology increases when the external temperature is lower. The consequences on the operative temperature and inner glass layer between implementing DL or SL in case2 is shown in (Fig.3.24b). The maximum difference is 3.5°C and it happens within weekend. While on other working day difference ranges between 0.5 and 2°C.

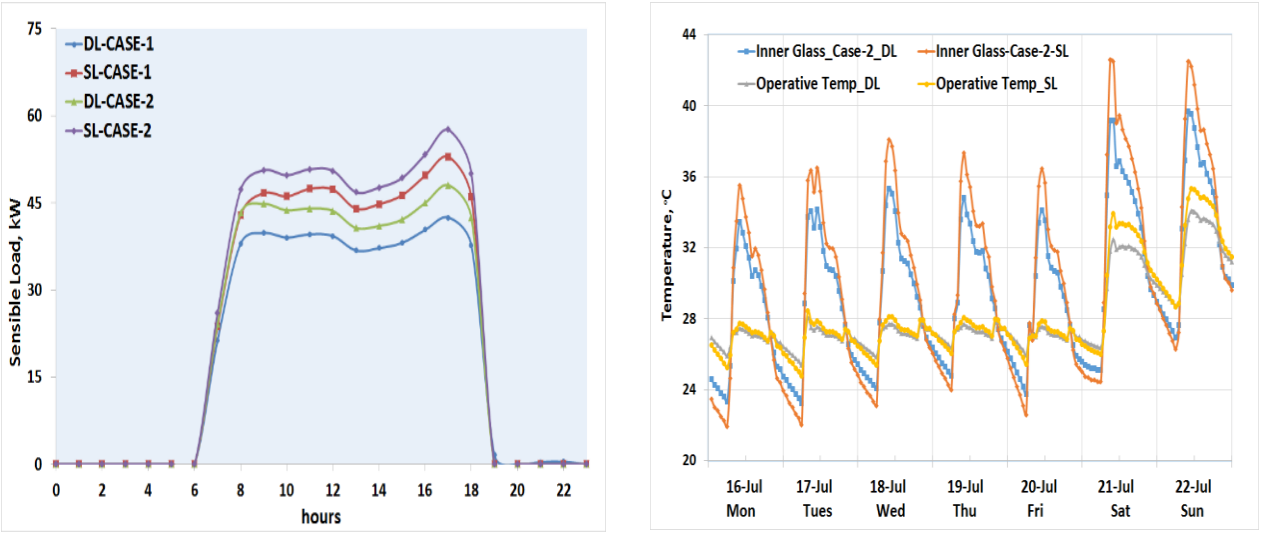

(a) **(b)**

Fig.3.24 Venice city results (a) Building thermal energy, (b) Operative and inner glass temperature

c- Wurzburg city case study

Daily cooling energy profiles in Wurzburg are illustrated in (Fig.3.25a) . DL case-1 is 310kWh/day increased in SL case-1 to 394 kWh/day. While in DL case-2 it reached 365 kWh/day and increased to 445 kWh/day in SL case-2. In (Fig.3.25b) the weekly distribution of inner glass layer between DL and SL in case-1 is showing the difference ranges between 1°C and 2°C during weekends and decreases to be almost equal during working days. For the operating temperature the difference is negligible .It is important to mention that the difference between operating temperature and inner glass temperature did not exceed 6°C in the peak hour 17hr in 15-Jun, which in general reflects the high expected thermal comfort with in the office. According to low incident ambient temperature in 16 and 17 June, the difference between case1 and case2 in the operative and inner glass layer temperatures were not high comparing to latter cases.

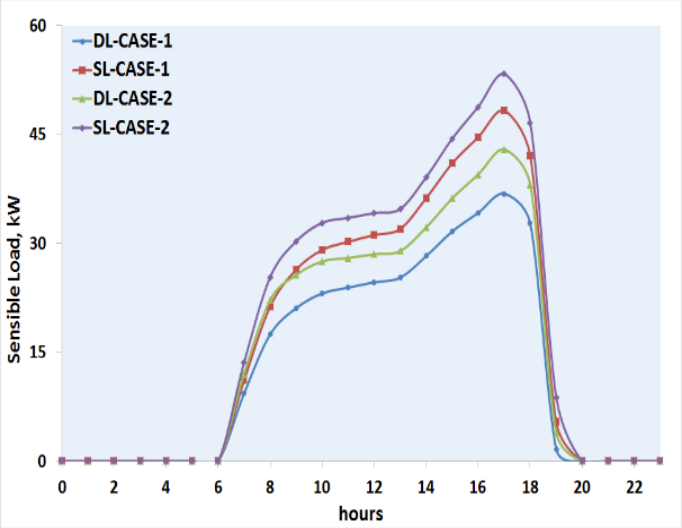

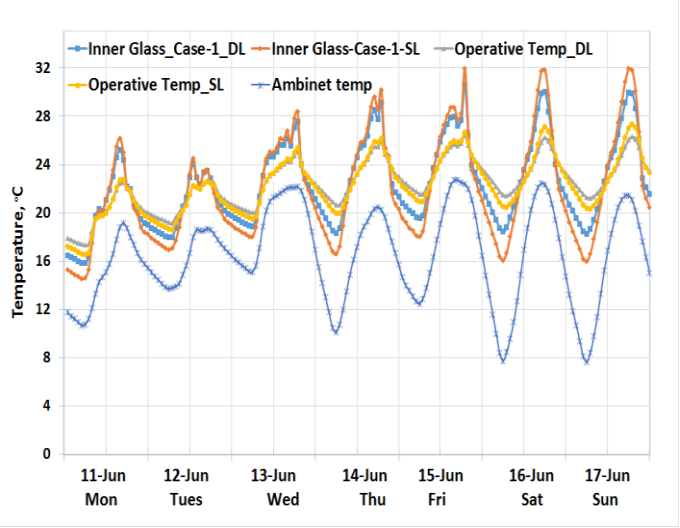

(a) **(b)**

Fig.3.25 Wurzburg city results (a) Building thermal energy, (b) Operative and inner glass temperature

3.6.2 Integrated PV system

In the simulated results, case-1 of forced ventilation typology is always superior case 2 at the two European cities with different electrical production. However in Abu Dhabi city this pattern was not precisely realized, in fact SL has preceded DL. Due to high coincident external ambient temperature in Abu Dhabi city the thermal resistance value of the inner layer of air conditioned room is not high in SL, accordingly it helps in decreasing surface temperature of adjacent PV layer installed inside the cavity due to the mutual radiation heat transfer between PV surface and inner glass layer. On the contrary in Venice and Wurzburg, the outer temperature could be lesser than inside glass layer temperature which is related to set point temperature equals to 26°C, therefore the increasing of the inner glass thermal resistance "DL" is a privilege to obtain higher thermal performance.

In Abu Dhabi as shown in (Fig.3.26a) the maximum monthly production in summer months reached 225 kWh in SL case-1, the minimum is 161 kWh with DL case-2. In Venice city (Fig.3.26b) the maximum summer PV electrical production occurred with DL case-1 with 3016kWh the minimum was SL case-2 with 393 kWh. In (Fig.3.26c) Wurzburg the maximum electrical production in DL case-1 reached 6797kWh while the minimum was in SL case-2 recorded as 1287kWh. It is important to highlight that hot humid climates and cloudy sky of Abu Dhabi city are reducing the produced energy from the PV system in comparing to European cities.

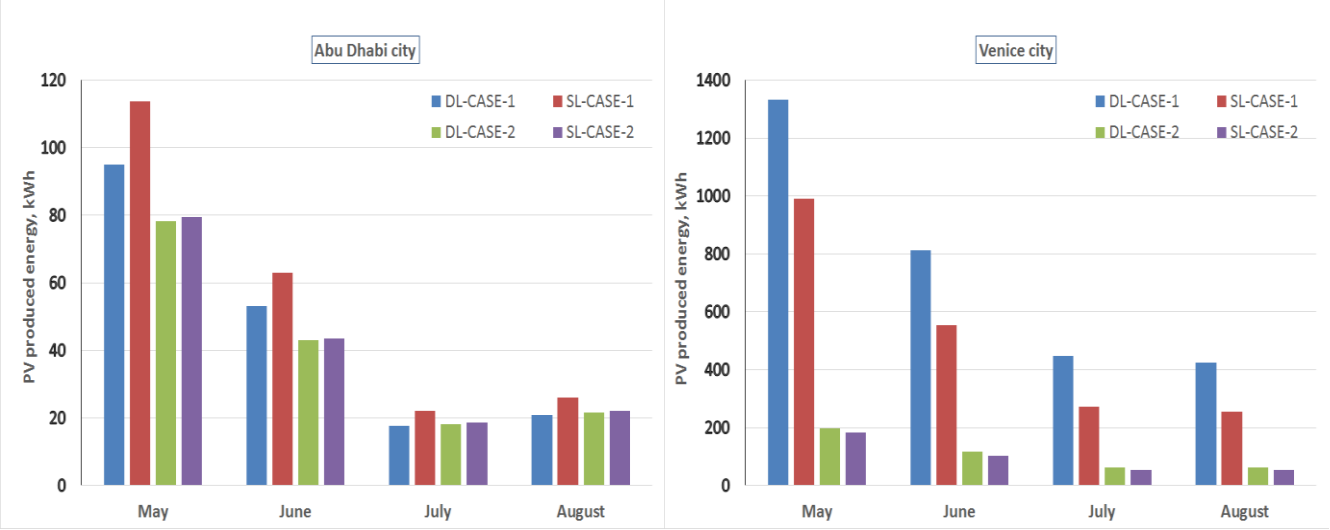

(a) **(b)**

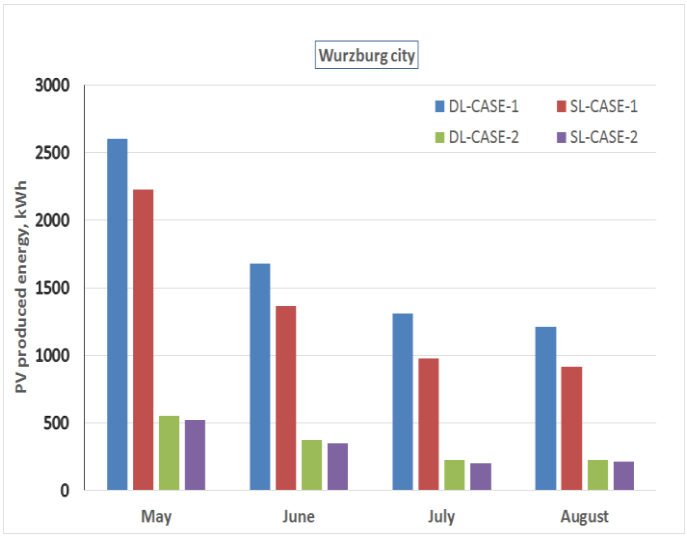

(c)

Fig.3.26 PV summer electrical production (a) Abu Dhabi, (b) Venice, (c) Wurzburg

Summary of energy assessment results

- **Sensible building cooling loads**

Different strategies which have been applied in the present study affected on the energy consumption (Fig.3.27a, b) and peak power. (Fig.3.27c, d). In Abu Dhabi city the decrement in peak power from case1 to case2 was -4% while in SL the decrement reached -2.3%. However the energy consumption reduced by -1.5% in case-1 versus case-2 in DL, and -1.9% lesser in SL. The improving percentages of energy and peak power between case-1 and case-2 are continued at Venice city, Peak power reduced by -11.6%, and building thermal energy -15% in DL. However in SL peak power difference

reached -8% while in energy consumption savings reached -11.5%. According to the colder ambient temperature in Wurzburg city comparing to the latter city, all improving percentages have been increased. Peak power decrement within DL reached -14%, while the thermal energy decreased by -22%. On the other hand in SL the peak power reduction reached -9.5% while -17% was attained in the energy consumption savings.

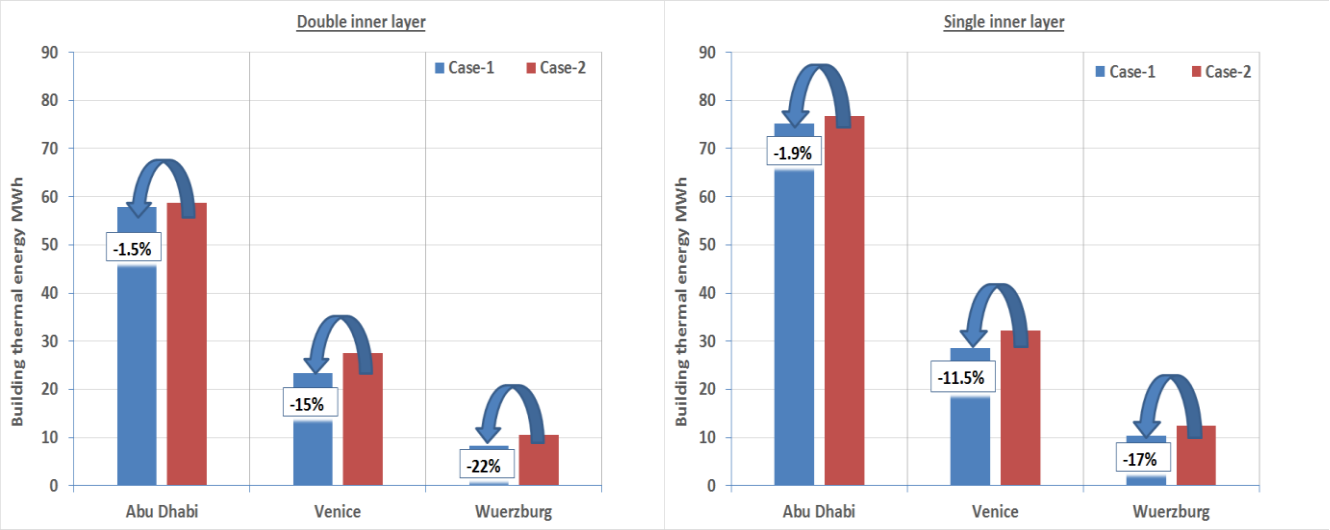

(a)Building thermal energy-DL **(b)Building thermal energy-SL**

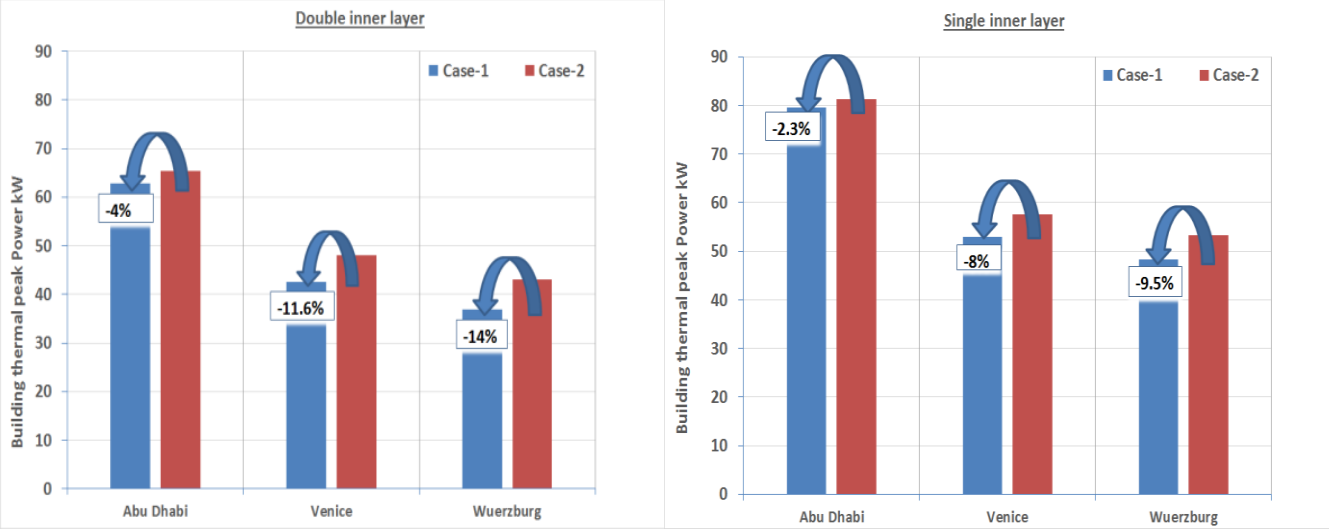

(c)Building Peak power-DL **(d)Building Peak power-SL**

Fig.3.27 Building thermal energy and peak power assessment

- **PV yearly energy production**

The summary yearly results of PV integrated system at the three cities are show in (Fig.3.28a) and (Fig.3.28b) .Abu Dhabi annual energy production increased by 2.5% in case of DL and 6% in SL. On the contrary, in Venice city the improvement in PV electrical production within DL reached 53%

while in SL was 34%. The same pattern of performance happened in Wurzburg city in DL the improvements reached 57% while decreased in SL to 50%.

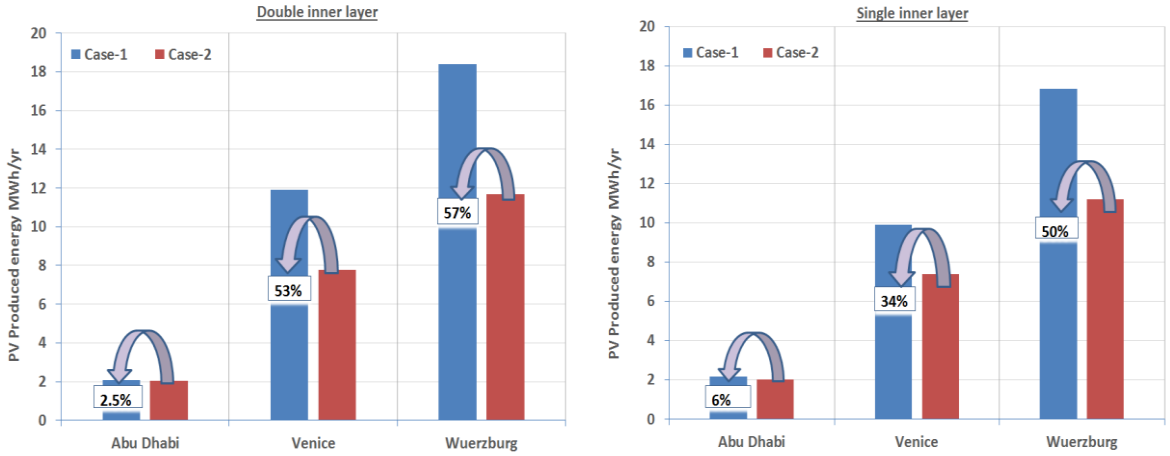

(a) PV Yearly electrical produced energy -DL

(b) PV Yearly electrical produced energy -SL

Fig.3.28 PV electrical produced energy assessment

3.7 Traditional integration of PV systems in buildings as external layer vs. innovative installation

One of the beneficial aspects of integrating the PV modules inside the cavity is to enlarge PV life time, decrease the risk of electrical shocks occurs while rain fall, be employed as a heat sink which will enforce the ventilation energy recovery reduce thermal losses during winter. On the other hand to conclude an objective point of view about the PVIB, it was essential also to evaluate the performance of the convenient installation of PV module as external layer (Fig.3.29). The same numerical methodology in TRNSYS and previously assumed office building Figure (Fig.3.17) were implemented to evaluate the required ventilation energy and PVIB overall thermal and electrical performance.

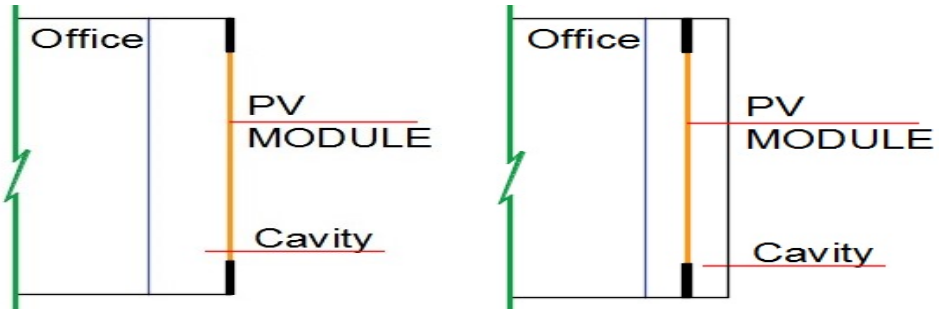

(a) **(b)**

Fig.3.29 (a) PV module on external layer –PVEXT, (b) PV module inside the cavity –PVIN

3.7.1 Integrated thermal loads evaluation

Overall approach

The purpose of a ventilation system is to provide acceptable microclimate in the indoor space. Microclimate refers to thermal environment as well as air quality. Ventilation flow rates which assure the acceptable indoor air quality have to be obtained. These flow rates are determined by many standards (ASHRAE 62, European stds, Directive 2008/50/EC). For each indoor application, there is a minimum value has to be supplied in a specific pretreated thermal conditions i.e. temperature and relative humidity. Approximately 30% of the energy delivered to buildings is dissipated in the departing ventilation and exfiltration air streams [23]. The exhaust air from the façade cavity integrated with PV system is used in a heat exchange process, since the PV modules works as heat sink due to high solar radiation absorption capability. The following section is clarifying the expected savings due to this innovative integration through different climatic conditions.

Ventilation loads evaluation

The required ventilation load without energy recovery depending on sensible heating coil Q_{vent} (Fig.3.30a) and with the energy recovery unit $Q_{vent/ER}$ (Fig.3.30b) are estimated from Equations (3.20) and (3.21). Whilst the effectives of the energy recovery wheel ε is evaluated in Equation (3.22) where. $\dot{m}_s$ is the supplied fresh air flow rate required to attain the indoor air quality for the whole building and it equals 3175L/s, $\dot{m}_{exh}$ and T_{exh} are the exhausted mass flow rate equals 1250L/s and air temperature exhausted from the façade respectively see (Fig.3.18). The effectiveness was assumed to be 0.7 and T_s is the supply air temperature equals 20˚C. Hence by compensate in Equation (3.22), T_1 is defined for each time step.

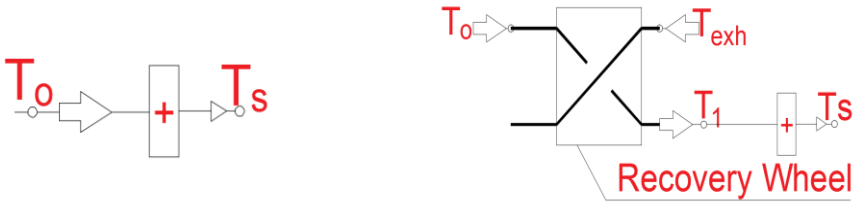

(a) (b)

Fig.3.30 (a) heating coil scheme,(b)Ventilation energy recovery scheme

$$Q_{vent} = \dot{m}_s C_P (T_s - T_o) \quad \textbf{(3.20)}$$

In case of implementing the energy recovery unit

$$Q_{vent/ER} = \dot{m}_s \, C_P \, (T_s - T_1) \quad \textbf{(3.21)}$$

$$\varepsilon = \frac{\dot{m}_{exh}}{\dot{m}_s} \, \frac{T_1 - T_o}{T_{exh} - T_o} \quad \textbf{(3.22)}$$

For each city the ventilation loads were evaluated through three possibilities, in case that PV is inside the façade cavity PVIN, PV is the external layer PVEXT and without using energy recovery unit. As shown in (Fig.3.31 a, b and c) PVIN case is the lowest kWh/m^2 of ventilation energy consumption during all heating season followed by PVEXT. This Superiority pattern varied in savings percentages depending on the climatic conditions, In Venice city PVIN savings comparing to PVEXT ranged from 15 to 51% and compared to the convenient method ranged from 19 to 65 %. Whilst in Helsinki city and as also the PVIN is the reference case, PVEXT ventilation energy requirements exceeded by 6 to 25% and in comparing to the convenient method ranged from 10 to 35% savings. Finally, in Wurzburg city and PVEXT performance is higher with 7 to 35% and from 10 to 43% saving in case of using heating system without any recovery technique.

i.e. Savings were determined by considering $\left(\frac{PVEXT-PVIN}{PVEXT}\right)$%.

Overall thermal loads evaluation

The overall thermal energy for the building is the hourly summation of internal loads, solar gains, convection losses and ventilation loads have been also clarified. In (Fig.3.32a) Venice city, The yearly overall thermal energy loads per m^2 between installing PV as an external layer (PVEXT case) is higher than the other case of PV inside cavity layer (PVIN case) within the heating months of January until April and, then, within the cooling season thermal energy loads decreased comparing to the latter case. On the other hand, the same trend was followed in Helsinki and Wurzburg cities. Along the heating season integrating of PV modules inside the cavity is lower than PV installation as external layer. Taking into consideration that in Helsinki and due to its cold climate the summer season started in June. Whilst in cooling season PVEXT is better (Fig.3.32b and c).

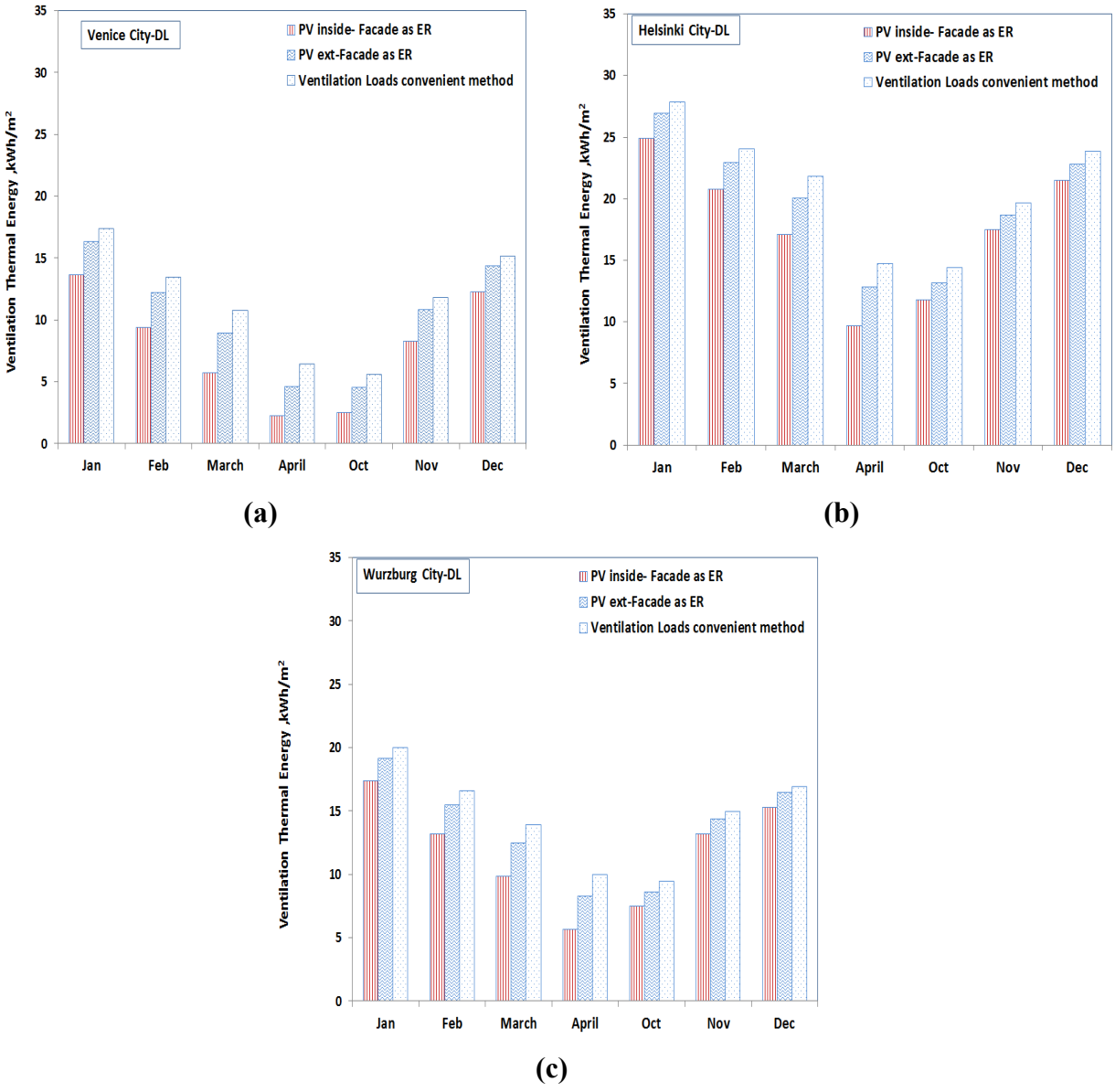

Fig.3.31 Ventilation thermal energy, (a) Venice, (b) Helsinki, (c)Wurzburg

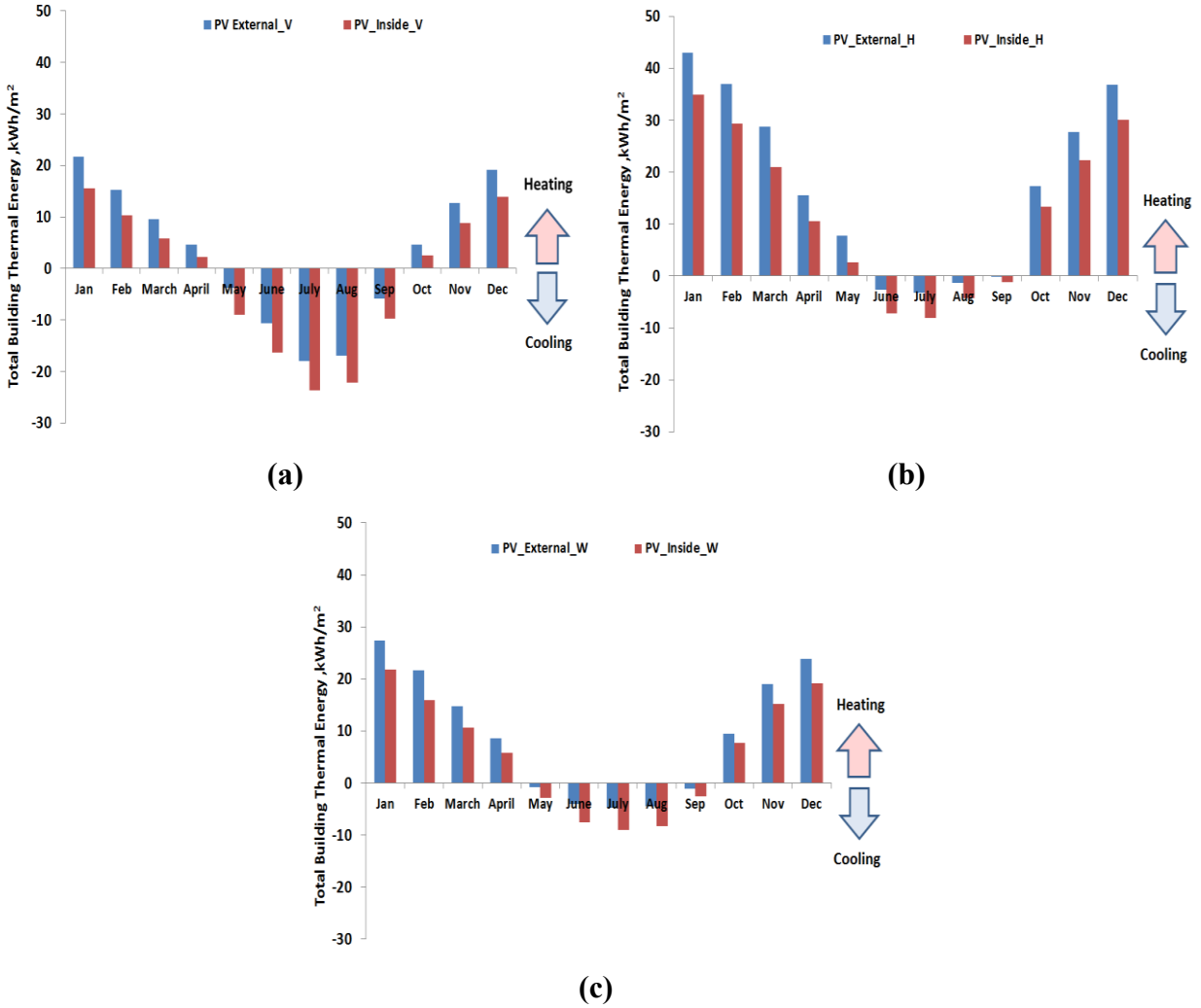

Fig.3.32 Total building energy kWh/m^2 ,(a) Venice,(b) Helsinki, (c)Wurzburg

In Table 3.7 the percentage difference between the two studied cases as the PVIN is shown with reference to the three cities considered. In Venice the PVIN savings are confined in winter season by reaching the maximum of 51% for the PVEXT, whilst in summer the PVEXT is lower with 58% during May. However in Helsinki and Wurzburg cities PVEXT case has always lower energy consumption in summer months with high percentages per m^2, reaches 95%, and in winter season the savings in PVIN case ranged between 19 to 34%.

Table 3.7 Thermal loads performance differences%

City/Months	Jan	Feb	Mar	Apr	May	Jun	Jul	Aug	Sep	Oct	Nov	Dec
Venice	28%	33%	39%	51%	-58%	-34%	-24%	-24%	-40%	45%	31%	28%
Helsinki	19%	21%	27%	32%	67%	-63%	-60%	-68%	-81%	23%	19%	18%
Wurzburg	20%	27%	28%	34%	95%	-91%	-89%	-90%	-95%	19%	21%	20%

3.7.2 PV electrical production

As shown in (Fig.3.33a, b and c) the overall trend is higher for PVEXT comparing to PVIN case with percentages ranging between 7% to 17% as a maximum percentage in Venice. In Helsinki the percentages ranges between 6% and 14% and finally in Wurzburg city PVEXT performance was higher by 7 to 14%.

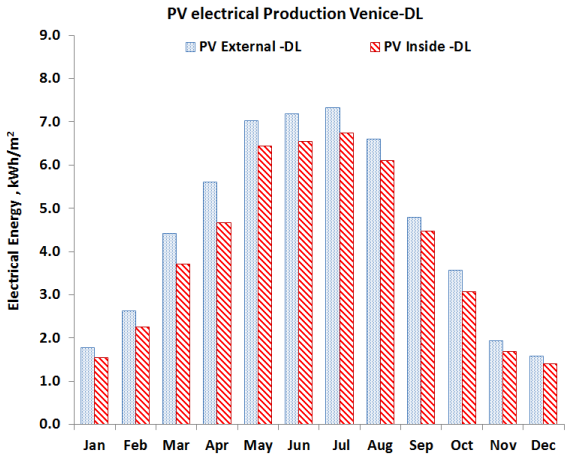

(a)Venice city

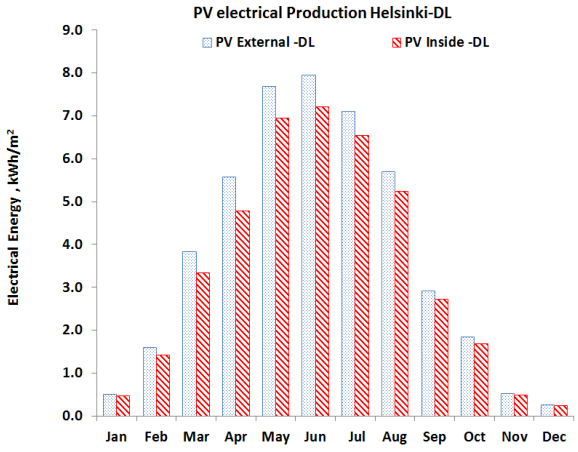

(b)Helsinki city

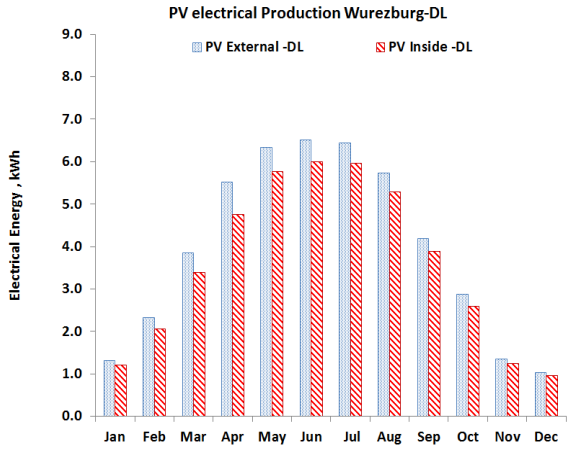

(c)Wurzburg city

Fig.3.33 PV electrical production, kWh/m^2 ,(a) Venice,(b) Helsinki, (c) Wurzburg

3.8 Conclusions

The chapter has discussed the how of modelling multiple skin façade by TRNSYS and integrating of the PV system in vertical parts of building envelopes. A detailed comparative study including several parameters as climatic conditions, ventilation methodologies and PV module system locations have

been carried out to conclude that the integration of PV modules inside a façade cavity increases the thermal performance efficiency within the heating months in warm temperature climates. However it is reducing the PV system electrical production with a range of 7 to 14% during cooling season and it is due to that radiation heat exchange between PV module and the sky surface is better than radiation heat exchange with glazed surface inside the cavity. Nevertheless, the reduction in PV electrical production could be neglected comparing to the savings in building thermal heating energy. The innovative integration of PV modules inside the cavity would be considered a good ecological solution in cold climates, not only acting as an active insulating layer but also producing free energy. On the other hand, in hot and humid climates, it is more complicated in summer season and some other technologies could solve these obstructions such as applying PCM, which is dealt with in the following chapter 4.

3. Nomenclature-Chapter 3

A	Cross section area (m^2)
a	Solar absorption coefficient (-)
V_{oc}	Open circuit voltage (V)
I_{sc}	Short circuit current (A)
a-si	Amorphous silicon
T_{exh}	Exhaust air temperature from the façade cavity (˚C)
h_c	Convection heat transfer coefficient (W/(m^2 K))
R_e	Reynolds number (-)
R_a	Rayleigh number (-)
P_r	Prandtl number (-)
C_d	Coefficient of discharge (-)
D_h	Hydraulic diameter (m)
DL	Double Layer
H	Height of the plate (m)
h_o	Reference height at the building site (m)
h_m	Pylon height at meteo station (m)
h_b	Height of boundary layer, 60m for α_o<0.34
IL	Internal Loads (W)
K_a	Air Thermal conductivity (W/(m K))
L	Length of the plate (m)
ΔP	Pressure induced by wind effect (Pa)
P	Cross sectional perimeter (m)
SL	Single Layer
U_o	Wind Velocity at the building site (m/s)
U_m	Wind velocity at the meteo station at pylon height (m/s)
ε	Specific loss factor of air inside duct (-)
λ	Friction factor (-)
ρ	Air density (kg/m^3)
α_o	Wind velocity profile exponent at the building site (-)
α_m	Wind velocity profile exponent at the meteo station (-)
τ	Transmission coefficient (-)

3. References –Chapter 3

1. Bjørn Petter Jelle , Christer Breivik b, State-of-the-art Building Integrated Photovoltaics Volume 20, 2012, Pages 68-77,
2. D. Infielda, ,L. Meia, U. Eickerb, Thermal performance estimation for ventilated PV facades, Solar Energy 76 (2004) 93–98.
3. T.Fung, H. Yang, Study on thermal performance of semi-transparent building integrated photovoltaic glazing, Energy and Buildings 40 (2008) 341–350.
4. J-H Song, Y-S An, S-G Kim, S-J Lee, J-H Yoon, Y-K Choung, Power output analysis of transparent thin-film module in building integrated photovoltaic system(BIPV), Energy and Buildings 40 (2008) 2067–2075
5. KE Park, GH Kang, HI Kim, GJ Yu, JT Kim, Analysis of thermal and electrical performance of semi-transparent photovoltaic (PV) module. Energy 35 (2010) 2681–2687.
6. L. Mei, D. Infield , U.Eicker, V. Fux , Thermal modelling of a building with an integrated ventilated PV façade, Energy and Buildings 35 (2003) 605–617.
7. B. Marion, A method for modeling the current voltage curve of a PV module for outdoor conditions. Progress in photovoltaics: research and applications, National Renewable Energy Laboratory 10 (2002) 205-210.
8. E .Skoplaki, A.G Boudouvis, J A Palyvos, A simple correlation for the operating temperature of photovoltaic modules of arbitrary mounting , Solar Energy Materials & Solar Cells 92 (2008) 1393-1402.
9. H.Elarga, M.De Carli, A.Zarrella, C.Alavarez , M .Abo Elazm, Assessment of Active Double Skin Façade Integrated With PV Cell.(2015) ASHRAE Winter conference- Chicago USA.
10. S. Klein, W. Beckman, J. Mitchell, J. Duffie, N. Duffie, T. Freeman et al., TRNSYS 16 - A transient system simulation program, User manual, University of Wisconsin, Madison, US, 2004.
11. R Høseggen, B.Wachenfeldt, S.Hanssen, Building simulation as an assisting tool in decision making Case study: With or without a double-skin facade?, Energy and Buildings 40 (2008) 821–827
12. Department of Energy-DOE, Window v6.3.9.0, Energy efficiency and renewable energy office of building technology, USA, 2010.
13. D. Saelens, B. Blocken, S. Roels, H. Hens, optimization of the energy performance of multiple-skin facades 9th Ibpsa international conference Montréal, Canada august 15-18, 2005.

14. R.Kemperman, 2012. A naturally ventilated office building through solar chimneys and 'venturi' exhausts MSc.thesis Publication Faculty of Architecture, Urbanism & Building sciences Delft University of technology Netherland.
15. American Society of Heating, Refrigerating and Air-Conditioning Engineers. ASHRAE handbook: Fundamentals (2009). Atlanta, GA, USA.
16. J.Joe,W.Choi,Y.Kwak, J.Ho Huh, Optimal design of a multi-story double skin façade, Energy and Buildings 76 (2014) 143–150.
17. Belgian Building Research Institute (BRRI), Source book for a better under-standing of conceptual and operational aspects of active facade, Department of Building Physics, Indoor Climate and Building Services, version 1, 2002.
18. N. Hamza, Double versus single skin facades in hot arid areas, Energy and Buildings 40 (2008) 240–248.
19. E Gratia, A De Herde, The most efficient position of shading devices in a double-skin facades Energy and Buildings 39 (2007) 364–373.
20. M. Kottek, J. Grieser, C. Beck, B. Rudolf, F. Rubel, World Map of the Köppen-Geiger climate classification updated, Meteorol. Z 15 (2006) 259-263.
21. Abu Dhabi urban planning council, www.estidama.org
22. ASHRAE standard 55-2004.thermal environment conditions for human occupancy, ASHRAE.
23. AIVC Technical Note 49, 1998, 43pp.
24. John Seem , Modelling of heat transfer in buildings, PhD thesis University of Wisconsin, Madison, USA, 1987.

Chapter-4
PV/PCM Numerical Integration

4.1 Introduction

In this chapter, the performance of a system that integrates a photovoltaic (PV) layer and a phase changing material (PCM) layer in a double skin façade (DSF) is investigated. A physical–mathematical model is developed to simulate the dynamic thermal behavior of the system, and numerical simulations are carried out for different climates (Venice, Helsinki and Abu Dhabi) in order to evaluate the performance of the proposed solution. The numerical model combines different validated codes for the simulation of optical, thermal, and electrical behavior of PCM, PV and DSF. The model is then coupled with the indoor air heat balance Equation to evaluate the impact of the proposed façade system on the heating and cooling energy demand. The adoption of a PCM layer in the DSF cavity, in combination with a semi-transparent PV layer, leads to a reduction in the monthly cooling energy demand in the 20% to 30% range. This result is particularly relevant for hot climates – where cooling loads are seen throughout the year. The improvement in terms of heating load in more cold-dominated locations is limited. The smoothing of the PV module temperature leads to an increase in the electrical energy converted by the PV, with peak values of improvement in the range of 5% to 8% when the DSF is equipped with the PCM–PV configuration. Ventilation strategies of the façade cavity, coupled with the correct selection of PCM (and of its transition-phase temperature range), are the key aspects to ensure effective management of the proposed technology.

Objectives

1- Development of two numerical methods describing thermal performance of PCM
2- Analysis of shortwave radiation through PCM as a function of the substance temperature.
3- Integration of PV/PCM systems in buildings, and investigates the thermal and electrical improvements due to implementation of the PCM layer.

4.2 Background

Thermal energy storage (TES) systems could be used to reduce a building's dependency on fossil fuels and to contribute to a more efficient environmental energy use. The main advantage of using TES is that it can help with matching supply and demand when they do not coincide [1]. Thermal energy storage could be accomplished using either sensible or latent TES: sensible heat storage has been used for centuries by builders to store/release thermal energy, but a much larger volume of material is required to store the same amount of energy in comparison to latent heat storage

(LHTES). An example of this is the use of a phase change material (PCM) as a storage medium [2]. A PCM solidifies when cooling resources are available and melts through thermal energy absorption, thus reducing cooling loads [3]. Within the building sector, the incorporation of PCMs to different construction elements or HVAC components can increase the thermal capacity of the building and thus contribute to reducing indoor temperature fluctuation, reducing heating and cooling loads and lowering energy use [4]. To enhance the energy storage capacity of a transparent building envelope component, Goia et al. [5,6] have compared a conventional double glass unit (DGU) with a PCM-integrated DGU, and it was found that the higher the outdoor solar radiation, the greater the benefits on thermal comfort and energy performance that are achieved through the DGU_PCM due to shading and energy buffering effects provided by the paraffin layer. Weinlader et al. [7] have investigated the thermal and optical performance of façade panels using a PCM. It was concluded that such integration improves thermal comfort, reduces heat gains through the course of the day while overnight, non-desired heat gains can be drawn off. Silva et al. [8] have analysed the dynamic thermal behaviour of a latent heat thermal energy store within PCMs both numerically and experimentally. The study highlighted the importance of each heat transfer mechanism and concluded that the initial charge period, and almost all discharge process are dominated by heat conduction. Melting time is dominated by the imposed heat flux and PCM thickness, while the solidification time depends only on the number of thermal units, i.e. the convective heat transfer rate and PCM thickness. Kuznik et al. [9] have highlighted the importance of the hysteresis phenomena and the need to take them into account in order to predict the thermal behaviour of the PCM composite.

The adoption of PCM in buildings is an effective way to enhance the integration of technologies for renewable energy conversion through a better exploitation of solar energy, both through passive components (e.g. PCM in glazing systems and in walls) and active components (e.g. PCM in HVAC systems or advanced building envelope systems). The effects of the semi-transparent property, the PCM thickness, and the zenith angle on thermal performance of a PCM-filled double-glazing roof were investigated numerically by Liu et al. [10]. It was concluded that the effect of thickness of double-glazing roof on its thermal performance is large, with an increase in thickness resulting in an increase in temperature time lag.

4.3 PCM thermal and optical numerical analysis

4.3.1 Equivalent heat capacity Method

The equivalent specific heat capacity method has been implemented to account for the heat storage within the PCM layer and a one-dimensional nodal transient heat transfer model has been used. A

linear approximation of the heat flux between nodes has been estimated according to Equation (4.1), which was numerically solved using the implicit fixed grid scheme that employs linearization, initial conditions and adopts an iterative procedure until convergence is obtained [11]:

$$K \frac{\partial^2 T}{\partial x^2} = \rho \frac{C_p(T) \partial T}{\partial \tau} \quad \textbf{(4.1)}$$

The heat balance at PCM node (P) can be expressed as in Equation (4.2). Refer to (Fig.4.1) also.

$$\frac{K_P}{\Delta X^2} (T_{P-1} - T_P) + \frac{K_P}{\Delta X^2} (T_{P+1} - T_P) = \rho_P C_P(T) \frac{T_P - T_P^{\circ}}{\Delta t} \quad \textbf{(4.2)}$$

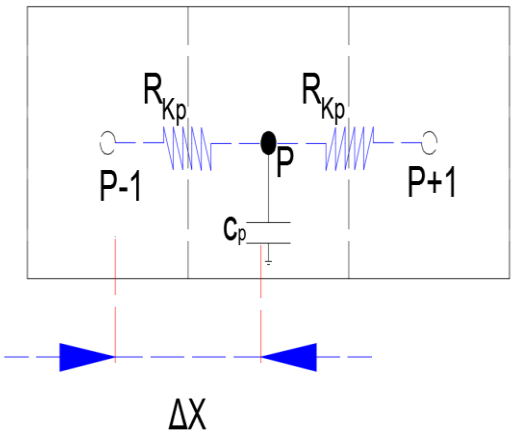

Fig.4.1 Thermal Node heat balance

At the start of each time step, the initial fields are set to the previously solved time step nodal temperatures values. Since the thermal properties of each PCM node, i.e. specific heat capacity and density, change with respect to the nodal temperature, the approximated values are evaluated as a function of the previous time step temperature input T_P°. Accordingly, the nodal temperature T_P can be obtained. Nevertheless, there is an iterative loop which is of key importance in the code. A temperature correction scheme is implemented by saving the solution of the matrix in the previous iteration and then re-solving the system until the iteration error (difference between the current temperature evaluation and the values of the previous time step) is lower than a specified tolerance (assumed equal to 0.1 °C) the code thus saves, and starts a new time step, (Fig.4.2). The solution domain is defined by number of grid points in which the derived linear Equations form a matrix system as shown in Equation (4.3), where A is the matrix of coefficients, X is the vector of

unknowns and B is the column vector of known terms. The system is solved by inverting the matrix to obtain the temperature values according to the previously mentioned iterative scheme.

$$[A]\{X\} = \{B\} \quad \textbf{(4.3)}$$

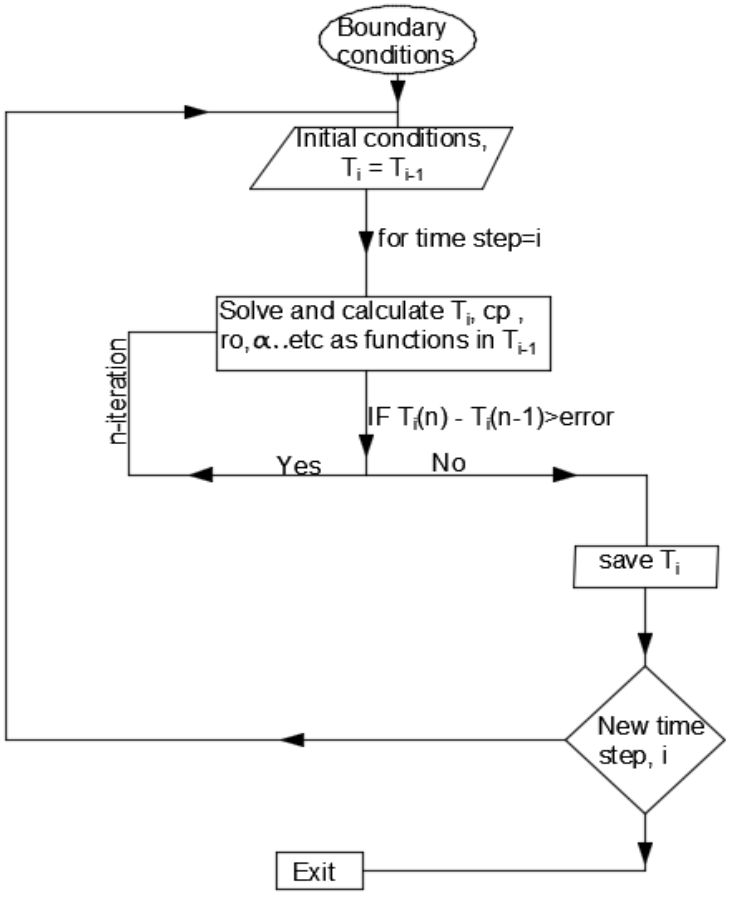

Fig.4.2 Numerical code flowchart

For each node, the C^*_{PCM} (T_{PCM}) was evaluated using a continuous linear function determined by the physical properties of the PCM ($T_{PCM,l}$, $T_{PCM,s}$, $T_{PCM,m}$, h_{PCM} , $C_{PCM,s}$, $C_{PCM,l}$) which are provided by the manufacture [17]. The linear employed formulas (Fig.4.3) are shown from (4.4) to (4.7). Furthermore $C^*_{PCM,m}$, which is the maximum specific heat capacity of the considered PCM, is defined by Equation (4.8), [16].

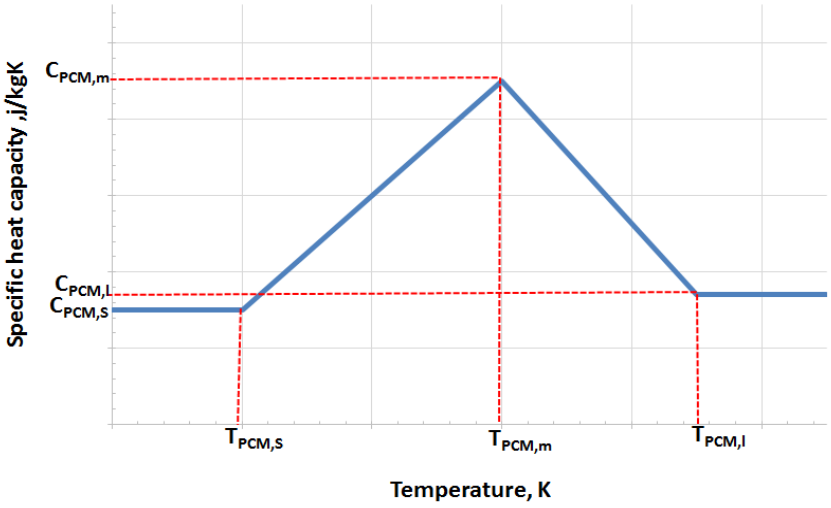

Fig.4.3 PCM Specific capacity /Temperature linearization

Value of specific heat capacity	Temperature range	
$C^*_{PCM}(T_{PCM}) = C_{PCM,s}$	$T_{PCM} \leq T_{PCM,s}$	**(4.4)**
$C^*_{PCM}(T_{PCM}) = C_{PCM,s} + \frac{C^*_{PCM,m} - C_{PCM,s}}{T_{PCM,m} - T_{PCM,s}} (T_{PCM} - T_{PCM,s})$	$T_{PCM,s} < T_{PCM} \leq T_{PCM,m}$	**(4.5)**
$C^*_{PCM}(T_{PCM}) = C_{PCM,l} + \frac{C^*_{PCM,m} - C_{PCM,l}}{T_{PCM,m} - T_{PCM,l}} (T_{PCM} - T_{PCM,l})$	$T_{PCM,m} > T_{PCM} < T_{PCM,l}$	**(4.6)**
$C^*_{PCM}(T_{PCM}) = C_{PCM,l}$	$T_{PCM} \geq T_{PCM,l}$	**(4.7)**

$$\boldsymbol{C^*_{PCM,m} = \frac{T_{pcm,s} - T_{pcm,m}}{\Delta T_h} . C_{PCM,s} + \frac{T_{pcm,m} - T_{pcm,l}}{\Delta T_h} . C_{PCM,l} + \frac{2h_{pcm}}{\Delta T_h}} \quad \textbf{(4.8)}$$

Where $\Delta T_h = T_{pcm,l} - T_{pcm,s}$

The PCM layer was discretised into five homogenous sub-layers, each of 3mm thickness (0a), A nodal sensitivity analysis was performed, and the numerical results ensured the optimisation of the five-nodes/PCM layer. The complete resistance capacitance RC transient model is represented in (0b).

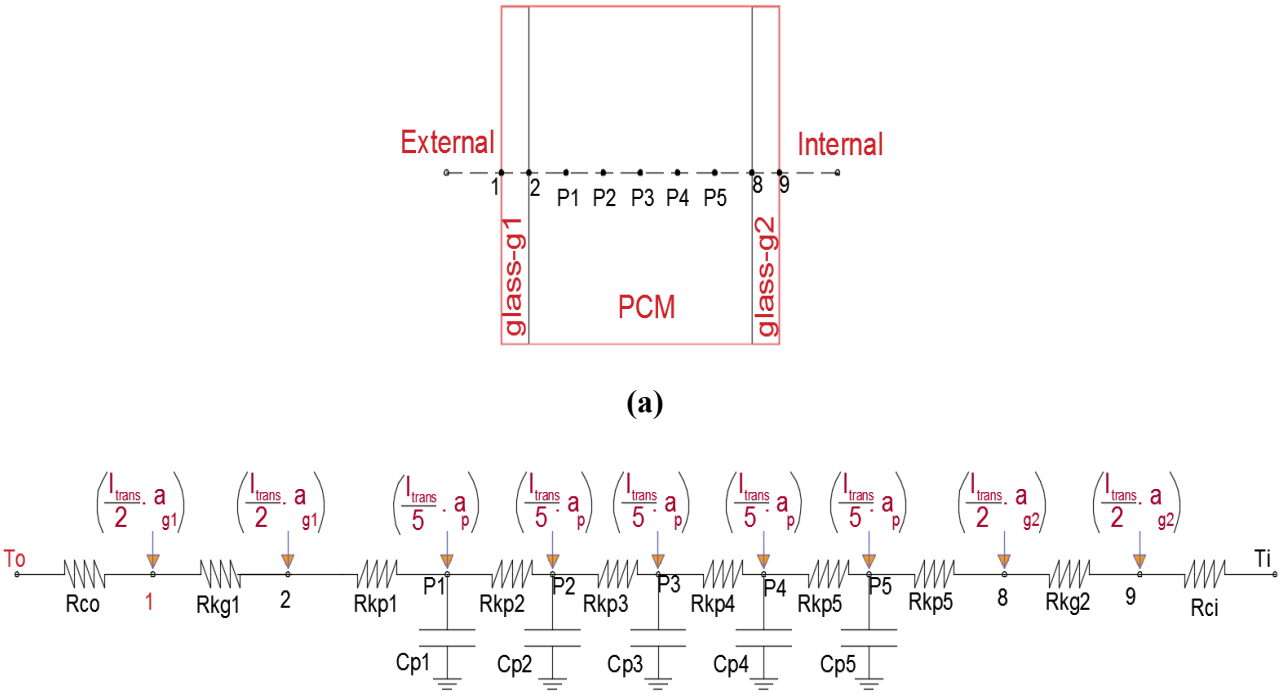

Fig.4.4 PCM glazing scheme (a), complete RC model (b)

Mathematical model description:

According to the RC model and different thermal resistances (R_c, R_K and R_r) which were explained before in chapter (2), the set of linear Equations describing the system are classified based on similarity in (4.9) to (4.12).

- *Nodes (1), (9)*

Thermal conduction and convection resistances are moderating the thermal performance of nodes (1) and (9).

$$\left(\frac{-K_{gl}}{x_{g1}} - h_o\right) T_1 + \left(\frac{K_{gl}}{x_{g1}}\right) T_2 = -I_{trans}\left(\frac{a_{g1}}{2}\right) - (T_o h_o) \quad \textbf{(4.9)}$$

$$\left(\frac{K_{g2}}{x_{g2}}\right) T_8 + \left(-h_i - \frac{K_{g2}}{x_{g2}}\right) T_9 = -I_{trans}\left({}^{a_{g2}}/_{2}\right) - (T_i h_i) \quad \textbf{(4.10)}$$

Nodes (2), (8)

$$\left(\frac{K_{g1}}{x_{g1}}\right) T_1 + \left(-\frac{K_{g1}}{x_{g1}} - \frac{K_{p1}}{x_{p1}}\right) T_2 + \left(\frac{K_{p1}}{x_p}\right) T_{p1} = -I_{trans}\left({}^{a_{g1}}/_{2}\right) \quad \textbf{(4.11)}$$

$$\left(\frac{K_{g2}}{x_{g2}}\right) T_9 + \left(-\frac{K_{g2}}{x_{g2}} - \frac{K_{p5}}{x_{p5}}\right) T_8 + \left(\frac{K_{p5}}{x_p}\right) T_{p5} = -I_{trans}\left({}^{a_{g2}}/_{2}\right) \quad \textbf{(4.12)}$$

PCM nodes (3:7)

Each homogenous sub-layer (from the five nodes comprising PCM layers) is represented by a conductive resistance and a capacitance. The resulting thermal balance Equation (4.13) is shown for one node only (P2).

$$\left(\frac{K_p}{x_p}\right)T_{p1} + \left(-2\frac{K_p}{x_p} - \frac{\rho \cdot x_p \cdot c_{p2}}{\Delta\tau}\right)T_{p2} + \left(\frac{K_p}{x_p}\right)T_{p3} = -I_{trans} \cdot \left(\frac{a_{p2}}{2}\right) - \left(\frac{\rho \cdot x_p \cdot c_{p2}}{\Delta\tau}\right) \cdot \left(T_{p2}\right)^{\tau-1} \quad \textbf{(4.13)}$$

Where, as previously clarified in Equation (4.2), c_{p2} is a function of the nodal temperature and evaluated in the previous time step value$\left(T_{p2}\right)^{\tau-1}$.

4.3.2 Enthalpy linearization method

This method was proposed by Voller and Swaminathan [12]. its key feature to assume that phase change occurs over an arbitrarily thin temperature range. In this way the enthalpy can related to the temperature by a piecewise continuous function. The implicit fixed grid scheme was also followed here in this method. Assuming constant specific heat capacity in each phase, the enthalpy can be approximated as in Equation (4.14).

$$H = \begin{cases} c_s T & T \le T_{m-\epsilon} \\ c_s(T_m - \epsilon) + \left[\frac{c_s + c_l}{2} + \frac{L}{2\epsilon}\right](T - T_m + \epsilon) & T_{m+\epsilon} < T < T_{m-\epsilon} \\ c_l T + (c_s - c_l)T_m + L & T \ge T_{m+\epsilon} \end{cases} \quad \textbf{(4.14)}$$

Where ϵ is an arbitrarily small value representing half the phase change temperature interval. The approximate definition H(t) can be readily differentiated with respect to temperature to obtain.

$$C^A = \frac{dH}{dT} = \begin{cases} c_s & T \le T_{m-\epsilon} \\ \left[\frac{c_s + c_l}{2} + \frac{L}{2\epsilon}\right] & T_{m+\epsilon} < T < T_{m-\epsilon} \\ c_l & T \ge T_{m+\epsilon} \end{cases} \quad \textbf{(4.15)}$$

The definitions of H(T) and C^A can be used to linearize the discretized enthalpy equation in iterative form as:

$$\sum a_{nb}\, T_{nb} - (a_p + \rho\, C^A) T_p{}^n \;=\; a_p\, \rho\, C^A\, T_p{}^{n-1} - \rho \cdot \frac{v}{\Delta\tau}\left[H_P{}^{\circ} - H_P{}^{n-1}\right] \qquad \textbf{(4.16)}$$

Where:

$H_P{}^{\circ}$: Enthalpy node value of the previous time step

$H_P{}^{n-1}$: Enthalpy node value of iteration n-1

a: Nodal coefficients

τ: Time Step

At the start of the time step the initial iterative fields are set to the previous time step values. From the known temperature and enthalpy fields at iteration n-1 all temperatures nodes are obtained .In order to ensure solution consistency a correction and iterative loop has to be followed by saving the solution of the matrix in the previous iteration and then re-solving the system after correcting the nodal temperature $T_p{}^n$ by Equation (4.17) to convergence, the code thus saves, and starts a new time step. Furthermore, the solution domain is defined in which the derived linear Equations form a matrix system and solved instantaneously by inverting the matrix to obtain the temperature values according to the previously mentioned iterative scheme.

$$T_p{}^n = \begin{cases} \dfrac{H_P{}^n}{c_s} & H_P{}^n \le c_s(T_m - \in) \\ \dfrac{H_P{}^n + \left[\dfrac{c_s + c_l}{2} + \dfrac{L}{2\in}\right](T_m - \in)}{\dfrac{c_s + c_l}{2} + \dfrac{L}{2\in}} & T_{m+\in} < T < T_m - \in \\ \dfrac{H_P{}^n - (c_s - c_l)T_m - L}{c_l} & H_P{}^n \ge c_l(T_m + \in) + L \end{cases} \qquad \textbf{(4.17)}$$

Mathematical model description:

The same set of linear Equations illustrated in the previous method apart of the PCM nodes mathematical description. The thermal balance Equation (4.18) is shown for one node only (P2).

$$\left(\frac{K_p}{x_p}\right)T_{p1} + \left(-2\frac{K_p}{x_p} - \frac{(\rho \cdot x_p \cdot c^A)_{p2}}{\Delta\tau}\right)T_{p2} + \left(\frac{K_p}{x_p}\right)T_{p3} = -I_{trans} \cdot \left(\frac{a_{p2}}{2}\right) + \left(\frac{(\rho \cdot x_p \cdot c^A)_{p2}}{\Delta\tau}\right)^{n-1} {T_{p_2}}^{n-1} - \rho \cdot \frac{x_p}{\Delta\tau}\left[{H_P}^{\circ} - {H_P}^{n-1}\right] \quad \textbf{(4.18)}$$

4.3.3 Short-wave radiation

The radiative heat transfer based on the grey surface model was implemented. This model is defined by considering only spectral-average thermo-optical properties (one value in each band) corresponding to non-overlapping regions of the spectrum, with spectral uniformity in each of the two considered bands: solar short- and long-wave radiation.

Short-wave radiation through PCM module

Within the PCM layer, the analysis of the optical performance – and accordingly, the short-wave radiation is not simple because the PCM has variable optical characteristics, which depend on the current physical status of the material. When the PCM is in solid state, the dominant transmission mode is direct-to-diffuse and the scattering effect is prominent [13] while in liquid phase, as the transparency increases, direct-to-direct transmission takes place. While the material is within the phase changing zone (i.e. mushy zone), the PCM optical data becomes even more complicated, since the behaviour is somehow in-between that of a fully solid PCM layer and that of a fully liquid PCM layer. The modelling of the optical properties of the PCM layer therefore must include the transient physical state of the material.

Accordingly, the optical properties such as absorption, scattering, and transmission, which control the radiation propagation within the PCM, have been evaluated based on some mathematical Equations. (4.19) (4.25), which compute the nodal optical properties as a function in the liquid fraction β. The liquid fraction value is the relative amount of liquid phase present in the PCM. The study has been explained thoroughly in Gowreesunkera et al. [14].

If $T_{PCM} <= T_s$, then

$$\beta = 0 \quad \textbf{(4.19)}$$

Else if $T_{PCM} > T_l$,

$$\beta = 1 \quad \textbf{(4.20)}$$

Else if T_s <Tpcm<T_l,,

$$\beta = \frac{T_{PCM} - T_s}{T_l - T_s} \quad \textbf{(4.21)}$$

$$\delta = \frac{\tau_{r,l} - \tau_s}{1 - \tau_s} \quad \textbf{(4.22)}$$

$$d = \left[\beta\ \sigma_{\varepsilon,l} + (1 - \beta\ )\sigma_{\varepsilon,s}\right] S \quad \textbf{(4.23)}$$

$$\tau\tau_{r,PCM} = 10^{-d} \quad \textbf{(4.24)}$$

$$\alpha_{PCM} = [\delta\ \beta + (1 - d)]\ (1 - \tau_{PCM}) \quad \textbf{(4.25)}$$

Hence, by correlating the optical properties to the liquid fraction (i.e. temperature of each node), accurate and descriptive results are expected from the numerical model. After identifying values of absorptivity and transmissivity for each i^{th} node within the PCM layer, based on the state of the node, these are combined with the angular optical properties of the two glass layers represented by two nodes. In which the net radiation method is applied [15]. The method expresses the radiation that leaves the glass on its outer face I1(i), and that which leaves the same glass from its inner surface I2(i), as a function of the boundary conditions and the technical characteristics of the glass (See Section 2.2.1b). The code is then able to identify the solar radiation energy balance for each time step of the entire glazing-PCM assembly. The final resultant solar radiation transmitted to the indoor zone, (i.e. the solar gain), has been applied to the indoor energy balance to evaluate the required hourly thermal loads.

4.4 PCM Numerical Model validation

4.4.1 Equivalent capacity method

Validation of the model was carried out by comparing the measured data by [13], regarding surface temperature values of the inner and outer glass surfaces of the PCM glazed unit, with the numerical results. As illustrated in (Fig.4.5a) and (Fig.4.5b), a good agreement is reached in the model.

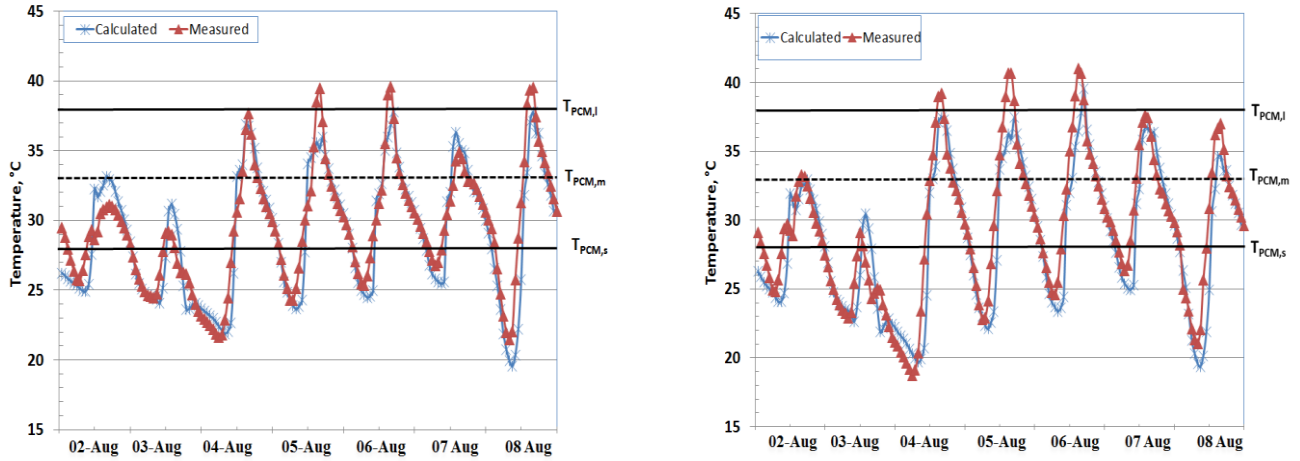

(a) **(b)**

Fig.4.5 Numerical Model validation, calculated vs measured, (a) Inner glass surface, (b) Outer glass Surface

The evaluated root mean square error (RMSE) for the inner glass was 2.4 °C and within the outer glass was 2.7°C.

4.4.2 Enthalpy linearization method

The same set of measured date [13] were used, and as shown in (Fig.4.6a&b) there is a good agreement between the numerical and experimental results. The RMSE for the inner glass reached 1.6 °C and within the outer glass as 2°C.

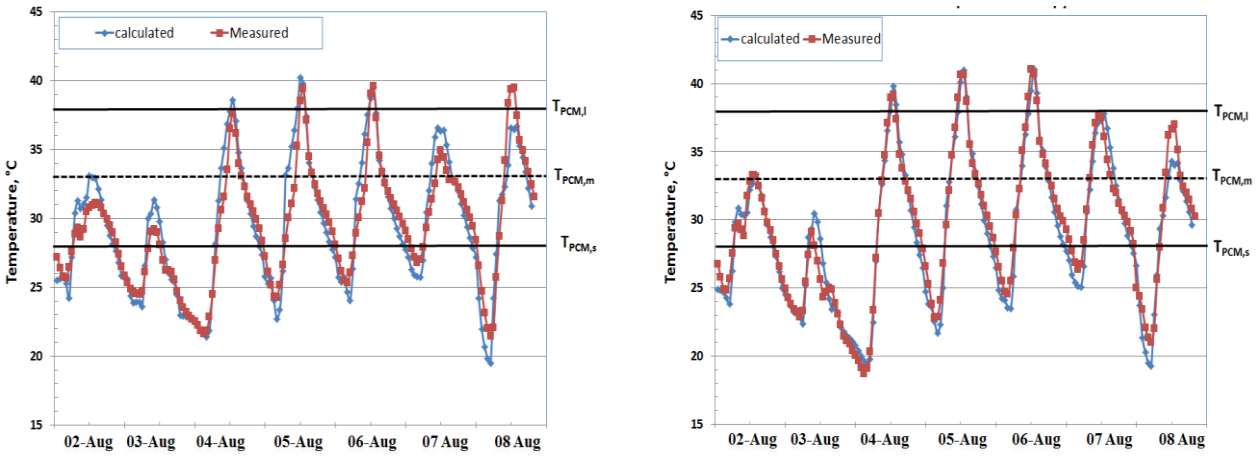

(a) **(b)**

Fig.4.6 Numerical Model validation, calculated Vs measured, (a) Inner glass surface, (b) Outer glass

4.5 PV/PCM integration numerical heat transfer models

4.5.1 PV/PCM building integration back ground

One particular use of PCM in combination with other technologies for solar energy conversion is seen in its use for moderating temperature rise in PV modules, where efficiency loss due to the increase in module temperature can be reduced: in crystalline silicon solar cells, the associated elevation of PV temperature reduces the solar to electrical energy conversion efficiency by 0.4–0.5 %/K Batagiannis et al. [18]. Ciulla et al. [19] have presented a one-dimensional thermal analysis of an isothermal PV-PCM model by using an explicit finite-difference approach. The numerical model results have been validated against experimental data obtained from a test facility in Palermo, Italy. The model can be then used to determine the thermal behaviour of a multilayer (opaque) wall in which there is a PCM coupled with a PV module. Aelenei et al. [20] analysed a simplified thermal network model for building integrated photovoltaic BIPV-PCM which has been developed in MATLAB/SIMULINK and has been validated with experimental results during the heating period. The comparison has demonstrated a good agreement, with most discrepancies occurring when airflow begins to flow into the gap. The maximum electrical efficiency of the PV system reached 10%. Hasan et al. [21] have investigated the economic consequences of applying PCM in a PV system in two different climatic conditions. It was concluded that such a system is financially viable in higher temperature and higher solar radiation environments. The numerical investigation of PV/PCM combination has been handled through two models. The first was one dimensional heat transfer model, the PCM thermal performance has been described based on the equivalent capacitances method. Then the 1-D model has been coupled with the indoor air heat balance Equation to evaluate the impact of the proposed façade system on the heating and cooling energy demand. In order to develop the numerical model and to take into consideration some physical phenomena's such as air stratification through facades the second model was two dimensional heat transfer model using the enthalpy method to describe the PCM performance, and the model were linked to TRNSYS simulation studio to describe in details the building yearly thermal demands. In this chapter the two models have been clarified thoroughly with different cases studies and boundary conditions.

4.5.2 One dimensional model of the integrated DSF+PV-PCM system:

One-dimensional transient model has been developed to include the PV-PCM integration in the building façade. The RC model is clarified in (Fig.4.7b) and MATLAB [30] is used to develop the code. The cavities (i.e., cav1 and cav2) were assumed to be forced-ventilated by the outside air (out-out) methodology.

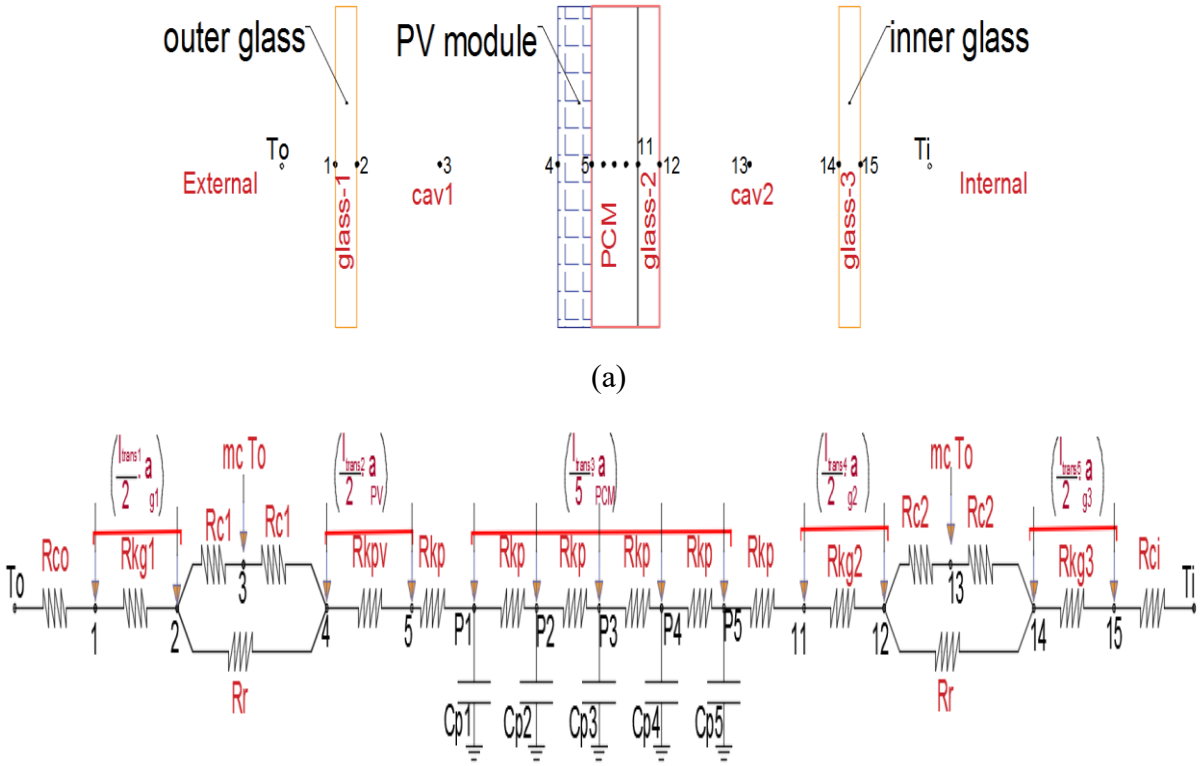

Fig.4.7 . PV/PCM- RC model (a) PV/PCM configuration scheme (b) RC model

The solution domain has been covered by 15 node grid points in which the derived linear Equations form a matrix system as shown in Equation (26), where A is the matrix of coefficients, X is the vector of unknowns and B is the column vector of known terms. The system is solved by inverting the matrix to obtain the temperature values. The set of linear Equations describing the system are classified based on similarity in Equations (4.26) to (4.35).

Nodes (1), (15)

Thermal conduction and convection resistances are moderating the thermal performance of nodes (1) and (15).

$$\left(-K_{gl}/x_{g1} - h_o\right)T_1 + \left(K_{gl}/x_{g1}\right)T_2 = -I_1\left(a_{g1}/2\right) - (h_o T_o) \quad \textbf{(4.26)}$$

$$\left(-K_{g3}/x_{g3} - h_i\right)T_{15} + \left(K_{g3}/x_{g3}\right)T_{14} = -I_5\left(a_{g3}/2\right) - (h_i T_i) \quad \textbf{(4.27)}$$

Nodes (2), (4), (12) and (14)

Radiation heat exchange between surfaces appears in the energy balance between nodes (2) and (4), and between (12) and (14).

Node-2

$$\left({}^{K_{gl}}/_{x_{g1}}\right)T_1 + \left({}^{-K_{gl}}/_{x_{g1}} - h_{c1} - h_r\right)T_2 + (h_{c1})T_3 + (h_r)T_4 = -I_1\left({}^{a_{g1}}/_{2}\right) \quad \textbf{(4.28)}$$

Node-4

$$(h_r)\,T_2 + (h_{c1})T_3 + \left(-h_r - h_{c1} - \frac{K_{pv}}{x_{pv}}\right)T_4 + \left(\frac{K_{pv}}{x_{pv}}\right)T_5 = -I_2\left({}^{a_{pv}}/_{2}\right) \quad \textbf{(4.29)}$$

Node-12

$$\left(\frac{K_{g2}}{x_{g2}}\right)T_{11} + \left(-h_r - h_{c2} - \frac{K_{g2}}{x_{g2}}\right)T_{12} + (h_{c2})T_{13} + (h_r)\,T_{14} = -I_4\left({}^{a_{g2}}/_{2}\right) \quad \textbf{(4.30)}$$

Node-14

$$\left({}^{K_{g3}}/_{x_{g3}}\right)T_{15} + \left({}^{-K_{g3}}/_{x_{g3}} - h_{c2} - h_r\right)T_{14} + (h_{c2})T_{13} + (h_r)T_{12} = -I_5\left({}^{a_{g3}}/_{2}\right) \quad \textbf{(4.31)}$$

Node (3) and (13)

Forced convection was implemented within both cavities represented by nodes (3) and (13).

$$(h_{c1})\,T_2 + (-2\,h_{c1} - m\cdot c)T_3 + (h_{c1})T_4 = -(m\cdot c)T_o \quad \textbf{(4.32)}$$
$$(h_{c2})\,T_{12} + (-2\,h_{c2} - m\cdot c)T_{13} + (h_{c2})T_{14} = -(m\cdot c)T_o \quad \textbf{(4.33)}$$

Node (5) and (11)

$$\left(\frac{K_{pv}}{x_{pv}}\right)T_4 + \left(-\frac{K_{pv}}{x_{pv}} - \frac{K_{p1}}{x_{p1}}\right)T_5 + \left(\frac{K_{p1}}{x_{p1}}\right)T_{p1} = -I_2\left({}^{a_{pv}}/_{2}\right) \quad \textbf{(4.34)}$$

$$\left(\frac{K_{p5}}{x_{p5}}\right)T_{p5} + \left(-\frac{K_{p5}}{x_{p5}} - \frac{K_{g2}}{x_{g2}}\right)T_{11} + \left(\frac{K_{g2}}{x_{g2}}\right)T_{12} = -I_4\left({}^{a_{g2}}/_{2}\right) \quad \textbf{(4.35)}$$

PCM nodes (6:10)

Each homogenous sub-layer (from the five nodes comprising PCM layers) is represented by a conductive resistance and a capacitance. The resulting thermal balance Equation (4.36) is shown for one node only, for the sake of brevity.

$$\left(\frac{K_p}{x_p}\right)T_{p1}+\left(-2\frac{K_p}{x_p}-\frac{\rho\cdot x_p\cdot c_{p2}}{\Delta\tau}\right)T_{p2}+\left(\frac{K_p}{x_p}\right)T_{p3}=-I_3\cdot\left(\frac{a_{p2}}{2}\right)-\left(\frac{\rho\cdot x_p\cdot c_{p2}}{\Delta\tau}\right)\cdot\left(T_{p2}\right)^{\tau-1} \quad \textbf{(4.36)}$$

Whereas previously clarified in Equations. (1) and (2), c_{p2} is a function of the nodal temperature and evaluated in the previous time step value $\left(T_{p2}\right)^{\tau-1}$.

4.5.3 Required hourly thermal loads

The expected improvements due to integration of PCM are included in the PV modules' thermal/electrical performance and the building thermal loads. Accordingly, to reach a more realistic evaluation, an hourly-simplified thermal energy model is used alongside the nodal temperature results obtained from the code in both comparative cases. The internal loads [22] summarized in Table (5), are switched on only during hours of occupancy; the schedule for which is clarified in Table (1). It is expected that thermal loads calculated with the model herewith presented are higher than thermal load achieved with more advanced models such as TRNSYS [23], which takes into consideration the room's thermal capacity and radiation heat exchange between internal surfaces of the indoor space. However, the main scope of this section is to state a simplified platform for numerical modelling concerning the PV-PCM integration within totally glazed façade buildings. Hence, the zone thermal energy evaluation depended on identifying the convection losses due to inner glass layer, solar gains and internal loads (Table 4.1) on an hourly basis (see section 2.3.2). The room energy balance is evaluated by Equations. (4.37) and (4.38), where a negative sign represents the required cooling loads and a positive sign represents the required heating loads. All office room walls, except for the glazed façade wall are considered adiabatic.

$$Q=-(IL+SG)+Convection\ losses \quad \textbf{(4.37)}$$

$$Convection\ losses=h_i\,A\,(T_{room}-T_{inner\ glass}) \quad \textbf{(4.38)}$$

Table 4.1 Internal loads

Persons W	Light W/m²	Equipment's W
70	10	130

The input data to the code are values summarized in the physical specification of the façade composition: the site climatic conditions and thermal characteristics of the PCM. All climatic data have been evaluated from TRNSYS model [23] on the west vertical orientation, based on a 15 min time step i.e. data extracted depends on the test reference year TRY. The input data are listed below:

1- Beam and diffuse solar radiation.
2- Solar radiation vertical incidence angles.
3- Mass flow rate for the cavity ventilation (based on specific working hours, as the building under study is assumed to be administrative).
4- External and internal temperatures. As mentioned, the internal design temperature follows a work schedule, which is clarified in Table 4.2.
5- The angular values of the absorption coefficients for different glass layers. The method to obtain it was previously clarified in detail in (section 2.3.2)
6- Thermal characteristics of the PCM layer.

4.6 Numerical study parameters

4.6.1 Climates and inside design conditions

The study includes three different locations to investigate thoroughly the climate influence on implementing PCM in BIPV. The climate categories which were considered are: warm temperate, snow fully humid, and hot arid, Kottek et al. [24] represented by: Venice (Italy), Helsinki (Finland) and Abu Dhabi (United Arab of Emirates), respectively. Due to this diversity, (i.e. ambient temperatures, solar radiation intensity, incident angles), the parameters for indoor air set-points are also different. Those design parameters directly affect the building's energy performance. For the cities of Venice and Helsinki, the summer season starts in May and finishes by the end of September. The inside thermal design conditions for both cities are within the accepted range [25]. Nevertheless, and particularly in Helsinki, certain design conditions were followed in NZEB project YmparistoItalo office building [26] according to colder climatic conditions compared to Venice. On the other hand, the city of Abu Dhabi does not face a winter season as the minimum coincident ambient temperature, with 0.4 % as an annual percentile value, equal to 9°C happens in January. Accordingly, the design temperature as per [27] is considered to be 23°C and 25°C at the weekends, and that to avoid mold formation on walls and furniture. The design temperature is assumed to be 4°C higher than that outside. In (Table 4.2), the settings for occupancy and indoor air temperature set-point used in the numerical simulations are summarized.

4.6.2 Double skin façade (DSF) configuration

The DSF tested in the simulations have two configurations: one that includes a semi-transparent PCM-PV layer in the cavity, and one that includes only a semi-transparent PV layer in the cavity. The layer structures of the two DSF and the correspondent nodal scheme are shown in (Fig.4.8a and b). Illustrated in (Table 4.3) are some technical specifications of the glazed layers that were used. The type of PV that was used is a semi-transparent amorphous-silicon (a-si) module. (Table 4.4) lists the technical characteristics of the used module.

Table 4.2 Summary of simulation parameters

CITY		Inside temperature	Working hours	Season
Venice[31]	Occupancy	26°C	8am:7pm (Mon. to Fri.)	Summer months (May to Sep.)
	Non occupancy	32°C		
	Occupancy	20°C	8am:7pm	Winter months (Jan to April) and (Oct to Dec.)
	Non occupancy	15°C		
Helsinki [33]	Occupancy	25°C	8am:7pm	Summer months (May to Sep.)
	Non occupancy	32°C	-	
	Occupancy	21°C	8am:7pm	Winter months (Jan. to April) and (Oct. to Dec.)
	Not occupied	15°C	-	
Abu Dhabi [25]	Occupancy	23°C	8am:7pm	Summer months (Feb. to Nov.)
	Non occupancy	26°C	-	
	Occupancy	23°C	8am:7pm	Winter months (Jan. and Dec.)
	Non occupancy	Toutside+4°C	-	

Table 4.3 Optical specification of inner glass layer

	Thickness	U W/m^2K	Transmissivity τ	Absorptivity α
glass1	8mm clear glass	5.3	0.7	0.2
glass2 & glass3	4mm clear glass	5.6	0.8	0.1

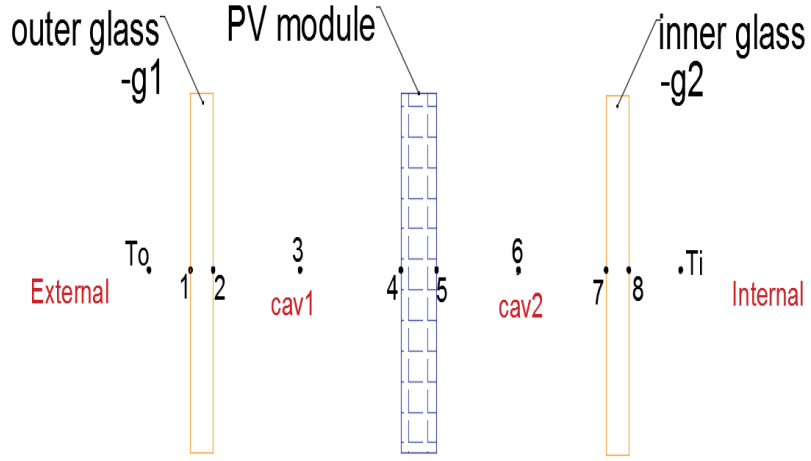

(a)

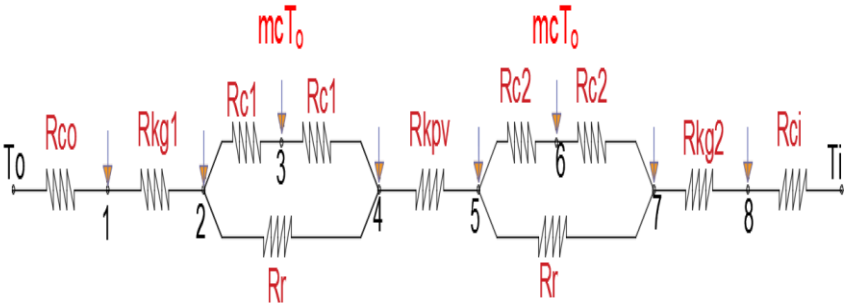

(b)

Fig.4.8 PVIB- RC model (a) PV configuration scheme (b) RC model

Table 4.4 PV module technical specifications

Nominal peak power	140(W)
Voc	185(V)
Isc	1.15 (A)
Cell type	a-si Thin film
Front glass	3mm tempered glass
PV glass	3.2 float glass
$\boldsymbol{\psi}$	-0.19 %/°C
$\boldsymbol{\eta_r}$	15%
Sol. Transmission	7.4%
Sol. Reflection	10.2%

The two comparative cases of the façade configuration are clarified in (Fig.4.9a): the PV-PCM layer and (Fig.4.9b): the PV layer. The façade is applied to a virtual office room, with the following dimensions: 3.0 m width, 3.30m depth, and 3.5m height, and west-oriented. As suggested by Goia [28], it is possible to find an optimal percentage of transparent area for a given location, where the total energy use of the building is minimized. The optimal range, for a façade with conventional windows and walls construction, lies in the range of 20% to 60%. In this simulation, considering the different nature of the façade (an active façade), it is less straightforward to determine an optimal value for the transparent surface. Considering the advantages given by the presence of the PV in the semi-transparent part of the façade, the following configuration was used in this study: 30% fully transparent DSF, 70% semi-transparent façade (either with PCM-PV layer or just with PV layer), see (Fig.4.9c).

4.6.3 Control strategy for cavity ventilation

As clarified previously, the effective specific heat capacity C^*_{PCM} is estimated as a continuous function of the PCM nodal temperature [16]. The maximum value of C^*_{PCM} , which is considerably larger than C_s, occurs when the nodal temperature reaches the PCM peak temperature value T_m. Accordingly, to maximize the efficiency of the PCM implementation, a certain compromise has to be made. The surface temperature of the PV module has to be kept within transition phase of the PCM in order to represent an effective solution.

The proposed ventilation scenario for the DSF cavity is to ventilate the cavity during non-working hours. It was concluded that if the cavity ventilation results in T_{PCM} that is lower than $T_{s,}$, then the benefit of adopting a PCM layer is reduced, since it does not accumulate heat within the transition phase temperature range. On the contrary, it is important to avoid the PCM layer melting completely, in which case it cannot properly discharge the heat accumulated during the daytime in order to be able to regain the solid state and have the potential to store heat the following day. The schedule of the cavity ventilation is illustrated in (Fig.4.10). The cooling process is starting before the end of working hours at 7 pm and proceeds until the start of working hours on the following day.

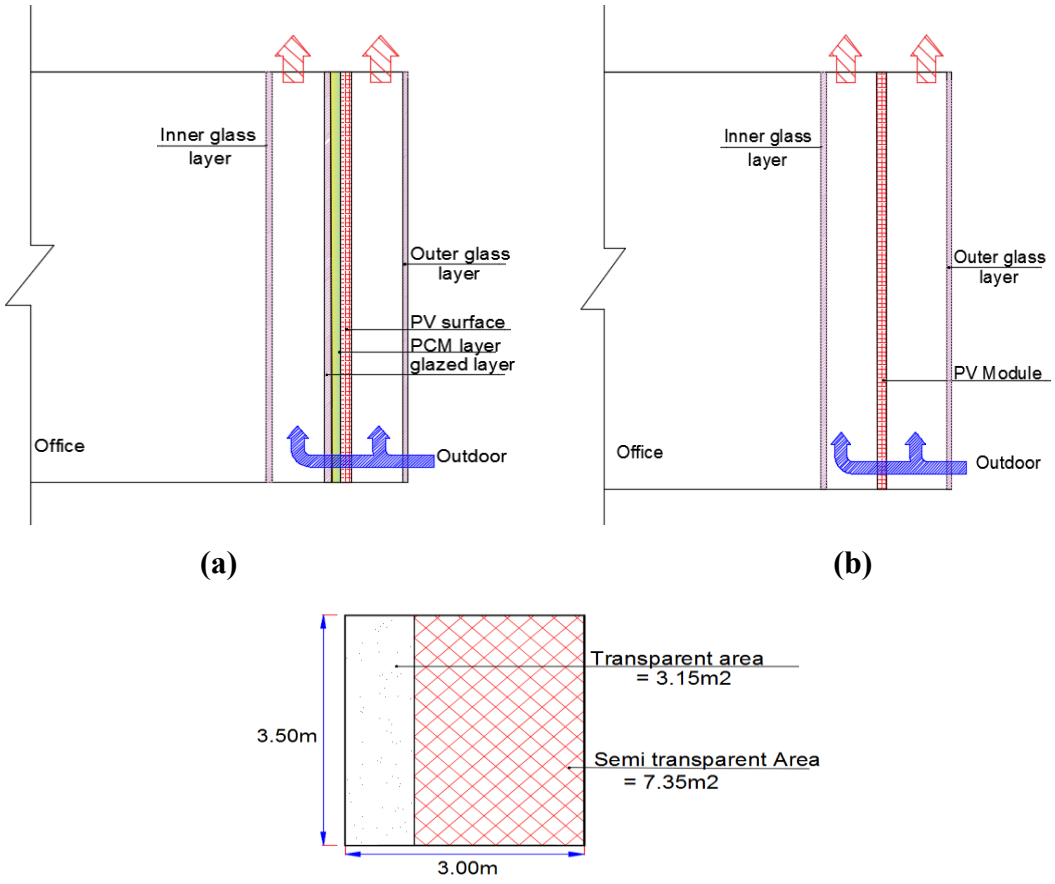

Fig.4.9 Glazed office integrated with PV module Scheme (a) with PCM, (b) without PCM, (c) façade configuration optimization

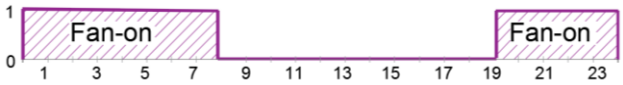

Fig.4.10 Day time(hours)

4.7 PCM selection

The selection of the PCM characteristics is connected to the climate, since it is necessary that it presents the phase change over a suitable temperature range, in order to adequately smooth the temperature increase over the PV surface. For this reason, two different PCMs were chosen for Helsinki and Venice, than for Abu Dhabi. The material for the first two locations is characterized by a lower phase change transition temperature (nominal temperature 41 °C), and the one for the latter location has a higher phase change transition temperature (nominal temperature 55 °C). The two materials have similar latent heat of fusion. The thermo-physical properties of the two PCM layers, based on paraffin waxes [17], are reported in Table 4.5).

Table 4.5 PCM Table of properties

City	Venice/ Helsinki	Abu Dhabi
Name	RT42- Organic material	RT55- Organic material
Solid temperature (lower limit of phase change range)	38°C	51°C
Nominal melting temperature	41°C	55°C
Liquid temperature (upper limit of phase change range)	43°C	57°C
Specific heat Capacity	2 kJ kg^{-1} K^{-1}	2 kJ kg^{-1} K^{-1}
Latent heat of fusion	175 kJ kg^{-1}	170 kJ kg^{-1}

4.8 Results

The numerical study results are divided into two main sections. The first reports the office thermal performance and highlights the specific monthly energy usage of the glazed office as a block load in the two comparative cases (expressed in kWh/m^2) for the three cities. The second section reports PV modules' thermal improvements, and presents a comparison of the yearly solar energy conversion for the two different façade configurations.

4.8.1 Energy demand for heating and cooling

(Fig.4.11a) shows the specific monthly thermal energy demand in Venice. As shown during the heating season, the demand is almost the same between having the integration of PCM layer and not having it. When starting from the cooling season, the trend starts to change as cooling energy demand is reduced by an average of 29% for the case where the PCM layer is implemented. In Helsinki (Fig.4.11b) the heating demand is, in general, higher than in Venice, but a similar trend is shown: in summer season the PCM layer has a positive influence and provides a decrease in the cooling energy demand in the range of 20% to 23%. As shown in (Fig.4.11c), Abu Dhabi is the location where the integration of PCM shows the largest potentials, due to the higher cooling energy demand. The overall average cooling load improvement reaches 22%. The energy saving percentages for all months of the year are reported in (Table 4.6).

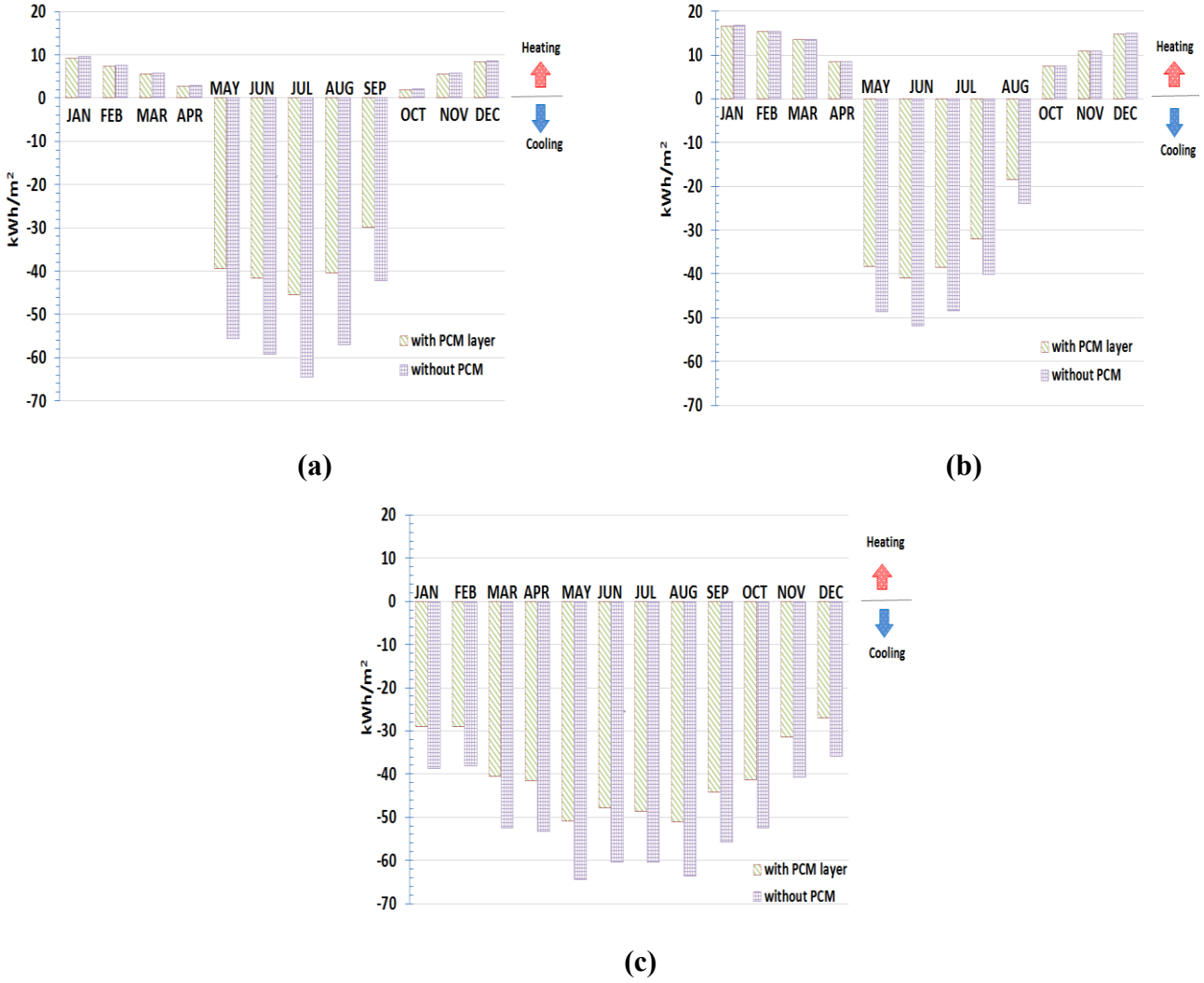

Fig.4.11 Monthly thermal loads - kWh/m² (a) Venice City, (b) Helsinki city, (c) Abu Dhabi City

Table 4.6 Summary of monthly reduction of energy use, for different locations

City	Venice	Helsinki	Abu Dhabi
Months	kWh/m^2 - Decrement %		
Jan	3%	0%	25%
Feb	4%	1%	24%
Mar	4%	1%	23%
Apr	3%	-1%	22%
May	29%	22%	21%
Jun	30%	21%	21%
Jul	29%	20%	20%
Aug	29%	20%	20%
Sep	29%	23%	21%
Oct	5%	1%	21%
Nov	4%	0%	23%
Dec	4%	1%	25%

4.8.2 PV system energy production

The study investigated the thermal and electrical influence of applying a PCM layer behind PV modules. (Fig.4.12 a,b and c) shows the weekly temperature profiles performance in cities for Venice, Helsinki and Abu Dhabi respectively. The overall trend in all cases is that PV module average surface temperature was lower in cases that used PCM. A more focused clarification is shown in (Fig.4.13), where the temperature peak shifts with and without the PCM layer is shown, highlighting the temperature curve accretion/decay due to irradiance. The daily temperature profiles for the three cities are illustrated, and it is clear that by combining a PCM layer with the PV module one guarantees a smoother temperature profile, especially when it reaches its peak value.

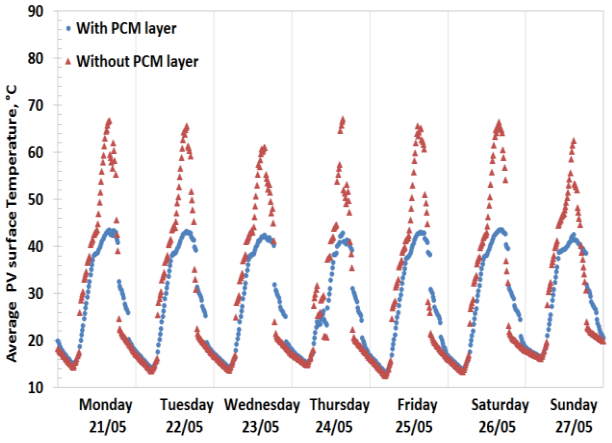

(a)

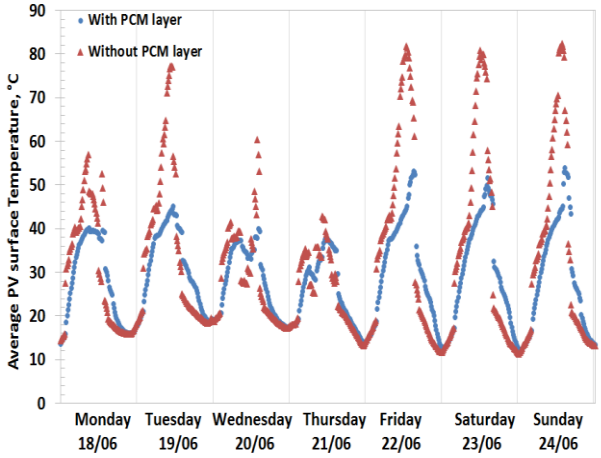

(b)

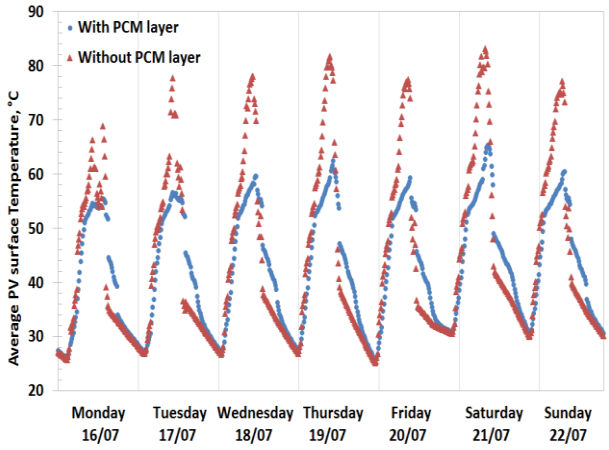

(c)

Fig.4.12 PV average surface temperature comparison, (a) Venice, (b) Helsinki, (c) Abu Dhabi

As shown in (Fig.4.13a), in Venice, the comparison between average surface temperature with and without a PCM layer is illustrated in 14th of August. The PCM worked as a heat sink, and its effect started by 7 am in the morning, causing a divergence of 5°C cooler. Between the two compared cases, i.e. with and without PCM, the PV module surface temperature differences have continued steadily until they reached the peak region between 3pm and 6pm. As was mentioned previously, a west orientation was used, and so it was expected that the solar radiation, which maximized the PCM performance, would be around this time of the day. The PCM has allowed an almost constant surface temperature, while without the PCM layer the gradient of the PV module surface temperature was increasing. The temperature profile of the PV module without PCM started to cool down rapidly compared to the PCM case with a divergence that reaches 10°C degrees as a maximum value until the end of the PCM solidification phase. However, the higher temperature of the PV layer when not

irradiated, or with low irradiation, has no influence on the module performance, since electrical energy conversion is, at that time, very low or nil. The utilization of the cavity forced ventilation strategy after that peak region has been shown to be an effective means to cool down the PCM layer and take it back to the solid state before the start of a new day. In Helsinki, due to the early sunrise in summer season, (see Fig.4.13b), corresponding to 19th July), the overall pattern of the surface temperature profiles is repeated with different divergence values seen in Venice, and reaches its peak with about 20°C degrees difference. In Abu Dhabi (Fig.4.13c), corresponding to 6th August), the PCM performs as in the previous cases with lower divergence values between the configurations with and without PCM application. The maximum peak reached was 17 C degrees difference.

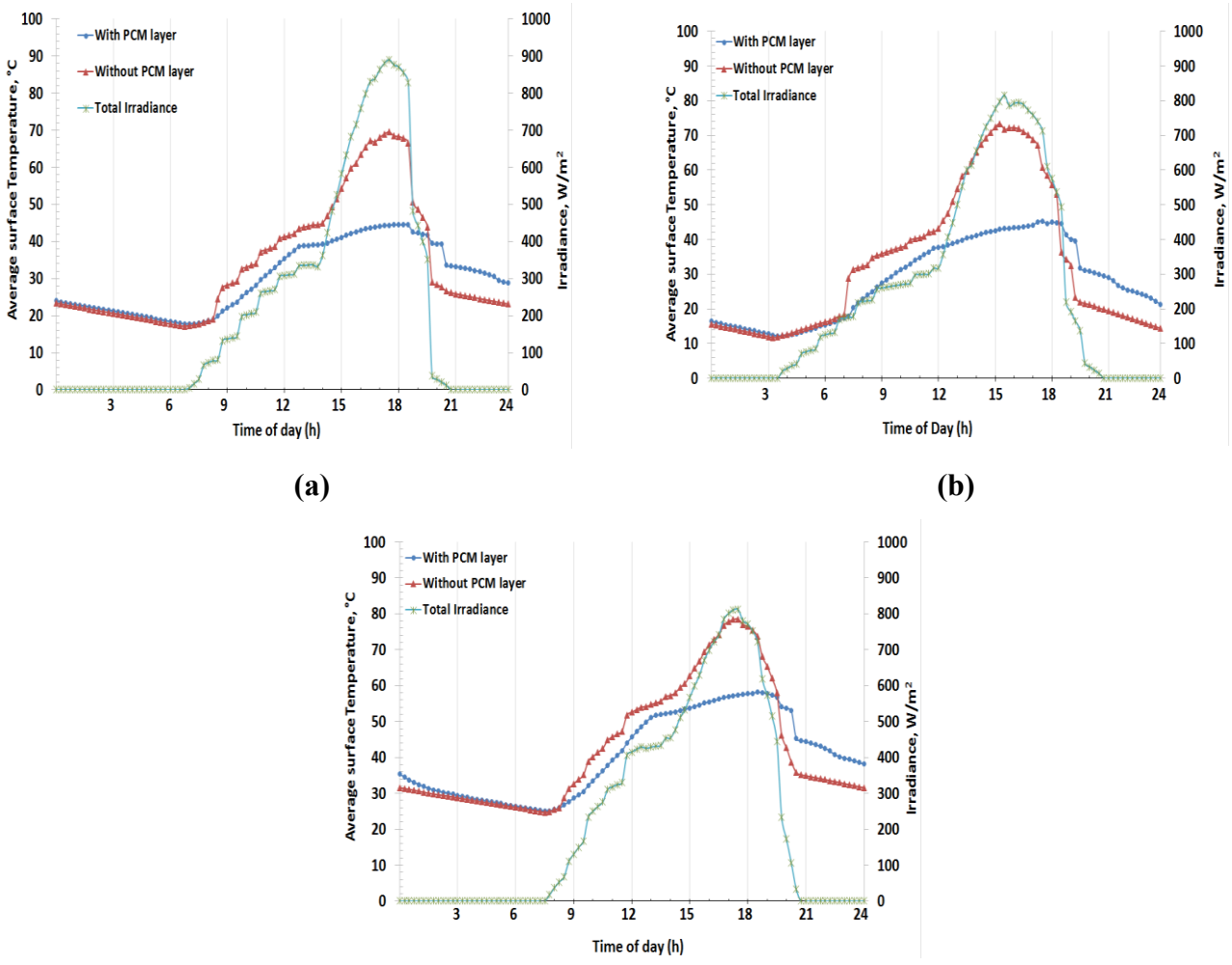

Fig.4.13 Temperature daily profile of the PV PCM module, for a given summer day, in (a) Venice, (b) Helsinki, (c) Abu Dhabi

The hourly produced power was estimated for the PV module using a correlation between the PV efficiency, the surface temperature, and the irradiance according to Equations (4.39) and (4.40)[29]:

$$P = I\,\eta_{\mathrm{PV}m}\,A_{PV} \quad \textbf{(4.39)}$$

$$\eta_{\mathrm{PV}m} = \eta_r\,[1 - \psi\,(T_{\mathrm{PV}m} - T_r] \quad \textbf{(4.40)}$$

where A_{PV} was assumed to equal 7.2m^2, I is the hourly total component of the solar radiation, calculated by the code that is impinging the PV module, and the efficiency of the PV $\eta_{\mathrm{PV}m}$ decreases as the temperature of the module increases. As shown in Figure (Fig.4.14), the overall trend in the three case studies (a, b and c) was higher in PV-PCM than for the PV module alone from the produced electrical power per unit area because of the improved temperature conditions of the PV modules which is due to the presence of the PCM, as previously described. These difference values per day ΔP ranged from -0.2 to 1.8 (W/m^2). The difference in energy-converted power between the two configurations has been magnified by a factor of 10 for the sake of readability. In Venice, the maximum percentage of improvement exceeded 5%, in Helsinki it was almost 8% and in Abu Dhabi it was a little less than 5%. Negative values appeared on (Fig.4.14 c) with lower solar radiation values, due to the PV layer getting cooler sooner without PCM. However, this small worsening of energy conversion performance under those specific conditions was greatly outweighed by the higher energy conversion efficiency during the remaining time.

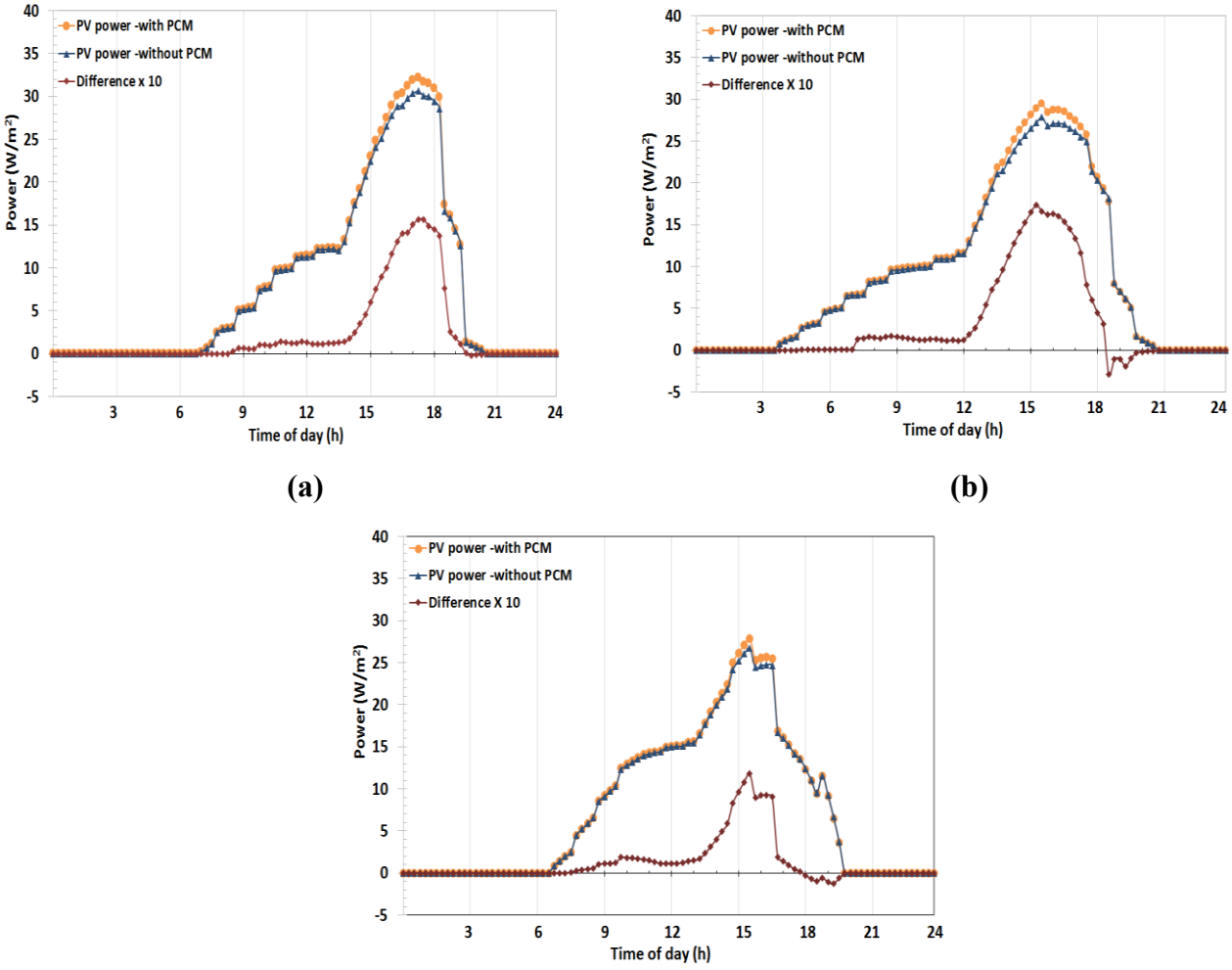

Fig.4.14 PV converted power (W/m^2), for a given summer day in (a) Venice, (b) Helsinki, (c) Abu Dhabi

4.9 Discussion

In this chapter, a physical–mathematical model for a DSF with PCM-PV layer has been conceived and developed in order to carry out numerical simulations to evaluate the integration of a PCM layer into a ventilated transparent façade. The study shows that the integration of PCM layers in double skin façades, in combination with PV modules, can be effective to significantly reduce the cooling load of an indoor space and to increase the solar energy to electrical energy conversion efficiency. Results of the simulations have revealed that the monthly cooling load is always reduced, regardless of the climate, in the range from 20% to 30%, while the implication of the use of PCM in the cavity on the heating energy demand is limited. However, this latter result might be connected to the selected ventilation strategy for the DSF cavity (i.e. out-out through-the-night methodology). It is reasonable to assume that a different ventilation path (e.g. indoor air curtain) might result in a

reduction of the heating load too, especially for climates characterized by not-extreme-cold conditions (e.g. Venice).

The study highlights that the correct choice of the transition temperature of the PCM, coupled with the ventilation strategy, are the key features to ensure the effectiveness of this solution. Dedicated control algorithms to ensure a proper management of the façade cavity's airflow are necessary to enable future development of this technology. In particular, it is important that the PCM layer is maintained, as much as possible, within its transition phase range. Ventilation therefore becomes a powerful tool to cool down the PCM when it is reaching the upper limit of the transition phase, and to assure that the PCM layer is restored to the solid state before the solar irradiation appears on the following day. On the other hand, it is important to avoid overcooling of the PCM layer, which might lead to a worse performance.

With the use of a simplified control for the ventilation, the simulations presented in this paper have shown the possibility of reducing the PV module temperature by up to 20°C C, with small differences among the different locations. This is a particularly promising result that has a dual impact, both on the thermal load of the room, and on the conversion efficiency of the PV module. Implications on thermal comfort were not assessed in this research, but based on previous studies in literature; it is reasonable to foresee an improvement in thermal comfort conditions when a PCM layer is adopted in the DSF.

4.10 Linking of TRNSYS- PV/PCM MATLAB model

Thermal inertia of building components has an influence on the overall energy balance. Accordingly to expand and enforce the PV/PCM module implementation study, the MATLAB code was linked to TRNSYS model clarifying the yearly thermal loads of a fictitious building. As previously clarified; TRNSYS takes into account the stored heat in the building components.

4.10.1 Methodology

The interaction between MatLab and TRNSYS simulation studio is carried out using TYPE 155 from TRNYS library. This type is dedicated to read external codes executed by MATLAB. The numerical solution as clarified in (Fig.4.15) starts by reading the required weather condition from TYPE 16, which includes:

-Ambient temperature

-Vertical beam and diffuse solar radiation

-Incident solar radiation

These are considered the boundary conditions for both the Façade PV/PCM module and the building.

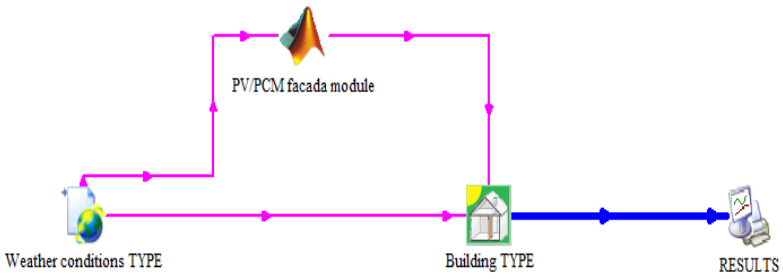

Fig.4.15 Matlab TRNSYS linkage simulation studio

As Clarified previously in the PV/PCM -1D model the numerical code estimates the surface nodal temperature for each of the module components till the last node which represents the inner surface layer temperature. However in the linking process between the PV/PCM module the MATLAB code delivers only the air node-a and the estimated transmitted solar radiation in cavity 2 (Fig.4.16) to be as user defined transient values for the room inner layer.

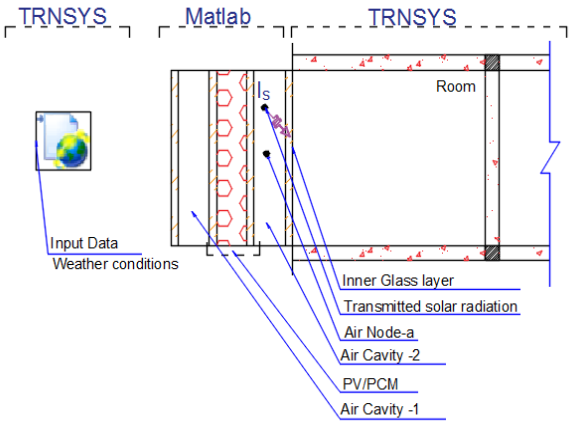

Fig.4.16 Matlab TRNSYS scheme

The reason behind not considering the output temperature of the inner glass layer calculated by MATLAB is that the complete room structure accordingly the radiation heat exchange and thermal storage of the room components which will contributes in the energy balance of the inner glass layer and its final surface temperature are taken into account in TRNSYS simulation model. the inner glass layer been identified in TRNbuild TYPE56 library with the following specifications in Table (4.7):

Table 4.7 Glazed layer specifications

Density (Kg/m^3)	2500
Heat Capacity kJ/(Kg.K)	0.84
Conductivity kJ/(h m.K)	0.27

4.10.2 PV/PCM module cavity Ventilation schedule

The influence of the façade cavity ventilation schedule is considered prominent card through the building energy performance, especially after PCM integration since the ventilation strategy is controlling the pattern of phase changing. A compromise evaluation through three strategies has been analyzed. Strategy1 assumes the ventilation all year at daytime, Strategy 2 during the winter season the ventilation has stopped entirely while in the summer season it was on during night hours. The third strategy is ventilation off all year (Fig.4.17).

Ventilation control strategy-1

The ventilation system of the façade cavity is On all year during working hours only

Ventilation control strategy-2

This strategy investigates the ventilation influence through summer season during only night hours from 8pm to 7am of the next morning. While in heating season the cavity left without ventilation

No ventilation –Strategy-3

To investigate the PCM discharge phase, it was focal to consider the PCM layer without any passive or active cooling system.

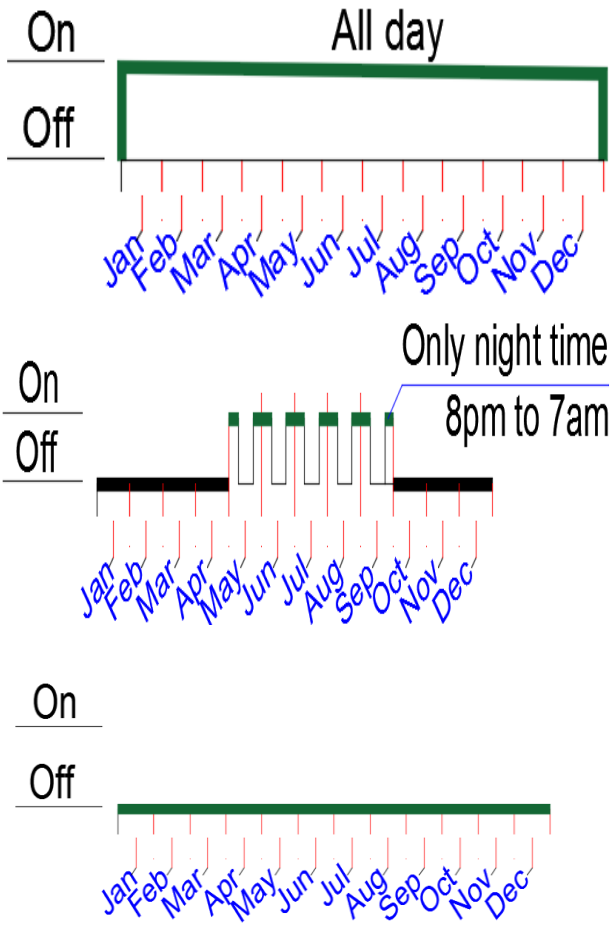

Fig.4.17 Different ventilation strategies

4.10.3 Fan electrical power estimation

Another important aspect to objectively evaluate the energetic performance of the system is the ventilation system energy consumption. For each strategy the hourly fan power were estimated by Equation (4.41).

$$\text{Fan Power W} = \frac{Q \times P_{tot}}{\eta} \quad \textbf{(4.41)}$$

Where:

Q volume flow rate m^3/s

P_{tot} Total pressure increase in the fan (Pa)

η: Fan efficiency

4.10.4 PCM proper selection:

Although the focal point behind implementing The PCM layers within buildings envelopes is to increase building components thermal inertia and improve the energetic behavior but a wrong type selection could worsen this energetic performance in comparing of not implementing PCM at all. Temperature working ranges, specific heat capacity value, the expected heat flux and the strategy of discharging absorbed heat are parameters which control the efficient and successful integration of PCM. The preliminary step in PCM selection within PV modules integration is to determine the average daily surface temperature without PCM. In the present case the average surface temperature without PCM reached 30.5°C, hence the nominal melting PCM temperature selection range was assumed to be ±3°C. Clarified in (Table 4.8) the two types of PCM have been examined.

Table 4.8 PCM types technical specifications

Name	RT-28 Organic material	RT- 35Organic material
Solid temperature (lower limit of phase change range)	27°C	29°C
Nominal melting temperature	28°C	33°C
Liquid temperature (upper limit of phase change range)	29°C	36°C
Specific heat Capacity	2 kJ kg^{-1} K^{-1}	2 kJ kg^{-1} K^{-1}
Latent heat of fusion	250 kJ kg^{-1}	160 kJ kg^{-1}

As shown in (Fig.4.18) the overall pattern of RT-35 is smoother than RT-28, especially after the end of working hours and the start of the cavity free ventilation and discharging process. PV module integrated with RT-28 surface temperature is lower than RT-35 until the ventilation starts over in the following day. The sudden changes in temperature profiles appear in the RT-28 of lower melting temperature though higher specific heat capacity. Accordingly the decision was made up to implement RT-35.

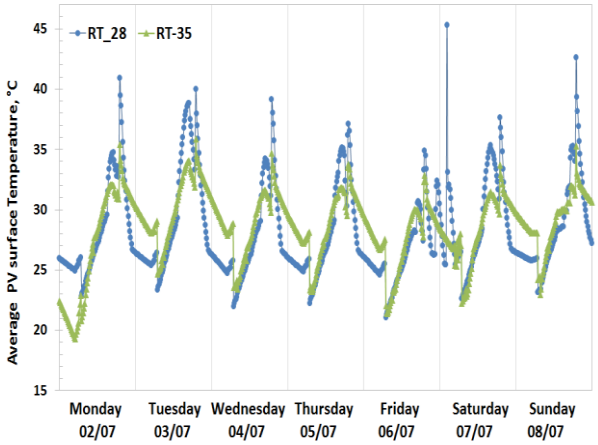

Fig.4.18 Temperature profile for RT28, and RT 35PCM types

4.11 Result

The above-clarified model was applied in two different climatic conditions, Venice as per Koppen classification [24] it is warm temperate fully humid and warm summer. On the other hand, Helsinki is the second City and it is classified as snow fully humid and cool summer.

4.11.1 Venice city

As shown in (Fig.4.19a) in Venice city thermal energy loads were clarified for the two ventilation strategies and also for the case without PCM. Ventilating the cavity all day working hours is worsen the thermal performance of the PCM specially during the heating season, while the second strategy was sufficient for obtaining higher performance during both heating and cooling seasons. In the third strategy of not ventilating the cavity, thermal loads requirements have increased within summer season as a result of inefficiency of PCM solicitation process. However not applying PCM at all is recording the highest trend in summer months specifically. (Fig.4.19b) illustrated the hourly PV surface temperature profile, as shown both strategies are close. Apart of day peak time 5 to 7 pm

with the highest solar radiation intensity rate in which the non-ventilated PCM is transformed into liquid.

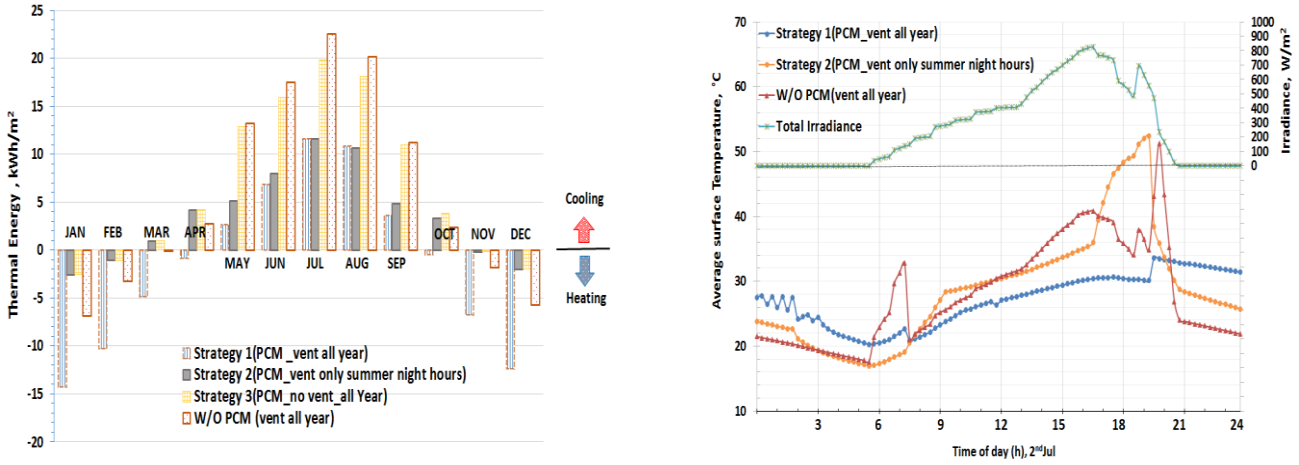

(a) **(b)**

Fig.4.19 Yearly thermal loads vs. cavity ventilation strategies

Venice energy evaluation

The air volume flow rate was considered 200L/s for the cavity, total pressure of 300PA and fan efficiency of 0.75, and by substituting in Equation (4.41) the fan yearly electrical energy consumption was evaluated for each strategy .In both strategies 1 and 3 the electrical energy was estimated by 350kWh/yr.. While in strategy 2 the fan electrical energy consumption reached 190kWh/year. Although expected electrical energy savings due to not ventilating the cavity in strategy 3 but on the other hand the increment of thermal loads reached 60% as an average percentage through summer season.

4.11.2 Helsinki city

Due to the cold climatic conditions i.e. average low coincident external temperatures in Helsinki Fig.4.20a), the possibility of not having a forced ventilation system inside the cavity all year have been investigated. It was noticed that although ventilating the cavity is improving the PCM discharge process during night however during daytime the performance is almost the same as not ventilating the cavity system during winter season. Whilst implementing forced cavity ventilation system has recorded the highest consumption followed by the without PCM case. However, in summer thermal consumption trends had a different order. Forced ventilating the cavity all working hours (strategy 1) had recorded the lowest thermal energy in months of May till September and the heating requirements appeared in first and last summer season months could be ignored since the HVAC system in this case could be totally turned off. Trend is followed by forced ventilation of the

cavity during night hours. Almost not ventilating the cavity thermal energy requirements was equal to the without PCM case. Taking into consideration that without PCM case is always forced ventilated during working hours 8am to 7pm, accordingly the electrical energy fan savings is the articulated item in the overall system energy evaluation. (Fig.4.20b) is illustrating average surface temperature of integrated PV module inside the façade cavity implementing the ventilation strategies. Although strategy 2 has a better thermal energy performance in comparing to strategy 3 but both strategies had the highest profiles and it occurred during the peak time of the west façade direction. It is important to highlight that is due to propagation of solar radiation PCM module starts to totally transform into liquid phase and accordingly sensible surface temperature of the PV has increased. Hence, due to the dynamic and variable phases of PCM performance the overall energy evaluation has to be carried out to comprehend objectively the pros and cons of the system.

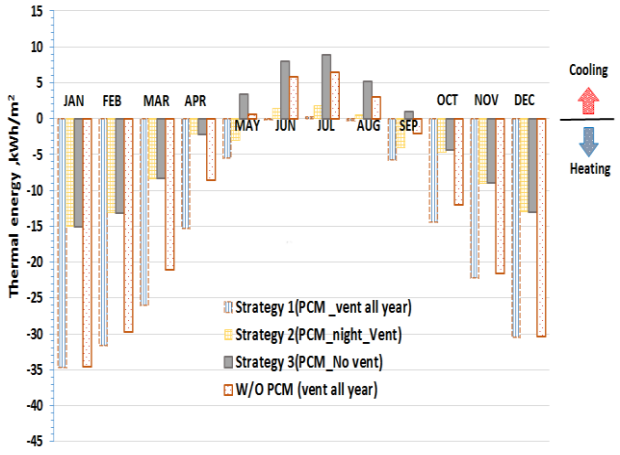

(a)Yearly thermal loads vs. cavity ventilation strategies

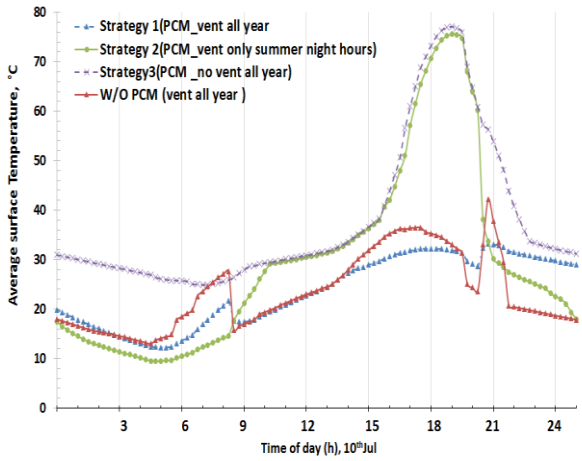

(b)Average PV surface temperature

Fig.4.20 Helsinki Energy evaluation

Strategy 1 has the highest electrical energy consumption of 350kWh/yr., followed by strategy 2with 190kWh/yr. However in the yearly thermal loads evaluation strategy 1 has the highest during winter season with an average increment of 60 % compared to strategies 2 and 3. In summer season and due to high solar radiation intensity and cooler external temperatures during night Strategy 1recorded the lowest thermal energy inquires almost zero. While not ventilating the cavity at all or ventilating it through the night's hours were not the right procedure to efficiently take advantage of the PCM latent thermal storage.

4.11.3 Optimization of ventilation strategy

Study included different strategies to reach an optimum combination of ventilation system capable of achieving the highest efficiency of PCM implementation. For climates similar to Venice city it is recommended to implement PCM, not ventilate the cavity during heating season and ventilate it through summer season during night to improve the PCM discharge efficiency. However, in Nordic climates it is preferable to implement daytime ventilation during only summer season.

4.12 Two dimensional model of the integrated DSF+PV/PCM system:

The reason behind developing the model into two dimensional is to investigate the stratification effect along the facade height especially that integrating the PV/PCM inside the cavity might create draught caused by air density differences. Nevertheless, the conduction heat flow remains in one dimensional 1D, but the 2D heat transfer has been illustrated to support the comprehension of any future improvements includes the heat conduction in the y axis.

Introduction:

The physical system is represented by nodal scheme. The double skin façade is divided into increments in the x and y-directions denoted by Δx_i and Δy_j (Fig.4.21)

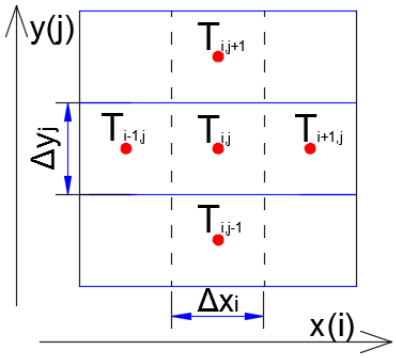

Fig.4.21 2D heat transfer

For each node the energy balance Equation is determined and by solving these linear Equations; the unknown nodal temperatures are determined. The governing 2D transient heat transfer Equation (4.42) is

$$\frac{\partial^2 T}{\partial x^2} + \frac{\partial^2 T}{\partial y^2} = \rho\, C_p \frac{\partial T}{\partial t} \qquad \textbf{(4.42)}$$

The thermal coupling between the mesh nodes is described by thermal resistances in between the considered temperature node $T_{i,j}$ and all neighbour nodes (Fig.4.22) where (i) is the number of nodes in horizontal direction and (j) in vertical direction [32].

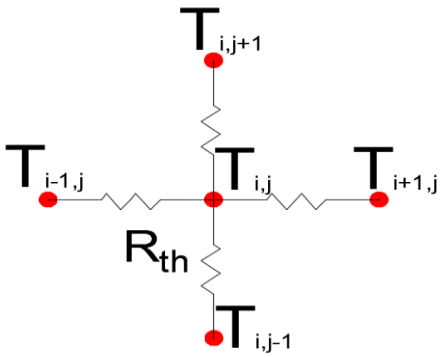

Fig.4.22 2D /RC scheme

Accordingly to form the 2D mesh with respect to the 15 nodes (i's) representing heat transfer in x-direction described previously in the 1D model and by discretizing the façade into number of (j) in y-direction, the obtained set of linear Equations $= i \times j$, i.e. (Fig.4.23) .

In the developed model PV/PCM , the conduction heat transfer is only along x direction as illustrated in (Fig.4.24) the PV/PCM façade integration mesh scheme. However the vertical interaction is happening through façade cavity air nodes to take into consideration the stratification effect.

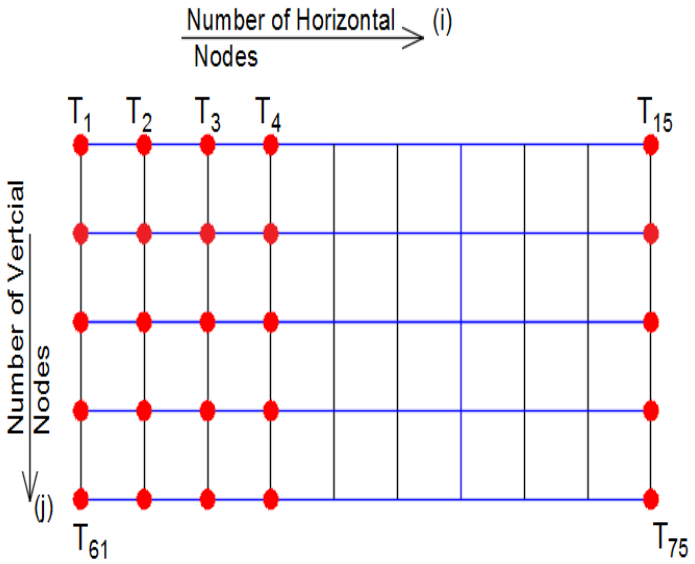

Fig.4.23 2D node scheme

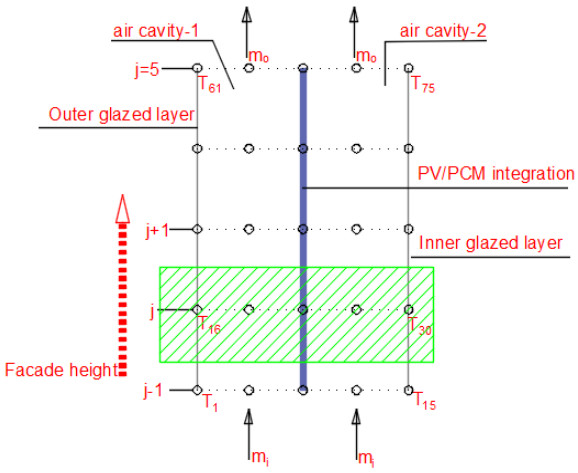

Fig.4.24 PV/PCM façade subdivision

Heat balance Equations for the 2D- PV/PCM mode

The PV/PCM facade is discretized into (j) volumes, (Fig.4.25) and in each volume the glazing elements, PV module, PCM layer are linked through resistance network .The surfaces of each volume simultaneously exchange heat by conduction through the glass, by convection with the air layer in the cavity and by infrared radiation with other surfaces. Inside each cavity the infrared heat exchange between surfaces is supposed to take place within the j^{th} volume only.

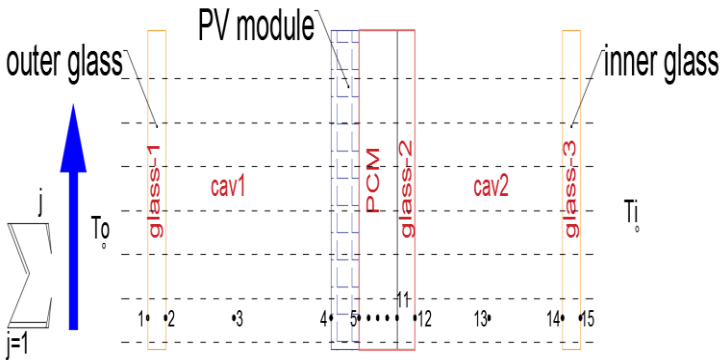

Fig.4.25 PV/PCM façade 2D scheme

For outer and inner glass elements g1 and g3 outer and inner surface nodes respectively, the surface node heat balance is related mainly to convection heat transfer $(q_{conv})_{\tau(j)}$through ambient or boundary conditions and conduction $(q_k)_{\tau(j)}$through the element itself, the energy balance for outer glass element nodes is as follows in Equation (4.43) to (4.45), (similar energy balance for inner glass element could be considered):

$$(q_k)_{\tau(j)} + (q_{conv})_{\tau(j)} = (q_{A,i})_{\tau(j)} \quad \textbf{(4.43)}$$

$$(q_k)_{\tau(j)} = \frac{K}{x_{g1}} . A_{(j)} . (T_{1(g1)} - T_{2(g1)})_{(j)} \quad \textbf{(4.44)}$$

$$(q_C)_{\tau(j)} = h_{co} \, . \, A_{(j)} \, . (T_o - T_{1(g1)})_{(j)} \quad \textbf{(4.45)}$$

Where:

The CHTC values whether in outer conditions $(h_{Co})_\tau$ or $(h_{Ci})_\tau$ has been clarified before in chapter (2).

For glazed (g1, g2, g3) and PV module, elements which are adjacent to the air cavities. The node heat balance has considered the conduction through the element$(q_k)_{\tau(j)}$, the convection $(q_c)_{\tau(j)}$ and the infrared radiation $(q_R)_{\tau(j)}$ with opposed element Equation (4.46):

$$(q_k)_{\tau(j)} + (q_c)_{\tau(j)} + (q_R)_{\tau(j)} = (q_{A,i})_{\tau(j)} \quad \textbf{(4.46)}$$

Considering the inner surface node 2 of the g1 glazed element (the other surface similar nodes balances can be written as the following set of Equations (4.47) to (4.50):

$$(q_k)_{\tau(j)} = \frac{K}{x_{g1}}.A_{(j)}.(T_{1(g1)} - T_{2(g1)})_{(j)} \quad \textbf{(4.47)}$$

$$(q_C)_{\tau(j)} = h_C.A_{(j)}.(T_3 - T_{2(g1)})_{(j)} \quad \textbf{(4.48)}$$

$$(q_R)_{\tau(j)} = A_{(j)}.\frac{4.\sigma.{T_{avg}}^3}{\left[\frac{1}{\epsilon_{(i+1)}}+\frac{1}{\epsilon_{2(i)}}-1\right]}.(T_{4(PV)} - T_{2(g1)})_{(j)} \quad \textbf{(4.49)}$$

$$A_{(j)}.\frac{4.\sigma.{T_m}^3}{\left[\frac{1}{\epsilon_{(i+1)}}+\frac{1}{\epsilon_{2(i)}}-1\right]}.(T_{4(PV)} - T_{2(g1)})_{(j)} + \frac{K}{x_{g1}}.A_{(j)}.(T_{1(g1)} - T_{2(g1)})_{(j)} + h_C.A_{(j)}.(T_a - T_{2(g1)})_{(j)} = A_{(j)}.\frac{I_{sol(i,j)}}{2} \quad \textbf{(4.50)}$$

Taking into consideration that T_{avg} is the average temperature of opposed surfaces Equation (4.51) . It was evaluated in the code as a variable for each time step (τ) and accordingly variable also for each iteration cycle where:

$$T_{avg(\tau,j)} = \left(\frac{{T^{n-1}}_{4(PV)} + {T^{n-1}}_{2(g1)}}{2}\right) \quad \textbf{(4.51)}$$

${T^{n-1}}_{4(PV)}$ is the nodal surface temperature of PV at the previous iteration.

PCM energy balance

For each (j) the PCM layer is discretised into five homogenous layers. The energy balance Equation for each node based on the enthalpy method is as explained before in section (4.3.2) and as follows:

$$\frac{K_p}{xp}(T_{i-1,j}) - (\frac{K_p}{xp} + \rho\, C^A){T_{i,j}}^n + \frac{K_p}{xp}(T_{i+1,j}) = \rho\, C^A {T_{i,j}}^{n-1} - \rho \cdot \frac{v}{\tau}\left[{H_{P(i,j)}}^{\circ} - {H_{P(i,j)}}^{n-1}\right] \quad \textbf{(4.52)}$$

Air nodes balance considers the convective heat transfer on the face 2 of the glass element (g1) $(q_{c1})_\tau$, convective heat transfer of PV modules (node 4) on face 1 $(q_{c2})_\tau$, the heat transfer caused by the ventilation $(q_v)_\tau$ and the change of internal energy $\left(\frac{\Delta U_a}{\Delta \tau}\right)$ associated to the air volume V_a(j). The following Equation can be written at the time step τ:

$$(q_{c1})_{\tau(j)} + (q_{c2})_{\tau(j)} + (q_v)_{\tau(j)} = \frac{\Delta U_a}{\Delta\tau}_{(j)} \quad \textbf{(4.53)}$$

Where

$$(q_{C1})_{\tau(j)} = h_a . A_{(j)} . (T_{2(g1)} - T_3)_{(j)} \quad \textbf{(4.54)}$$

$$(q_{C2})_{\tau(j)} = h_a . A_{(j)} . (T_{4(PV)} - T_3)_{(j)} \quad \textbf{(4.55)}$$

$$(q_v)_{\tau(j)} = \dot{m}_a . c_{pa} . (T_{3(j-1)} - T_{3(j)}) \quad \textbf{(4.56)}$$

$$\frac{\Delta U_{a(j)}}{\Delta\tau} = V_{a(j)} . \rho_a . c_{va} . \frac{\left((T_{3(j)})_\tau - (T_{3(j)})_{\tau-1}\right)}{\tau} \quad \textbf{(4.57)}$$

The linear system is solved by inverting the matrix.

4. Nomenclature-Chapter 4

A	Cross sectional area (m^2)
A_{pv}	PV module cross sectional area (m^2)
$Abs(i)$	Absorbed solar radiation in glass layer (i) (W/m^2)
a	Solar absorption coefficient (-)
a-si	Amorphous silicon
C	Specific heat capacity ($J\ kg^{-1}\ K^{-1}$)
C^*	Equivalent specific heat capacity ($J\ kg^{-1}\ K^{-1}$)
d	Optical thickness (-)
hc	Convection heat transfer coefficient ($W\ m^{-2}\ K^{-1}$)
h	Specific enthalpy of fusion ($kJ\ kg^{-1}$)
h_o	Outside convection heat transfer coefficient ($W\ m^{-2}\ K^{-1}$)
h_i	Inside convection heat transfer coefficient ($W\ m^{-2}\ K^{-1}$)
H	Height of the façade (m)
IL	Internal loads (W)
I	Impinged solar radiation (W/m^2)
I_{sc}	Short circuit current (A)
K	Thermal conductivity coefficient ($W\ m^{-1}\ K^{-1}$)
L	Length of the plate (m)
Nu	Nusselt number (-)
Pr	Prandtl number (-)
P	Power (W)
Q	Thermal loads (W)
r_n	Reflectivity of surface n (-)
Re	Reynolds number (-)
Ra	Rayleigh number (-)
R_C	Specific convection thermal resistance ($m^2\ K\ W^{-1}$)
R_K	Specific conduction thermal resistance ($m^2\ K\ W^{-1}$)
R_{rad}	Specific radiation thermal resistance ($m^2\ K\ W^{-1}$)
S	Physical thickness (m)
T	Temperature (˚C)

V	Air velocity (m s^{-1})
V_{oc}	Open circuit voltage (V)
x	Layer thickness (m)
Greek symbols	
β	Liquid fraction (-)
δ	Overall fractional change in transmittance (-)
ΔT_h	Temperature range of phase change (˚C)
ΔP	Specific power (10^{-1} W/m^2)
ε	Emissivity (-)
η_{PVm}	PV module efficiency (-)
η_r	PV module reference efficiency (-)
μ	Dynamic viscosity (kg m^{-1} s^{-1})
ν	Wind velocity (m s^{-1})
ρ	Air density (kg m^{-3})
σ	Stefan-Boltzmann constant, 5.67 x 10^{-8} (W m^{-2} K^{-4})
$\sigma_{\varepsilon,l}$	Extinction coefficient, liquid phase (m^{-1})
$\sigma_{\varepsilon,s}$	Extinction coefficient, solid phase (m^{-1})
τ_r	Transmission coefficient (-)
τ ·	Time step (s)
ψ	Temperature coefficient of PV module (°C $\%^{-1}$)
subscripts	
c_1	Air cavity 1
c_2	Air cavity 2
g_n	Glass layer number
i	Indoor
l	Liquid state
m	Melting peak
o	Outdoor
P	PCM node
PVm	PV module
r	Reference
s	Solid state

superscripts

°	Previous time step
*	Equivalent

Abbreviations

ASTF	Active Solar Thermal Façade
BIPV	Building Integrated Photovoltaics
DGU	Double Glazed Unit
DSF	Double Skin Façade
HVAC	Heating, Ventilation and Air Conditioning
LHTES	Latent Heat Thermal Energy Storage
PCM	Phase Change Material
PV	Photovoltaics
TES	Thermal Energy Storage

4. References –Chapter 4

1. H. Mehling, L.F. Cabeza, 2008. Heat and Cold Storage with PCM: An Up to Date Introduction into Basics and Applications, Springer, Berlin.
2. D. David, F. Kuznik, J.J. Roux, Numerical study of the influence of the convective heat transfer on the dynamical behavior of a phase change material wall, Applied thermal Engineering 31 (2011),pp.3117-3124.
3. N. Soares, J.J. Costa, A.R. Gaspar, P. Santos, Review of passive PCM latent heat thermal energy storage systems towards buildings' energy efficiency, Energy and Buildings 59 (2013), pp.82–103.
4. Y. Cui, J. C Xie , S. Pan, L. Jiaping, Review of PCM integrated in buildings wall for energy savings, Procedia Engineering, 12 (2015), pp. 763–770.
5. F. Goia, M. Perino, V. Serra, Improving thermal comfort conditions by means of PCM glazing systems, Energy and Buildings 60 (2013), pp. 442–452.
6. F. Goia, M.Perino, V. Serra, Experimental analysis of the energy performance of a full-scale PCM glazing prototype, Solar Energy 100 (2014), pp. 217–233.
7. H. Weinlader, A.Beck, J. Fricke, PCM-façade-panel for daylighting and room heating, Solar Energy 78 (2005), pp. 177–186.
8. P.D.Silva, L.C. Goncalves, L. Pires, Transient behaviour of a latent-heat thermal energy store: numerical and experimental studies, Applied Energy 73 (2002), pp. 83–98.
9. F.Kuznik, J.Virgone, Experimental investigation of wallboard containing phase change material: data for validation of numerical modeling. Energy and Buildings 41(2009),pp. 561–570.
10. C. Liu, Y. Zhou, D. Li, F. Meng, Y. Zheng, X. Liu,Numerical analysis on thermal performance of a PCM-filled double glazing roof, Energy and Buildings 125(2016)), pp. 267–275.
11. V.R.Voller, 1996. An overview of numerical methods for solving phase-change, Advances in Numerical Heat Transfer 1, Chapter 9, Taylor & Francis, London
12. Swaminathan, C.R. & Voller, V.R. MTB (1992) 23: 651. doi:10.1007/BF02649725.
13. F. Goia, M. Zinzi, E. Carnielo, V. Serra, Spectral and angular solar properties of a PCM-filled double glazing unit, Energy and Buildings 87 (2015), pp. 302–312.
14. B.L. Gowreesunkera, S.B. Stankovicb, S.A. Tassoua, P.A. Kyriacou, Experimental and numerical investigations of the optical and thermal aspects of a PCM-glazed unit, Energy and Buildings 61 (2013), pp. 239–249.

15. R. Siegel, 1973, Net radiation method for enclosure systems involving partially transparent walls, NASA technical note, NASA TN D-7384.
16. F. Goia, M. Perino M. Haaseb, A numerical model to evaluate the thermal behavior of PCM glazing system configurations, Energy and Buildings 54 (2012), pp. 141–153.
17. www.rubitherm.com (Access: 04/2016).
18. P. Batagiannis, C. Gibbons, Thermal assessment of silicon based composite materials used in photovoltaics, Proceedings of Renewable Energy in Maritime Island Climates Conference, Belfast, September, UK (2001), pp. 151–157.
19. G. Ciulla,V. Lo Brano, M. Cellura, V. Franzitta, D.Milone, A finite difference model of a PV-PCM system, Energy Procedia 30 (2012), pp. 198 – 206.
20. L. Aelenei, R. Pereira, H. Gonçalves, A. Athienitis, Thermal Performance of a Hybrid BIPV-PCM: Modeling, Design and Experimental Investigation, Energy Procedia 48(2014), pp.474-483.
21. Hasan, S. J. McCormack , M. J. Huang , B. Norton, Energy and Cost Saving of a Photovoltaic-Phase Change Materials (PV-PCM) System through Temperature Regulation and Performance Enhancement of Photovoltaics, Energies 7(2014),pp. 1318-1331.
22. ASHRAE Handbook. Heating, Vent. Air Cond. Fund. SI edition, 2001.
23. S. Klein, W. Beckman, J. Mitchell, J. Duffie, N. Duffie, T. Freeman et al., TRNSYS 16 - A transient system simulation program, User manual, University of Wisconsin, Madison, US,
24. M. Kottek, J. Grieser, C. Beck, B. Rudolf, F. Rubel, World Map of the Köppen-Geiger climate classification updated, Meteorol. Z 15 (2006), pp. 259-263.
25. ASHRAE standard 55-2004.thermal environment conditions for human occupancy, American Society of Heating, Air-Conditioning and Refrigeration Engineers, Inc.
26. www.rehva.eu/publications-and-resources/rehva-journal/2012/022012/nzeb-office-building-ympaeristoetalo-in-helsinki-finland.html (Access: 04/2016).
27. www.estidama.org, Abu Dhabi urban planning council (Access: 10/2016).
28. F. Goia , Search for the optimal window-to-wall ratio in office buildings in different European climates and the implications on total energy saving potential**,** Solar Energy 132 (2016)**,** pp. 467–492**.**
29. D.L. Evans, Simplified method for predicting photovoltaic array output, Solar Energy 27(1981), pp. 555-60.
30. MATLAB 6.1, The MathWorks Inc., Natick, MA, 2000.
31. Heat conduction in two and three dimensions Computer Modelling of Building Physics Applications Thomas Blomberg, Lund University.

Chapter-5

Investigation of different roof attic construction technologies. Experimental and Numerical study

5.1 Introduction

In this chapter different technologies applied on opaque envelopes have been analysed numerically and experimentally. The evaluation clarified the influence of the phase change materials (PCM) proper selection and the reflective surfaces implementation through five different parallel samples in a residential roof attic space under summer climatic conditions in Italy. The first sample A is considered as a reference case without integrating either the two technologies. Samples B and C integrated with reflective surfaces differently in order to compromise the applied location in respect to long wave radiation. While in samples D and E, two PCM's typologies with different melting temperatures were implemented. A numerical model was developed and validated for each sample to expand the results. Phase transition modelling was derived based on the equivalent capacitance method. An overall analysis of the measured data concluded that it is vital to synchronize PCM/building thermal performance. This could be reached by carrying out an extensive numerical thermal evaluation before selecting the proper PCM type and it is better to allow a passive cooling methodology for the PCM module to assure the efficiency of charge /discharge process.

Objectives

a- Evaluate the thermal improvements due to PCM integration in summer season;
b- Highlight the importance of the proper PCM type selection;
c- Optimize the reflective surface/paint locations within roof surface.

5.2 Opaque building envelopes technologies background

Building retrofitting concept is not only about improving the overall energy performance and sustainability due to building's structural, thermal and electrical systems refurbishment but also to transform all unused areas such as roof attic into livable spaces. In which improves the density of urban areas without consuming new soil. For this reason in Italy, several policies at regional level have promoted this kind of conversions [1].

A key issue in such conversions is the structural configuration energetic retrofitting of the roof component, because it represents the largest exposed area to the outdoor environment, accordingly the highest thermal load gains and losses through summer and winter seasons respectively.

The integrated energy refurbishment technologies i.e. (insulation, high specifics capacity layers etc.) of the existing roof components are limited to not compromise:

- The height of the internal zone (otherwise the living space is reduced);
- The existing roof structure (to avoid additional intervention);

Different technologies can overcome these two limitations and assuring the reduction of the insulation thickness and weight in order to reduce the heat gain/losses through the roof:

- Super insulating materials allow high insulation value in very thin layers [2,3,4]
- Radiant heat barriers allow to reduce the radiation heat exchange in air gaps [5]
- Integrating ventilated air cavity contribute on removing the summer heat via convection [6,7,8]
- Enhancing the solar reflectance properties of the outer layer reducing the solar heat loads [9,10,11]

On the other hand implementation of thermal storage system TES through phase changing materials PCM is a promising option concerning the optimization of buildings energy performance. PCM integration in buildings generally can be classified both as passive and active system [12]. Different locations of PCM are possible: it could be incorporated to walls, roof, windows, thermal insulation materials and furniture [13]. Kuzniket al. [14] investigated a renovation project in the south of Lyon-France using PCM wallboards. By testing a room in the same building that was renovated without PCM and then comparing it to the room with PCM, they concluded that the PCM increased the indoor thermal comfort, but it appeared unable to use its latent heat storage capacity for a number of durations due to the incomplete discharge overnight. Xu et al. [15] investigated the thermal performance of PCM floor system in passive solar buildings. This performance is affected by several factors such as the choice of covering material, thickness of PCM layer, PCM melting temperature, its thermal conductivity and heat of fusion, and the air gap between the PCM and covering material. The results showed that the thickness of PCM should not be greater than 20 mm and the heat of fusion and thermal conductivity of PCM should respectively exceed 120 kJ/ kg and 0.5 W/(m K). Kong et al[16] have investigated thermal energy savings through PCM implementation in roof component and it reached 40%.

5.3 The Five cases descriptions

Five different configurations were considered in the study. Sample-A, which is the reference case (Fig.5.1), consists of three layers (roof tiles, XPS and gypsum board). The adjacent compartments are Sample B and C with the same order, dimensions and technical specifications of Sample A

layers. However the concept of low emissivity reflective surface location has been analysed through sample B in which reflective aluminium foil has covered the XPS layer, and in sample C and reflective paint has implemented on the inner side of the roof tiles.

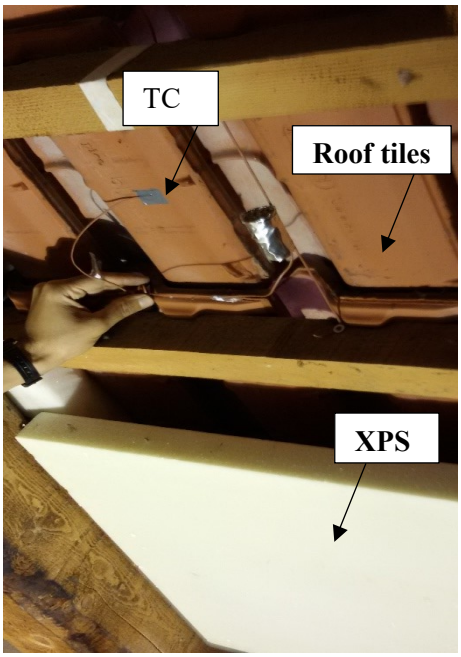

(a) Sample A

(b) Sample B

(c) Sample C

Fig.5.1 Roof configurations

In order to analyse the influence of the PCM integration in building components and to comprehend the thermal trends of this technology two different PCM types were considered to be monitored. Whilst the PCM is contained in a hollow polycarbonate panels [17]. Sample D and E respectively filled with RT28 and RT35 [18] and were installed between the gypsum board and the XPS layers, (Fig.5.2). Taking into consideration that apart of implementing PCM layers and reflective surfaces,

the overall composition of all samples i.e. (Roof tiles, air cavity thickness, XPS layer and Gypsum board) are all the same. Technical specifications of roof sections are summarized in Table (5.1).

(a) **(b)**

Fig.5.2 Samples D&E, (a) PCM polycarbonate layer, (b) PCM filled panel installation

Table (5.1) Roof section: material properties layer 02 is included only in samples Band C, layer 05 is included only in samples D and E, *, data retrieved from [5].

Layer	Material	s (mm)	ρ (kg/m^3)	λ (W/mK)	cp (J/kgK)	α (-)
01	Brick tiles	30	1700	0.7	840	0.55*
02	Aluminium coating					
03	air gap	70	1.2	N.A.	1020	N.A.
04	XPS	50	32	0.034	1500	N.A.
05 (sample D and E)	PCM	10	800	0.14	2000	N.A.
06	gypsum board	9.5	800	0.2	1000	N.A.

5.4 Methodology

The monitored roof sections have south south-west orientation with a slope of 28°. During the monitoring period the indoor space (floor area ~ 110 m^2) was in free-floating regime with high ventilation rate. The air exchanges were guaranteed by:

- The infiltration through the roof tiles;

- The presence of a window opening (~1.25 m^2 of opening area).

5.4.1 Experimental methodology

The outdoor boundary conditions (air temperature, relative humidity and wind speed and direction) were continuously monitored with a time step of 5 minutes by means of a weather station installed 1.5 m above the roof-top (Fig.5.3a). Moreover, a second-class pyranometer LP02 (calibration uncertainty ≤ 1.8%) was installed for the measurement of the incident global solar radiation (Fig.5.3b).

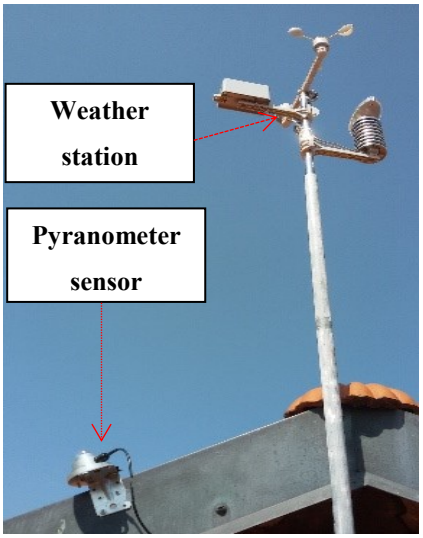

(a) Weather station and pyranometer sensor

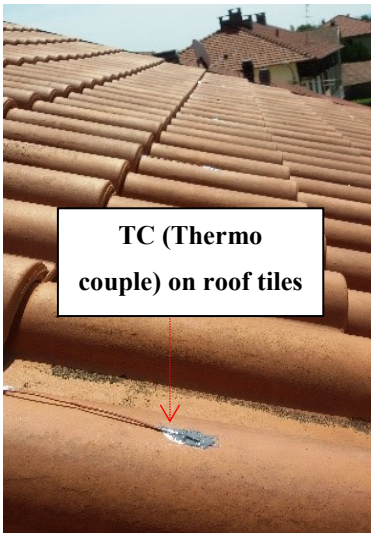

(b) Thermocouples installed above the roof tiles

Fig.5.3 Experimental Instruments

Temperatures across the roof sections were measured by means of type-T thermocouples (nominal accuracy ± 0.25K). Moreover, the heat fluxes were measured by means of HFP01 heat flux sensors (measurement uncertainty ± 5%) placed in the indoor side (0).

Fig.5.4 Overall view of the 5 samples, From left to right, Sample A, B and C with heat flux sensors and thermocouples placed in the indoor side

In order to avoid the influence of the radiation heat exchange between the roof and the indoor surrounding surfaces (floor, walls), the indoor roof surfaces were covered with a reflective aluminium shine foil. The measurements were carried out with a time interval of 5 min (according to the measurement of the weather conditions) using a data logger DT600 with channel expansion module. The roof clay tiles are characterised by high air permeability, because the joints of the tiles allow air exchanges between the cavity and the outside. For this reason, a characterization of the infiltration rate in the cavity below the roof tiles was carried out by means of the gas-tracer method. To this purpose, a small scale sealed room was built under the roof portion without insulation samples (0). The measurement were repeated several times during the monitoring days and an average infiltration rate ~3.3 $(m^3/h)/m^2$ was estimated. It is important to remark that this infiltration rate value is strictly dependent by the wind speed, the measurements were carried out whit slow wind speed ($v < 7$ km/h) in line whit the average statistically values reported in the Italian Climatic data collection “Gianni De Giorgio” (IGDG – ITA_Torino-Caselle 45.10N 7.39E).

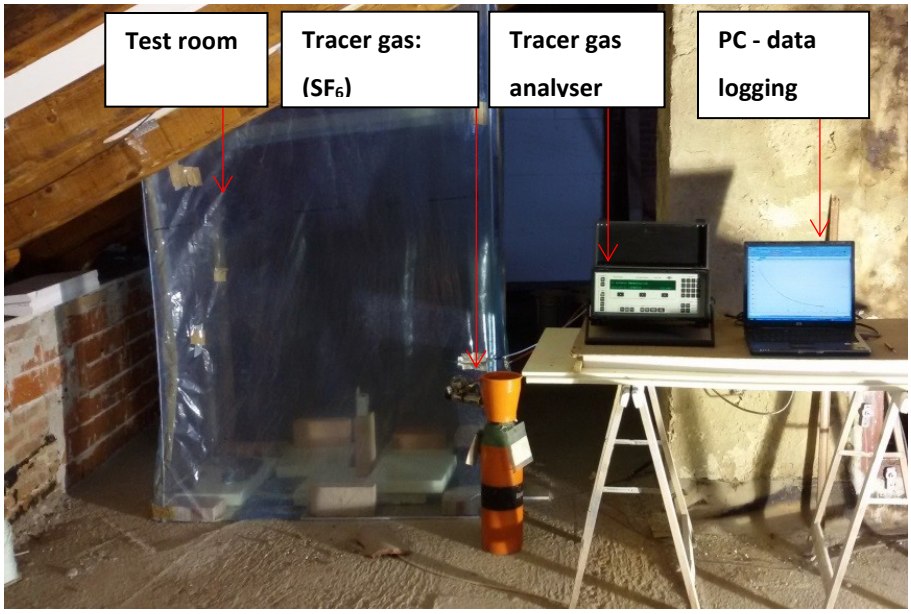

Fig.5.5 Tracer gas technique used for the determination of the air infiltartion rate under the roof tiles

5.4.2 Numerical modelling

a- PCM thermal numerical simulation

There are several methods to take into account the transient physical state of PCM, such as enthalpy method or the equivalent heat capacity method which was implemented in the present study. The technique has been explained in section (4.3.1). The linear approximation of the heat flux between PCM nodes was assumed. The numerical grid was numerically solved using the implicit fixed scheme that employs linearization, initial conditions and adopts an iterative procedure until convergence is obtained [19].

b- RC models

Finite difference method is implemented to describe numerically each of the five cases under study. The solution domain is defined by number of grid points in which the derived linear equations form a matrix system. The system is solved by inverting the matrix to obtain the temperature values. For each sample a resistance capacitance RC model was developed, for more details (refer to section 2.2.2). Taking into consideration that roof tiles and gypsum board were represented in the **(1-D)** model by two conductive resistances and a capacitance.

Model A

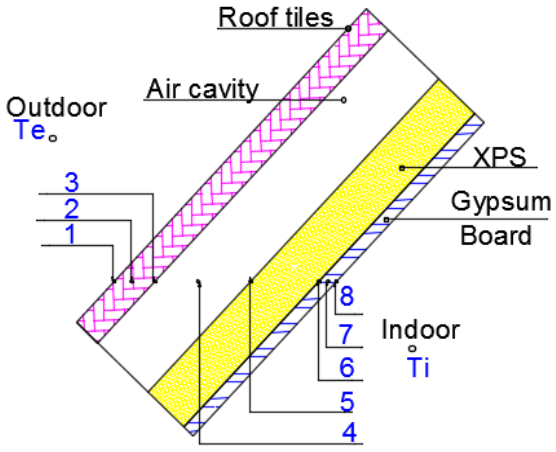

(a)

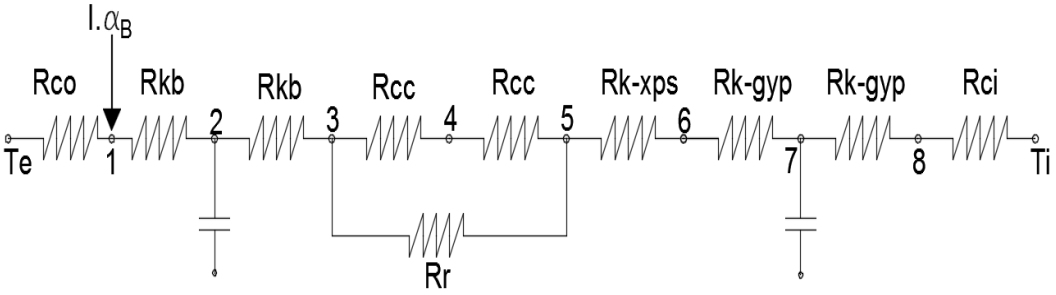

(b)

Fig.5.6 (Model –A), (a) Scheme, (b) RC model

Model A is considered as the comparison reference case. The specific heat capacity of the roof tiles and gypsum board are considerably higher than the XPS layer, hence each layer is represented in the RC scheme (Fig.5.6) by two conductance resistances and a capacitance. The mathematical equations for the 8 nodes are classified below based on similarity:

Node (1) and Node (8)

The heat transfer through the outer and inner layers of the roof surface is described by two thermal resistances, the convection heat transfer with the ambient conditions and the conduction transfer within the layer itself.

$$T_1\left(-\frac{1}{R_{co}}-\frac{1}{R_{kB}}\right)+T_2\left(\frac{1}{R_{kB}}\right)=-\frac{1}{R_{co}}T_e-I.\alpha_B \tag{5.1}$$

$$T_8\left(-\frac{1}{R_{ci}}-\frac{1}{R_{k-gyp}}\right)+T_7\left(\frac{1}{R_{k-gyp}}\right)=-\frac{1}{R_{ci}}T_i \tag{5.2}$$

Node (2) and Node (7)

The energy balance of nodes 2 and 7 included the thermal storage influence and nodal temperature changes with the time. Taking into consideration that T_n° is the node temperature evaluated at the previous time step.

$$T_1\left(\frac{1}{R_{kB}}\right)+T_2\left(\frac{-2}{R_{kB}}-\frac{\rho\,\Delta x_{br}\,C_{br}}{\Delta\tau}\right)+\,T_3\left(\frac{1}{R_{kB}}\right)=-\frac{\rho\,\Delta x_{br}\,C_{br}}{\Delta\tau}T_2^{\circ} \tag{5.3}$$

$$T_6\left(\frac{1}{R_{k-gyp}}\right)+T_7\left(\frac{-2}{R_{kgyp}}-\frac{\rho\,\Delta x_{gyp}\,C_{gyp}}{\Delta\tau}\right)+\,T_8\left(\frac{1}{R_{k-gyp}}\right)=-\frac{\rho\,\Delta x_{gyp}\,C_{gyp}}{\Delta\tau}T_7^{\circ} \tag{5.4}$$

Node (3) and Node (5)

The radiation heat exchange coefficient h_r between nodes 3 and 5 is considered as a function in nodal temperatures Equation (1.21). The average temperature of the two opposed surface is evaluated in the previous time step.

$$T_{avg}=\frac{T_3^{\circ}+T_5^{\circ}}{2}$$

The convection heat transfer within the air cavity and the conduction heat transfer through the element are showed in the energy balance Equations (5.5 and 5.6).

$$T_2\left(\frac{1}{R_{kB}}\right)+T_3\left(\frac{-1}{R_{kB}}-\frac{1}{R_c}-\frac{1}{R_r}\right)+\,T_4\left(\frac{1}{R_c}\right)+T_5\left(\frac{1}{R_r}\right)=0 \tag{5.5}$$

$$T_3\left(\frac{1}{R_r}\right)+T_4\left(\frac{1}{R_c}\right)+T_5\left(\frac{-1}{R_{k-xps}}-\frac{1}{R_c}-\frac{1}{R_r}\right)+\,T_6\left(\frac{1}{R_{k-xps}}\right)=0 \tag{5.6}$$

Node (4)

While the infiltration airflow rate m_v estimated by the experimental measurements. Accordingly the air cavity node energy balance is:

$$T_3\left(\frac{1}{R_c}\right)+T_4\left(-\frac{2}{R_c}-m_vC\right)+\,T_5\left(\frac{1}{R_c}\right)=-m_vC\,T_v \tag{5.7}$$

Node (6)

The energy balance of the interaction node between two layers of the XPs and gypsum board is:

$$T_5\left(\frac{1}{R_{k-xps}}\right)+T_6\left(\frac{-1}{R_{k-xps}}-\frac{1}{R_{k-gyp}}\right)+\,T_7\left(\frac{1}{R_{k-gyp}}\right)=0 \tag{5.8}$$

Models B and C

The mathematical set of equations describing models B and C (Fig.5.7) are the same as model A apart of the location of the low emissivity layer used to control the radiation heat exchange which has been taken into consideration Through nodes 3 and 5. In model- B $\varepsilon_5 = 0.05$, while in model-C $\varepsilon_3 = 0.05$. The radiation heat exchange coefficient h_r between nodes 3 and 5 is considered as a function in the nodal temperatures values of the previous time step.

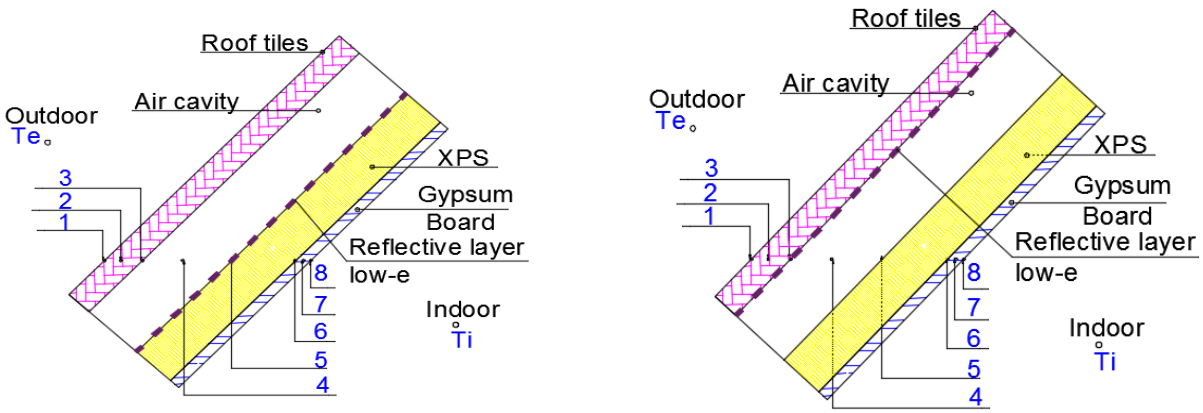

(a) **(b)**

Fig.5.7 Samples Scheme, (a) Sample B, (b) Sample C

Model D &E and PCM analysis

The mathematical description of cases D and E clarified in (Fig.5.8) is similar for case A, apart of the PCM layer analysis. One of the study focal points is to investigate the influence of PCM melting/solidification range on the overall energy balance Equation (5.9).

The 1 cm thickness PCM layer is discretised into three homogenous nodes, therefore the energy balance equation of each PCM node is:

$$\rho_p \, C_p^{*}(T) \, \frac{T_P - T_P^{\circ}}{\Delta \tau} = \frac{K_p}{\Delta x} \, (T_{P-1} - T_P) + \frac{K_P}{\Delta x} \, (T_{P+1} - T_P) \qquad (5.9)$$

Whilst two PCM have been considered, RT-28 HC and RT- 35.The technical specifications are listed in (Table 5.2).

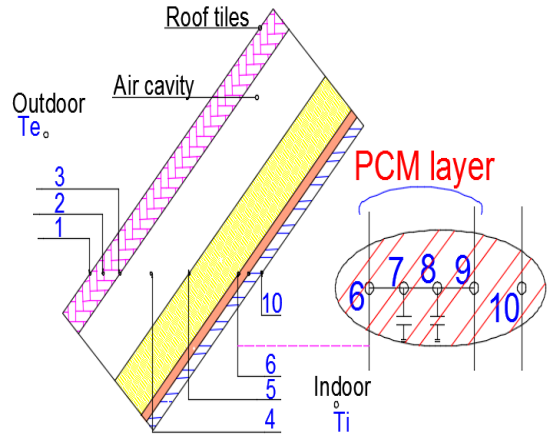

(a)

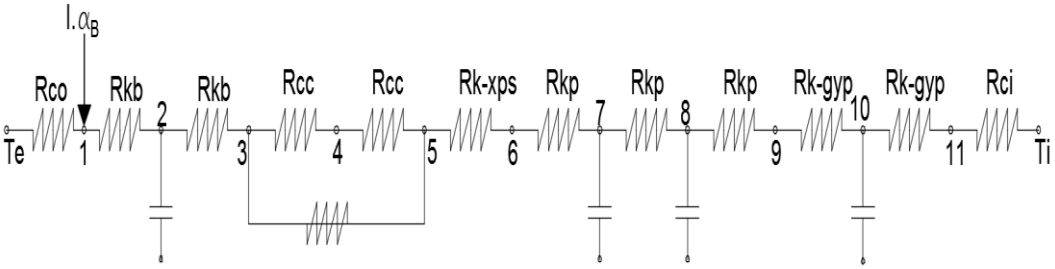

(b)

Fig.5.8 (Model –D&E), (a) Scheme, (b) RC model

Table 5.2 PCM physical properties [18]

PCM name	**RT28**	**RT35**
Solid temperature (lower limit of phase change range)	27˚C	34˚C
Nominal melting temperature	28˚C	35˚C
Liquid temperature (upper limit of phase change range)	29˚C	36˚C
Specific heat Capacity [kJ kg^{-1} K^{-1}]	2	2
Latent heat of fusion [kJ kg^{-1}]	250	160

5.4.3 Models validation

The numerical model's validation has been carried out but comparing the experimental measurements of surface temperatures with the calculated values. It is important to highlight that indoor zone is not thermally controlled, windows are kept open day and night .As clarified in Figures (Fig.5.10 and Fig.5.10) a clear consistent is shown for the indoor and outdoor surface temperature profiles. The RMSE have been estimated for both the indoor and outdoor surfaces. The Root Mean Square Error (RMSE [°C]) calculated according to Eq. (5.10) were used to identify the model reliability:

$$RMSE = \sqrt{n^{-1} \cdot \sum_{j=1}^{n} (s_j - e_j)^2} \quad (5.10)$$

Where: s_j and e_j are respectively the predicted values and measured values for times j, and n is the number of values of the series. As clarified in (Table 5.3) for each sample.

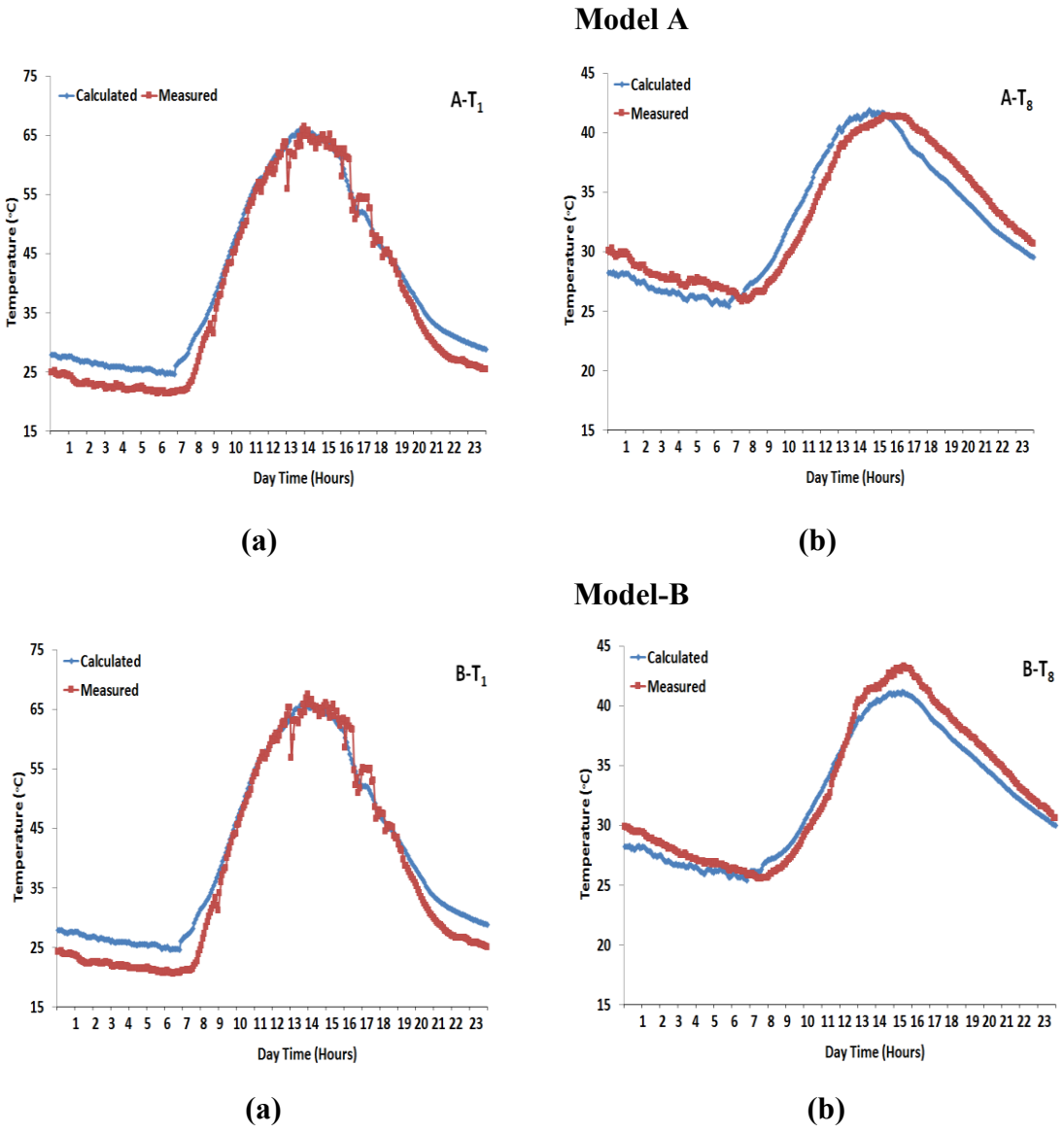

Fig.5.9 Comparison between measured and calculated temperature profiles for all models (A ,B), (a) Outdoor surface layer, (b) Indoor surface layer

Model-C

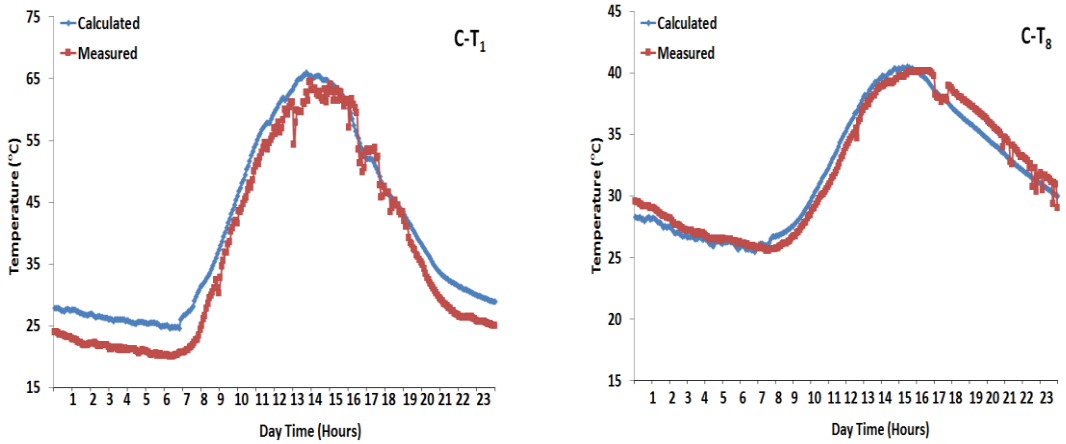

(a) **(b)**

Model-D

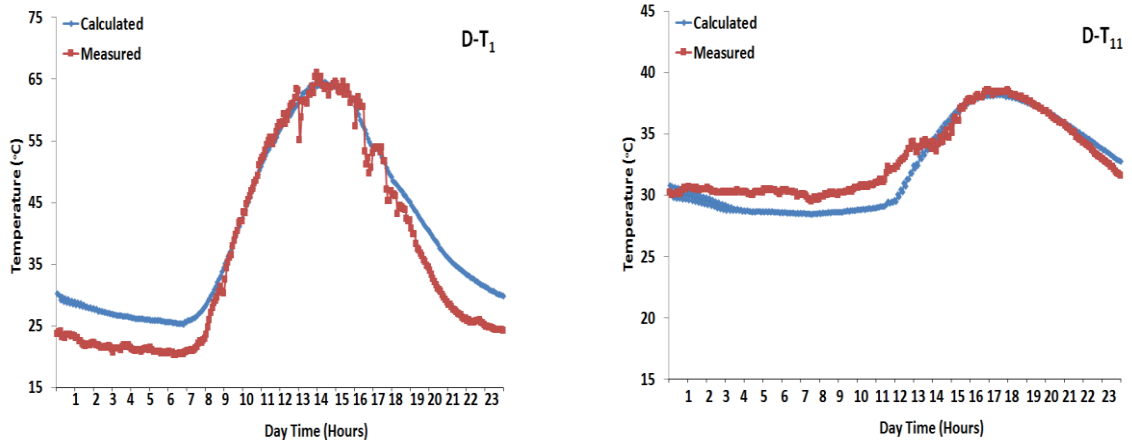

(a) **(b)**

Model-E

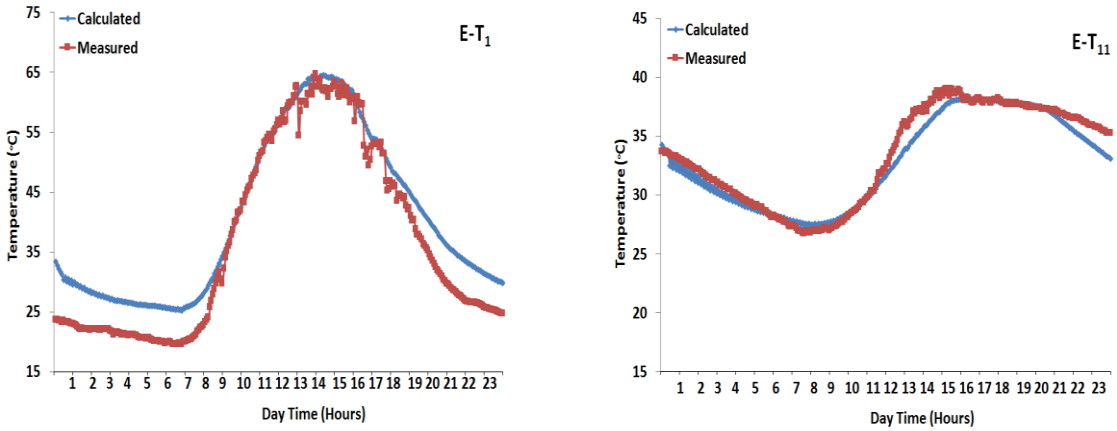

(a) **(b)**

Fig.5.10 Comparison between measured and calculated temperature profiles for all models (C,D,E), (a) Outdoor surface layer, (b) Indoor surface layer

Table (5.3) RMSE Values

RMSE	Sample-A	Sample-B	Sample-C	Sample-D	Sample-E
Indoor	1.5℃	1.2℃	1.6℃	1℃	1.2℃
Outdoor	2.9℃	3.2℃	3.7℃	4℃	3.9℃

5.5 Experimental Data analysis

5.5.1 Overall evaluation

To comprehend the cons, pros and thermal performance for each sample, the hourly convention losses have been evaluated Equation (5.11) for 31-July. The losses are in W/m^2 and expected to occur due to increment in the inner surface temperature taking into consideration that the inner zone is not thermally controlled.

$$q = h_i(T_s - T_i) \qquad (5.11)$$

The hourly inner surface temperature profiles (Fig.5.11), shows that Sample-A is the highest during the peak time range, comes after samples B, C, E and finally D.

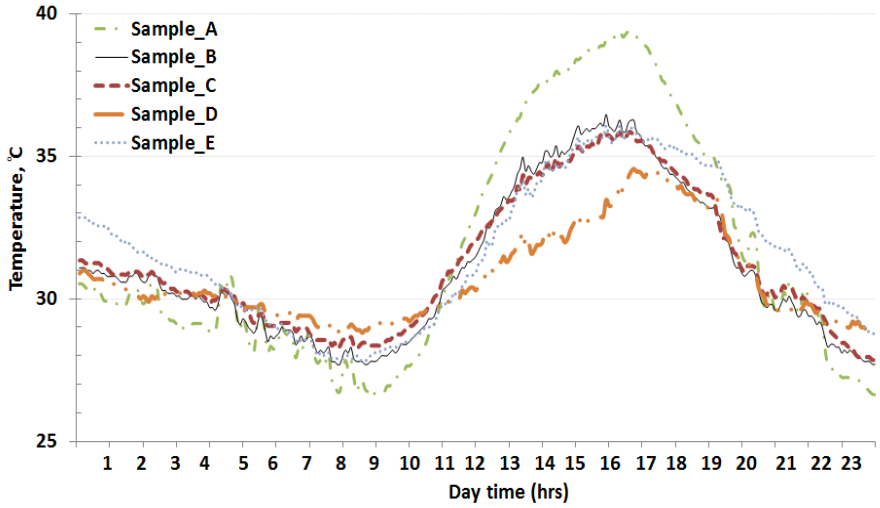

Fig.5.11 Inner surface temperature-31 July

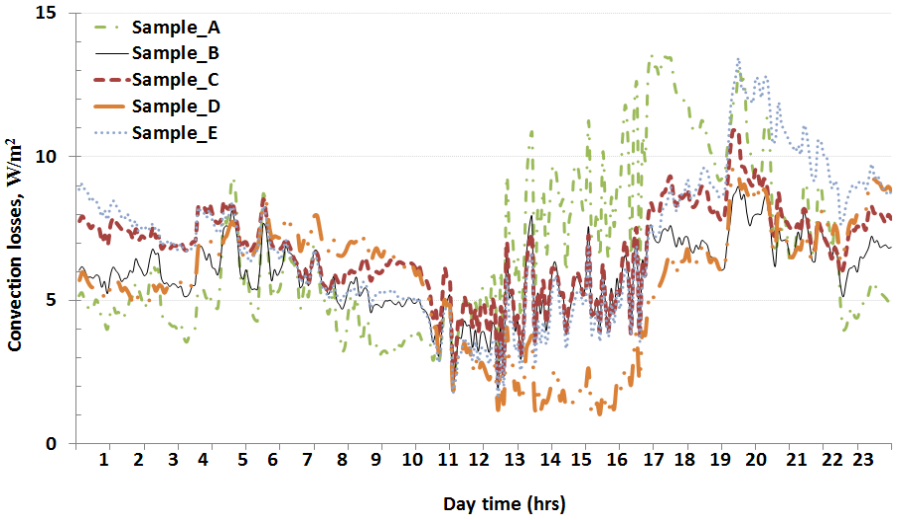

Fig.5.12 Convection Losses -31 July

(Fig.5.12) clarifies the convection losses profiles in all samples ranges between 5 to 9W/m^2 till about 11 am and by the start of solar radiation and external temperature propagation, profiles are separated. Sample A with the higher inner surface temperature precedes the losses followed by B and C.

5.5.2 Analysis of different PCM thermal performance

To highlight the importance of PCM type selection, the temperature profiles of samples D vs. Sample E have been illustrated in (Fig.5.13). Sample D has a flattered inner surface temperature between 27°C and 29°C, which indicates that the substance is in its transition phase with the higher values of equivalent specific heat capacity, until the solar radiation and external temperature propagation starts. The PCM (RT28-HC) temperature has increased slightly however it did not exceed the upper limit of phase change range to totally being transferred into liquid. However in sample E and RT 35. The PCM mostly is under the solid state since the melting starts at 34℃ and accordingly the specific heat capacity is in its minimum value of 2 kJ/kg K. PCM temperature profile is due to the external temperature sinusoidal trend and solar radiation energy flux profile. To conclude PCM-RT28 has been properly synchronized to contain the heat gains and accordingly to improve the thermal behavior.

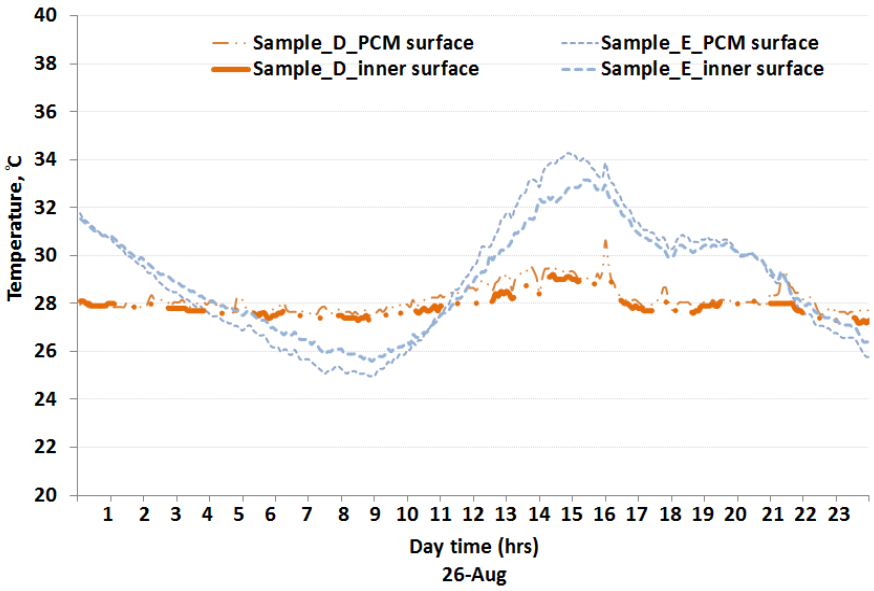

Fig.5.13 Temperature surface comparison between 2 PCM types

5.5.3 Reflective layers location

The location of reflective surface has an influence on the thermal behavior of the building. As shown in (Fig.5.14) sample B with a reflective surface on the XPS layer is causing the increment of inner surface temperature in comparing with sample C which has a reflecting painting on the inner side of the roof tile. These results indicate that it is better to implement the reflective surface technology on the expected higher temperature surface i.e. roof tiles in which the long wave radiation exchange with opposite surface shall be reduced and accordingly the heat transfer to the inside zone.

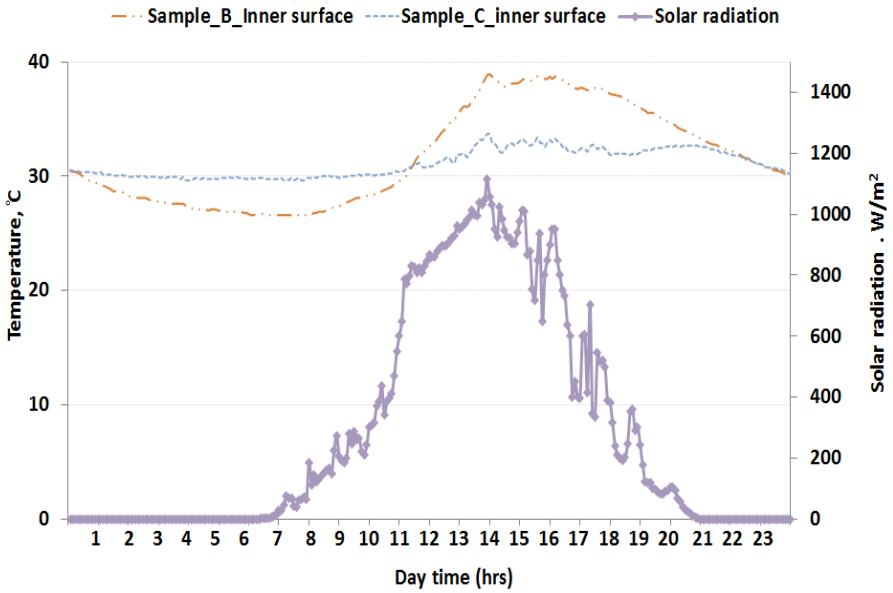

Fig.5.14 Samples B and C inner surface comparison

5.6 Conclusions

The investigated technologies can affect appreciably the building energy performance. Implementing one or two techniques would support reducing cooling loads requirements. The reflective surfaces is reducing the radiation heat exchange; however its location is vital. Integration of PCM is an efficient solution in building components especially if it is implemented in roof, which have the highest solar radiation exposure in respect to other building vertical surfaces. Moreover, the selection of PCM is critical step to assure that the maximum heat transfer is occurring within the PCM transition phase to take advantage of the material specific heat capacity blooming. The proper type selection step is achieved by carrying out a numerical investigation in both with and without PCM cases to comprehend the appropriate working temperature range. It is important to locate the PCM in a way that allows a proper ventilation to ensure an efficient discharge process.

5. Nomenclature-Chapter 5

A	Cross section area	m^2
T	Temperature	˚C
hc	Convection heat transfer coefficient	W m^{-2} K^{-1}
R_C	Specific convection thermal resistance	m^2 K W^{-1}
R_K	Specific conduction thermal resistance	m^2 K W^{-1}
R_{rad}	Specific radiation thermal resistance	m^2 K W^{-1}
Pr	Prandtl number	(-)
C	Specific heat capacity	J kg^{-1} K^{-1}
C^*	Equivalent Specific heat capacity	J kg^{-1} K^{-1}
H	Height of the surface	m
h	Specific enthalpy of fusion	kJ kg^{-1}
h_0	Outside convection heat transfer coefficient	W $m^{-2}K^{-1}$
h_c	Cavity convection heat transfer coefficient	W $m^{-2}K^{-1}$
h_i	Inside convection heat transfer coefficient	W $m^{-2}K^{-1}$
IL	Internal Loads	W
I	Impinged solar radiation	W m^{-2}
K	Thermal conductivity coefficient	W m^{-1} K^{-1}
x	Layer thickness	m

Greek symbols

α	Short wave solar absorption coefficient	(-)
v	Wind velocity	(m/s)
ε	Long wave radiation emissivity	(-)
ρ	Air density	kg/m^3
σ	Stefan-Boltzmann constant, (5.67×10^{-8})	W/(m^2 K^4)
ΔT_h	Temperature range of phase change	˚C
τ ·	Time step	s

Subscripts

s	Solid state
l	Liquid state
h	PCM Melting/solidification temperature range difference

m	Melting peak
P	PCM node
r	Reference
i	Indoor
o	Outdoor

Superscripts

°	Previous time step
*	Equivalent

PCM	Phase Change Material
XPS	Extruded Polystyrene
TES	Thermal Energy Storage
HVAC	Heating Ventilation and Air Conditioning
RMSE	Root Mean Square Error

5. References –Chapter 5

1. Consiglio regionale del Piemonte - Regional law 6th august 2008 n.21, Norme per il recupero del sottotetto a fini abitativi.
2. K.S. Ong, Temperature reduction in attic and ceiling via insulation of several passive roof designs, Energy Conversion and Management, 52-6 (2011), 2405-2411, http://dx.doi.org/10.1016/j.enconman.2010.12.044.
3. A. Lorenzati, S. Fantucci, A. Capozzoli, M. Perino, Coupling VIPs and ABPs: Assessment of Overall Thermal Performance in Building Wall Insulation, Energy Procedia, Volume 78, 2015, Pages 2760-2765, ISSN 1876-6102, http://dx.doi.org/10.1016/j.egypro.2015.11.620.
4. A. Lorenzati, S. Fantucci, A. Capozzoli, M. Perino, Experimental and numerical investigation of thermal bridging effects of jointed Vacuum Insulation Panels, Energy and Buildings, Volume 111, 1 January 2016, Pages 164-175, ISSN 0378-7788, http://dx.doi.org/10.1016/j.enbuild.2015.11.026.
5. A.L. Pisello, E. Fortunati, S. Mattioli, L.F. Cabeza, C. Barreneche, J.M. Kenny, F. Cotana, Innovative cool roofing membrane with integrated phase change materials: Experimental characterization of morphological, thermal and optic-energy behavior, Energy and Buildings, 112 (2016), 40-48. http://dx.doi.org/10.1016/j.enbuild.2015.11.061.
6. F. Isaia, S. Fantucci, A. Capozzoli, M.Perino, Thermal bridges in vacuum insulation panels at building scale, Proceedings of the Institution of Civil Engineers - Engineering Sustainability (2016).
7. A. Gagliano, F. Patania, F. Nocera, A. Ferlito, A. Galesi, Thermal performance of ventilated roofs during summer period, Energy and Buildings, Volume 49, June 2012, Pages 611-618, ISSN 0378-7788.
8. C. Marinosci, G. Semprini, G.L. Morini, Experimental analysis of the summer thermal performances of a naturally ventilated rainscreen façade building, Energy and Buildings, Volume 72, April 2014, Pages 280-287, ISSN 0378-7788.
9. D. Mazzeo, G. Oliveti, N. Arcuri, Mapping of the seasonal dynamic properties of building walls in actual periodic conditions and effects produced by solar radiation incident on the outer and inner surfaces of the wall, Applied Thermal Engineering, Volume 102 (2016), 1157-1174.
10. M. Saffari, A. de Gracia, S. Ushak, L.F. Cabeza, Economic impact of integrating PCM as passive system in buildings using Fanger comfort model, Energy and Buildings 112 (2016),

11. A. L. Pisello, V. L. Castaldo, C. Fabiani, F. Cotana, Investigation on the effect of innovative cool tiles on local indoor thermal conditions: Finite element modeling and continuous monitoring, Building and Environment 97 (2016),
12. Farah Souayfanea, Farouk Fardouna, Pascal-Henry Biwoleb,Phase change materials (PCM) for cooling applications in buildings: A review, Energy and Buildings 129 (2016) 396–431.
13. M. Pomianowski, P. Heiselberg, Y. Zhang, Review of thermal energy storage technologies based on PCM application in buildings, Energy Build. 67(December) (2013) 56–69.
14. F. Kuznik, J. Virgone, K. Johannes, In-situ study of thermal comfort enhancement in a renovated building equipped with phase change material wallboard, Renew. Energy 36 (May (5)) (2011) 1458–1462.
15. X. Xu, Y. Zhang, K. Lin, H. Di, R. Yang, Modeling and simulation on the thermal performance of shape-stabilized phase change material floor used in passive solar buildings, Energy Build. 37 (October (10)) (2005)1084–1091.
16. Xiangfei Kong, Shilei Lu, Yiran Li, Jingyu Huang, Shangbao Liu, Numerical study on the thermal performance of building wall and roof incorporating phase change material panel for passive cooling application, Energy and Buildings 81 (2014) 404–415.
17. A. Komerska, L. Bianco, V. Serra, S. Fantucci, M. Rosiński, Experimental Analysis of an External Dynamic Solar Shading Integrating PCMs: First Results, Energy Procedia 78 (2015) 3452-3457.
18. www.rubitherm.com,(Access: 10/2016).
19. R.Voller, An overview of numerical methods for solving phase-change ,Advances in Numerical Heat Transfer 1, Taylor & Francis, London (1996), Chapter 9.

Chapter6

CFD modelling of glazed facades

6.1 Introduction

This chapter represents a brief clarification of how to analyze thermal performance of glazed façade. The illustrated CFD numerical models of infrared, solar radiation through semi transparent elements have been validated. Steady state case study of 3D model have been clarified .The aim of this chapter is to summarize the set of models in order to analyze the glazed façade component.

Objectives

1- **Illustrate and validate the proper set of CFD modes to simulate glazed facades.**
2- **Clarification of innovative integration of PV in glazed buildings**

6.2 CFD modelling Background

Although implementing CFD is considered an accurate method to investigate the air circulation, and thermal performance of glazed facades, however it needs a strong scientific background and high computing capabilities. Zollner et al. [1] mentioned that in mechanically ventilated DSF systems, because of relatively high air flow speeds in comparison with naturally ventilated systems, the use of turbulent models in CFD numerical simulations is usually justified over the laminar models. Corgnati et al.[2] have mentioned that during the hot season the exhaust air flowing inside the air gap removes part of the heat loads (solar and transmission loads) through the facade, thus reducing the heat gains in the indoor environment. Due to the cooling action of the air flow, the surface temperature of the indoor facing glass panes is reduced compared to a non-ventilated transparent surface, which leads to a better local thermal comfort. Moreover it is possible to integrate PV cells in the DSF ,Han et al.[3]. Nemati [4] have presented a numerical and experimental study on the thermal behavior of combined multiple skin façade integrated with photovoltaic (PV) cells combined with shading system, panes venetian blinds, under mechanical ventilation to attain thermal energy in the form of preheated fresh air and produce electricity. Di Maio et al.[5], have carried out a dynamic simulation of a four-floor building in order to reduce the energy use for heating and cooling by coupling properly the integration of Double Skin Facades and HVAC systems. Gan [6] developed a numerical method for the prediction of thermal transmittance of multiple glazing based on Computational Fluid Dynamics. As he describes “the predicted thermal resistance of glazing agrees with reference data for double glazing unit”. Fuliotto [7] presented a comprehensive CFD analysis to understand double-skin

facades behavior in the different environmental conditions that could be a background for the development of an easy-to-use tool for designers that are approaching to the problem without specific thermos-fluid dynamics knowledge. He has validated his work by experimental data The results show that the thermo–fluid phenomena can be approximated to be two-dimensional. The CFD can calculate the temperature distribution in the DSF with reasonably good accuracy. The results also show that the decoupled method for radiative heat transfer is reasonable acceptable for such an advanced DSF.

6.3 Governing Equations[9]

The fluid dynamics main governing equations are Navier-Stokes , Continuity and Energy. All these equation in CFD are solved in different approaches. For steady incompressible flow the equations can be written in the form of Equations (6.1 to 6.3).

$$\frac{\delta u_i}{\delta x_i} = 0 \tag{6.1}$$

$$\rho \frac{\delta u_i u_{ij}}{\delta x_i} = \frac{\delta p}{\delta x_i} + \frac{\delta}{\delta x_i}\left[\mu\left(\frac{\delta u_i}{\delta x_j} + \frac{\delta u_j}{\delta x_i}\right)\right] \tag{6.2}$$

$$\rho \frac{\delta T u_j}{\delta x_j} = \frac{\delta}{c_p \delta x_i}\left(K \frac{\partial T}{\partial x_j}\right) \tag{6.3}$$

where ρ is the density, u the velocity, x_i the x is the postion tensor, K thermal conductivity, μ the dynamic viscosity, P the pressure, T temperature, c_p the specific heat capacity

6.4 Heat transfer modes

Heat transfer between double glass layers is governed by convection, conduction and radiation. The flow is considered turbulent flow between 2 plates as it driven by a ventilating exhaust fan. The numerical modeling of a BIPV/T system is a very complex task because of the presence of different coupled heat transfer mechanisms [8] .Laminar and turbulent, and free or forced (or mixed) convection, and long-wave and short-wave radiation exchange may all be present. Therefore, a successful model must be capable of successfully modeling all modes of heat transfer. Below the complexities mentioned above.

a- Heat Transfer by convection

Convection heat transfer is the transport mechanism made possible through the motion of fluid and it is described by the Equation (6.4):

$$q = h\,A\,(T_s - T_f) \tag{6.4}$$

Where q is the convective heat flux, A surface area, Ts surface temperature, T_f fluid temperature.

b- Radiative Transfer Equation

The radiative transfer equation (RTE) for an absorbing, emitting, and scattering medium at position $\vec{r}$ in the direction $\vec{s}$ is:

$$\frac{dI(\vec{r},\vec{s})}{ds} + (a+\sigma_s)I(\vec{r},\vec{s}) = an^2\frac{\sigma T^4}{\pi} + \frac{\sigma_s}{4\pi}\int_0^{4\pi} I(\vec{r},\overrightarrow{s'})\,\Phi(\overrightarrow{S'},\vec{S'})d\Omega' \tag{6.5}$$

Where:

$\vec{r}$ = position vector

$\vec{s}$= direction vector

$\overrightarrow{s'}$ = scattering direction vector

s = path length

a = absorption coefficient

n = refractive index

σs = scattering coefficient

σ = Stefan-Boltzmann constant (5.672 X10^8 W/m^2-K^4)

I = radiation intensity, which depends on position ($\vec{r}$) and direction ($\vec{S}$)

T = local temperature

Φ = phase function

Ω′= solid angle

(a + σs) = the optical thickness or opacity of the medium. The refractive index n was taken =1

c- **Turbulence**

There are in general three types of flow laminar, transient and turbulent and according to the value of Reynolds number the type of flow is determined $\mathrm{Re} = \frac{\rho v d_h}{\mu}$, To solve the governing equations without making approximations is very demanding, This led to some approximate approaches in a both robust and low error way. The RNG k-ε model was derived using a rigorous statistical

technique (called renormalization group theory). It is similar in form to the standard k-ε model, but includes the following refinements:

The RNG model has an additional term in its ε equation that significantly improves the accuracy for rapidly strained flows. The effect of swirl on turbulence is included in the RNG model, enhancing accuracy for swirling flows. The RNG theory provides an analytical formula for turbulent Prandtl numbers, while the standard k-ε model uses user-specified, constant values. The RNG theory provides an analytically-derived differential formula for effective viscosity that accounts for low Reynolds-number effects. Effective use of this feature does, however, depend on an appropriate treatment of the near-wall region. These features make the RNG k-ε model more accurate and reliable for a wider class of flows. The RNG-based k-ε turbulence model is derived from the instantaneous Navier-Stokes equations, using a mathematical technique called ”renormalization group" (RNG) methods. The analytical derivation results in a model with constants different from those in the standard k- ε model, and additional terms and functions in the transport equations for k and ε.

d- Transport Equations for the RNG k- ε Model

The RNG k- ε model has a similar form to the standard k- ε model:

$$\frac{\partial}{\partial x_i}(\rho K u_i) = \frac{\partial}{\partial x_i}\left(\alpha_k \mu_{eff} \frac{\partial k}{\partial x_i}\right) + G_k + G_b - Y_m - \sigma_E + S_k \tag{6.6}$$

$$\frac{\partial}{\partial x_i}(\rho \varepsilon u_i) = \frac{\partial}{\partial x_i}\left(\alpha_\varepsilon \mu_{eff} \frac{\partial \varepsilon}{\partial x_i}\right) + C_{1\varepsilon}\frac{\varepsilon}{k}(G_k + C_{3\varepsilon}G_b) + C_{2\varepsilon}\rho\frac{\varepsilon^2}{K} - R_\varepsilon + S_\varepsilon \tag{6.7}$$

In these equations, Gk represents the generation of turbulence kinetic energy due to the mean velocity gradients. Gb is the generation of turbulence kinetic energy due to buoyancy. YM represents the contribution of the fluctuating dilatation in compressible turbulence to the overall dissipation rate. The quantities α_ε and α_k are the inverse effective Prandtl numbers for k and ε, respectively. The model constants C1ε, C2ε, σk, and σε have the following default values **[9]**:

C1ε = 1.42, C2ε = 1.68, σk = 1.0, σε = 1.3.

6.5 Solar load Model

The right simulation of the solar load is considered the vital step of this research. The solar load model has been used at the simulation process consists of two main items:

6.5.1 Solar ray tracing

The solar ray tracing is a highly efficient and practical mean of applying solar loads as a heat sources in the energy equation. The solar load model's ray tracing algorithm has used to predict the direct illumination energy source that results from incident solar radiation. The resulting heat flux is coupled to the FLUENT via a source term in the energy equation. The sun direction vector and illumination parameters have been computed from the solar calculator after determining the global positioning, grid orientation, date & time.

6.5.2 DO radiation model

The discrete ordinates (DO) radiation model solves the radiative transfer equation (RTE) for a finite number of discrete solid angles, each associated with a vector direction fixed in the Cartesian system (x; y; z), (Fig.6.1). The solution method is identical to that used for the fluid flow and energy equations [9].

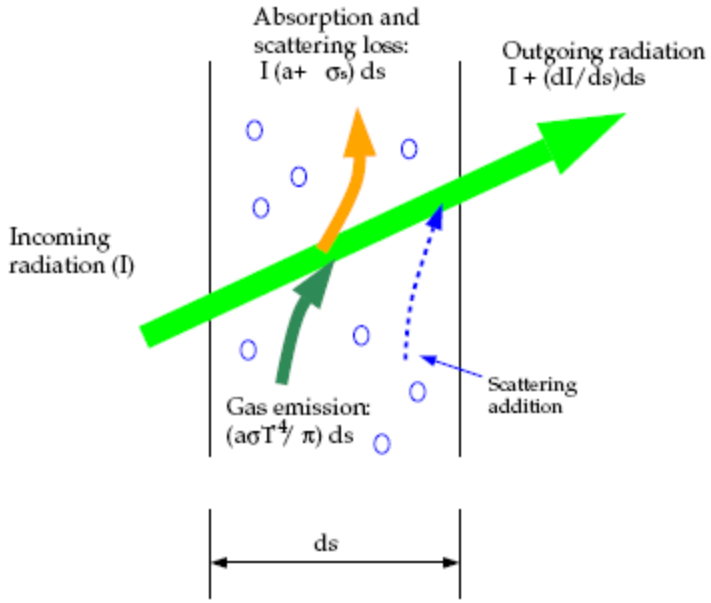

(Fig.6.1) Radiative Heat Transfer [14]

DO Model Equations

The DO model considers the Radiative Transfer Equation (RTE) in the direction $\vec{s}$ as a field equation. Thus, Equation (6.8) [9] is written as:

$$\nabla.(I_\lambda(\vec{r},\vec{s})\vec{s} + (a_\lambda + \sigma_s)I_\lambda(\vec{r},\vec{s}) = a_\lambda n^2 I_{b\lambda} + \frac{\sigma_s}{4\pi}\int_0^{4\pi} I_\lambda(\vec{r},\vec{s})\Phi(\vec{r},\vec{s}')d\Omega' \quad (6.8)$$

6.6 Air inlet and outlets

a- Velocity inlet

Velocity inlet boundary condition is defining the flow velocity, along with all relevant scalar properties of the flow, at flow inlets. The total (or stagnation) properties of the flow are not fixed, so they will rise to whatever value is necessary to provide the prescribed velocity distribution. The physical domain of the model uses both the velocity components and the scalar quantities which have been defined as boundary conditions to compute the inlet mass flow rate, momentum fluxes, and fluxes of energy and chemical species. The mass flow rate entering a fluid cell adjacent to a velocity inlet boundary is computed as:

$$m^{\circ} = \int \rho \, \vec{v} \, . d\vec{A} \tag{6.9}$$

b- Pressure outlet

At pressure outlets, the static pressure is considered the boundary conditions of the fluid at the outlet plane, and extrapolates all other conditions from the interior of the domain. The target mass flow rate could be identified and achieved by adjusting the pressure value at the pressure outlet up and down at every iteration until the target mass flow rate is obtained. The pressure iteration process includes loop over the pressure outlet boundary faces to calculate the mean static pressure and the mass flow rate; then the previously identified mass flow rate, the current computed mass flow rate, and mean static pressure in Bernoulli's equation are implemented to obtain a new mean static pressure value, applying under-relaxation to keep the solution stable.

Table 6.1 Summary of used glazed façade CFD models

Air inlet/outlet	Velocity inlet /pressure outlet
Viscous model	k-ε model
Radiation model	**DO** discrete ordinates
Solar load	Solar calculator
Semi transparent walls	convection and radiation boundary Mixed option

6.7 Tuning of the numerical model

A preliminary analysis related to the validation of applied numerical model has been carried out in order to check the mesh and if the CFD models and boundary conditions have been set in a proper way. For these purposes the work presented by (Safer et al. [10] was considered for tuning the

model. Safer has several published works discussing the use of CFD numerical simulation code to investigate thermal performance of DSF and the influence of several linked parameters such as the direct solar radiation, and the venetian blinds tilt angle effects [11,12]. In order to validate the CFD model, a 2D case with a simple flow inside a mechanically ventilated DSF has been carried out. Safer's DSF case is equipped with venetian blinds. The ventilation is external, i.e. (the air circulating in the cavity comes from and is rejected to the outside). As usual the inlet and the outlet are placed respectively in the bottom and the top of the external glazing, as shown in(Fig.6.2). Safer claimed that the 2D model should be enough to reduce the solving time as possible. The cavity was 0.2 m width and 3 m high. The blind slats were 25 mm in width. Inlet air open was at 100 mm from the bottom of the façade and outlet air open was a 100 mm from the top of the façade. It is important to mention that in Safer study several scenarios and configurations were considered, such as using blinds slats angles of 0°, 30°, 45°, 60°, varying direct solar radiation value, incident radiation angle and changing the blinds slats location with respect to the outer glass. The validation process in the present work has been based on the following scenario:

1- Blind slats deflection angle is 45°, slats located in the middle of the cavity**.**

2- Boundary conditions were fixed according to Safer's work, as illustrated in Table 6.2.

Temperature values have been calculated at middle of cavity height; the compared results showed a good agreement between Safer's and validation work to proceed with the same concept, as shown in (Fig.6.3).

Table 6.2 Safer's work boundary conditions

Component	Value
Direct solar radiation W/m²	910 (288.4)
Diffuse solar radiation W/m²	145 (45.9)
Incidence angle	66°
External temperature °C	29 (84.2)
External convective heat coeff. W/m².K	10 (1.76)
Internal temperature °C	25 (77)
Internal Convective heat coeff. W/m².K	2.5 (0.44)
Air inlet velocity m/s (fps)	0.22 (0.72)
Slat angle	45°

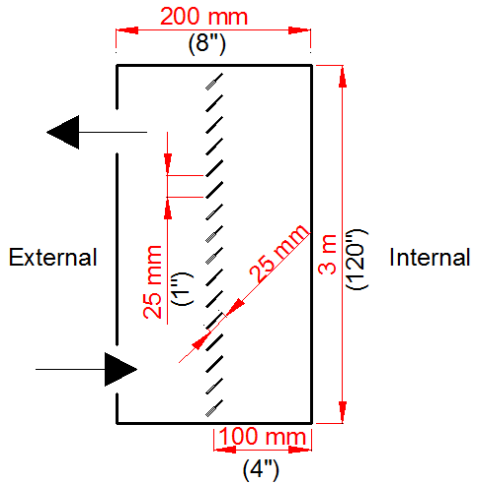

(Fig.6.2) Safer 2D model geometry with blinds slats angle of 45°

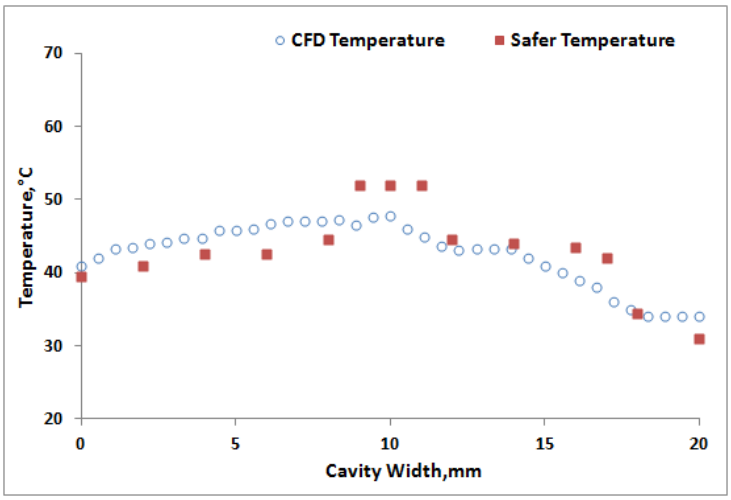

(FIG.6.3) CFD Model Validation

6.8 Case studies description

The aim of the CFD simulations case studies is to analyse the influence of implementing different types of air inlets on the air circulation efficiency inside the facade cavity. The considered DSF is integrated with PV module, mechanically ventilated (in-out) technique and by means of cooling the air cavity from the cold fresh air supplied to the inner zone [14] and left intentionally to keep the positive pressure relation of the air conditioned zone comparing to adjacent corridor, hence no increment in A/C loads shall be expected. A combination between diverse air inlets and outlets is clarified in Table 6.3. Accordingly the case studies are divided in to two sections, the first is with the circular air outlet in Cairo city, Egypt climatic conditions and the second is with the linear bar grille air outlet in Venice Italy and Abu Dhabi UAE cities. However investigating thermal performance of

the circular air outlet confronting different the five types of air inlets have been clarified thoroughly in Elarga et al. [15]. Results shown here for the best and worst performance.

Table 6.3 Air outlets cases

Air inlets types	Air outlets types
One rectangular opening Two symmetric rectangular openings Linear bar grille 90° deflection angle Linear bar grille 60° deflection angle Linear bar grille 30° deflection angle	→ Circular air outlet
Linear bar grille 30° deflection angle	→ Linear bar grille air outlet

a- Circular air outlet (Cairo city case study)

Since the efficient implementation of PV modules inside the façade cavity is a controversial issue, because it depends on many factors such as its surface temperature and solar radiation intensity (Table 6.4). Results shown for two geometrical cases represents the minimum and maximum thermal performance in the condition of the peak external temperature equals to 42°C.

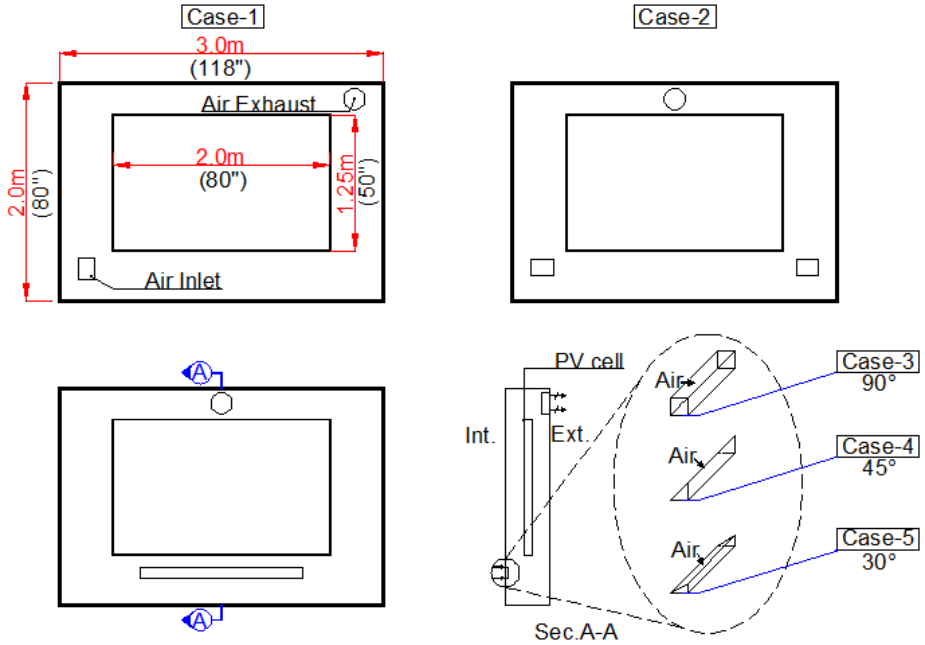

(Fig.6.4) Circular air outlet cases

The grids of the models were created in three-dimensions. In all cases, the mesh was based on tetrahedral cell; a range of 400000- 500000 volume cells has been used (Fig.6.5).

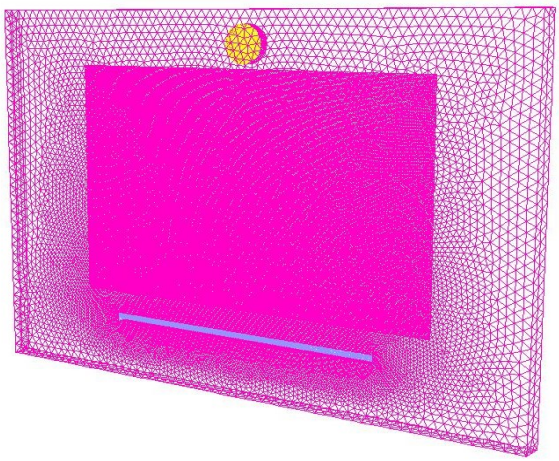

(Fig.6.5) 3D Grid Mesh display

Table 6.4 Boundary conditions (Cairo city case study)

Temperature Inside/ Peak °C	**Viscous model**	**Radiation model**	**Direct beam irradiation** W/m^2	**Glass density** kg/m^3	**Glass c_p** J/(kg K)	**Glass thermal conductivity**, W/(m K)
23/42	k-ε	DO	1000	2700	840	1

Electrical performance of PV modules

In order to evaluate the enhancement in PV cell performance voltage open circuit value Voc has been calculated based on Equation (6.10).

$$V_{oc} = Temp.coeff. \times (T_{stc} - T_{amb}) + V_{oc\,rated}) \quad (6.10)$$

Where:

Temp. coeff: is the temperature dependence of the PV module material type [V/°C]

V_{oc} is the open circuit voltage at module temperature [V]

T_{stc} is the module temperature at STC [°C]

T_{amb} is the module temperature [°C]

$V_{oc\,rated}$ is the open circuit voltage at STC [V]

The reduction in PV cell surface temperature has a positive consequence on its conversion efficiency and V_{oc} has improved by 2.25% from Case 1 of 22.2 V till Case 5 of 22.7 V. In order to assess

accurately the PV cell electrical performance; a cooling factor f_c is derived as below in Equation (6.11), and as shown in Table 6.5 the f_c for Case 5 equals to 0 which is considered the optimum value when the surface temperature of PV cell equals to STC.

$$f_c = \frac{V_{oc/STC} - V_{oc/after\ cooling}}{V_{oc/STC}} \tag{6.11}$$

Table 6.5 $f_c$cooling factor values

Cases	Case 1	Case 2	Case 3	Case 4	Case 5
f_c	0.019	0.016	0.011	0.004	0.0

The contours of temperature at both, , of the inner glass layer, which is attached to the conditioned zone, and of the PV cell front surface are shown in ((Fig.6.6). The temperature contours is affected by different geometries as denoted by variation in blue/red color scale, the blue color is denoting the minimum temperature of ventilating air which is considered the inside room design temperature equal to 22°C . For Case 1 with one rectangular opening on the low level, the average temperature on the inner glass layer has reached 27°C. On the other hand average temperature of inner glass in Case 5 has reached 25°C which is considered a good result for both thermal comfort and decreasing zone thermal loads. The average temperature of the PV cell in Case 1 reached 32°C and decreased down to 25°C in Case 5 due to the enhanced air circulation inside the cavity by using the linear bar grille with 30° as a deflection angle.

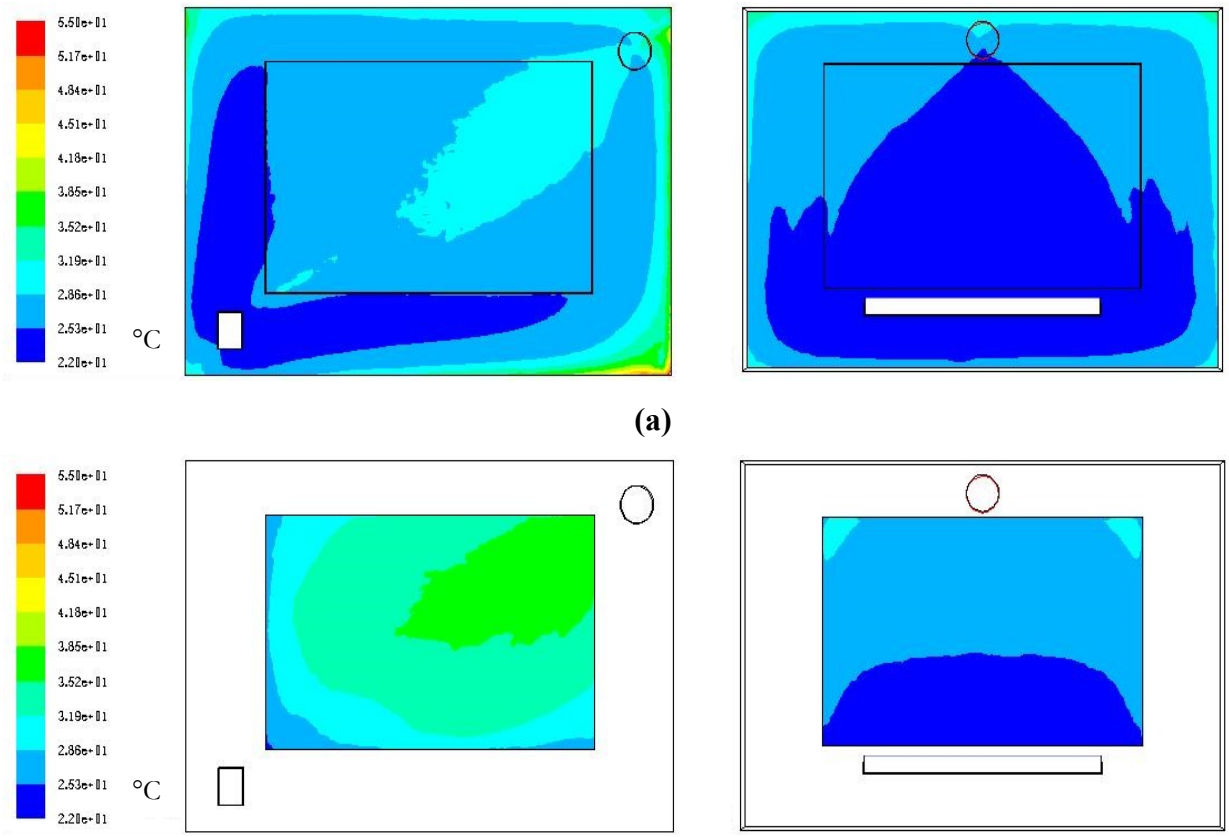

(Fig.6.6) (a) Temperature contours of Inner glass, Case 1 and Case 5 (b) Temperature contours of PV cell front face Case 1,and, Case 5 (Respectively from left side)

To confirm the effect of cavity ventilation another numerical simulation was carried out on Case 1 neglecting the ventilation. As result, the average surface temperature of PV cell equal 35° and it is higher than the ventilated Case 5 by 10°C, V_{oc} decreased by 2.8**%.** As illustrated in (Fig.6.7) the average temperature contours on PV cell are uniform due to the natural convection inside the cavity. Inverse proportional relation between average surface temperature of PV cell and its voltage open circuit value V_{oc} at the peak and the seasonal average external temperature values respectively has shown the improvement achieved **as** summarized in (Fig.6.8).

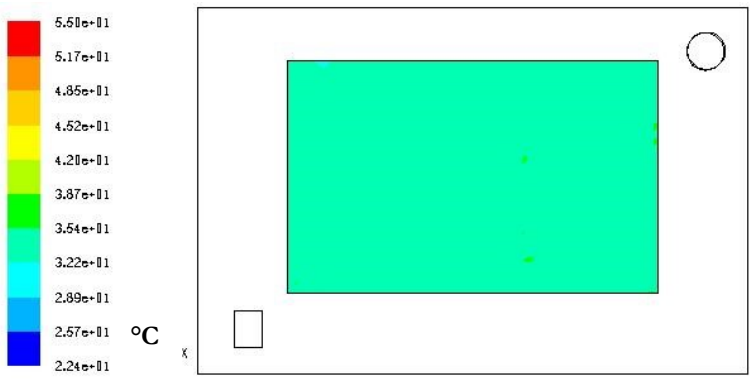

(Fig.6.7) Average temperature contours on PV cell in Case 1 without ventilation

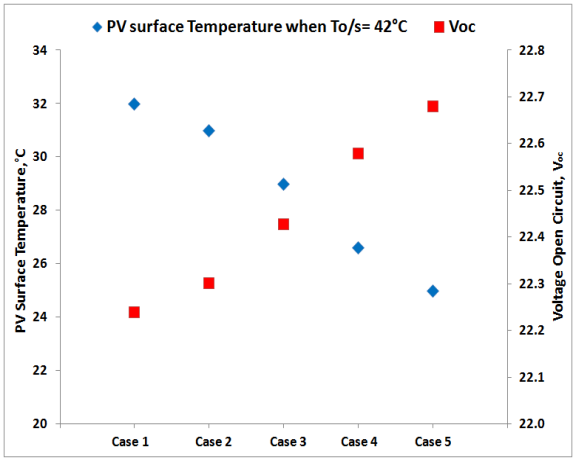

(Fig.6.8) (a) $T_{outside}$=42°C (PV Surface temperature and V_{oc}

b- Linear bar grille outlet, Venice and Abu Dhabi case studies

Investigation of different geometries aims to improve air circulation inside the façade cavity. Nevertheless as concluded from the previous case study in Cairo city that the best air circulation is due to the 30° deflection bar grille, Accordingly in Venice and Abu Dhabi case studies the same air inlet was assumed however another outlet air type was compared to the circular one.

Two geometries have been introduced. Case 1 represents the air inlet as a linear bar grille with a deflection throw angle of 30°, exhaust air outlet is a circular open installed at high level of outer glass (Fig.6.9). The geometry of Case 2 differs in exhaust outlet type which has been replaced by linear bar grille positioned in the upper part of the outer glass see(Fig.6.9). The air inlet remained as linear bar grille with deflection angle of 30°. To investigate the influence on the air circulation, external temperature was assumed to be the maximum coincident values of the Test Reference Year (TRY), inside temperature is assumed to be 26°C for Venice and 22°C for the later city due to Abu Dhabi urban planning council. Boundary (ESTIDAMA [13] conditions are illustrated in Table 6.6.

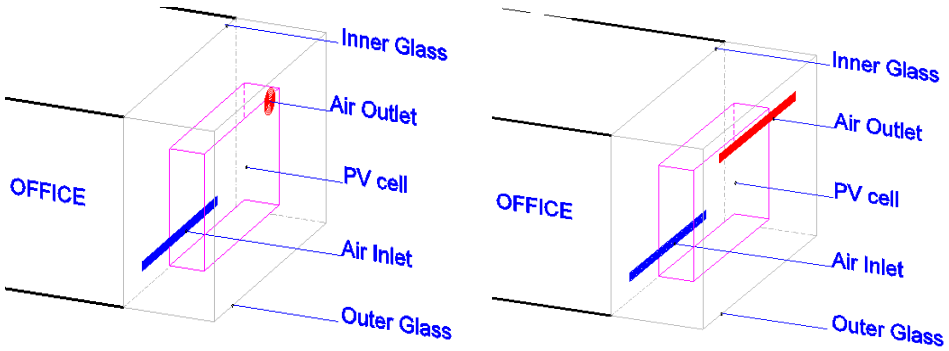

(a) **(b)**

(Fig.6.9) Case studies: (a) Case 1, (b) Case 2

Table 6.6 Boundary conditions

City	Venice	Abu Dhabi
Long./Lat. [°]	11.5/45.2	54.2/24.3
External Temperature [°C]	32	46
Inner Temperature [°C]	26	22
Ventilation air flow rate [L/s]	30	30
Air inlet velocity [m/s]	1.3	
Glass density [kg/m^3]	2700	
Glass specific heat capacity [J/(kg K)]	840	

Due to the inside design temperature difference of 4 °C higher in Venice comparing to Abu Dhabi, the average temperatures of inner glass and PV surfaces are lesser at the later city. In Case 1 at Venice, average inner glass temperature reached 30°C while PV average surface temperature computed as 32°C (Fig.6.10). On the other side, in Abu Dhabi (Fig.6.10) average surface temperature of the inner glass was 27°C and PV surface temperature was 31°C. In Case 2 inner glass

average temperature of Venice (Fig.6.11) increases to 31°C, furthermore PV average surface temperature increased to 49°C; while for the same case study (Case 2) in Abu Dhabi(Fig.6.11), inner glass average temperature remained 27°C while the PV average surface temperature reached 40°C. To conclude air circulation inside the cavity was not improved by replacing circular exhaust opening to a linear bar grille.

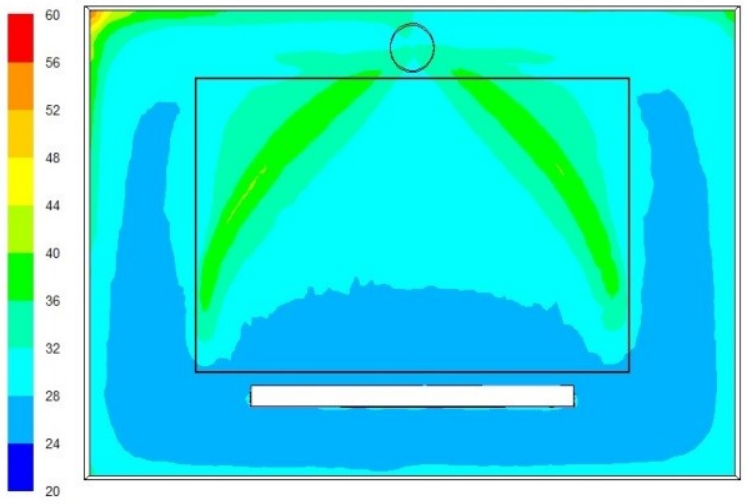

(a)

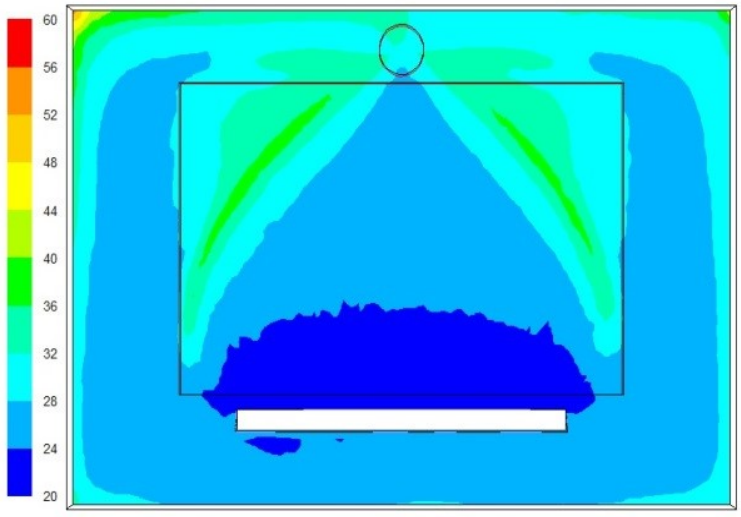

(b)

(Fig.6.10) Case1-Temperature contours (°C) on inner glass (a) Venice city, (b) Abu Dhabi city

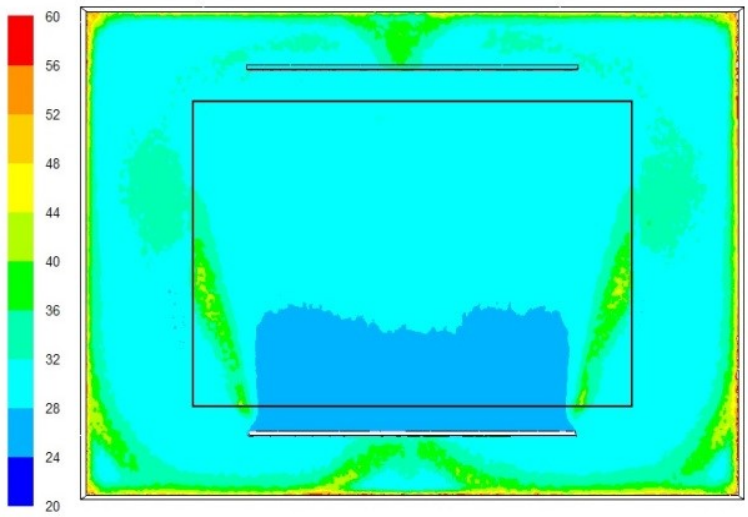

(a)

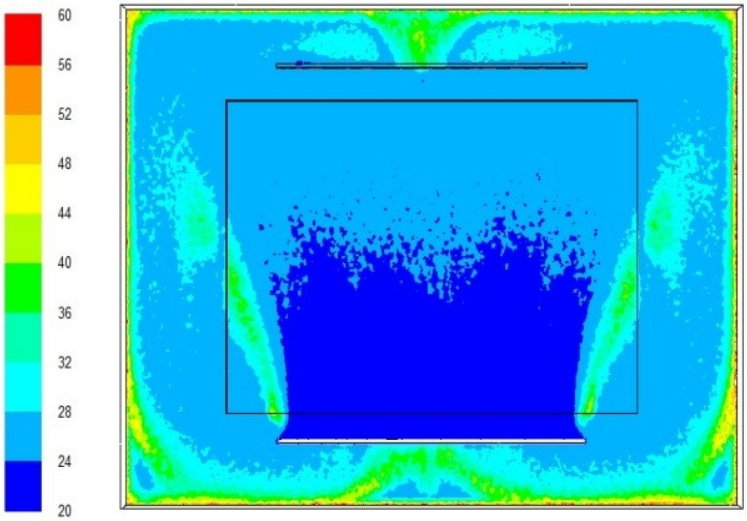

(b)

(Fig.6.11) Case2 Temperature contours (°C) on inner glass in Case 1: (a) Venice city, (b) Abu Dhabi city

PV module Electrical Production

The improvements in PV surface temperature reflected on output generated electric power. The Voc value was determined .The Voc of the PV cell in Case 1 in Venice city was equal to 22.2 V while it decreased to be 21.7 V in Case 2 due to air circulation inside the cavity On the other hand, in Abu Dhabi city, Voc was estimated at Case 1 to be equal to 22.3 V, while in Case 2 decreased to be 21.2 V.

Simplified Thermal Resistance Model

To investigate effect of cooling the cavity, a simplified thermal resistance model was derived to determine glass layers and PV cell surface temperature in case of no ventilation. As illustrated in (Fig.6.12) the schematic of the model, thermal resistances are considered as only conductive as a result of still air cavity except for thermal resistances between (node 1) outer glass layer and external and inner glass layer (node 3) and internal air node.

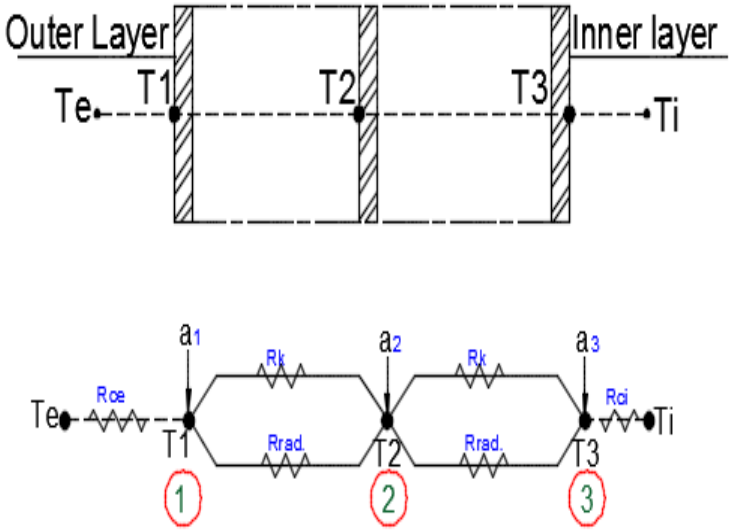

(Fig.6.12) Thermal resistance model

Thermal balance of each thermal node is presented through Equations (2), (3) and (4). Thermal balance in node 1 is presented by convection thermal resistance R_{ce} between T_e and surface temperature T_1, conduction thermal resistance R_k and radiative thermal resistance R_{rad} between node 1 and node 2. While in node 2 thermal balance considered conductive and radiative heat transfer with node 1 and node 3. Finally at node 3, convective resistance R_{ci} between node 3 and inner air node was considered, added to conductive and radiative resistance with previously mentioned node 2.

$$\left[\left({}^{-1}/_{R_{ce}}\right)+\left({}^{-1}/_{R_{equ}}\right)\right]T_1+\left({}^{1}/_{R_{equ}}\right)T_2=-I_{sol}.a_1-h_c\,T_e \tag{6.12}$$

$$\left({}^{1}/_{R_{equ}}\right)T_1+\left({}^{-2}/_{R_{equ}}\right)T_2+\left({}^{1}/_{R_{equ}}\right)T_3=-I_{sol}.a_2 \tag{6.13}$$

$$\left[\left({}^{-1}/_{R_{ci}}\right)+\left({}^{-1}/_{R_{equ}}\right)\right]T_3+\left({}^{1}/_{R_{equ}}\right)T_2=-I_{sol}.a_3-h_c\,T_i \tag{6.14}$$

Without ventilation of the cavity PV cell surface temperature reached in Venice city about 105 °C while in Abu Dhabi it reached 110 °C.

6.9 Conclusions

The main purpose of the chapter is to summarize the CFD models to investigate heat transfer modes in glazed façade layers through different geometries. The efficiency of air circulation and thermal distribution over façade layers integrated with PV modules was clarified. In Cairo city applying this technique of cooling with different geometries has increased PV/Voc by 2.25% and enhanced thermal performance of the façade by reducing inner glass temperature to 25°C which should reflect on energy consumption of the building. The improvement in Voc per PV module is considered accepted from surface cell temperature point of view because the cooling process is retaining surface temperature to the STC. It is expected to have better thermal performance inside the façade cavity and air conditioned zone if airflow rate is increased due to increment of occupancy. In order to improve the air distribution inside the air cavity, two linear grilles in opposite locations were implemented. A comparison was accomplished between two cities Venice and Abu Dhabi with different climatic conditions and indoor design temperatures due to variant perception of indoor thermal comfort. The inside inner glass temperature was investigated at both geometries. A simplified thermal resistance model presented three thermal nodes of glass layers temperatures, conduction and radiation heat transfer between these nodes without any kind of ventilation. Applying this technique of cooling with different cases has increased PV Voc by a range of 18 to 26% at Venice comparing to a non-ventilated cavity, on the other have range of improvements reached 22 to 28% in Abu Dhabi city.

6. References –Chapter 6

1. Zöllner, E.R.F. Winter, R. Viskanta, 2002. Experimental Studies of Combined Heat Transfer in Turbulent Mixed Convection fluid Flows in Double-Skin-Facades. International Journal of Heat and Mass Transfer 45:4401-4408.

2. S.P. Corgnati ,M. Perino , V. Serra, 2007. Experimental assessment of the performance of an active transparent facade during actual operating conditions. Solar Energy 81:993–1013.

3. J. Han, L. Lu, H. Yang, 2009.Thermal behavior of a novel type see-through glazing system with integrated PV cells, Building and Environment 44, 2129–2136.

4. Nemati, 2010, Analysis of a Mechanically Ventilated Multiple-skin Façade with Between-the-Panes Venetian Blinds,(M.Sc) University of Waterloo, Canada.

5. Di Maio, F., & van Paassen, A.H.C. (2000). Second skin façade simulation with Simulink code. International symposium air conditioning in high rise buildings (Shanghai), s.n.,s.l.,ISBN 2-913149-07-3, catc, Project code: 06A-V.
6. Gan, G. (2001). Thermal transmittance of multiple glazing: computational fluid dynamics prediction. Applied Thermal Engineering. 21 (2001) 1583-1592.
7. Roberto Fuliotto, January 2008, Experimental and Numerical Analysis of Heat Transfer and Airflow on an Interactive Building Façade.(PhD). Università degli Studi di Cagliari.

8. D.Saelens., 2002. Energy Performance Assessment of Single Storey Multiple-Skin Facades. PhD thesis publication, Katholieke Universiteit Leuven, Belgium.

9. Fluent user guide version 6.3.

10. N. Safer, M. Woloszyn, G. Rusaouën and J.J. Roux. 2004. Numerical studies with CFD approach of the heat and air flow transfers combined with solar radiation in double skin facades. The 21th Conference on Passive and Low Energy Architecture. Eindhoven, Netherlands,1-6.

11. Safer, N., Woloszyn, M., Roux, J-J. 2004a. Influence of solar radiation on heat and air flow transfers in double-skin facades with venetian blinds. 9th International Conference on Air Distribution in Rooms (ROOMVENT 2004), Coimbra Portugal.

12. Nassim Safer and Monika Woloszyn, 2005, Modeling of the double-skin facades for building energy simulations: radiative and convective heat transfer, Ninth International IBPSA Conference,1067-1074.

13. www.estidama.org, Abu Dhabi urban planning council (Access: 10/2016).

14. ASHRAE. 2007. ANSI/ASHRAE Standard 62.1-2007, Ventilation of Acceptable Indoor Air Quality. American Society of Heating, Air-Conditioning and Refrigeration Engineers, Inc.

15. H.Elarga,2013, Numerical simulation of mechanically ventilated DSF integrated with PV cells, Master of science thesis, Arab academy for science and technology , Alexandria , Egypt.

The Overall Conclusions

This research addressed the implementation of finite difference method to describe numerically the thermal performance of buildings envelopes with particular reference to the glazed facades integrated with different technologies.

The research firstly has clarified and validated a detailed mathematical model 'DIGITHON', as for the version that evaluates on transient basis the energy performance of glazed buildings. To follow, a parametric study included different climatic conditions, façade orientations and configurations to analyze the energy recovery through façade cavity. The preheating efficiency term for each case study has been evaluated. Results showed that an average pre-heating efficiency reached 8% in south Europe cities.

Later a simplified mathematical model coupled with thermal energy balance equations has been developed and validated with experimental data. This numerical transient model was based on finite difference/resistance capacitance methods. Comparison analysis showed that the simplified model can be adopted in the project's preliminary phase even with higher estimated values of the required thermal loads in respect to the detailed model DIGITHON. Indeed, this overestimated value can be considered a safety margin.

Innovative integration of PV modules in glazed buildings has been investigated and analyzed through commercial software TRNSYS. The investigated PV location combined with different ventilation strategies to obtain better PV surface temperatures in different climatic conditions have shown a good results in warm and cold climates during winter with savings range between 20 to 30%. On the other hand, in summer season the thermal loads results were higher by 40 to 50 % comparing to not integrating PV system as a result of the high solar absorption capability of the PV module. This fact increases the air cavity temperature, the indoor layer surface temperature and the required cooling loads. Accordingly, the phase changing material adoption took place in the research. The intention was to evaluate the latent thermal storage capability and its influence on the building required thermal loads. Two numerical methods have been explained and validated in respect of experimental data. It was shown that PV/PCM is a promising system in hot climates for summer season and in Nordic climates for winter season; thermal heating savings ranged between 25 to 30%. The research highlighted the importance of the proper selection of PCM and ventilation schedule.

Another topic was covered in experimental and numerical methods, namely the adoption of PCM and reflective surfaces in roof attic spaces in residential buildings. The right selection of PCM type is a focal aspect to assure the success of applied thermal storage system based on PCM. The proper selection can be carried out via a numerical evaluation using trial and error methodology. On the other hand it was shown that optimum reflective surface location is on the hottest surface in respect of roof section layers order. In this position the radiation heat exchange is minimized.

Finally CFD simulation modelling sets have been clarified and validated. Through different case studies for air inlets/outlets geometries, the air circulation and surface temperature profiles of a double skin façade integrated with a PV module have been shown.

Future Work

Improve the PV/PCM model to conclude the vertical conduction heat transfer through the PCM layer. Investigate PV/PCM system in different orientations.

List of publications

Journals

1- Elarga H ,Goia F, Zarrella A, Andrea Dal Monte ,Ernesto Benini. Thermal and electrical performance of an integerated PV-PCM system in double skin facades. A numerical study. **Solar energy Journal (2016).**

2- Elarga H, De Carli M ,Zarrell A, Dynamic energy evaluation and glazing layers optimization of façade building with innovative integration of PV modules. **Energy and buildings Journal (2016).**

3- Elarga H, Zarrella A, De Carli M , A simplified mathematical model for transient simulation of thermal performance and energy assessment for active facades. **Energy and buildings Journal (2015).**

4- De Carli M, Elarga H, Zarrella A, Tonon M. Evaluation of energy recovery of multiple skin facades: the approach of DIGITHON. **Energy and buildings Journal (2014)**.

International Conferences

5- Elarga H, De Carlli M, Zarrella A, Aboelazm M, Alvarez C . Assessment of Active Double Skin Façade Integrated With PV Cell. In: ASHRAE-PROCEEDINGS. Chicago,USA (2015).

6- Elarga H, De Carli M, Zarrella A, CFD Analysis of active facades integrated with PV cells in different climates. ASME-ATI- UIT proceedings, (2015).

7- Di Bella A, Giovanni G, Barbaresi L, Granzotto N, Elarga H Cosimo Marinosci , Balancing of thermal and acoustic insulation performance in building envelope design. NOISE-CON PROCEEDINGS, (ISSN:0736-2935), (2015).

8- Bedon G, De Betta S, Elarga H, De Carli M, Benini E. A Novel Implementation of Wind Energy in Buildings based on Synthetic Jet Concept. In: Proceedings of the EWEA 2015 Conference. Paris, France, (2015).

9- Elarga H, De Carli M .Benini.E. Overall energy evaluation for different integration methods of photovoltaic modules in facade building. CLIMA 2016 - proceedings of the 12th REHVA World Congress, Denemark, Volume:2, (2016).

10- Elarga H, Goia F., Benini.E PV-PCM integration in glazed buildings. Numerical study through MATLAB/TRNSYS link model. Building Simulation Applications Conference, Bolzano, Italy (ISSN: 2531-6702), (2017).

National Conference

11- Elarga H, De Carli M, Zarrella A, Valutazione energetica dell'edificio per uffici integrato con celle fotovoltaiche con TRNSYS 2-32° Convegno Nazionale di Padova "L'impiantistica per i climi estremi: tecnologie per i nuovi mercati della clima.

Appendix-A

The literature review experimental set of data used in the research has been collected via measuring campaign for a glazed building San Vendemiano (TV) of Permasteelisa property in Italy. The building Fig.1 in general contains 14 Tests rooms equipped with several facades types:

Fig.1 Glazed building view

-Active, Interactive, Shading, bioclimatic, Curtain and Traditional walls

Measuring instruments

The experimental camping included measuring air temperature, airflow rate in the cavity and vertical incident solar radiation.

1-Temperature sensors

Resistance thermometers have been used to measure air and glazed surface temperature. The principle of its operation is that the electrical resistance of the sensors is strongly temperature dependent, and changes with temperature in a predictable way. In Table-1 shown the technical specifications.

Table-1 Thermometers technical specifications

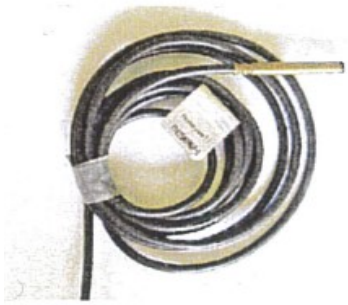

Manufacturer	Honeywell
Model	T7415A1007
Range	0-110℃
Sensitivity	3.85 Ω/℃
Nominal resistance	1000 Ω at1 ℃

2-Air flow rate sensors

X flow grid sensor was used to evaluate the volume flow rate of air. The Grid consists of a set of parallel tubes connected by manifolds. The tubes are perforated in such a way as to provide a single differential pressure signal, which is proportional to the square of the mean velocity in the airway. By connecting the output tubes to a suitable instrument, the pressure difference and hence the volume flow rate can be easily measured. A flow grid transmits a comparable and repeatable differential pressure proportional to the average airflow, see Table-2.

Table-2 X flow grid sensor technical specifications

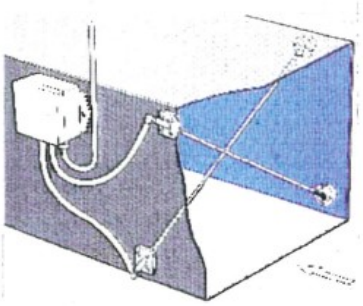

Manufacturer	Airflow
Model	Xflow grid
Velocity rate	1.5-130 m/s
Accuracy	±5%
Max Temperature	80℃

3-Pyranometers

It depends on the thermoelectric detection principle in its operation, whereby incoming radiation is almost completely absorbed by a horizontal blackened surface, over a very wide wavelength range. The resulting increase of temperature is measured via thermocouples connected in series or series-parallel to make a thermopile. See Table 3.

Table-3 Pyranometers technical specifications

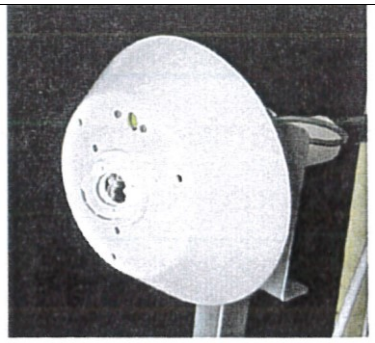

Manufacturer	MICROS
Model	RIP
Range	0-1300 W/m^2
Accuracy	±1.5
Response time	5 s
Temperature range	-30 / 80℃